

## 3D Radiation Dosimetry Using a Radio-Fluorogenic gel

Yao, Tiantian

**DOI**

[10.4233/uuid:e8590e7e-944c-4b4c-bc2b-3843400a9f85](https://doi.org/10.4233/uuid:e8590e7e-944c-4b4c-bc2b-3843400a9f85)

**Publication date**

2016

**Document Version**

Final published version

**Citation (APA)**

Yao, T. (2016). *3D Radiation Dosimetry Using a Radio-Fluorogenic gel*. [Dissertation (TU Delft), Delft University of Technology]. <https://doi.org/10.4233/uuid:e8590e7e-944c-4b4c-bc2b-3843400a9f85>

**Important note**

To cite this publication, please use the final published version (if applicable).  
Please check the document version above.

**Copyright**

Other than for strictly personal use, it is not permitted to download, forward or distribute the text or part of it, without the consent of the author(s) and/or copyright holder(s), unless the work is under an open content license such as Creative Commons.

**Takedown policy**

Please contact us and provide details if you believe this document breaches copyrights.  
We will remove access to the work immediately and investigate your claim.

# **3D Radiation Dosimetry Using a Radio-Fluorogenic gel**

Tiantian YAO

Cover: A 3D reconstruction of the fluorescent image of the radiation dose delivered by crossed round and square X-ray beams in a tissue-equivalent radio-fluorogenic gel.

# **3D Radiation Dosimetry Using a Radio-Fluorogenic gel**

**Proefschrift**

ter verkrijging van de graad van doctor  
aan de Technische Universiteit Delft,  
op gezag van de Rector Magnificus prof.ir. K.C.A.M. Luyben;  
voorzitter van het College voor Promoties,  
in het openbaar te verdedigen op  
maandag 16 januari 2017 om 10:00 uur

door

Tiantian YAO  
Bachelor of Science in Applied Physics,  
University of Science and Technology of China, Hefei, China  
geboren te Anhui, China

This dissertation has been approved by the  
promotor: Prof. dr. H.T. Wolterbeek  
copromotor: Dr. ir. A.G. Denkova

Composition of the doctoral committee:

Rector Magnificus	chairman
Prof. dr. H.T. Wolterbeek	Delft University of Technology
Dr. ir. A.G. Denkova	Delft University of Technology

Independent members:

Prof. dr. J.H. van Esch	Delft University of Technology
Prof. dr. S.A.J. Bäck	Lund University
Prof. dr. J.P. Pignol	Erasmus Medical Center
Prof. dr. E.H. Brüch	Delft University of Technology
Dr. ir. J.A. de Pooter	Dutch Metrology Institute

Reserve member:

Prof.dr. P. Dorenbos	Delft University of Technology
----------------------	--------------------------------

The work presented in this PhD thesis is financially supported by the Chinese Scholarship Council (CSC), and carried out at the section Radiation and Isotopes for Health (RIH), Faculty of Applied Sciences, Delft University of Technology (TUD).

Copyright © 2016 by Tiantian Yao  
ISBN 978-94-6295-563-9  
Printed by: ProefschriftMaken

An electronic version of this dissertation is available at  
<http://repository.tudelft.nl/>.

# Contents

## Chapter 1 Introduction

1.1.	Introduction	1
1.2.	Diagnostic methods	2
1.3.	Radiation therapy	4
	1.3.1. External sources	4
	1.3.2. Internal sources	8
1.4.	Dosimetry techniques	10
	1.4.1. Single volume measurements	11
	1.4.2. 2D measurements	13
	1.4.3. 3D measurements	15
1.5.	Radio-fluorogenic (RFG) gels	18
1.6.	Thesis overview	21

## Chapter 2 Polymer-gel formation and reformation on irradiation of tertiary-butyl acrylate

2.1.	Introduction	33
2.2.	Experimental	34
	2.2.1. Materials	34
	2.2.2. Sample preparation	35
	2.2.3. Irradiation procedure and monomer conversion	36
	2.2.4. Reformed gels	38
2.3.	Results and Discussion	39
	2.3.1. Gel properties	39
	2.3.2. Dose and dose rate dependence of monomer conversion	40
	2.3.3. Monomer conversion in a reformed gel	43
2.4.	Conclusions	45

## Chapter 3 The radiation-chemical and optical properties of a radio-fluorogenic solution

3.1.	Introduction	49
3.2.	Materials and Methods	50
	3.2.1. Materials	50
	3.2.2. Irradiation procedure	54
	3.2.3. Monomer conversion and gel formation	55

3.2.4.	Fluorimeter measurements	55
3.2.5.	CCD camera fluorescence imaging	56
3.3.	Results and Discussion	61
3.3.1.	Spectrophotometer and spectrofluorimeter measurements	61
3.3.2.	CCD camera fluorescence imaging	64
3.3.3.	Monomer conversion and gel formation	70
3.3.4.	The MPy concentration and dose rate dependence of the fluorescence	74
3.3.5.	An RFG solution as dosimeter	76
3.4.	Conclusions	78

#### **Chapter 4 A comparative study of the fluorogenic compounds N-(1-pyrenyl)maleimide, "MPy", and N-(1-pyrenyl)acrylamide, "PyAM"**

4.1.	Introduction	81
4.2.	Materials and methods	82
4.2.1.	Materials	82
4.2.2.	Optical equipment	83
4.2.3.	Irradiation equipment	83
4.3.	Results and Discussion	84
4.3.1.	Optical absorption spectra	84
4.3.2.	Optical emission spectra	86
4.3.3.	Gel formation and monomer conversion	88
4.3.4.	Fluorescence imaging	90
4.4.	Conclusions	92

#### **Chapter 5 The preparation and properties of a reformed radio-fluorogenic (RFG) gel**

5.1.	Introduction	95
5.2.	Materials and Methods	96
5.2.1.	Reformed radio-fluorogenic (RFG) gel preparation	96
5.2.2.	The radiation sources	98
5.2.3.	Fluorescence measurement	99
5.3.	Results and Discussion	100
5.3.1.	Reproducibility of reformed RFG gels	100
5.3.2.	Post-irradiation effect	102
5.3.3.	The dose rate dependence	103
5.3.4.	The MPy concentration dependence	104
5.3.5.	Combined dose rate and MPy concentration dependences	106
5.4.	Conclusions	109

## **Chapter 6 The dose and dose-rate dependences of four radiochromic films currently used for (2D) radiation dosimetry**

6.1.	Introduction	113
6.2.	Materials and Methods	114
6.2.1.	Radiochromic films	114
6.2.2.	Irradiation	115
6.2.3.	Digitalization and quantification	116
6.3.	Results and Discussion	120
6.3.1.	Color-separated pixel data	120
6.3.2.	Start-stop dose corrections	121
6.3.3.	Dose and dose rate dependences	125
6.4.	Conclusions	129

## **Chapter 7 Bulk and tomographic fluorescent imaging of X-ray beams**

7.1.	Introduction	137
7.2.	Materials and methods	138
7.2.1.	Materials	138
7.2.2.	Irradiation facilities	139
7.2.3.	Fluorescence imaging	141
7.2.4.	Image analysis using ImageJ	143
7.2.5.	Construction of 3D representations from tomographic images	144
7.3.	Results and discussion	145
7.3.1.	Radiochromic film measurements	145
7.3.2.	Bulk RFG gel measurements	146
7.3.3.	Tomographic RFG gel measurements	148
7.3.4.	3D image reconstructions	157
7.4.	Conclusions	161

<b>Summary</b>	163
<b>Samenvatting</b>	167
<b>Acknowledgements</b>	171
<b>Curriculum Vitae</b>	173
<b>List of Publications</b>	174





# Chapter 1

## Introduction

### 1.1. Introduction

Cancer treatment usually starts with the acquisition of tumour imaging data in order to assess the 3D shape, location and stage of the tumour in the patient and to determine the best therapy. Common treatments of solid tumours are surgery, external beam radiotherapy and brachytherapy, while chemotherapy and radionuclide therapy are often used to attack metastasis (Chatal and Hoefnagel, 1999; Dafermou et al., 2001; Demanes et al., 2005; Georg et al., 2008; Peschel and Colberg, 2003; Van Cutsem et al., 2009). The term radiation therapy (radiotherapy) encompasses external radiation therapy, brachytherapy and radionuclide therapy, but in this thesis only the first two cancer treatments will be considered. In radiotherapy, high-energy ionizing radiation is utilized to damage the genetic material of cancer cells, helping in this way to reduce or stop

entirely tumour growth and even to destroy completely malignant sites. Similar to other cancer treatment approaches, radiotherapy has adverse effects as it can also damage the DNA of healthy cells either directly or indirectly by the creation of free radicals, limiting in this way the chance of treatment success. Maximizing cell damage at the tumour site while minimizing collateral damage to neighbouring healthy tissue can, however, be achieved by improving the precision of the delivered radiation dose according to the 3D shape and position of the tumour in a patient.

Radiotherapy is a complex process in the clinic, which requires tumour imaging, radiation treatment planning, and high precision and accuracy of radiation dose delivery. To determine the tumour contour and to prepare a treatment plan, computed tomography (CT) is most commonly used, and often combined with other imaging modalities such as positron emission tomography (PET) or single photon emission computed tomography (SPECT). The treatment plan is computed based on imaging data of the 3D shape and location of the tumour and the output information of the dose delivering system. The treatment plan requires a proper 3D dose distribution verification to ensure tumour coverage and spare healthy tissue as much as possible. The effectiveness of a treatment plan is mostly verified by its robustness against various error sources. In some institutions, nevertheless an additional dose verification method is applied, which typically concerns online dosimetry verification by measuring the exit dose using electronic portal imaging devices (EPID) (van Herk and Meertens, 1987; Van Herk et al., 1993). In recent years offline dosimetry verification using 3D dosimeters, such as gel dosimeters, have also been considered for quality assurance (QA) in an end-to-end test for treatments where a lower dimension dosimeter could fail, as for new or sharp-edged treatments (White and Pharoah, 2014). To compare planned and delivered dose, various kinds of 3D gel dosimeters have been investigated (Baldock et al., 2010; Schreiner, 2004; Seco et al., 2014), combined with imaging techniques as read-out systems, such as the most commonly used magnetic resonance imaging (MRI) (De Deene, 2009, 2010). However, gel dosimetry is still considered to be in the research phase and the introduction to routine clinical use is proceeding slowly.

The purpose of this thesis is to develop a new type of 3D gel dosimeter, i.e. a radio-fluorogenic (RFG) gel, which becomes fluorescent upon irradiation. This chapter is devoted to different radiation therapy methods and various dosimetry techniques, including gel dosimetry and in particular previous research on RFG gels. Imaging techniques are also described in this chapter because of the importance of acquiring 3D information of tumour shape and location and because some of the techniques are used as read-out systems for 3D gel dosimeters. Finally, this chapter will end with a brief description of the contents of this thesis.

## **1.2. Diagnostic methods**

As mentioned above the 3D volume information of the tumour is used to prepare a treatment plan and a 3D radiation dosimeter can be employed to verify that the delivered dose matches the prescribed one, which will be described in details in section 1.4.3. Various imaging modalities

can provide information on the 3D shape and location of the tumour in a patient. The most often applied are MRI, X-ray computed tomography (X-ray CT), both providing anatomical information, and PET and SPECT, both delivering functional information. All of these techniques will be described below.

X-ray CT uses an X-ray beam and detectors rotating around the scanned object generating a large number of pictures, which can be reconstructed to obtain 3D images. X-ray CT can be applied for viewing the density difference in an object with high-contrast resolution, thus it is applicable to visualize the tumour and hard tissue, especially the bone structures with less than 1% difference in tissue density (White and Pharoah, 2014). The quality of the images is affected by the dose delivered to the tissue, i.e. a lower dose increases image noise, and a higher dose results in higher-resolution images (Crowther et al., 1970), but leads to a greater risk of radiation-induced cell damage. Since the allowed dose of medical exposure to radiation has different limits for different organs, there are a wide range of CT doses among similar scan types (Raeburn, 2000).

MRI uses a constant and uniform magnetic field (so-called strong or  $B_0$ ), with a field transient, and pulsed magnetic field (weak or a  $B_1$ ) of radio frequencies to generate images of the scanned object (Haacke et al., 1999). The MRI method is based on the response of a nuclear spin to these fields. In most clinical applications, the free spins of hydrogen atoms in the body, which contains 70% water, are applied to create a signal, generating in this way an anatomic view of the body. In those sequences where the strong magnetic field is used, it aligns the nuclear spins of the hydrogen atoms and creates an energy difference between the spins aligned with or against the field. When the system reaches equilibrium, the magnetization reaches a stable value. Afterwards a radio pulsed weak field is applied, using frequencies which can cause resonance effect. When the radio pulse stops, the hydrogen spins return to the relaxed state and they emit radio-waves at a frequency depending on the strength of the magnetic field and the material, which can be detected and transformed to spatially resolved images providing information of the nuclei distribution. The contrast of tissues with different structures is distinguished by the rate of the restoration rate of the equilibrium state, which is reflected in the spin-lattice (T1) and spin-spin (T2) relaxation times.

PET is a functional imaging technique that produces detailed 3D images of physiology, metabolism and biochemistry instead of anatomic structure of the body (Saha, 2015; Ter-Pogossian, 1983). Prior to a PET scan, a positron-emitting radioactive substance is injected in the body of a patient, which accumulates in the place of interest. The emitted positron annihilates with an electron producing two gamma rays of 511 keV emitted in opposite directions. The gamma rays are subsequently detected by a gamma detector, allowing a “physiological map” of accumulation and distribution of the radioactive source in the tissue of importance. 3D images are then reconstructed by specific algorithms (Kinahan and Rogers, 1989; Rogers et al., 1987). PET can be combined with CT or MRI into integrated PET/CT and PET/MRI scanners, which

provides both detailed anatomical structural information from CT and MRI scans and functional information from PET scans (Ciernik et al., 2003; Judenhofer et al., 2008).

SPECT uses gamma-emitting radioactive tracers, which are injected into the blood stream of a patient to create a non-invasive nuclear image, delivering the 3D distribution of the radionuclide. SPECT imaging is performed by rotating a gamma camera around a patient to obtain multiple 2D images, which creates 3D images by tomographic reconstruction. The  $\gamma$ -rays emitted in SPECT can be measured directly. However, due to the attenuation of the incident photons by the collimator in SPECT, the detector can only detect photons that are perpendicular to the detector, leading to a loss of part of the information and low sensitivity (Sharir, T. et al., 2010). PET provides more precise and higher spatial resolution images than SPECT, since PET scanners detect two  $\gamma$  photons in opposite directions and the photons can be detected from different angles.

### **1.3. Radiation therapy**

In this chapter, the most commonly applied radiation therapy treatment procedures including external and internal beam radiation therapies, and brachytherapy will be described. The efficiency of radiation damage is evaluated using the so-called relative biological effectiveness (RBE), which is the ratio of biological effectiveness of one ionizing radiation to another at the same amount of absorbed dose. RBE depends on the radiation types, energy and the biological end-point definition, i.e. single strand or multiple strands damage, cell death, or morbidity. For instance, photons and electrons in general have lower RBE than the more massive particles such as protons or carbon ions. The term linear energy transfer, LET, is usually used in dosimetry, which is the rate of energy loss of the incident particles per unit path length,  $-dE/dx$ . LET depends on the nature of the radiation and on the material traversed.

#### *1.3.1. External sources*

External beam radiation therapy (EBRT) treats patients with photon beams, such as X-rays and  $\gamma$ -rays, or charged particle beams such as electrons, protons and carbon ions. The total dose of radiation is usually split into small fractions delivered over a period of time, e.g. five days a week and five to eight weeks in total. This allows healthy cells to recover between dose deliveries, and for tumour tissue to shrink. The dose fractionation is aimed at increasing damage to the tumour cells while preserving the healthy tissue. The fractions are dependent on the location and type of targeted tumour and the source of radiation, for instance, a common dose fraction in photon therapy ranges from 2 to 3 Gy which results in a total dose around 50 Gy. Various external beam radiation therapies are presented in more detail below.

### 1.3.1.1. High energies photon beams

There are three mechanisms of energy loss depending on the photon energy and the effective atomic number ( $Z$ ) of the material, i.e. photoelectric effect, Compton scattering and pair production. In the case of irradiation of tissue with low effective  $Z$ , Compton scattering is the predominant primary interaction between megavoltage photons. It involves the inelastic scattering of a photon by an electron, during which part of the energy is transferred to the electron. This high-energy photons lead to excitations and ionizations of the medium via coulomb interactions of other electrons of the medium. In cellular systems this can lead to DNA damage and frequently cell death.

In photon therapy either gamma rays or X-rays are used. In X-ray therapy a linear particle accelerator (LINAC) is applied to generate high energy X-rays. Clinical LINACs use mono-energetic electron beams to hit a tungsten target and thus generate high energy X-rays. The high energy X-rays emitted from the accelerator gantry, are collimated and shaped before exiting the machine. The gantry is rotated around the patient, lying on a couch, to irradiate from different angles and conform to the shape of the tumour.

The LINAC can be employed to treat all body sites using conventional techniques, such as 3D conformal radiation therapy (3DCRT), intensity-modulated radiation therapy (IMRT) and volumetric modulated arc therapy (VMAT). The radiation oncologists choose from these techniques depending on the shape, location and depth of the patient's tumor.

3DCRT is a commonly used method, which is designed to deliver a variable number of radiation beams to a tumor on the basis of its 3D shape and location. Each beam is shaped with a multi-leaf collimator (MLC) according to the beam's eye view (BEV), thus the tumour-bearing site is irradiated selectively and the normal tissue exposure is reduced.

IMRT uses computer-controlled linear accelerators to deliver high-precision radiation doses to the tumor. Small volumes of radiation beams with modulated intensity are delivered during IMRT to cover the whole tumour volume and conform more precisely to its shape, which enables IMRT to treat more complicated tumor shapes and is an improvement of 3DCRT. A treatment planning system, on basis of 3D computed tomography or MRI images of the tumor, can generate highly tailored and computerized dose distributions, even to concave tumor shapes (Levitt et al, 2012).

VMAT is a new technique targeted to deliver highly conformal dose with minimal normal tissue irradiation, by varying a number of parameters during a full and continuous arc rotation. In VMAT the MLC can dynamically move through a sequence of programmed field shapes, changing the MLC aperture shape and orientation and creating a fast seamless field of dose delivery, and thus modulating the dose intensity. In this way, the delivery time of radiation is reduced. Moreover, VMAT delivers radiation by adjusting the speed of the rotating gantry and the fluence output rate of the LINAC or delivers dose with dual gantry arcs (Nithya et al., 2014).

### 1.3.1.2. High energy particle beams

Particle beams have finite ranges when penetrating a medium, creating primary particle tracks which damage the material in the particle track. Low-energy secondary electrons having shorter ranges create a second ionization track, usually called delta ray, by the recoil particle and further ionize the medium in the localized region. Delta rays appear as branches near the start of the main track of the particles.

One critical difference between non-charged particles and charged particles lies in the pattern of energy deposition in the medium. When penetrating the medium, the energy loss of megavoltage X-rays increases sharply to the highest level in the build-up region and subsequently decreases exponentially. On the other hand, charged particles release their entire energy when travelling in the medium, thus have finite ranges. In this process, charged particles slow down and the kinetic energy loss per unit length increases slowly with decreasing speed and increasing penetration depth. A peak occurs in a very short distance before all particles stop, where the deposited dose increases sharply to the top and then decreases even more sharply to (close to) zero. This phenomenon is called the Bragg-peak (see figure 1.1) and has been applied in proton therapy and carbon therapy. Cyclotrons or synchrotrons are used for proton therapy to produce proton source with energy in a range of 70 to 250 MeV (Verhaegen and Palmans, 2001).

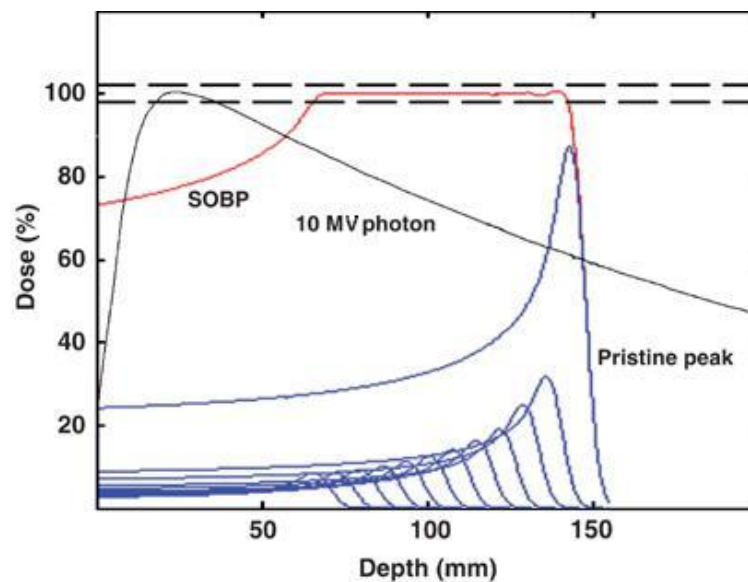


Figure 1.1. Depth-dose distributions for a spread-out Bragg peak (SOBP, red) including its constituent pristine Bragg peaks (blue), and a 10 MV X-ray beam (black) having the same maximum dose level as that of SOBP (Levin et al., 2005).

Figure 1.1 shows the depth-dose distributions in tissue for a 10 MV photon beam (black line), pristine Bragg peaks (blue lines) of proton beam, and a spread-out Bragg peak (SOBP) (red line) from the integration of the individual Bragg-peaks (Levin et al., 2005). Protons at given energies

have certain ranges, of which the most distal pristine peak determines the penetration depth of the SOBP dose distribution. Moreover, the SOBP can be modulated by adjusting the number and intensity of pristine Bragg peaks of proton beams, so that the dose distribution of the SOBP can provide complete target volume coverage in both depth and lateral directions to maximize tumour damage.

In figure 1.1 the megavoltage X-ray beam has the same maximum dose level in the tissue as the SOBP of the proton beam as shown by the dashed lines. As can be seen from the figure, the dose of the proton beam at the surface of the tissue (delivered to the skin) is higher than the one of the megavoltage X-ray beam, while the neighboring tissue at the backside of the tumor receives no radiation. This is also the major advantage of particle therapy, i.e. the possibility to spare the healthy tissue behind the tumour, making this technique especially suitable for tumors located near critical sites such as in the head, neck and kidney, or for vulnerable structures that are more sensitive to radiation.

In some cases, when treating eye tumours, a single proton beam is used, while in other cases multiple proton beams are usually delivered from different angles with the aim of distributing homogenous SOBP in the tumor volume, limiting the dose to the tissue along the proton beam. There are two methods of delivering proton radiation: the scattering method and the spot scanning method. The scattering method uses patient-specific beam-modifying devices to conform the dose to the treatment volume, i.e. a brass aperture to achieve lateral field conformation to the target volume based on a BEV and a plastic, usually polymethyl methacrylate (PMMA), range compensator to achieve distal conformation. To modulate a field with pristine Bragg peak curves, the proton beam energies are further adjusted with range modulation wheels which combine variable thickness absorbers in circular rotating tracks (Koehler et al., 1975). The distal falloff of the scattering method is not affected by the depth of the proton beam in tissue, but it depends on range straggling and increases with proton energy (De Laney and Kooy, 2008). The distal dose fall-off (distance from the 90% to the 10% dose level) of protons is sharp, i.e. is only a few mm (Paganetti and Bortfeld, 2005). Lateral falloff has a larger penumbra (lateral dose from the 80% dose to the 20% dose level) due to the large air gap between the range compensator and the patient. The large air gap is necessary in order to reduce the neutron dose generated when the proton beam hits the beam-modifying devices, which leads to further scattering and secondary radiation such as neutrons.

Spot scanning, also called pencil beam scanning, delivers large number of pencil beams, which are adjustable cylinder particle beams with diameters ranging from 2.5 to 10 mm (Marchand et al., 2000), to form a 3D conformal dose distribution. There are several modes of particle scanning techniques, including discrete, raster spot scanning and dynamic spot scanning methods. In discrete spot scanning, the prescribed dose is delivered to the given spot at a static position (Kanai et al., 1980) and the beam is switched off afterwards before moving to the next spot. In this process, the pencil beam is scanned in one direction and across the volume at various depths, where the beam intensity varies from spot to spot or continuously along the path



(Trofimov and Bortfeld, 2003). For raster scanning method, the beam is not switched off when moving to the next spot. In the dynamic spot scanning method, the beam is scanned fully continuously across the target volume, in which the output of the source or the speed of the scan can be changed to achieve intensity modulation. Compared to the scattering method, it is easier to achieve intensity and 3D shape modulation in the spot scanning method by modulating beam energies to control the depth in different layers.

Since a brass aperture is not necessary to collimate the proton beam in the scanning method, less neutrons are generated which leads to a decrease of the total dose in tissue. This is a significant advantage in pediatric cancer treatment, where the risk of developing secondary malignancies should be as low as possible (Boehling et al., 2012). In addition, the spot scanning beam penetrates deeper than the beam in the scattering method since there are no beam-modifying devices necessary. Distal dose falloff of a spot scanning proton beam, which is affected by range straggling and the momentum spread, is sharper than a scattered beam. Lateral dose falloff of a scanning beam can be affected by Coulomb scattering, which differs depending on the medium (e.g. bone or tissue), the initial spatial and angular properties, leading to different sizes of lateral penumbra at certain ranges (De Lanley and Kooy, 2008).

Carbon ion therapy uses more massive ions than protons, which have a narrower Bragg-peak, larger peak-to-plateau ratio and stronger linearity (Minohara et al., 2010). Compared to proton SOBP, the spread-out carbon beam has a lower effective entrance dose on the skin with the same SOBP dose level and a higher RBE which results in high local tumour control. There is a high efficiency of DNA damage (double or multiple strand damage) even in tumours developing under hypoxic conditions which is resistant to lower LET radiation source such as proton or photon beams where oxygen is required due to the free radicals formation increases the damage to target tissue. This makes carbon ion beams suitable for deep-located tumours or intractable cancers that are resistant to photon beams. One disadvantage is that due to nuclear reactions there is a higher production of lighter ions in tissue compared to protons, resulting in a higher effective dose to normal tissue at the depth beyond SOBP than proton beam at the same SOBP dose level.

### *1.3.2. Internal sources*

Internal radiation therapy treats patients with internal sources, such as radioisotopes and X-ray miniatures. The radiation sources are inserted in the tissue which cause less side effects in patient compared to external beam therapy. Brachytherapy and X-ray miniature are presented below.

#### *1.3.2.1. Brachytherapy*

Brachytherapy is a type of internal radiotherapy, in which a source of short-range radiation is directly inserted inside the tumour or is placed close to it. The radiation source is sealed in a capsule or a wire to prevent the source from leaking or moving in the tissue. Brachytherapy is

commonly applied for treating cancers of cervix, prostate, breast and skin. Commonly used radionuclides for brachytherapy include Cesium-137, Iodine-125, Palladium-103, and Iridium-192. The radiation seeds can be inserted in the patient for temporary or permanent treatment and the source does not shift once inserted. The tumor remains accurately irradiated ensuring a high level of dose conformity leaving the patient free to move during the whole long-term irradiation.

There are four types of brachytherapy treatment applied in the clinic depending on where the source is inserted, i.e. intracavity, interstitial, intrasurface, and intravascular. Different dose rates are applied in brachytherapy, i.e. low-dose rate (LDR) (40 to 200 cGy/h), moderate dose rate (200 to 1200 cGy/h), and high-dose rate (HDR) (higher than 1200 cGy/h) (Koukourakis et al. 2009). The radiation oncologist decides the best type of seed insertion procedure, i.e. how many seeds are needed, LDR or HDR seed insert etc. For instance, permanent seed implantation using  $^{125}\text{I}$  or  $^{103}\text{Pd}$  is common for LDR treatment, whereas temporary insertion using high-activity  $^{192}\text{Ir}$  is preferred for HDR treatment (Koukourakis et al. 2009). HDR seed insertion treatment has its advantages when compared to LDR brachytherapy, as it is cost effective, reusable and biologically effective with higher dose per fraction and conforming to the defined planning target volume.

Compared to external beam radiotherapy, brachytherapy is more suitable for tumours with small volume due to the short range of radiation sources, which is also an advantage as healthy tissue receives in this way a relatively low dose. Moreover, there are radiobiological studies showing that low dose and continuous radiation are more effective than the total dose delivered in fractionations with only 5 times per week as in external beam radiotherapy (Saunders et al., 1999). Although HDR brachytherapy can be used alone, a combination of HDR brachytherapy and external beam therapy shows better clinical results (Demanis et al. 2005).

#### 1.3.2.2. Miniature X-ray source

A miniature X-ray source device was developed for stereotactic interstitial radiosurgery of small (<3 cm diameters) and sphere shaped tumors (Beatty et al., 1996; Flickinger et al., 1992; Marks and Spencer, 1991). The device is electronically controlled and has a similar speed of dose delivery as used in external beam therapy. It is a needle-like probe, which has point source and generates low-energy X-rays with beam size of approximately 0.3 mm. The output dose rate of a 40 kV device measured in water with an ionization chamber was 150 cGy/min at a source-to-surface distance (SSD) of 10 mm (Beatty et al., 1996). The dose fall off in water was found to be the third power of the distance and the depth dose characteristics were comparable with two brachytherapy sources with a slightly reduced attenuation gradient (Karnas et al., 2001). Compared to brachytherapy techniques, miniature X-ray sources are easier to handle in the clinic since they do not require radioactive sources. Moreover, intensity and energy of X-rays are adjustable to optimize tumour control (Dinsmore et al., 1996). However, the miniature X-ray tubes have limitations especially when high dose rate irradiation is needed due to difficulties in steering the electron beam to the target, improving X-ray production efficiency, cooling the X-ray

target, and changing shape and energy of the emitted radiation (Gutman et al., 2004; Karnas et al., 2001).

## 1.4. Dosimetry techniques

Radiation dosimetry is the measurement of absorbed dose delivered by ionizing radiation. Dosimetry measurements are based on the fact that interactions of radiation with a medium cause a measurable change in its properties, providing a reading, which can be detected and analyzed. Dosimetry is used in clinical applications to evaluate the dose output accuracy of irradiation equipment. The output value is used in radiation treatment planning to produce a dose distribution for that specific system.

In dosimetry, absorbed dose is defined as the energy absorbed in the medium per unit mass with the unit of gray, Gy, which is equivalent to 1 J/kg. The dose rate, i.e. the amount of dose delivered per unit time, generally is given as Gy/min or cGy/s. The measurement of dosimetry is classified as either absolute or relative. Absolute dosimetry measures the absorbed dose directly under standard conditions, which provides a fixed and reproducible reference dosimeter with high accuracy. Relative dosimetry is performed by cross-calibration with absolute dosimeters under reference condition. Absolute dosimetry measures absorbed dose directly by temperature change which will be described in section 1.4.1.1. Otherwise calibration is needed to compute the known dose under reference conditions for further measurements. For instance, ionization chambers are accepted as primary standard dosimeters. Relative dosimetry is performed by conversion with one of the dosimeters under reference conditions. The accuracy of dose delivery compared to the prescribed absolute dose, for instance in IMRT, should be within 5% which is verified by using an accurate reference dosimeter (Das et al., 2008). The standard of dosimetry research was initially performed using ionization chamber in water phantoms, which is comparable with the dose given to a human body containing *ca* 70% water with overall density close to 1 g/cm<sup>3</sup>. This dosimetry measurement was performed with a water tank using X-ray and  $\gamma$ -ray beams with an ionization chamber immersed in the phantom (Constantinou et al., 1982). Phantom-to-water and density corrections should be considered when applying other calibration phantoms in radiation dosimetry. The absolute dosimetry measurements were also carried out with proton and heavy ion beams (AAPM Radiation Therapy Committee and Lyman, 1986). There are various techniques mainly for measuring relative radiation dose, for instance, low dimensional techniques, such as ionization chambers and radiochromic films, provide higher precision but lose dimensional information, while volume (3D) techniques provide more detailed spatial information.

### *1.4.1. Single volume measurements*

Single volume dosimetry measurements are especially used in standard field for commissioning and QA of systems or beamlets having high precision, low noise level and easy handling. There are four accepted types of devices performing point measurements, which are briefly described below.

#### 1.4.1.1. Calorimetry

Calorimetry is adopted to measure the absorbed dose in radiation dosimetry by measuring the temperature increase due to the energy deposited by ionizing radiation. Calorimetry is performed with either water or graphite calorimeter. The calorimetry experiment was initially carried out by Davison et al (1953) by measuring the output of a high-intensity cobalt-60 source with a small water calorimeter. Calorimetry is an absolute dosimetry method to establish absorbed dose standards (Ross and Klassen, 1996). However, calorimetry has its disadvantages such as lack of sensitivity and slow operation since the measurements take time to reach thermal equilibrium after irradiation, making this technique impractical to be applied in the clinic. Calorimetry is used as a standard method to calibrate other dosimeters such as ferrous sulphate dosimeter solution (Ross et al 1989) and ionization chamber (Schulz et al., 1987). The latter is suitable for establishing absorbed dose standards in radiation therapy (Aukett et al., 1996; Klevenhagen, 1991).

#### 1.4.1.2. Fricke solution

The Fricke ferrous sulphate solution was first investigated by Fricke and Morse (1927) as a chemical dosimeter to quantify absorbed radiation dose. The dosimetric response in the Fricke solution is based on the conversion of ferrous ions to ferric ions due to the radiolysis of an aqueous system. When the water in the Fricke solution is irradiated, hydroxyl radicals and solvated electrons are formed. These can further react with oxygen and ferrous ions to produce ferric ions. Information on the absorbed dose can thus be obtained by measuring the concentration change of ferrous to ferric ions. The concentration of ferric ions can be detected in the visible or ultraviolet range using spectrophotometers (Scharf 1971). Gore et al (1984) suggested that the concentration change of ferrous and ferric ions can be measured with nuclear magnetic resonance (NMR) relaxation measurements since ferrous and ferric ions have different paramagnetic spin states and enhancing effects on the spin relaxation rates of the water protons of the aqueous Fricke solution (Podgorsak and Schreiner, 1992). The Fricke solution is used as a primary standard method to calibrate other dosimeters or measure dose rate of ionizing radiation sources. For instance, the cobalt-60 sources used in this thesis were initially calibrated with Fricke solutions. As a water-based dosimeter the Fricke solution is considered to be near tissue equivalent, a favorable characteristic that was later adopted to develop Fricke gels having

possible application in radiotherapy as 3D dosimeters (Audet and Schreiner, 1997; Gore and Kang, 1984; Olsson et al., 1998).

#### 1.4.1.3. Ionization chambers

The gas (or liquid)-filled ion chamber is a type of ionization detector. The liquid-filled type of ion chamber follows the same principle as the gas-filled type, but is not used as a dosimetric standard. Inside the gas-filled ion detector there are two electrodes, i.e. anode and cathode, providing an electric field. Charged particles are produced on irradiation and move towards the electrode that has the opposite charge. For well-defined conditions of electric field strength an absorbed dose leads to a linear response in ionization current, measured by an electrometer circuit. Ion chamber has excellent stability, small directional dependence, beam-quality response independence and traceability to a primary calibration standard (Low et al., 2011). It gives a precise measurement and is used as a standard detector in almost all radiotherapy centers. The volume and energy response of new models are considered to guarantee the (spatial) accuracy, which is tried to be maintained at ~2% compared to the accepted standard measurements using ion chambers (Jordan, 2006).

#### 1.4.1.4. Diodes

Another type of ionization detector is the semiconductor detector which uses a semiconductor diode (usually silicon or germanium) to measure the incident particles or photons. When a high-energy photon or particle is absorbed by the detector, electron-hole pairs are formed in the solid material. In the detector, the voltage difference between the two electrodes results in the excited electrons moving towards the positive electrode. However, the holes do not move and can be neutralized by electrons from the negative electrode, generating a weak electric pulse. A silicon diode has high spatial resolution, having typical lateral sensitive areas of much less than 1 mm<sup>2</sup> (Jordan, 2006). A diamond detector is similar to a silicon diode but is much more expensive. The traditional diode detector is commonly applied in general photon-beam dosimetry and there was a study by Griessbach et al (2005) showing that the relative outputs for small fields agree with diamond detector results, making the diode based dosimetry preferred for small photon fields. Germanium detectors are mostly used for  $\gamma$ -ray and X-ray spectroscopy. Due to higher thickness than silicon diodes, germanium detectors are able to detect  $\gamma$ -rays with energy up to a few MeV.

#### 1.4.1.5. Scintillators

A scintillator emits light when exposed to ionizing radiation. The fact adopted in the scintillation detector is that after excitation the molecules or ions emit photons with a wavelength close to the blue violet or ultraviolet region when the atom returns to the ground state from the excited energy level. Afterwards the light can be carried by an optical fiber and the light signal

converted to an electric pulse, which can be read in the detector. By adjusting the physical and electronic density of the plastic, the scintillators have good agreement with tissue or water response. Plastic fiber scintillators are suitable for low-energy X-ray irradiation since the absorption coefficients are similar to tissue or water and can be tuned to agree for specific energies (Jordan, 2006).

#### 1.4.1.6. Thermoluminescent pills

A simpler scintillation detector is the thermo-luminescent dosimeter (TLD) pill, which becomes thermo-luminescent (or photo-luminescent) after exposure to radiation. In a TLD the thermo-luminescent crystal is heated after exposure, emitting in the process visible light with intensity proportional to absorbed dose. TLDs are mainly used as dosimeters for occupational workers to record their absorbed dose. There are two commonly used TLD materials: calcium fluoride for  $\gamma$ -ray detection and lithium fluoride for  $\gamma$ -ray and neutron detection, which have one or more impurities to produce trapped states for electrons.

#### 1.4.2. 2D measurements

Two-dimensional (2D) dosimeters are described below including ionization chamber arrays, diode arrays, radiographic film, radiochromic film, and computed radiography.

##### 1.4.2.1. Ionization chamber arrays

Ionization chamber arrays consist of a matrix of ion chambers, in which the distance between the chamber centres can be different. Ionization chamber arrays may provide isodose distributions with the spatial resolution depending on the spacing of the arrays, and each chamber provides a quantitative dose measurement (Low et al., 2011). One type of ionization chamber array consisting of 32x32 chambers with a distance of 7.6 mm between chamber centres was investigated by Herzen et al (2007) and the results showed that the detector is suitable for quality assurance and 2D dose verifications in IMRT clinical routines (Herzen et al., 2007; Poppe et al., 2006). The ionization chamber arrays provide fast 2D dose distribution information with high accuracy, and are also found to be suitable for quality assurance of proton therapy beams (Arjomandy et al., 2008).

##### 1.4.2.2. Diode arrays

2D diode arrays are used as dosimeter by applying a scintillation screen to convert the photon energy into visible light in the diodes, which can be converted to digital signal. 2D diode arrays were investigated (Létourneau et al., 2004) for routine IMRT quality assurance, which uses MapCheck (Sun Nuclear Corporation) to calculate both absolute and relative dose measurements simultaneously, simplifying and reducing in this way the IMRT quality assurance

(QA) workload. The fundamental properties of the 2D diode arrays, such as reproducibility, linearity and temperature dependence, were evaluated by using high-energy photon beams. The diode array response showed a linear dependence on dose up to 295 cGy and good reproducibility with low temperature sensitivity. The 2D diode array performance was compared to measurements made with conventional film and an ionization chamber in the case of an IMRT treatment plan using 7 beams (6 MV) to treat head and neck tumours. These results showed that the 2D array diode has a comparable performance to conventional film and ion chamber and can provide dosimetric characteristics required in relative and absolute dosimetry.

#### 1.4.2.3. Radiographic film

Radiographic film is routinely applied to X-ray dosimetry and is effectively capable of providing 2D dose distributions with high spatial resolution. It is composed of an emulsion-gelatin with radiation sensitive silver halide crystals. When the sensitive silver halide in the emulsion is exposed to X-rays, gamma rays or light, the  $\text{Br}^-$  ions are liberated and captured by the  $\text{Ag}^+$  ions, creating an image. Disadvantages of these films are their high sensitivity to light and the fact that the image quality can be affected by the film processing temperature and time (Brink et al., 1993).

#### 1.4.2.4. Radiochromic film

A radiochromic film instantly changes color upon exposure to ionizing radiation without chemical or physical processing. These films have sandwich-structure consisting of two clear polyester layers and in between a tissue-equivalent active layer. The active layer is composed of a monomer, which changes color on polymerization upon irradiation. Also included in recent films is a marked dye, which enables non-uniformity correction by using multichannel spectroscopy and decreases the sensitivity to UV/vis light. Different thicknesses and types of monomers of the active layer result in different sensitivities of the films to ionizing radiation. High-sensitivity dosimetry films have been especially developed to meet the needs of the clinical physicists working in the radiotherapy environment. Additional details on radiochromic films will be presented in chapter 6.

#### 1.4.2.5. Computed radiography

Computed radiography (CR) is similar to conventional radiography, which uses a film to create an image, but employs an imaging plate made of photo-sensitive phosphor which stores the radiation dose as a latent image. The imaging plate is placed under the patient body when treated with X-rays and subsequently scanned through a laser scanner or CR reader. In this procedure the electrons excited by radiation relax to lower energy levels by emitting light which can be detected and converted to an electronic signal and further amplified to produce digital images. In this way the imaging plate can be used repeatedly. The obtained CR digital image can be read and viewed

using imaging-processing software. CR has been proven reliable for medical application with low cost, reusability and faster processing speed (Schaetzing, 2003; Schaetzing et al., 2002).

#### *1.4.3. 3D measurements*

3D gel dosimeters have been developed with the purpose of guaranteeing precise and high-resolution verification of 3D dose distributions in radiotherapy, including brachytherapy, and IMRT. These gel dosimeters contain radiation-sensitive chemicals which undergo detectable changes that are proportional to the absorbed radiation dose. This enables recording the 3D spatial distribution of the delivered dose. It was first suggested by Day and Stein (1950) that radiation sensitive gels could be applied to produce color changes. Spectrophotometry was adopted afterwards to investigate the depth dose information in radiation sensitive gels (Andrews et al., 1957). Subsequently various gel dosimeters were developed for radiation dosimetry research, such as Fricke gels (Schreiner et al., 2010) and polymer gels (Baldock et al., 2010), which are the two types of gel dosimeters described in this chapter. Different imaging techniques such as magnetic resonance imaging (MRI) (described in section 1.2.) and optical computed tomography (optical CT) are applied to image and quantify the detectable changes caused by ionizing radiation. Optical CT uses visible light to analyze optical properties of an optical scattering system providing 3D images with micrometer resolution. The optical CT scanning system consists of laser beams as light source for scanning and a light detector. A 1D optical projection is obtained by laser scanning across the sample after which small-angle rotation of the object is performed. Physical techniques and image processing methods were developed to minimize deleterious effects of refraction, reflection, and scattered laser light, thereby achieving higher signal-to-noise in both projected and reconstructed images (Jordan, 2004; Oldham, 2004). Optical CT can function as a readout method for 3D gel dosimetry in which polymer gels become increasingly opaque after irradiation (Gore et al., 1996).

The greatest advantage of gel dosimetry over ionization chambers and radiochromic films is that they can provide directly 3D information of the absorbed dose. To be qualified as a 3D radiation dosimeter in the clinic, a gel dosimeter should ideally meet the following requirements: 1) be stable and homogenous in time and space; 2) be (near-) tissue equivalent with a volume comparable to that applied in the clinic; 3) guarantee the quality assurance (QA) with 1 mm isotropic spatial resolution in less than one hour with an accuracy of 3% and a precision of 1%; 4) be dose rate and energy independent and free from effects of temperature and pressure; 5) give an immediate (readable) response, such as optical changes or MRI detectable signals (De Wagter, 2004). These properties for the RFG gels will be reviewed in the summary chapter.

##### *1.4.3.1. Fricke gels*

The ferrous sulphate (Fricke) solution was initially investigated by Fricke and Morse (1927). It was then applied in 3D radiation dosimetry by Gore et al (1984) when a gel matrix was



incorporated in the Fricke solution, which provided stable geometric dose information. The Fricke gels were prepared in glass containers with triply distilled water, ferrous salts, and sulphuric acid added first before the solution was heated. During the preparation procedure, air is continuously bubbled in the solution since oxygen is required for the reactions to take place during irradiation. Subsequently gelatine powder was added during heating (Saur et al., 2005). The Fricke gel does not contain toxic components or require anoxic conditions for gel preparation contrary to some polymer gels, and is water equivalent, which makes correction factors minimal. Fricke gels follow the same mechanism as Fricke solution under high-energy ionizing radiation as mentioned in section 1.4.1.2.

The dose information in the Fricke gel can be measured by spectrophotometry, which is based on the strong absorbance of ferric ions in the ultraviolet, i.e. at 224 and 304 nm (Gore et al., 1984). Gore *et al* (1984) also proposed applying nuclear magnetic resonance (NMR) relaxation measurements for detecting the concentration of ferrous and ferric ions change in the Fricke gel. This suggestion was based on the observations that the spin-lattice relaxation rate ( $R_1 = 1/T_1$ ) of the solution is controlled by the dipolar interaction between the paramagnetic spins of the ions and the adjacent water protons. In addition, due to the different paramagnetic characteristics of ferrous and ferric ions, the relaxation of neighboring water protons is different. These NMR relaxation characteristics allow the use of MRI as a readout system as well (Olsson et al., 1990). The Fricke gels have linear dose dependence up to 20 Gy when using the optical readout method, and up to 400 Gy when applying MRI (Schreiner, 2004). The Fricke gels can also be imaged by optical CT due to optical changes after irradiation (Doran et al., 2001).

One disadvantage of the Fricke gels is that they require higher dose to induce a detectable change compared to polymer gels. Another disadvantage is the high ion diffusion rate after irradiation, which destroys the initial 3D dose information after a certain post-irradiation period. Schulz et al (1990) calculates that an idealized beam (zero penumbra) has an apparent 3 to 4 mm penumbra (90% to 10%) within 30 minutes, limiting the applicability in the clinic. Gelatin and agarose are commonly used as gelling agents, but some other gelling (e.g. sephadex and agar) or chelating agents (e.g. xylenol orange (XO)) have been investigated to further inhibit this diffusion issue in Fricke gels. However, these solutions have not completely managed to eliminate the ion diffusion problem. Recently a new type of nanocomposite Fricke gel dosimeter was reported by Maeyama et al (2014) to have no diffusion during nine days after irradiation and no LET dependence with a good linearity up to 800 Gy when irradiated with a carbon beam. Future studies will show if the Fricke gels can be used in the clinic.

#### 1.4.3.2. Polymer gels

Most tissue-equivalent polymer gels undergo radiation-induced polymerization. This process is initiated by free radicals which are generated by the radiolysis of water and can react with the vinyl group of monomers. The free radicals combine with bulk monomers and eventually form long polymer chains, which can precipitate in water to form microgels. This leads to changes in

the optical property of the gel dosimeters, which can be detected by MRI, and optical CT, generating a 3D dose map in the gel dosimeters.

The ion diffusion problem of Fricke gels was solved with the commercial BANG gel dosimeters, consisting of Bis<sup>1</sup>, AAm<sup>2</sup>, nitrogen and aqueous gelatin (Maryanski et al., 1994). The optical-CT readout method was adopted in the BANG gel dosimeters due to the optical change in the gels, from visibly transparent to optically-opaque, which results from the increase of the number density of radiation-induced polymer micro-particles (Gore et al., 1996). The BANG gel dosimeters were shown to be dose rate and energy independent based on experiments using four different energies: 300 kV X-rays, 1.25 MeV Co gamma rays, 6 MV X-rays, and 8 MV X-rays having different dose rates (Farajollahi et al., 1999; Farajollahi, 1998). Although these gels have favourable behaviour they are susceptible to light scattering artefacts (Oldham, 2004; Oldham and Kim, 2004; Oldham et al., 2003) and need complicated preparation procedures.

Soon after the BANG gels, the so-called polyacrylamide gel (PAG) dosimeters were developed and investigated using different compositions (Lepage et al., 2001; Pappas et al., 1999). The PAG gel dosimeters were tested in the clinic by making use of different read-out systems such as MRI (Baldock et al, 1998; De Deene, 2009; Vandecasteele and De Deene, 2012, 2013; Venning et al, 2004), and optical CT (Gore et al., 1996; Oldham et al., 2003) to image dose distribution. The PAG gel dosimeters, investigated for dose rates ranging from 30 cGy min<sup>-1</sup> to 400 cGy min<sup>-1</sup>, were found to have very small dose-rate dependence (the dose sensitivity change amounts to 12%) (De Deene et al., 2006).

Due to the nature of free radical polymerization, most of the polymer gels are sensitive to oxygen, which inhibits the polymerization process. A new type of so-called normoxic gel, MAGIC gel consisting of methacrylic acid, ascorbic acid, gelatin and copper, was proposed by Fong *et al* (2001). In MAGIC gel the ascorbic acid, which consumes oxygen, solved the problem of oxygen inhibition and simplified the gel preparation procedures. A study shows 6% difference of energy dependence when going from cobalt  $\gamma$ -ray beams to 10 MV X-ray beams and less than 5% difference in dose rate dependence for dose rates from 100 cGy/min to 600 cGy/min using LINAC (Pavoni and Baffa, 2012). Afterwards other antioxidant, such as THPC<sup>3</sup> as an oxygen scavenger, were found to provide high dose sensitivity but have significant dose rate dependences and only no dose rate dependence at low dose levels (< 2 Gy) (Bayreder et al., 2006). The MAGIC gel dosimeters were also investigated with MRI for potential IMRT verification and the data showed good agreement between measured and calculated dose (Gustavsson et al 2003)(Gustavsson, 2003 #7;Guo, 2006 #9). The MAGIC gel dosimeters were also tested with electron beams and were found to be dose rate independent but energy dependent (Adinehvand et al., 2008).

---

<sup>1</sup> N,N'-Methylenebisacrylamide

<sup>2</sup> acrylamide

<sup>3</sup> Tetrakis(hydroxymethyl)phosphonium chloride

Another oxygen insensitive dosimeter is the PRESAGE<sup>TM</sup>, which is transparent and contains a leuco dye that exhibits a radiochromic response when exposed to ionizing radiation. The gel can be handled without a container, which simplifies the modelling of the optical path through the dosimeter (Doran and Krstajić, 2006). The gel shows good linear dose response at low energies and exhibits a slow increase of opaqueness with time while good stability up to 90 hours post-irradiation. 3D dose readout agrees well with the Gafchromic EBT film measurement within 2% dose difference and 2 mm distance-to-agreement (DTA) (Sakhalkar et al., 2009). The adopted readout method is optical CT, which measures optical density change instead of light scattering, providing in this way higher accuracy due to the low optical contrast. A small dose rate effect (~2% deviation) was observed when irradiated by both photon and electron beams at different dose rates i.e. 200, 400, and 1000 cGy/min (Guo et al., 2006).

The chain termination in polymer formation follows different rules depending on the type of gel. For instance, in polyacrylamide gel (PAG) and N-isopropylacrylamide (NIPAM) gel dosimeters, the chain is terminated by a chain-transfer reaction. This chain termination process is accomplished by using a small molecule such as gelatin, which generates quite stable gelatin radicals and these radicals finally terminate very slowly with the monomer rather than propagate. Therefore, the rate of polymer chain formation is nearly independent of the radical concentration, which is proportional to the dose rate of the radiation source, since both chain-terminating reactions are first-order reactions. Another type of gel, methacrylic acid gel (MAG), follows a second-order chain-terminating reaction in the radical concentration, i.e. the rate of termination is proportional to the square of the radical concentration, making it more dose rate dependent than the above-mentioned gels (Jirasak et al., 2009).

## **1.5. Radio-Fluorogenic (RFG) gel**

A recently developed new type of 3D dosimeter is the so-called radio-fluorogenic (RFG) gel, which is optically clear and near tissue-equivalent. The mass and electron densities and elemental composition of different medium are provided in table 1.1 as below.

Table 1.1. Comparison of mass and electron densities, elemental composition for different media.

Medium	Density (g cm <sup>-3</sup> )	Electron density (x)	C (%)	H (%)	O (%)	N (%)	Other (%)
Water	1.00	3.34	0	11.1	88.9	0	0
Soft tissue	1.06	3.44	14.3	10.2	3.4	70.8	1.3
Bone	1.40	4.51	15.5	3.4	43.5	4.2	33.4
Fricke	1.00	3.34	2	10.7	0.67	85.7	0.93
PRESAGE	1.10	3.61	60.7	8.9	21.7	4.5	4.2
PAG	1.04	3.44	6.2	10.7	81.0	2.2	0.1
MAG	1.05	3.49	7.4	10.7	80.5	1.4	0
RFG	0.91	3.28	65.5	9.4	25	<0.1	0

The RFG gel contains no water but only two components, i.e. a bulk polymerizable monomer (tertiary butyl acrylate, TBA) and a small concentration (~100 ppm) of a non-fluorescent but fluorogenic dye (maleimido pyrene, MPy). The non-fluorescent dye becomes fluorescent when co-polymerized into the growing polymer chains of the bulk monomer initiated by radiation-induced free-radicals. The mechanism is shown in figure 1.2. The intensity of the fluorescence in the irradiated gel was found to be proportional to the degree of polymerization which in turn is proportional to the yield of initiating free radicals produced by the radiation, and hence to the radiation dose (Warman et al., 2009a).

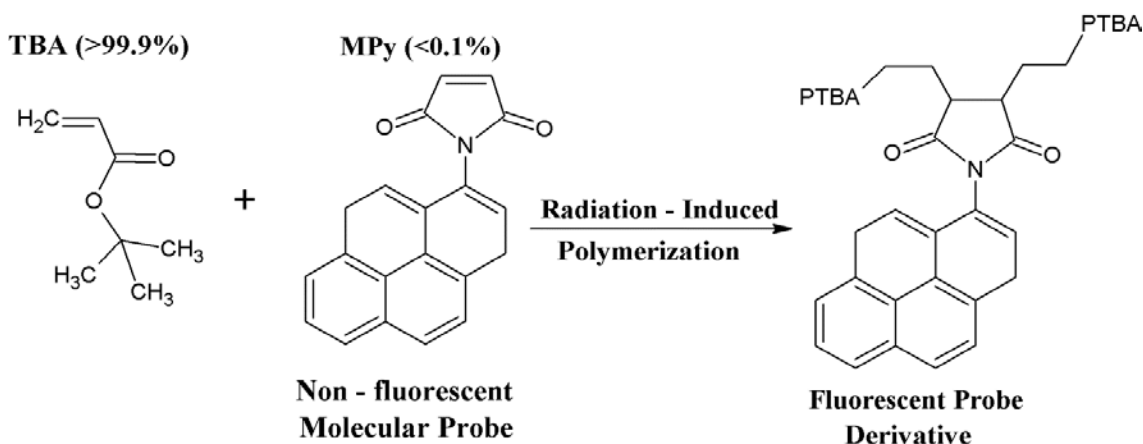


Figure 1.2. The molecular structures of TBA and MPy and the underlying mechanism of radio-fluorogenic co-polymerization (RFCP) in a dilute solution of MPy in TBA.

The fluorescence of the gel can be visualized using UV excitation light, providing fixed, highly spatially-resolved fluorescent images (Warman et al., 2009a, b). The radiation-induced fluorescence is permanent, which distinguishes it from transitory optical emission or scintillation

effects. The fluorescence emission in the gel is fixed and proportional to local radiation dose. The RFG gel has advantages over other polymer gels: simplicity (only two chemical components); optically clear after irradiation with no change in optical absorption or turbidity thus simplifying the imaging process; immediate and stable fluorescence response enabling real-time, *in situ* monitoring (Warman et al., 2011a).

The early work in developing this dosimeter was carried out using the monomer methyl methacrylate (MMA), in which dose and dose rate dependences of monomer conversion and fluorescence were investigated. The sensitivity to radiation of TBA was found to be much higher than that of MMA, which led to the replacement of MMA by TBA. Several fluorescent molecular probes, such as N-(1-pyrene)maleimide (MPy) (Frahm et al., 2001b), N-(1-pyrene)methacrylamide (PyMA) (Frahm et al., 2001a), N-(2-anthracene)methacrylamide (AnMA) (Frahm et al., 2003), were investigated in MMA solution. MPy was found to be a suitable fluorescent dye, having both fully quenched fluorescence before irradiation and a higher propagation rate,  $k_p$ , than the other fluorescent probes.

Early RFG dosimetry research was conducted using small volume solutions which are suitable for in-situ and real-time monitoring of accumulated radiation dose (Warman et al., 2009a; Warman et al., 2011a). RFG gels were later used to obtain fixed images of various radiation sources including collimated X-ray beams (Warman et al., 2011b), a 3 MV electron beam (Warman et al., 2013b), an 80 MeV proton beam (Warman et al., 2013a) and an Ir-192 brachytherapy seed (Warman et al., 2011b). Figure 1.3 shows some of the fluorescent images of RFG gels irradiated with the above mentioned high-energy radiation sources. The spatial resolution was found to be about 0.1 mm based on JPEG images for all beam sources used (Warman et al., 2011a).

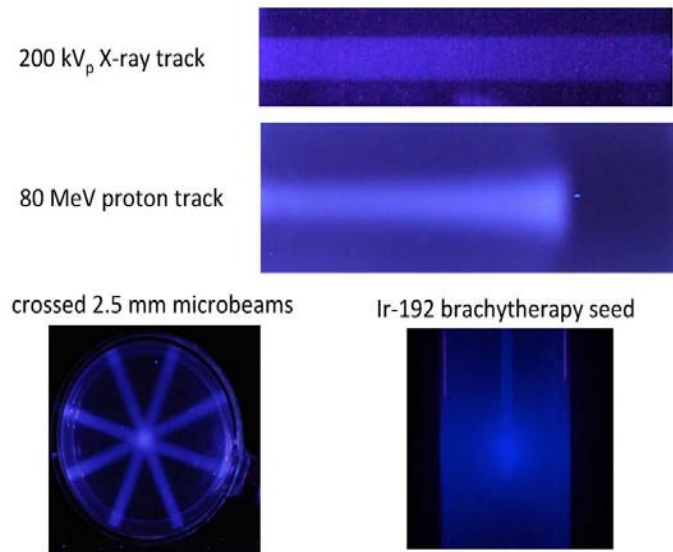


Figure 1.3. Fluorescent images of RFG gels irradiated with the different radiation sources irradiated (Warman et al., 2011a, b, 2013a).

These first spatially resolved images of dose deposition showed that the RFG gel can be potentially used as a 3D dosimeter enabling high-precision and high-resolution verification of 3D dose distributions. This dosimetry method is considered to be mostly relevant for clinical radiotherapy treatments where 3D dose information is essential (such as in proton therapy). Systematic studies and gel characterization combined with fundamental knowledge are needed to develop this dosimeter system so that it can be applied in the clinic.

## 1.6. Thesis overview

The ultimate aim of this gel dosimetry research is to provide a method of quantitative, 3D resolved dosimetry applicable to high-energy radiation having complex dose distributions by using a near-tissue equivalent RFG gel. The gel formation and reformation properties, the dose and dose rate dependence, optical property, concentration effects of the fluorescent dye etc, are all of interest when developing this gel dosimeter.

Chapter 2 describes the details of gel formation and reformation using the polymerizable monomer tertiary-butyl acrylate (TBA), which is used as the reference system for the investigations in subsequent chapters. This includes the detailed gel formation steps and the dose and dose rate dependence of TBA based polymer gels.

Chapter 3 discusses the radiation-chemical properties of the MPy in TBA solution based on  $\gamma$ -ray irradiation. Optical properties of the RFG solution are studied to obtain information about the relationship between the fluorescence emission and solute concentration. Dose rate effects on the fluorescence emission are also investigated in this chapter.

Chapter 4 discusses the potential of using a TUD-synthesized compound, N-(1-pyrenyl)acrylamide (PyAM), as fluorogenic dye for RFG gel. The radiation-chemical and optical properties of PyAM in TBA solution were studied and compared to that for MPy. It was decided to stay with commercially available MPy in the rest of this thesis.

Chapter 5 discusses the preparation and the radiation-chemical and optical properties of a reformed RFG gel. The relationship between the fluorescence emission and solute concentration in RFG gel was studied and compared to that in RFG solution.

Chapter 6 describes 2D radiochromic (RC) film dosimetry, involving four films with different sensitivities to high energy radiation. The aim was to find a dose-rate independent RC film that could provide complementary 2D dose information within the dose range used in RFG gel dosimetry, i.e. 2 to 40 Gy.

Chapter 7 discusses the non-homogeneous irradiation of RFG gel using in-house collimated and crossed X-ray beams producing fluorescent tracks in RFG gels. A slit-scanning method was developed to generate tomographic fluorescent slices of an irradiated gel. 3D animations and fluorescence reconstruction of the crossed X-ray beams are made afterwards.

Summary summarizes the properties of RFG gels and the application as a 3D radiation dosimeter.

## References

AAPM Radiation Therapy Committee, Lyman, J.T., 1986. Protocol for Heavy Charged-particle Therapy Beam Dosimetry: A Report of Task Group 20, Radiation Therapy Committee, American Association of Physicists in Medicine. American Association of Physicists in Medicine.

Adinehvand, K., Zahmatkesh, M.H., Aghamiri, M.R., Akhlaghpour, S.H., Bagheri, S., 2008. Verification of dose rate and energy dependence of MAGICA polymer gel dosimeter with electron beams. *Iran Journal of Radiation Research* 6, 31-36.

Andrews, H.L., Murphy, R.E., LeBrun, E.J., 1957. Gel Dosimeter for Depth-Dose Measurements. *Review of Scientific Instruments* 28, 329-332.

Arjomandy, B., Sahoo, N., Ding, X., Gillin, M., 2008. Use of a two-dimensional ionization chamber array for proton therapy beam quality assurance. *Medical Physics* 35, 3889-3894.

Audet, C., Schreiner, L.J., 1997. Multiple-site fast exchange model for spin-lattice relaxation in the Fricke-gelatin dosimeter. *Medical Physics* 24, 201-209.

Aukett, R.J., Harrison, R.M., Moretti, C., Nahum, A.E., Rosser, K.E., 1996. The IPEMB code of practice for the determination of absorbed dose for x-rays below 300 kV generating potential (0.035 mm Al-4 mm Cu HVL; 10-300 kV generating potential). *Physics in Medicine and Biology* 41, 2605-2625.

Baldock, C., Burford, R.P., Billingham, N., Wagner, G.S., Patval, S., Badawi, R.D., Keevil, S.F., 1998. Experimental procedure for the manufacture and calibration of polyacrylamide gel (PAG) for magnetic resonance imaging (MRI) radiation dosimetry. *Physics in Medicine and Biology* 43, 695-702.

Baldock, C., De Deene, Y., Doran, S., Ibbott, G., Jirasek, A., Lepage, M., McAuley, K.B., Oldham, M., Schreiner, L.J., 2010. Polymer gel dosimetry. *Physics in Medicine and Biology* 55, R1-R63.

Bayreder, C., Georg, D., Moser, E., Berg, A., 2006. Basic investigations on the performance of a normoxic polymer gel with tetrakis-hydroxy-methyl-phosphonium chloride as an oxygen

scavenger: reproducibility, accuracy, stability, and dose rate dependence. *Medical Physics* 33, 2506-2518.

Beatty, J., Biggs, P.J., Gall, K., Okunieff, P., Pardo, F.S., Harte, K.J., Dalterio, M.J., Sliski, A.P., 1996. A new miniature x-ray device for interstitial radiosurgery: Dosimetry. *Medical Physics* 23, 53-62.

Boehling, N.S., Grosshans, D.R., Bluett, J.B., Palmer, M.T., Song, X., Amos, R.A., Sahoo, N., Meyer, J.J., Mahajan, A., Woo, S.Y., 2012. Dosimetric comparison of three-dimensional conformal proton radiotherapy, intensity-modulated proton therapy, and intensity-modulated radiotherapy for treatment of pediatric craniopharyngiomas. *International Journal of Radiation Oncology\* Biology\* Physics* 82, 643-652.

Brink, C., De Villiers, J.F.K., Lötter, M.G., Van Zyl, M., 1993. The influence of film processing temperature and time on mammographic image quality. *The British Journal of Radiology* 66, 685-690.

Chatal, J.F., Hoefnagel, C.A., 1999. Radionuclide therapy. *The Lancet* 354, 931-935.

Ciernik, I.F., Dizendorf, E., Baumert, B.G., Reiner, B., Burger, C., Davis, J.B., Lütolf, U.M., Steinert, H.C., Von Schulthess, G.K., 2003. Radiation treatment planning with an integrated positron emission and computer tomography (PET/CT): a feasibility study. *International Journal of Radiation Oncology\* Biology\* Physics* 57, 853-863.

Constantinou, C., Attix, F.H., Paliwal, B.R., 1982. A solid water phantom material for radiotherapy x-ray and  $\gamma$ -ray beam calibrations. *Medical Physics* 9, 436-441.

Crowther, R.A., DeRosier, D.J., Klug, A., 1970. The reconstruction of a three-dimensional structure from projections and its application to electron microscopy, *Proceedings of the Royal Society of London A: Mathematical, Physical and Engineering Sciences*. The Royal Society, pp. 319-340.

Dafermou, A., Colamussi, P., Giganti, M., Cittanti, C., Bestagno, M., Piffanelli, A., 2001. A multicentre observational study of radionuclide therapy in patients with painful bone metastases of prostate cancer. *European Journal of Nuclear Medicine* 28, 788-798.

Das, I.J., Ding, G.X., Ahnesjö, A., 2008. Small fields: nonequilibrium radiation dosimetry. *Medical Physics* 35, 206-215.

Davison, S., Goldblith, S.A., Proctor, B.E., Karel, M., Kan, B., Bates, C.J., 1953. Dosimetry of a kilocurie cobalt-60 source. *Nucleonics (US) Ceased publication* 11.



Day, M.J., Stein, G., 1950. Chemical effects of ionizing radiation in some gels. *Nature* 166, 146-147.

De Deene, Y., Vergote, K., Claeys, C., De Wagter, C., 2006. The fundamental radiation properties of normoxic polymer gel dosimeters: a comparison between a methacrylic acid based gel and acrylamide based gels. *Physics in Medicine and Biology* 51, 653-673.

De Deene, Y., 2009. Review of quantitative MRI principles for gel dosimetry, *Journal of Physics* 164, 012033.

De Deene, Y., 2010. How to scan polymer gels with MRI?, *Journal of Physics: Conference Series* 250, 012015.

De Laney, T.F., Kooy, H.M., 2008. Proton and charged particle radiotherapy. Lippincott Williams & Wilkins. ISBN: 0781765528

De Wagter, C., 2004. The ideal dosimeter for intensity modulated radiation therapy (IMRT): What is required?, *Journal of Physics: Conference Series* 3, 4-8.

Demanis, D.J., Rodriguez, R.R., Schour, L., Brandt, D., Altieri, G., 2005. High-dose-rate intensity-modulated brachytherapy with external beam radiotherapy for prostate cancer: California endocurietherapy's 10-year results. *International Journal of Radiation Oncology\* Biology\* Physics* 61, 1306-1316.

Dinsmore, M., Harte, K.J., Sliski, A.P., Smith, D.O., Nomikos, P.M., Dalterio, M.J., Boom, A.J., Leonard, W.F., Oettinger, P.E., Yanch, J.C., 1996. A new miniature x-ray source for interstitial radiosurgery: Device description, *Medical Physics*, pp. 45-52.

Doran, S.J., Koerkamp, K.K., Bero, M.A., Jenneson, P., Morton, E.J., Gilboy, W.B., 2001. A CCD-based optical CT scanner for high-resolution 3D imaging of radiation dose distributions: equipment specifications, optical simulations and preliminary results. *Physics in Medicine and Biology* 46, 3191-3213.

Doran, S.J., Krstajić, N., 2006. The history and principles of optical computed tomography for scanning 3-D radiation dosimeters, *Journal of Physics: Conference Series* 56, 45-57.

Farajollahi, A.R., 1998. An investigation into the applications of polymer gel dosimetry in radiotherapy. University of Leicester.

Farajollahi, A.R., Bonnett, D.E., Ratcliffe, A.J., Aukett, R.J., Mills, J.A., 1999. An investigation into the use of polymer gel dosimetry in low dose rate brachytherapy. *The British Journal of Radiology* 72, 1085-1092.

Flickinger, J.C., Lunsford, L.D., Kondziolka, D., 1992. Dose prescription and dose-volume effects in radiosurgery. *Neurosurgery Clinics of North America* 3, 51-59.

Fong, P.M., Keil, D.C., Does, M.D., Gore, J.C., 2001. Polymer gels for magnetic resonance imaging of radiation dose distributions at normal room atmosphere. *Physics in Medicine and Biology* 46, 3105-3113.

Frahn, M.S., Abellon, R.D., Jager, W.F., Luthjens, L.H., Warman, J.M., 2001a. Synthesis and characterization of a new fluorogenic probe molecule N-(1-pyrene) methacrylamide for monitoring radiation-induced polymerization. *Nuclear Instruments and Methods in Physics Research Section B: Beam Interactions with Materials and Atoms* 185, 241-247.

Frahn, M.S., Luthjens, L.H., Warman, J.M., 2003. N-(2-Anthracene) methacrylamide: a new fluorogenic probe molecule for monitoring in situ the radiation-induced polymerization of methyl methacrylate in bulk and in solution. *Polymer* 44, 7933-7938.

Frahn, M.S., Warman, J.M., Abellon, R.D., Luthjens, L.H., 2001b. Monitoring the radiation-induced bulk polymerisation of methyl methacrylate with N-(1-pyrene) maleimide. *Radiation Physics and Chemistry* 60, 433-437.

Fricke, H., Morse, S., 1927. The relation of chemical, colloidal and biological effects of roentgen rays of different wave lengths to the ionization which they produce in air—I. Action of roentgen rays on solutions of oxyhemoglobin in water. *American Journal of Roentgenology Radium Therapy* 18, 426-432.

Georg, D., Kirisits, C., Hillbrand, M., Dimopoulos, J., Pötter, R., 2008. Image-guided radiotherapy for cervix cancer: high-tech external beam therapy versus high-tech brachytherapy. *International Journal of Radiation Oncology\* Biology\* Physics* 71, 1272-1278.

Gore, J.C., Kang, Y.S., 1984. Measurement of radiation dose distributions by nuclear magnetic resonance (NMR) imaging. *Physics in Medicine and Biology* 29, 1189-1197.

Gore, J.C., Ranade, M., Maryanski, M.J., Schulz, R.J., 1996. Radiation dose distributions in three dimensions from tomographic optical density scanning of polymer gels: I. Development of an optical scanner. *Physics in Medicine and Biology* 41, 2695-2704.

Griessbach, I., Lapp, M., Bohsung, J., Gademann, G., Harder, D., 2005. Dosimetric characteristics of a new unshielded silicon diode and its application in clinical photon and electron beams. *Medical Physics* 32, 3750-3754.

Guo, P.Y., Adamovics, J.A., Oldham, M., 2006. Characterization of a new radiochromic three-dimensional dosimeter. *Medical Physics* 33, 1338-1345.

Gustavsson, H., Karlsson, A., Bäck, S.Å., Olsson, L.E., Haraldsson, P., Engström, P., Nyström, H., 2003. MAGIC-type polymer gel for three-dimensional dosimetry: Intensity-modulated radiation therapy verification. *Medical Physics* 30, 1264-1271.

Gutman, G., Sozontov, E., Strumban, E., Yin, F.F., Lee, S.W., Kim, J.H., 2004. A novel needle-based miniature x-ray generating system. *Physics in Medicine and Biology* 49, 4677-4688.

Haacke, E.M., Brown, R.W., Thompson, M.R., Venkatesan, R., 1999. *Magnetic resonance imaging: physical principles and sequence design*. Wiley-Liss New York.

Herzen, J., Todorovic, M., Cremers, F., Platz, V., Albers, D., Bartels, A., Schmidt, R., 2007. Dosimetric evaluation of a 2D pixel ionization chamber for implementation in clinical routine. *Physics in Medicine and Biology* 52, 1197-1208.

Jirasek, A., McAuley, K.B., Lepage, M., 2009. How does the chemistry of polymer gel dosimeters affect their performance?, *Journal of Physics: Conference Series* 164, 012003.

Jordan, K., 2004. Advances in optical CT scanning for gel dosimetry, *Journal of Physics: Conference Series* 3, 115-121.

Jordan, K., 2006. Review of recent advances in non gel dosimeters, *Journal of Physics: Conference Series* 56, 132.

Judenhofer, M.S., Wehrl, H.F., Newport, D.F., Catana, C., Siegel, S.B., Becker, M., Thielscher, A., Kneilling, M., Lichy, M.P., Eichner, M., 2008. Simultaneous PET-MRI: a new approach for functional and morphological imaging. *Nature Medicine* 14, 459-465.

Kanai, T., Kawachi, K., Kumamoto, Y., Ogawa, H., Yamada, T., Matsuzawa, H., Inada, T., 1980. Spot scanning system for proton radiotherapy. *Medical Physics* 7, 365-369.

Karnas, S.J., Avvakumov, N., Yu, E., Battista, J.J., 2001. Operational characteristics of a prototype x-ray needle device. *Physics in Medicine and Biology* 46, 97-106.

Kinahan, P.E., Rogers, J.G., 1989. Analytic 3D image reconstruction using all detected events. *IEEE Transactions on Nuclear Science* 36, 964-968.

Klevenhagen, S.C., 1991. Report of the IPSM working party on low-and medium-energy x-ray dosimetry.

Koehler, A.M., Schneider, R.J., Sisterson, J.M., 1975. Range modulators for protons and heavy ions. *Nuclear Instruments and Methods* 131, 437-440.

Koukourakis, G., Kelekis, N., Armonis, V., Kouloulis, V., 2009. Brachytherapy for prostate cancer: a systematic review. *Advances in Urology* 2009. DOI: 10.1155/2009/327945

Lepage, M., Jayasakera, P.M., Bäck, S.Å.J., Baldock, C., 2001. Dose resolution optimization of polymer gel dosimeters using different monomers. *Physics in Medicine and Biology* 46, 2665-2680.

Létourneau, D., Gulam, M., Yan, D., Oldham, M., Wong, J.W., 2004. Evaluation of a 2D diode array for IMRT quality assurance. *Radiotherapy and Oncology* 70, 199-206.

Levin, W.P., Kooy, H., Loeffler, J.S., DeLaney, T.F., 2005. Proton beam therapy. *British Journal of Cancer* 93, 849-854.

Levitt, S.H., Purdy, J.A., Perez, C.A., Vijayakumar, S., 2012. *Technical basis of radiation therapy*. Springer. ISBN: 3642115713

Low, D.A., Moran, J.M., Dempsey, J.F., Dong, L., Oldham, M., 2011. Dosimetry tools and techniques for IMRT. *Medical Physics* 38, 1313-1338.

Maeyama, T., Fukunishi, N., Ishikawa, K.L., Furuta, T., Fukasaku, K., Takagi, S., Noda, S., Himeno, R., Fukuda, S., 2014. A diffusion-free and linear-energy-transfer-independent nanocomposite Fricke gel dosimeter. *Radiation Physics and Chemistry* 96, 92-96.

Marchand, B., Prieels, D., Bauvir, B., Sépulchre, R., Gérard, M., 2000. IBA proton Pencil Beam Scanning: an innovative solution for cancer treatment, *Proceedings of EPAC*.

Marks, L.B., Spencer, D.P., 1991. The influence of volume on the tolerance of the brain to radiosurgery. *Journal of Neurosurgery* 75, 177-180.

Maryanski, M.J., Schulz, R.J., Ibbott, G.S., Gatenby, J.C., Xie, J., Horton, D., Gore, J.C., 1994. Magnetic resonance imaging of radiation dose distributions using a polymer-gel dosimeter. *Physics in Medicine and Biology* 39, 1437-1455.

Minohara, S., Fukuda, S., Kanematsu, N., Takei, Y., Furukawa, T., Inaniwa, T., Matsufuji, N., Mori, S., Noda, K., 2010. Recent innovations in carbon-ion radiotherapy. *Journal of Radiation Research* 51, 385-392.

Nithya, L., Raj, N.A.N., Rathinamuthu, S., Sharma, K., Pandey, M.B., 2014. Influence of increment of gantry angle and number of arcs on esophageal volumetric modulated arc therapy planning in Monaco planning system: A planning study. *Journal of Medical Physics/Association of Medical Physicists of India* 39, 231-237.

Oldham, M., Siewerdsen, J.H., Kumar, S., Wong, J., Jaffray, D.A., 2003. Optical-CT gel-dosimetry I: basic investigations. *Medical Physics* 30, 623-634.

Oldham, M., 2004. Optical-CT scanning of polymer gels, *Journal of Physics: Conference Series* 3, 122-135.

Oldham, M., Kim, L., 2004. Optical-CT gel-dosimetry II: Optical artifacts and geometrical distortion. *Medical Physics* 31, 1093-1104.

Olsson, L.E., Baeck, S., Magnussen, P., Haraldsson, P., 1998. 3D dosimetry using gels and MRI. *Imaging in Radiation Therapy* 34, 41-48.

Olsson, L.E., Fransson, A., Ericsson, A., Mattsson, S., 1990. MR imaging of absorbed dose distributions for radiotherapy using ferrous sulphate gels. *Physics in Medicine and Biology* 35, 1623-1631.

Paganetti, H., Bortfeld, T., 2005. Proton beam radiotherapy-the state of the art. in: *New Technologies in Radiation Oncology (Medical Radiology Series)*, (Eds.) W. Schlegel, T. Bortfeld and A.L. Grosu, Springer Verlag, Heidelberg.

Pappas, E., Maris, T., Angelopoulos, A., Paparigopoulou, M., Sakelliou, L., Sandilos, P., Voyiatzi, S., Vlachos, L., 1999. A new polymer gel for magnetic resonance imaging (MRI) radiation dosimetry. *Physics in Medicine and Biology* 44, 2677-2684.

Pavoni, J.F., Baffa, O., 2012. An evaluation of dosimetric characteristics of MAGIC gel modified by adding formaldehyde (MAGIC-f). *Radiation Measurements* 47, 1074-1082.

Peschel, R.E., Colberg, J.W., 2003. Surgery, brachytherapy, and external-beam radiotherapy for early prostate cancer. *The lancet oncology* 4, 233-241.

Podgorsak, M.B., Schreiner, L.J., 1992. Nuclear magnetic relaxation characterization of irradiated Fricke solution. *Medical Physics* 19, 87-95.

Poppe, B., Blechschmidt, A., Djouguela, A., Kollhoff, R., Rubach, A., Willborn, K.C., Harder, D., 2006. Two-dimensional ionization chamber arrays for IMRT plan verification. *Medical Physics* 33, 1005-1015.

Raeburn, S., 2000. Radiation doses in computed tomography. *BMJ* 320, 593-594.

Rogers, J.G., Harrop, R., Kinahan, P.E., 1987. Reconstruction for PET. *IEEE Transactions on Medical Imaging* 6, 239-243.

Ross, C.K., Klassen, N.V., 1996. Water calorimetry for radiation dosimetry. *Physics in Medicine and Biology* 41, 1-29.

Saha, G.B., 2015. *Basics of PET imaging: physics, chemistry, and regulations*. Springer.

Ter-Pogossian, M.M., 1983. Positron emission tomography (PET), *Diagnostic Imaging in Medicine*. Springer, pp. 273-277. ISBN: 3319164236.

Sakhalkar, H.S., Adamovics, J., Ibbott, G., Oldham, M., 2009. A comprehensive evaluation of the PRESAGE/optical-CT 3D dosimetry system. *Medical Physics* 36, 71-82.

Saunders, M., Dische, S., Barrett, A., Harvey, A., Griffiths, G., Parmar, M., 1999. Continuous, hyperfractionated, accelerated radiotherapy (CHART) versus conventional radiotherapy in non-small cell lung cancer: mature data from the randomised multicentre trial. *Radiotherapy and Oncology* 52, 137-148.

Saur, S., Strickert, T., Wasboe, E., Frengen, J., 2005. Fricke gel as a tool for dose distribution verification: optimization and characterization. *Physics in Medicine and Biology* 50, 5251-5261.

Schaetzing, R., 2003. *Computed radiography technology*. Advances in digital radiography. Course syllabus, RSNA, Inc. Oak Brook, 7-22.

Schaetzing, R., Fasbender, R., Kersten, P., 2002. New high-speed scanning technique for computed radiography, *Medical Imaging 2002*. International Society for Optics and Photonics, pp. 511-520.

Scharf, K., 1971. Spectrophotometric measurement of ferric ion concentration in the ferrous sulphate (Fricke) dosimeter. *Physics in Medicine and Biology* 16, 77-86.

Schreiner, L.J., 2004. Review of Fricke gel dosimeters, *Journal of Physics: Conference Series* 3, 9-21.

Schreiner, L.J., Olding, T., McAuley, K.B., 2010. Polymer gel dosimetry, *Journal of Physics: Conference Series* 250, 012014.

Schreiner, L.J., 2015. True 3D chemical dosimetry (gels, plastics): Development and clinical role, *Journal of Physics: Conference Series* 573, 012003.

Schulz, R.J., Wu, C.S., Weinhaus, M.S., 1987. The direct determination of dose-to-water using a water calorimeter. *Medical Physics* 14, 790-796.

Schulz, R.J., Nguyen, D.B., Gore, J.C., 1990. Dose-response curves for Fricke-infused agarose gels as obtained by nuclear magnetic resonance. *Physics in Medicine and Biology* 35, 1611-1622.

Seco, J., Clasié, B., Partridge, M., 2014. Review on the characteristics of radiation detectors for dosimetry and imaging. *Physics in Medicine and Biology* 59, R303-R347.

Sharir, T., Slomka, P.J., Berman, D.S., 2010. Solid-state SPECT technology: fast and furious. *Journal of Nuclear Cardiology* 17, 890-896.

Trofimov, A., Bortfeld, T., 2003. Optimization of beam parameters and treatment planning for intensity modulated proton therapy. *Technology in Cancer Research & Treatment* 2, 437-444.

Van Cutsem, E., Köhne, C.H., Hitre, E., Zaluski, J., Chang Chien, C.R., Makhson, A., D'Haens, G., Pintér, T., Lim, R., Bodoky, G., 2009. Cetuximab and chemotherapy as initial treatment for metastatic colorectal cancer. *New England Journal of Medicine* 360, 1408-1417.

Van Herk, M.V., Meertens, H., 1987. 99: A digital imaging system for portal verification, *The use of computers in radiation therapy*. ISBN: 0-444-70263-6

Van Herk, M., Bel, A., Gilhuijs, K.G.A., Vijlbrief, R.E., 1993. A comprehensive system for the analysis of portal images. *Radiotherapy and Oncology* 29, 221-229.

Vandecasteele, J., De Deene, Y., 2012. On the validity of 3D polymer gel dosimetry: III. MRI-related error sources Both authors contributed equally to this study. *Physics in Medicine and Biology* 58, 63-85.

Vandecasteele, J., De Deene, Y., 2013. Evaluation of radiochromic gel dosimetry and polymer gel dosimetry in a clinical dose verification. *Physics in Medicine and Biology* 58, 6241-6262.

Venning, A.J., Brindha, S., Hill, B., Baldock, C., 2004. Preliminary study of a normoxic PAG gel dosimeter with tetrakis (hydroxymethyl) phosphonium chloride as an anti-oxidant, *Journal of Physics: Conference Series* 3, 155-158.

Verhaegen, F., Palmans, H., 2001. A systematic Monte Carlo study of secondary electron fluence perturbation in clinical proton beams (70–250 MeV) for cylindrical and spherical ion chambers. *Medical Physics* 28, 2088-2095.

Warman, J.M., De Haas, M.P., Luthjens, L.H., 2009a. High-energy radiation monitoring based on radio-fluorogenic co-polymerization. I: small volume in situ probe. *Physics in Medicine and Biology* 54, 3185.

Warman, J.M., Luthjens, L.H., de Haas, M.P., 2009b. In-situ radiation dosimetry based on Radio-Fluorogenic Co-Polymerization, *Journal of Physics: Conference Series* 164, 012048.

Warman, J.M., de Haas, M.P., Luthjens, L.H., Murrer, H.P., 2011a. A Radio-Fluorogenic Organic Gel for Real-Time, 3D Radiation Dosimetry. *Advanced Materials* 23, 4953-4955.

Warman, J.M., Luthjens, L.H., De Haas, M.P., 2011b. High-energy radiation monitoring based on radio-fluorogenic co-polymerization II: fixed fluorescent images of collimated x-ray beams using an RFCP gel. *Physics in Medicine and Biology* 56, 1487-1508.

Warman, J.M., de Haas, M.P., Luthjens, L.H., Denkova, A.G., Kavatsyuk, O., van Goethem, M.J., Kiewiet, H.H., Brandenburg, S., 2013a. Fixed fluorescent images of an 80MeV proton pencil beam. *Radiation Physics and Chemistry* 85, 179-181.

Warman, J.M., De Haas, M.P., Luthjens, L.H., Hom, M.L., 2013b. High-energy radiation monitoring based on radio-fluorogenic co-polymerization III: Fluorescent images of the cross-section and depth-dose profile of a 3MV electronbeam. *Radiation Physics and Chemistry* 84, 129-135.

White, S.C., Pharoah, M.J., 2014. *Oral radiology: principles and interpretation*. Elsevier Health Sciences. ISBN: 032309634





## Chapter 2

# Polymer-gel formation and reformation on irradiation of tertiary-butyl acrylate<sup>4</sup>

### 2.1. Introduction

In their pioneering paper Day and Stein (1950) said “In the search for a suitable system which would enable three-dimensional distributions of absorbed energy to be demonstrated, we have experimented with gels containing dyes which are reduced with change of colour on irradiation”. The gel matrix in their study functioned to limit the free diffusion of chromophoric radiolytic products, resulting in their (at least temporary) spatial fixation in the location where they were formed. This idea has been the basis of most subsequent attempts to produce physico-chemical-based, 3D radiation dosimeters (Baldock 2006, Jirasek 2006, McAuley 2006, Baldock *et al* 2010, Schreiner *et al* 2010). Until recently only aqueous gels have been used with natural

---

<sup>4</sup> This chapter has been published in part as "Radiation Physics and Chemistry, 97 (2014) 147, authors T. Yao, A. G. Denkova and J. M. Warman"

polymers such as gelatin or agarose forming the gel matrix. Invariably two or more additional chemical components are included in order to induce the particular radiogenic effect to be probed and related to the dose deposition. The great variety and chemical complexity of gel recipes proposed can be found in the recent reviews of the topic given above. There is little doubt that this complexity, and the associated difficulty of assuring an (internationally) consistent composition and quality of the chemicals used (including the water!), presents one of the barriers holding back the general clinical adoption of the polymer-gel method of 3D dosimetry.

A chemically simpler, two-component gel recipe capable of producing three-dimensional images of the dose distribution produced by a variety of radiation sources has been demonstrated by Warman *et al.* (2011ab, 2013ab). The method is based on the radiation-induced, free-radical polymerization of a bulk monomer (tertiary-butyl acrylate, TBA) and the co-polymerization of a second monomer component (maleimido-pyrene, MPy) present in low (*ca* 100 ppm) concentration. The *non-fluorescent* MPy is converted into the *fluorescent* succinimido derivative, -SPy-, on incorporation into the poly-TBA chain. In this way the medium develops a fluorescent intensity in ultraviolet light that is proportional to the yield of free-radicals formed by the radiation and hence to the dose deposited (Warman *et al.* 2009a,b).

In order to prevent diffusion of the fluorescent polymer chains from their point of formation, their motion is restricted by a 3D polymer-gel network, as in other polymer-gel dosimeters. In this case however the overall gel consists for 99.99% of a single chemical component, *i.e.* partially (*ca* 15%) polymerized and cross-linked tertiary-butyl acrylate. An initially non-fluorescent form of the radio-fluorogenic gel (RFG) is prepared by a process of: irradiation of pure TBA to *ca* 15% monomer conversion; removal of remaining monomer by evacuation; addition of an equal volume of a dilute solution of MPy in TBA to the remaining polymer; swelling of the polymer back to its original gel form and consistency. This procedure is necessary because straightforward formation of a gel by irradiation of an MPy solution directly would result in a gel with an initial high background fluorescence over its whole volume.

Because of the dominance of TBA polymerization in both the passive gel formation procedure and the active dosimetric co-polymerization process, we decided to carry out a thorough study of the radiation chemistry of TBA with particular attention given to the dependence of monomer-to-polymer conversion on accumulated dose and dose rate, and the reproducibility of the radiation-chemical properties after a gel reformation procedure. The work presented here concerns therefore only pure TBA. In future studies the present results will be related to monomer conversion and fluorescence studies on RFGs containing MPy.

## 2.2. Experimental

### 2.2.1. Materials

The radiation-polymerizable monomer investigated in this work was tertiary-butyl acrylate, TBA (Sigma-Aldrich >98%, #327182); a colourless liquid with the elemental composition C<sub>7</sub>H<sub>12</sub>O<sub>2</sub> and molecular weight 128.2 g.mol<sup>-1</sup>. The molecular structure of TBA is given in figure 2.1. As supplied the liquid contains *ca* 20 ppm hydroquinone stabilizer. This was removed by passage over an inhibitor removal column (Sigma-Aldrich #306312) after which the liquid was stored in glass vessels, in the dark, at 5 °C. The density of the liquid at 20 °C is 0.89 kg.L<sup>-1</sup> corresponding to a monomer concentration of 6.94 mol.L<sup>-1</sup>. The density of fully-polymerized TBA resin is 1.09 kg.L<sup>-1</sup>. For a fractional monomer-to-polymer conversion C<sub>M</sub> the density will be approximated by:

$$\rho(C_M) = [0.89(1 - C_M) + 1.09C_M] \text{ kg.L}^{-1} \quad (2.1)$$

For C<sub>M</sub> = 15%, ρ = 0.92 kg.L<sup>-1</sup>.

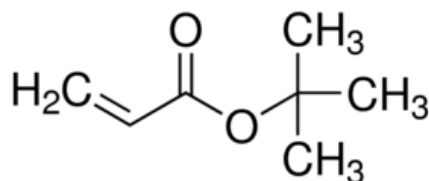


Figure 2.1. The molecular structure of tertiary-butyl acrylate.

Other properties of TBA relevant to the procedures used here are the boiling point, 120<sup>0</sup>C, and the room temperature vapor pressure, 16 mbar. The former needs to be reasonably high to prevent evaporation of large amounts of monomer during de-aeration by purging with nitrogen. On the other hand, the vapor pressure should be high enough that removal of the remaining monomer by evacuation after polymerization does not require an excessively long time.

Note: TBA is non-explosive but flammable and precautions should be taken to ensure good ventilation of the vapor during handling. It is also aggressive towards many plastics and should be contained only in glass or polyethylene vessels. General information on health and safety precautions when handling TBA are readily available (MSDS, [http://www.chemicalbook.com/CASEN\\_1663-39-4.htm#MaterialSafetyDataSheetMSDS](http://www.chemicalbook.com/CASEN_1663-39-4.htm#MaterialSafetyDataSheetMSDS))

Testament to the lack of serious health hazards; TBA is widely used as a copolymer in over-the-counter hair-styling gels.

### 2.2.2. Sample preparation

Approximately 100 mL TBA in a glass flask was pre-purged with nitrogen in a fume hood for *ca* 2 minutes prior to placing the closed flask in the transfer compartment of a glove box (PLAS LABS model GB 818). Several coded and weighed sample containers were transferred

open, together with the closed TBA flask into the glove box. The sample containers used for the gravimetric measurements of monomer conversion were 20 mL glass “liquid scintillation vials” (LSVs) with metal-foil-lined polypropylene screwcaps. Figure 2.2 and 2.3 show the glove box and LSVs used for preparing deaerated TBA samples. The LSVs and TBA container were allowed to stand for at least 24 hours in the glove box, which was continuously flushed, with nitrogen, to remove any traces of oxygen on the surfaces of the vessels. The TBA was then purged with nitrogen in the glove box for 30 minutes after which 10 mL aliquots were pipetted into each LSV. These were then closed and placed in the glove-box transfer compartment.



Figure 2.2. The glove box PlasLabs GB818 used for deaerating TBA liquid.



Figure 2.3. Liquid scintillation vials (LSVs) with Al-lined cap. A sample with 10 mL TBA liquid is shown on the right.

For optical absorption measurements, a square, 10x10 mm<sup>2</sup> (internal dimensions) quartz glass cell fitted with a GL14 screwcap was used. This could be placed in the cell holder of a UV/vis spectrophotometer (Kontron Uvikon-940). For these measurements a 3.5 mL aliquot of de-aerated TBA was used.

### 2.2.3. Irradiation procedure and monomer conversion

The LSVs containing 10 mL de-aerated TBA were placed in the irradiation chamber of a GC200 (Atomic Energy of Canada) or a GC220 (Nordion) gamma-ray source (see figure 2.4) with dose rates of *ca* 3.5 or 49 cGy.s<sup>-1</sup> (*ca* 2.0 or 30 Gy.min<sup>-1</sup>) respectively. The precise dose rates on the day of irradiation were based on Fricke dosimetry corrected for the 2,778 day exponential decay time (5.27 yr half-life) of cobalt-60.

A schematic drawing of the irradiators is shown in figure 2.5. Samples are mechanically transported to be irradiated in the source chamber. The source timer is triggered by a micro-switch on complete insertion of the sample in the irradiation zone and irradiated for the time set on the timer. During transport the sample is exposed to radiation prior to and subsequent to complete insertion. The *effective* transit times for GC200 and GC220 have been determined to be 10 and 6 seconds respectively (see chapter 4). The transit times are added to the set time for dose calculation.



Figure 2.4. Cobalt-60 irradiators gammacell 200 from Atomic Energy of Canada (left) and 220 from Nordion (right).

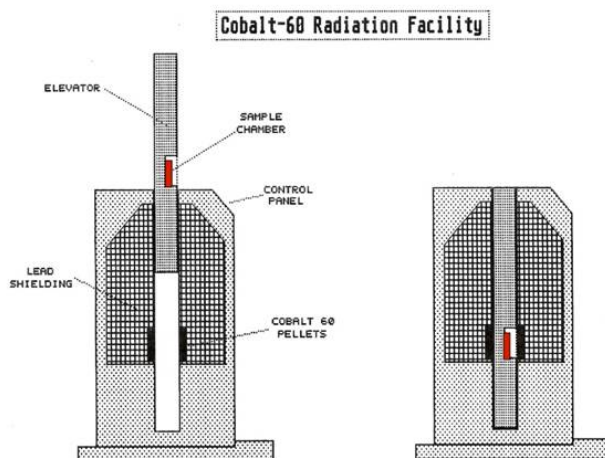


Figure 2.5. Schematic drawing of the internal design of the gamma source: samples are placed in the chamber (left) and are transported and irradiated in the source pellet region(right).

The fractional monomer conversion,  $C_M$ , after a given dose  $D$  Gy was determined gravimetrically: after irradiation the LSVs were opened and weighed prior to being placed in a vacuum oven (Heraeus) at room temperature. The remaining monomer was removed by evacuation using a diaphragm pump. At regular intervals the LSVs were removed from the oven, weighed and replaced. From this the fraction of monomer plus polymeric TBA remaining  $h$  hours after the start of evacuation,  $W(h)/W(0)$ , was determined. Some representative data for different doses are plotted in figure 2.6 for an evacuation period of approximately 2 weeks (336 hours).

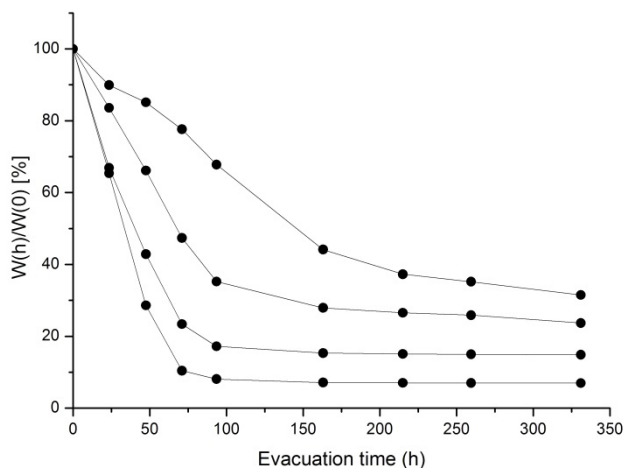


Figure 2.6. The decrease in weight of TBA as a function of evacuation time after a gamma-ray exposure in source GC200 of, from bottom to top trace, 4, 8, 12 and 16 minutes (8.3, 16.6, 24.9 and 33.1 Gy).

For doses up to *ca* 20 Gy a constant plateau value of  $W(h)/W(0)$  was reached within a week (168 hours) of beginning evacuation. For doses in excess of 20 Gy the time required to reach a plateau value increased substantially. This can be associated with the formation of a complete 3D gel network that restricts monomer motion to the surface and hence retards evacuation. For such samples the weighing procedure was extended until the weight loss over an intervening period of two days was less than 2%. The value of  $C_M$  was taken to be equal to the ultimate plateau value of  $W(h)/W(0)$ , *i.e.*  $C_M = W(\infty)/W(0)$ .

#### 2.2.4. Reformed gels

In “gel reformation” a sample of liquid monomer is irradiated to yield a gel with polymer fraction,  $C_M$ . The remaining monomer is removed by evacuation leaving only polymer. A volume of monomer equal to that removed by evacuation is then added to the polymer which is allowed to swell for several days. Our interest was in whether the properties of the gel are the same before and after the reformation procedure. This swelling of poly(butyl acrylate) has been suggested as a method for the recovery of organic solvents (Kattan and Al-Kassiri, 2010).

In the present work we used the following reformation procedure: several LSVs containing 10 mL de-aerated TBA were irradiated for 6 minutes (*ca* 12 Gy) in GC200. These were subsequently evacuated for 1 week to remove monomer. As an example of the reproducibility of this procedure the  $C_M$  values found for 8 separate LSV samples were 10.6, 10.7, 10.7, 10.3, 10.6, 10.7, 10.5 and 10.7 percent. After monomer evacuation the LSVs with the remaining polymer were transferred to the glove box and 9 mL of de-aerated liquid TBA was added and allowed to stand for 2 weeks. The reformed gels, so obtained, were then irradiated in GC200 and GC220 with a range of doses and were subjected to the same gravimetric procedure for determining  $C_M$  as for the initial liquid samples.

## 2.3. Results and Discussion

### 2.3.1. Gel properties

During preliminary measurements the viscosity of TBA was observed to increase considerably even after an exposure of only 2 minutes (*ca* 4 Gy) in the GC200 source. For higher doses a clear, quasi-rigid gel was formed. This behaviour is characteristic of irradiated bulk alkyl acrylates and is a result of chain transfer leading to chain-branching, cross-linking and ultimately to the formation of a complete three-dimensional gel network (Charlesby, 1960; Chapiro, 1962; Hayashi et al, 1988; Kattan and Al-Kassiri, 2010). In the case of the tertiary-butyl derivative chain transfer can only occur via abstraction of the backbone hydrogen atom alpha to the carbonyl group while for other alky derivatives abstraction of the hydrogen alpha to the ester oxygen provides an additional route for cross-linking (Shultz and Bovey, 1956).

As a qualitative test of the increase in viscosity, five LSVs containing 10 mL de-aerated TBA were irradiated to different doses after which they were placed on their side and photographed at increasing elapsed times, as shown in figure 2.7.

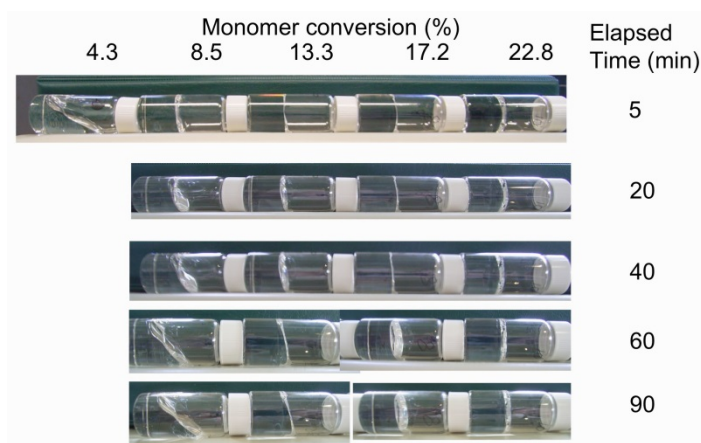


Figure 2.7. Five vials containing 10 mL TBA irradiated with doses (from left to right) of 5, 10, 15, 20, 25 Gy photographed after lying on their sides for the elapsed times shown on the right.



The increase in “rigidity” of the medium with increasing monomer conversion is illustrated by the decreasing rate of creep of the meniscus. For  $C_M$  in excess of *ca* 15% the gel is seen to remain stable (“quasi-rigid”) for close to an hour or more. These observations are relevant to the practical application of such TBA gels in radio-fluorogenic imaging since the medium should remain geometrically stable and molecular diffusion should be negligible during the course of the irradiation and imaging procedures.

The clarity of the gel is also an important factor in its application as an optical imaging medium. The absorption spectra of de-aerated TBA before irradiation and after a dose of 17 Gy ( $C_M \approx 15\%$ ) are shown in figure 2.8.

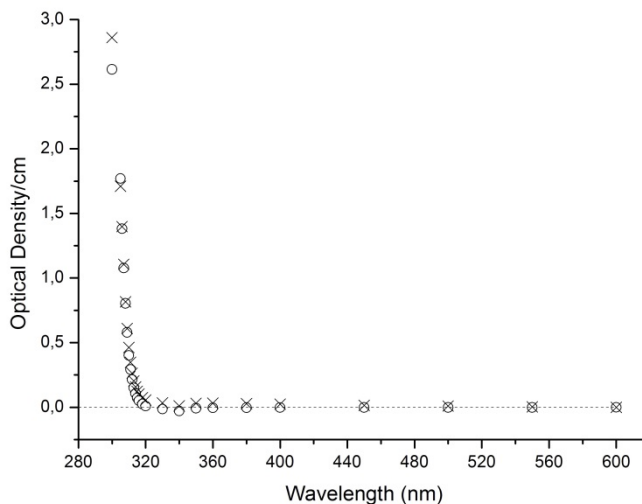


Figure 2.8. Absorption spectra of tertiary-butyl acrylate: circles, pure, unirradiated liquid; crosses, gel with  $C_M \approx 15\%$ .

For both the liquid and gel the absorption in the visible and near UV is seen to be extremely low with an OD less than  $0.1 \text{ cm}^{-1}$  from 600 nm down to the acrylate absorption beginning at 310 nm. There is no evidence of colouration or turbidity on irradiation. The preservation of optical clarity is also evident in the gel photographs in Figure 2.7. This clarity contrasts with water-based polymer-gel systems, which often become turbid on irradiation due to phase separation; an effect that has in fact been used for 3D dose imaging (Gore et al, 1996).

### 2.3.2. Dose and dose rate dependence of monomer conversion

In figure 2.9A the monomer conversion,  $C_M$ , is plotted against dose for irradiations in the GC200 ( $3.5 \text{ cGy.s}^{-1}$ ) and GC220 ( $49 \text{ cGy.s}^{-1}$ ). In the case of the GC200 measurements, three separately prepared TBA batches were used. This is indicated in the figure by the use of 3 different open symbols. The agreement between the 3 data sets demonstrates the good reproducibility of the combined glove-box preparation, gamma-ray irradiation, and gravimetric

analysis procedures. Importantly, the data extrapolate back to zero at zero dose with no indication of a delay in the onset of polymer formation attributable to the presence of traces of oxygen. This demonstrates the efficacy of the glove box de-aeration procedure used.

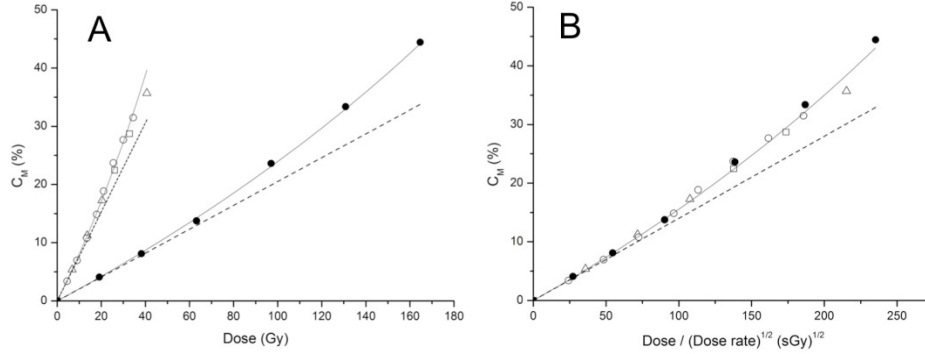


Figure 2.9. The fractional monomer-to-polymer conversion,  $C_M$ , on irradiation of deaerated liquid TBA. **A:** as a function of dose using gamma-ray source GC200 (open symbols) and GC220 (filled circles). The different open symbols represent different batch preparations. **B:** as a function of dose normalized by the square root of the dose rates of 3.5 and 49 cGy/s respectively. The full lines are superlinear fits calculated using equation (2.4) and the dashed straight lines are the low-conversion limiting linear dependence of this equation.

It is clear that there is a strong dose rate dependence of monomer conversion. This is as expected for a free-radical polymerization process where the chain reaction is limited only by the radical-radical termination processes of combination and disproportionation. The process of free radical polymerization involving four steps: primary free radical formation, initiation, propagation and termination, are shown below:

Free radicals are formed with a rate  $g(R)$  with the unit of moles per Gy,



The free radicals initiate chain polymerization by reacting with a monomer  $M$ ,



Chain propagation is followed by repeating addition of bulk monomers, with a rate coefficient  $k_p$ ,



Chain polymerization is terminated by reaction of two growing radical chains, with rate coefficient  $k_t$ ,



Under these conditions  $C_M$  should display a dependence on dose,  $D$ , and dose rate,  $D'$ , for low conversions given by (Charlesby, 1960; Luthjens et al, 2001),

$$C_M = KD/\sqrt{D'} \quad (2.2)$$

$$\text{with } K = k_p[\rho g(R)/2k_t]^{0.5} \quad (2.3)$$

In (2.3),  $k_p \text{ L.mol}^{-1}.\text{s}^{-1}$  is the average chain propagation rate coefficient,  $\rho \text{ kg.L}^{-1}$  is the medium density,  $g(R) \text{ mol.J}^{-1}$  is the yield of initiating free-radicals, and  $k_t \text{ L.mol}^{-1}.\text{s}^{-1}$  is the overall rate coefficient of radical-radical chain termination. Accordingly, the  $C_M$  data have been re-plotted against the dose normalized by the square root of the dose rate in figure 2.9B. As predicted by (2.2), the two sets of data, for dose rates differing by more than an order of magnitude, are now seen to fall on the same line.

As mentioned above, there is a tendency for the dose dependence of  $C_M$  to be superlinear. This is counter-intuitive since the monomer concentration and hence the rate of chain propagation,  $k_p[\text{TBA}]$ , should decrease with conversion and hence result in a negative deviation from the initial linear dependence. The superlinear behaviour actually observed has been explained by a decrease in the (diffusion-controlled) rate coefficient of termination,  $k_t$ , caused by the increasing viscosity of the medium. This apparently more than compensates for the decrease in the rate of chain propagation. A second possible explanation is that the free-radical yield from irradiation of the polymer is larger than on irradiation of the monomer.

To take the superlinear behaviour into account we have used as a first approximation the following relationship to fit the data,

$$C_M = (1 + AC_M)KD/\sqrt{D'} \quad (2.4)$$

The full lines drawn through the data points in figures 2.9A and 2.9B were made using equation (2.4) with  $K = 1.43 \times 10^{-3} \text{ Gy}^{-0.5}.\text{s}^{-0.5}$  and  $A = 0.70$  (for  $C_M$  a fraction). The limiting linear dependence, of slope  $K$ , is drawn as a straight dashed line in figures 2.9A and 2.9B. The experimental data are seen to be well described by relation (2.4). To calculate the monomer conversion for a given dose and dose rate, equation (2.4) can be written as:

$$C_M(D) = [\sqrt{D'}/KD - A]^{-1} \quad (2.5)$$

To calculate the dose required for a given monomer conversion, equation (2.4) can be written as:

$$D(C_M) = C_M \sqrt{D'}/[K(1 + AC_M)] \quad (2.6)$$

A similar gravimetric study of monomer conversion on irradiation of methyl methacrylate (MMA) was carried out using the GC200 and GC220 sources several years ago when the dose rates were considerably higher (Luthjens et al, 2001). From an analogous plot for MMA to that shown in figure 2.9B a value of  $K_{\text{MMA}} = 3.6 \times 10^{-5} \text{ Gy}^{-0.5}.\text{s}^{-0.5}$  can be determined. This is a factor of 40 lower than the value of  $K_{\text{TBA}}$  determined in the present work. This can be attributed mainly to the much higher chain propagation rate coefficient for acrylates compared with methacrylates

(Matheson *et al*, 1951; Charlesby, 1960; Hayashi *et al*, 1988; Beuermann *et al*, 1996; van Herk, 1997). Values at 25 °C of  $k_p = 1.61 \times 10^4$  and  $3.42 \times 10^2 \text{ L.mol}^{-1}.\text{s}^{-1}$  have been determined for butyl acrylate (isomer not given) and MMA respectively giving a ratio of 47 (van Herk, 1997).

If the yield of initiating free-radicals is known, the average size, in monomer units, of the polymers formed can be estimated. The concentration of free-radicals produced for an accumulated dose  $D$  Gy is  $\rho g(R)D \text{ mol.L}^{-1}$ . The concentration of monomer TBA converted to polymer for the same dose is  $[1000\rho/M][KD/\sqrt{D}'] \text{ mol.L}^{-1}$  with  $M$  g/mol the monomer molecular weight. The ratio of the latter to the former concentration gives the average number of monomer units incorporated per initiation event,  $\langle n \rangle$ ,

$$\langle n \rangle = 1000K/Mg(R)\sqrt{D'} \quad (2.7)$$

Taking the value of  $g(R)$  for TBA to be similar to the value of  $5 \times 10^{-7} \text{ mol.J}^{-1}$  found for MMA (Luthjens *et al*, 2001), together with  $K = 1.43 \times 10^{-3} \text{ Gy}^{-0.5}.\text{s}^{-0.5}$  gives  $\langle n \rangle \approx 2.2 \times 10^4 / \sqrt{D}'$ . The average monomer per initiator values for the low and high dose rates in the present work are therefore approximately  $1.2 \times 10^5$  and  $3.1 \times 10^4$ . These correspond to fully outstretched chain lengths of 23 and 6.2  $\mu\text{m}$  respectively. Because of chain-contortions, branching and cross-linking the actual chain lengths will be considerably shorter. The timescale of the polymerization process from initiation to termination can be estimated from  $\tau_p \approx \langle n \rangle / k_p [\text{TBA}]$  which is 1.4 second for the low dose rate source.

### 2.3.3. Monomer conversion in a reformed gel

The aim of these particular measurements was to see if after completely removing the monomer from a gel by evacuation, the gel could be reformed by adding to the remaining polymer the same amount of monomer that had been removed and allowing the liquid and polymer to stand for several days. Even if a gel did form by swelling a question remained as to whether the network structure, and the polymerization dynamics within the monomer-rich regions, were the same as for the initial gel.

In figure 2.10 are shown the monomer conversion data as a function of dose starting with the pure liquid, together with the total  $C_M$  for a reformed gel with an initial  $C_M$  of 10.2% and a pre-irradiation dose of *ca* 12 Gy. The good agreement between the two sets of data, indicates that the environment of the monomer within the gel network has not been substantially changed by the intervening reformation procedure.

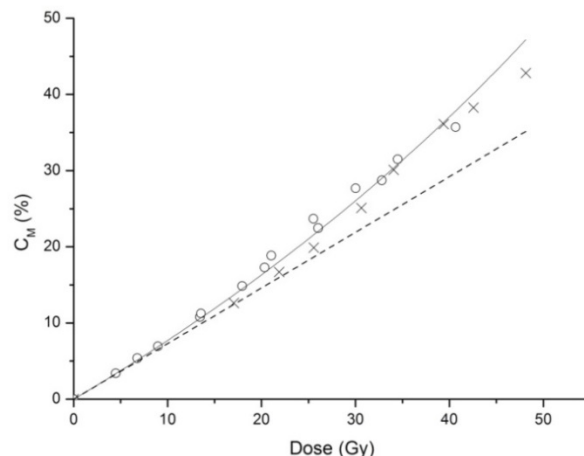


Figure 2.10. Monomer conversion as a function of total dose for TBA irradiated in source GC200: open circles, starting with pure monomer liquid; crosses, starting with a reformed gel with preirradiation dose 12.8 Gy (initial  $C_M = 10.2\%$ ). The full and dashed lines were drawn using equation (2.4) and the same values of  $K$  and  $A$  as in figure 2.9.

For radio-fluorogenic dosimetry applications a reformed gel is the starting material (Warman *et al*, 2011a). Rather than pure TBA however a dilute solution of a fluorogenic compound in TBA is used in the reformation step. Of interest therefore are the dose and dose rate dependences of the subsequent, further increase in  $C_M$ ,  $\Delta C_M$ , which would result in copolymerization and hence fluorescence of the fluorogenic compound if present. Values of  $\Delta C_M$  determined using the GC200 and GC220 sources are plotted against the incremental dose to the reformed (with pure TBA) gel in figure 2.11.

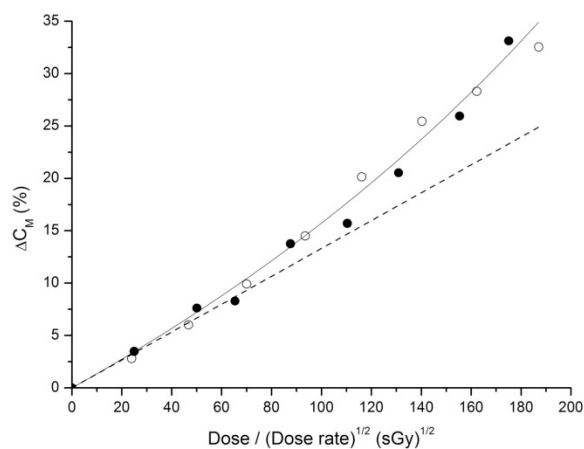


Figure 2.11. The increase in monomer conversion,  $\Delta C_M$ , of a reformed TBA gel (initial  $C_M$  ca 10%) as a function of dose using gamma-ray source GC200 (open symbols) and GC220 (filled circles). The dose has been normalized by the square root of the source dose rates of 3.5 and 49 cGy/s respectively. The full line was calculated using equation (2.8) and the dashed straight line is the low-conversion linear limit to this equation.

When normalized by the square root of the dose rate the two sets of data are seen to be in good agreement although with somewhat more scatter than the analogous data starting with the unirradiated liquid shown in figure 2.9B. The square root dose rate dependence shows that chain termination within the reformed gel matrix still occurs via radical-radical combination and disproportionation reactions.

The full line drawn through the data points in figure 2.11 was calculated using an analogous relationship to (2.4),

$$\Delta C_M = (1 + B\Delta C_M)KD/\sqrt{D'} \quad (2.8)$$

The values of  $K = 1.33 \times 10^{-3} \text{ Gy}^{-0.5} \cdot \text{s}^{-0.5}$  and  $B = 1.2$  found are to be compared with the values of  $K = 1.43 \times 10^{-3} \text{ Gy}^{-0.5} \cdot \text{s}^{-0.5}$  and  $A = 0.7$  determined from the data in figure 2.9 for the pure liquid with no intervening reformation.

## 2.4. Conclusions

As mentioned in the introduction the aim of the present work was to provide information on tertiary-butyl acrylate relevant to its role in radio-fluorogenic polymer-gel (RFG) dose imaging (see Warman *et al*, 2011ab, 2013ab). TBA plays in fact a double role; firstly forming a quasi-rigid, transparent, 3D gel network and secondly undergoing radiation-induced copolymerization with a fluorogenic compound present within the reformed network.

The first role requires homogeneous irradiation of pure, de-aerated TBA to a monomer-to-polymer conversion of approximately 15%; which we show here to be enough to form a stable 3D gel network by cross-linking. The use of high-energy radiation to produce the gel has the advantage that the process is accurately controllable, which results in the excellent batch-to-batch reproducibility we have found. In addition, the lack of necessity of initiator compounds results in excellent transparency in the visible and near UV. Since the gel has a density of 0.92 kg/L and a light-element composition of  $\text{C}_7\text{H}_{12}\text{O}_2$ , it may be considered to be “tissue equivalent”.

The second role depends on being able to remove the *ca* 90% monomer TBA in the gel and replace it with a solution containing a low (ppm) concentration of a fluorogenic compound in TBA. We show in the present work that it is possible to reform the gel after monomer evacuation by swelling the poly-TBA with monomer TBA with no discontinuity in the polymerization kinetics within the gel network. While the presence of a dilute solute should have no influence on the reformation process, it may affect the polymerization dynamics. This is the subject of ongoing research. Of particular interest in current work is how the dose rate dependence of monomer conversion found in the present work is reflected in the fluorescence yields of a radio-fluorogenic gel. This is of importance if the RFG method is to be used as a quantitative method of

3D dosimetry for variable dose rate fields as in brachytherapy or proton therapy. Results of this research are presented in subsequent chapters of this thesis.

## References

Baldock, C., 2006. Historical overview of the development of gel dosimetry: a personal perspective. *Journal of Physics: Conference Series* 56, 14-22.

Baldock, C., De Deene, Y., Doran, S., Ibbott, G., Jirasek, A., Lepage, M., McAuley, K.B., Oldham, M., Schreiner, L.J., 2010. Polymer gel dosimetry. *Physics in Medicine and Biology* 55, R1-R63.

Beuermann, S., Paquet, D.A. Jr., McMinn, J.H., Hutchinson R.A., 1996. Determination of free-radical propagation rate coefficients of butyl, 2-ethylhexyl, and dodecyl acrylates by pulsed-laser polymerization, *Macromolecules* 29, 4206-4215.

Charlesby, A., 1960. *Radiation effects in materials*, vol. 1 Atomic radiation and polymers. (Pergamon press, Oxford).

Chapiro, A., 1962. *Radiation chemistry of polymeric systems*. (John Wiley & Sons, New York, London).

Day, M.J., Stein G., 1950. Chemical effects of ionizing radiation in some gels. *Nature* 166, 146-147.

Gore, J.C., Ranade, M., Maryanski, M.J., Schulz, R.J., 1996. Radiation dose distributions in three dimensions from tomographic optical density scanning of polymer gels: I. Development of an optical scanner. *Physics in Medicine and Biology* 41, 2695-2704.

Hayashi, K., Takezaki, J., Okada, T., Sakurada, I., 1988. Radiation-induced polymerization of methyl methacrylate and alkyl acrylates at high dose rate. *Journal of Applied Polymer Science* 36, 295-308.

Herk, A.M. van, 1997. Pulsed initiation polymerization as a means of obtaining rate coefficients in free-radical polymerizations. *Journal of Macromolecular Science*, C37(4) 633-648.

Jirasek, A., 2006. Experimental investigations of polymer gel dosimeters. *Journal of Physics: Conference Series* 56, 23-34.

Kattan, M., Al-Kassiri, H., 2010. Radiation-induced polymerization of butyl acrylate for recovery of organic solvents. *Journal of Applied Polymer Science* 115, 3623-3627.

Luthjens, L.H., Frahn, M.S., Abellon, R.D., Hom, M.L., Warman, J.M., 2001. Steady-state and pulsed studies of the radiation-induced polymerization of methyl methacrylate. *Research on Chemical Intermediates* 27, 765-773.

McAuley, K.B., 2006. Fundamentals of polymer gel dosimeters. *Journal of Physics: Conference Series* 56, 35-44.

Material Safety Data sheet, [http://www.chemicalbook.com/CASEN\\_1663-39-4.htm#MaterialSafetyDataSheetMSDS](http://www.chemicalbook.com/CASEN_1663-39-4.htm#MaterialSafetyDataSheetMSDS)

Matheson M.S., Auer E. E., Bevilacqua E. B., Hart E. J., 1951. Rate constants in free-radical polymerizations. IV Methyl acrylate. *Journal of the American Chemical Society* 73, 5395-5400.

Schreiner, L.J., Olding, T., McAuley, K.B., 2010. Polymer gel dosimetry, *Journal of Physics: Conference Series* 250, 012014.

Shultz, A.R., Bovey, F.A., 1956. Electron irradiation of polyacrylates, *Journal of Polymer Science* XXII, 485-494.

Warman, J.M., Luthjens, L.H., de Haas, M.P., 2009a. In-situ radiation dosimetry based on Radio-Fluorogenic Co-Polymerization. *Journal of Physics: Conference Series* 164, 012048 (1-5)

Warman, J.M., Luthjens, L.H., de Haas, M.P., 2009b. High-energy radiation monitoring based on radio-fluorogenic co-polymerization. I: Small volume in-situ probe. *Physics in Medicine and Biology* 54, 3185-3200.

Warman, J.M., de Haas, M.P., Luthjens, L.H., 2011a. High-energy radiation monitoring based on radio-fluorogenic co-polymerization II: fixed fluorescent images of collimated X-ray beams using an RFCP gel. *Physics in Medicine and Biology* 56, 1487-1508.

Warman, J.M., de Haas, M.P., Luthjens, L.H., Murrer, H.P., 2011b. A radio-fluorogenic organic gel for real-time, 3D radiation dosimetry. *Advanced Materials* 23, 4953-4955. <http://dx.doi.org/10.1002/adma.201102831>

Warman, J.M., de Haas, M.P., Luthjens, L.H., Hom, M.L., 2013a. High-energy radiation monitoring based on radio-fluorogenic co-polymerization III: fluorescent images of the cross-section and depth-dose profile of a 3 MV electron beam. *Radiation Physics and Chemistry* 84, 129-135. <http://dx.doi.org/10.1016/j.radphyschem.2012.06.031>



Warman, J.M., de Haas, M.P., Luthjens, L.H., Kavatsyuk, O., van Goethem, M-J., Kiewiet, H.H., Brandenburg, S., 2013b. Fixed fluorescent images of an 80 MeV proton pencil beam. *Radiation Physics and Chemistry* 85, 179-181. <http://dx.doi.org/10.1016/j.radphyschem.2012.11.011>

## **Chapter 3**

# **The radiation-chemical and optical properties of a radio-fluorogenic solution**

### **3.1. Introduction**

The suggestion that the radio-fluorogenic co-polymerization effect could be applied as a fluorescent method of monitoring the dose delivered by high-energy radiation was first made in a publication by Warman et al (2009a). The method is based on the radiation-induced initiation of polymerization of a bulk monomer containing a small, millimolar concentration of a compound which is non-fluorescent but which becomes fluorescent when it is incorporated into a growing chain of the bulk monomer. The potential of the method for dosimetry was demonstrated initially by measurements on small volume (0.2 mL) encapsulated samples of the fluorogenic compound maleimido-pyrene dissolved in methyl methacrylate, MMA, which were irradiated in a cobalt-60  $\gamma$ -ray source. Further measurements (Warman et al, 2009b) showed that an order of magnitude increase in sensitivity could be achieved by using tertiary-butyl acrylate, TBA, as the bulk

monomer.

TBA proved to have the additional advantage that it undergoes gelation and becomes quasi-rigid on irradiation with doses of several gray. This made it possible to produce radio-fluorogenic (RFG) gels which have been used to illustrate the possible application as a three-dimensional dosimetric medium (Warman, 2011a,b; 2013a,b). The latter measurements on complex radiation fields were not however quantitative in the sense of being able to directly relate the intensity of the fluorescence to the local dose delivered. To do this requires a fuller understanding of the actual dose dependence and the influences of dose rate and solute concentration on the co-polymerization process as well as on the optical properties of the medium. This is the purpose of the present chapter in which measurements are made of monomer-to-polymer conversion and changes in the optical properties of irradiated RFG solutions. A short preliminary publication has appeared (Yao et al, 2015). The preparation and radio-fluorogenic properties of *reformed RFG gels* will be presented in chapter 5.

## 3.2. Materials and Methods

### 3.2.1. Materials

The radio-fluorogenic (RFG) solutions used in this work consist of >99% tertiary-butyl acrylate, TBA (Sigma-Aldrich > 98%, #327182), and a small concentration of a non-fluorescent but fluorogenic compound N-(1-pyrenyl)maleimide, MPy (Sigma-Aldrich #P7908). The radio-fluorogenic function is based on MPy becoming fluorescent when incorporated into the polymer chains of TBA formed on exposure to high-energy radiation. The mechanism is shown in figure 3.1.

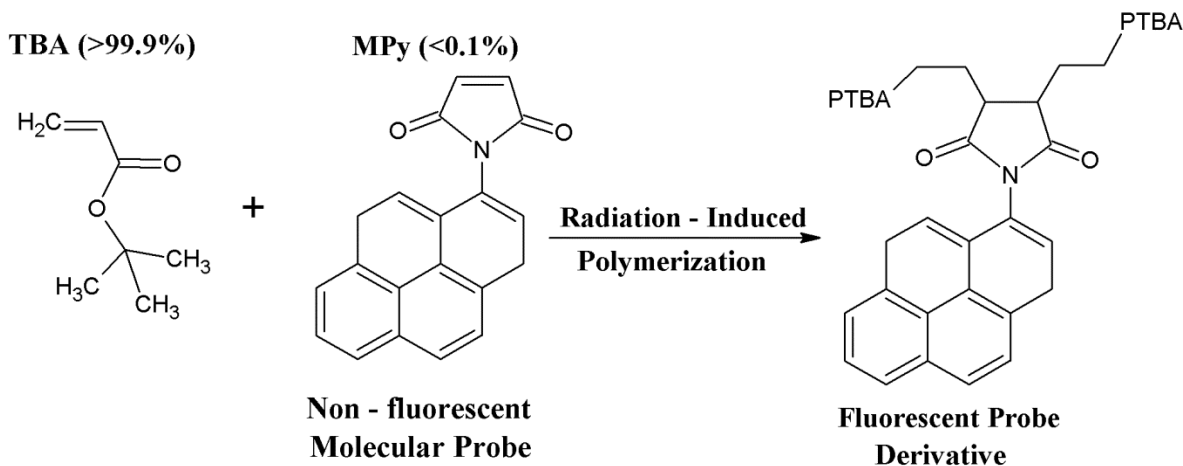


Figure 3.1. The molecular structures of TBA and MPy and the underlying mechanism of radio-fluorogenic co-polymerization (RFCP) in a dilute solution of MPy in TBA.

TBA liquid was initially purified by passage over a DHR-4 column to remove the 10-20 ppm monomethyl ether hydroquinone stabilizer and was stored in the dark at 5 °C. The molecular weight of TBA is 128.2 g mol<sup>-1</sup> and the density of the liquid is 0.89 kg L<sup>-1</sup> at 20 °C. The density of the fully-polymerized solid PTBA is 1.09 kg L<sup>-1</sup>. TBA has an extremely low optical density per cm in the visible and near UV region, i.e. less than 0.1 at wavelengths longer than 320 nm (see figure 2.8 in chapter 2).

MPy is a yellow solid with molecular weight 297 g/mol and the molecular structure shown in figure 3.1. It was used without further purification. It is weakly soluble in TBA but readily soluble in para-dioxane, which was used as solvent for accurate determination of the optical extinction coefficient. The optical density was measured with a 1 cm quartz glass cell in a Uvikon 940 spectrophotometer (Kontron Instruments). The extinction coefficient of MPy was obtained by measuring the optical density of MPy in dioxane solutions with accurately known MPy concentrations. In figure 3.2 is shown the wavelength dependence of the extinction coefficient over the range from 300 to 500 nm. A much-magnified representation of the spectrum above 360 nm is also shown in the figure. The extinction coefficient of MPy at selected wavelengths is given in table 3.1. The absorption of RFG solutions at 365 nm was routinely measured and applied for MPy concentration calculations using  $\epsilon_{365}$  of 791 L/mol.cm.

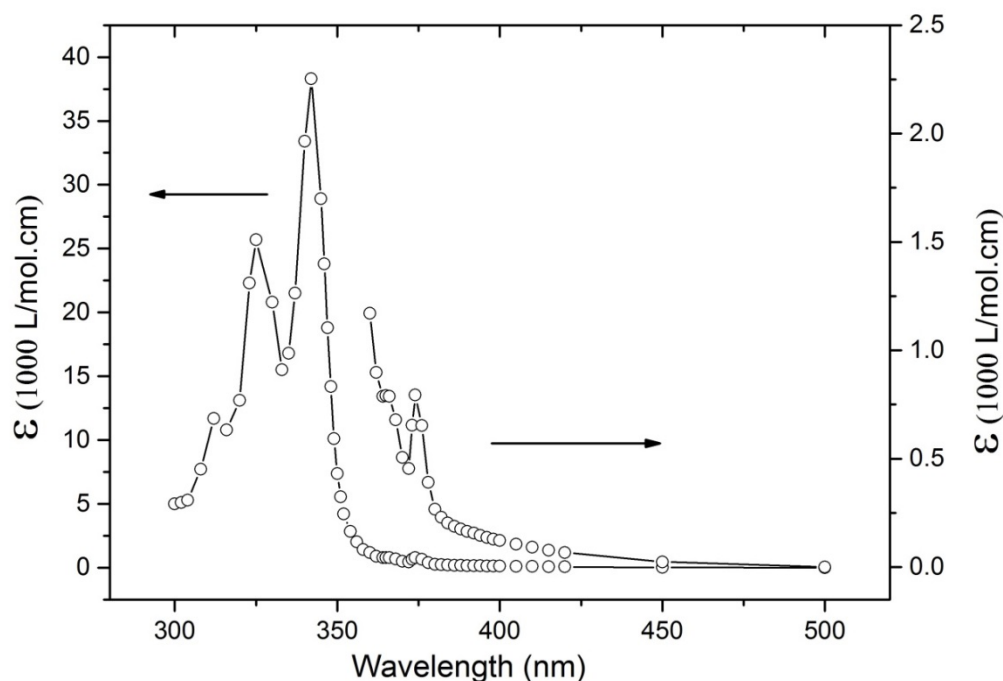


Figure 3.2. The wavelength dependence of the extinction coefficient of MPy. The very weak  $S_0 \rightarrow S_1$  absorption above 360 nm is shown expanded in the figure.

Table 3.1. Extinction coefficient of MPy at selected wavelengths in the 300 - 500 nm spectral region.

Wavelength (nm)	$\epsilon \times 10^{-3}$ (L/mol.cm)	Wavelength (nm)	$\epsilon \times 10^{-3}$ (L/mol.cm)	Wavelength (nm)	$\epsilon \times 10^{-3}$ (L/mol.cm)
300	5.0	349	10.1	380	0.267
302	5.1	350	7.37	382	0.230
304	5.3	351	5.56	384	0.204
308	7.7	352	4.21	386	0.188
312	11.7	354	2.83	388	0.176
316	10.8	356	2.03	390	0.165
320	13.1	358	1.42	392	0.157
323	22.3	360	1.17	394	0.146
325	25.7	362	0.898	396	0.137
330	20.8	364	0.788	398	0.129
333	15.5	365	0.791	400	0.123
335	16.8	366	0.788	405	0.105
337	21.5	368	0.679	410	0.091
340	33.4	370	0.506	415	0.078
342	38.3	372	0.454	420	0.067
345	28.9	373	0.655	450	0.024
346	23.8	374	0.794	500	0
347	18.8	376	0.653		
348	14.2	378	0.391		

The absorption spectrum of MPy is similar to that of unsubstituted pyrene: highly structured with sharp  $S_0$  to  $S_2$  and  $S_0$  to  $S_3$  bands below *ca* 360 nm and a very weak absorption above this wavelength due to the forbidden  $S_0$  to  $S_1$  transition (Tanaka *et al.* 1965). The underlying photophysics is shown in the Jablonski diagram in figure 3.3. The first electronic transition in pyrene is symmetry forbidden resulting in a greatly reduced oscillator strength and hence extremely low extinction coefficient. The similar shape in the absorption spectra of MPy and pyrene is due to that fact that substitution of the maleimide group at the 1 position does not change the symmetry forbidden character of the  $S_0$  to  $S_1$  transition. Note that the UV-A absorption of MPy is determined mainly by the aromatic pyrene moiety, which remains unchanged on co-polymerization. Quenching of the  $S_1$  to  $S_0$  fluorescence by intersystem crossing induced by the maleimide group is removed on its conversion into a succinimido group resulting in an increase in fluorescence.

### A Jablonski Diagram

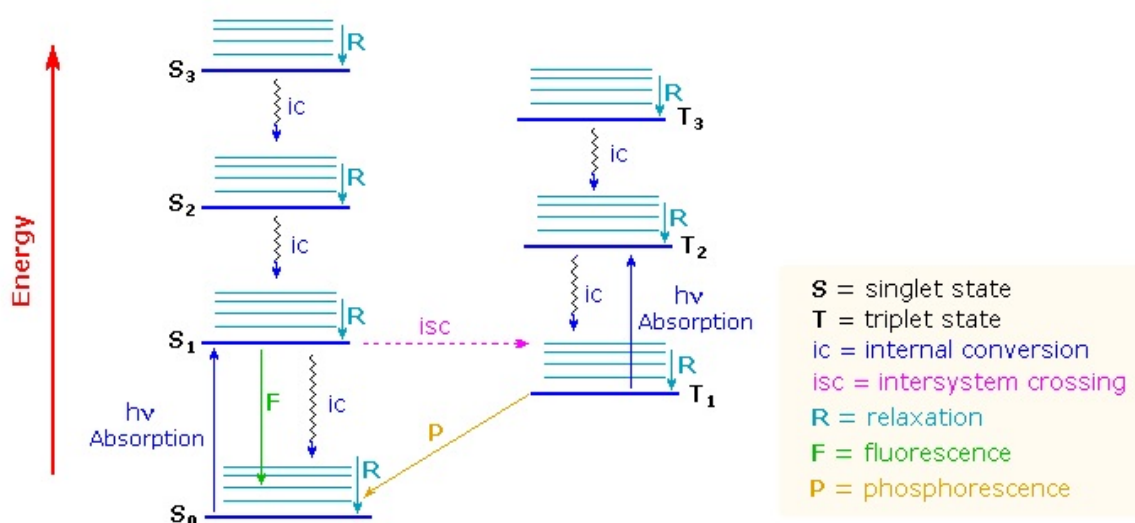


Figure 3.3. A Jablonski diagram of the photo-physical processes occurring for a molecule with singlet and triplet manifolds.

Deaerated solutions of MPy in TBA were prepared as follows: a saturated solution (MPy concentration  $\sim 1.7$  mM) was initially prepared by mechanically shaking excess MPy powder in TBA and decanting off the saturated liquid. Solutions of lower concentration were obtained by dilution of this saturated solution with pure TBA either prior to or after transfer to the glove box. All liquids were prebubbled with nitrogen for several minutes before transferring them to the glove box to remove most of the oxygen. In the glove box they were further bubbled with nitrogen for 30 minutes before pipetting known aliquots into sample cells. Because of solvent evaporation the solute concentrations after bubbling were higher than before and therefore had to be measured in a 1 cm square cell filled with the bubbled liquid in the glove box. A series of 7 one cm square sample cells were filled in this way with different known mixtures of a saturated solution of MPy and pure TBA. After removal from the glove box the optical densities at 365 nm were measured and as expected were found to be linearly dependent on [MPy] as shown in figure 3.4. The zero concentration intercept of  $\sim 0.05$  is due to the use of a quartz cell containing cyclohexane as the blank compared with the borosilicate glass and TBA of the experimental cells.

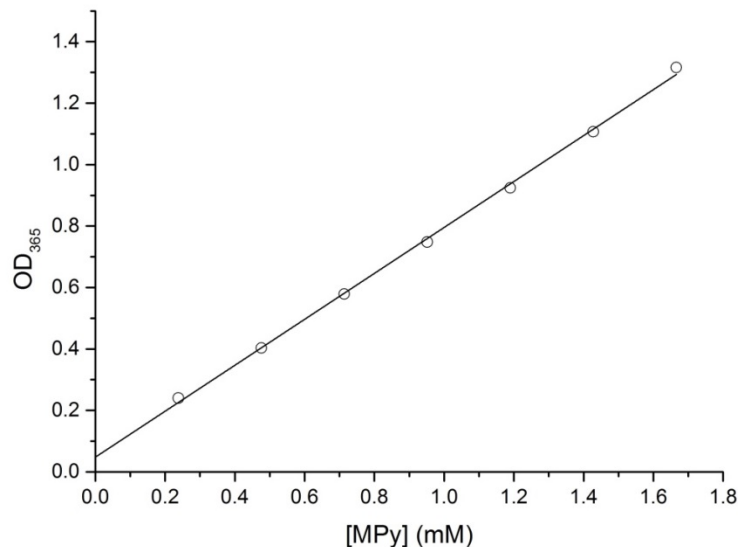


Figure 3.4. The optical density at 365 nm in a 1 cm cell as a function of MPy concentration in TBA.

The highly fluorescent compound, 9, 10-Diphenylanthracene (DPA, Molecular Probes #D7801), dissolved in cyclohexane (*ca* 1  $\mu\text{M}$ ) was used as fluorescence standard (Hamai *et al.* 1983). The fluorescence quantum yield and lifetime are  $\sim 0.9$  and 7.5 ns at 20 °C (Eaton *et al.* 1988). DPA has a maximum emission intensity at  $\sim 400$  nm (Du *et al.* 1998) which is close to that of co-polymerized MPy (Warman *et al.* 2009b).

### 3.2.2. Irradiation procedure

Two cobalt-60 gamma-ray sources were used to irradiate the RFG samples: a GC200 (Atomic Energy of Canada), dose rate *ca* 3.5  $\text{cGy s}^{-1}$  (2  $\text{Gy min}^{-1}$ ) and a GC220 (Nordion), dose rate *ca* 50  $\text{cGy s}^{-1}$  (30  $\text{Gy min}^{-1}$ ). The dose rate, which was determined by Fricke dosimetry, was calculated on the day of irradiation based on the 5.27 years half-life of the natural decay of cobalt-60.

The cylindrical cavities of the GC200 and GC220 irradiators have diameters of 8.5 cm and 15 cm, and heights of 11 cm and 20 cm respectively. The RFG samples were placed in the center of the cavity and mechanically lowered into the center of the radiation field. The sample was irradiated for a time,  $t$ , set on the auto-timer, after which it was raised. During transportation of the sample it is exposed to extra radiation, with a corresponding "transit time",  $\Delta t$ , which should be accounted for in calculating the total dose delivered to the sample. The values of both transit times were obtained by irradiating EBT3 and MD-V3 radiochromic films, which give  $\Delta t = 9.3$  s and 4.9 s for GC200 and GC220 respectively (see chapter 6). These transit times were taken into account but are in fact almost negligible compared with the radiation exposures of several minutes actually used.

### 3.2.3. Monomer conversion and gel formation

The monomer-to-polymer conversion ( $C_M$ ) was measured using 20 mL glass “liquid scintillation vials” (LSVs), containing 10 mL of deaerated MPy/TBA solutions (see figure 2.3 chapter 2). After irradiation the samples were opened and placed in a vacuum oven (Heraeus) at room temperature to evaporate off the residual monomer. The samples were weighed prior to,  $W(0)$ , and after  $h$  hours of evacuation,  $W(h)$ , and the fractional monomer-to-polymer conversion,  $W(h)/W(0)$  was determined by weighing the samples every two days until the weight became constant.  $W(\infty)/W(0)$  was equated with the fractional monomer-to-polymer conversion,  $C_M$ .

A qualitative measure of the viscosity of the MPy/TBA solutions after irradiation was obtained by laying the LSVs on their side and photographing the gradual flow of the meniscus at increasing elapsed times, as was done for pure TBA (see figure 2.7 in chapter 2). The results are shown in section 3.3.3.

### 3.2.4. Fluorimeter measurements

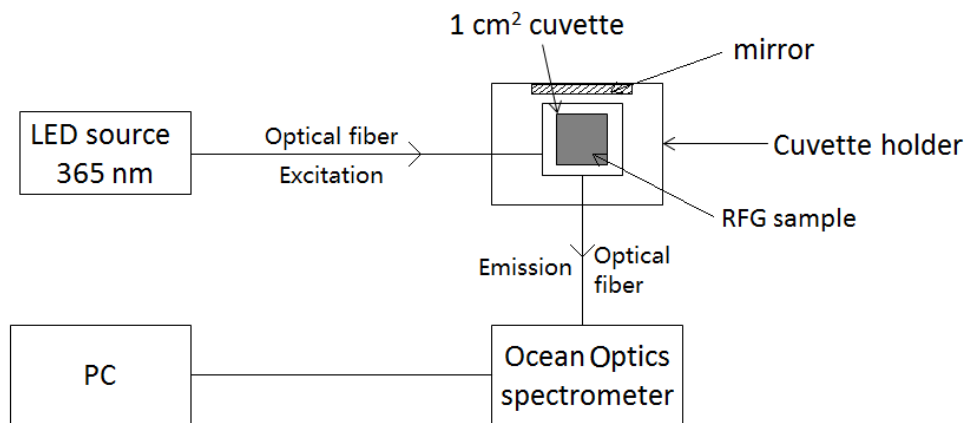


Figure 3.5. The setup of the Ocean Optics spectrofluorimeter.

The fluorescence of irradiated RFG solutions was monitored using 1 cm square borosilicate glass cells in a fibre-optic spectro-fluorimeter (Ocean Optics) as shown in figure 3.5. The excitation light source from a light-emitting diode had a maximum output in the near UV at 365 nm. The long wavelength tail of the LED spectrum was cut off above 400 nm using an in-line filter holder containing a 3 mm thick UG11 filter. Fluorescence light emitted from the excited RFG sample was detected with an SD2000 spectrophotometer. Before measuring RFG samples, the fluorimeter was tested with a dilute (*ca* 1  $\mu\text{M}$ ) solution of DPA in cyclohexane. The fluorescence emission spectra were viewed and recorded using 'SpectraSuite' software from Ocean Optics. The value of the height of the fluorescence emission was used to monitor the dose dependence of the fluorescence response of the radiation-induced co-polymerization.



### 3.2.5. CCD camera fluorescence imaging

The fluorescence imaging setup shown in figure 3.6 consists of two LED UV lamps in opposition at a separation of 30 cm and a CCD camera in front of the RFG sample which is placed in a cell holder between the two lamps. The cells and the aluminum holders used to position them are shown in figure 3.7.

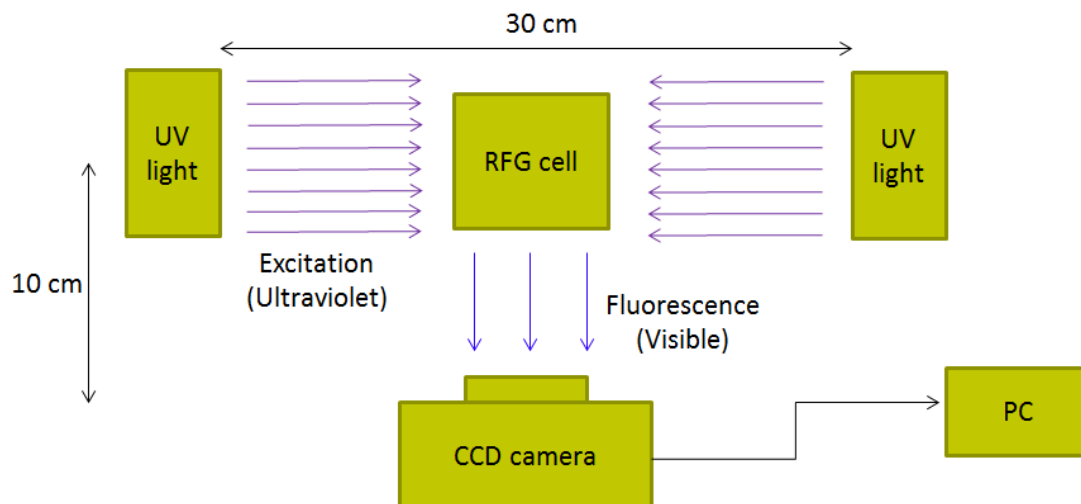


Figure 3.6. The setup used for fluorescence imaging of RFG samples.

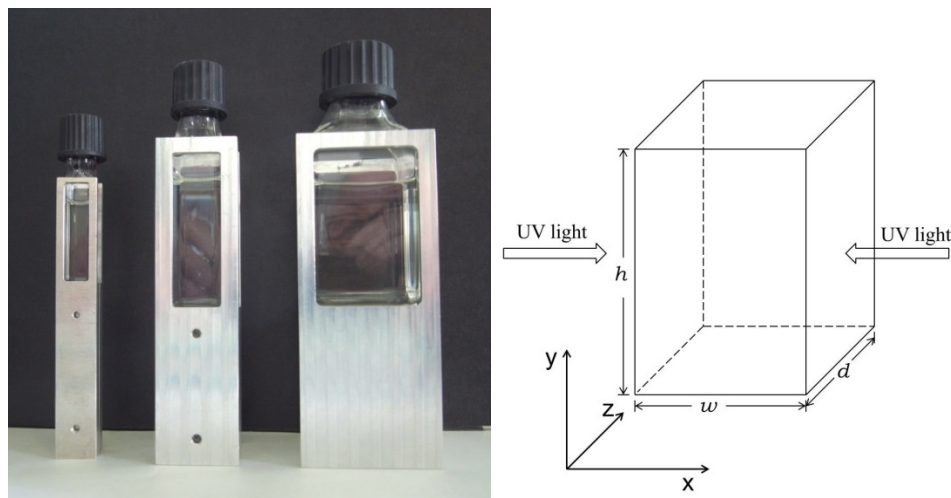


Figure 3.7. The glass cells and aluminum cell holders used for fluorescence imaging of RFG samples. From left to right a 1 cm, 2 cm and 4 cm internal dimension square cell and holder. The coordinate axes used within the samples are shown on the right.

The ultraviolet light sources were produced by 4PICO ([www.4PICO.NL](http://www.4PICO.NL)). They consisted of a 16.3 cm long linear array of 22 light emitting diodes with a rectangular Fresnel lens for beam collimation. The lens was covered by a 1 mm thick UG1 ("Woods glass" from Schott) filter to

attenuate any visible wavelength components of the LED emission. The spectrum of the resulting beam,  $I(\lambda)_{EX}$ , had a maximum at 381 nm and an FWHM of  $\sim 10$  nm. This is shown in figure 3.8 together with the absorption spectrum of MPy in the same wavelength region. The effective, mean value of the MPy extinction coefficient,  $\bar{\epsilon}_{EX}$ , for this excitation spectrum is  $\Sigma[I(\lambda)\epsilon(\lambda)]/\Sigma[I(\lambda)] = 294.8$  L/mol.cm. This is a factor of 1.1 higher than the value of 267 L/mol.cm at the maximum excitation wavelength of 381 nm and a factor of 2.68 lower than the value of 791 L/mol.cm at 365 nm; the wavelength routinely used to determine the MPy concentration. The decadic attenuation coefficient of the extinction light  $\alpha_{EX} = \bar{\epsilon}_{EX}c$  cm<sup>-1</sup> is related to the optical density by  $\alpha_{EX} = OD_{EX}/l$  with  $l$  the path length in cm over which the OD was measured. When images were not being taken the UV light was blocked to prevent possible photolysis of the sample.

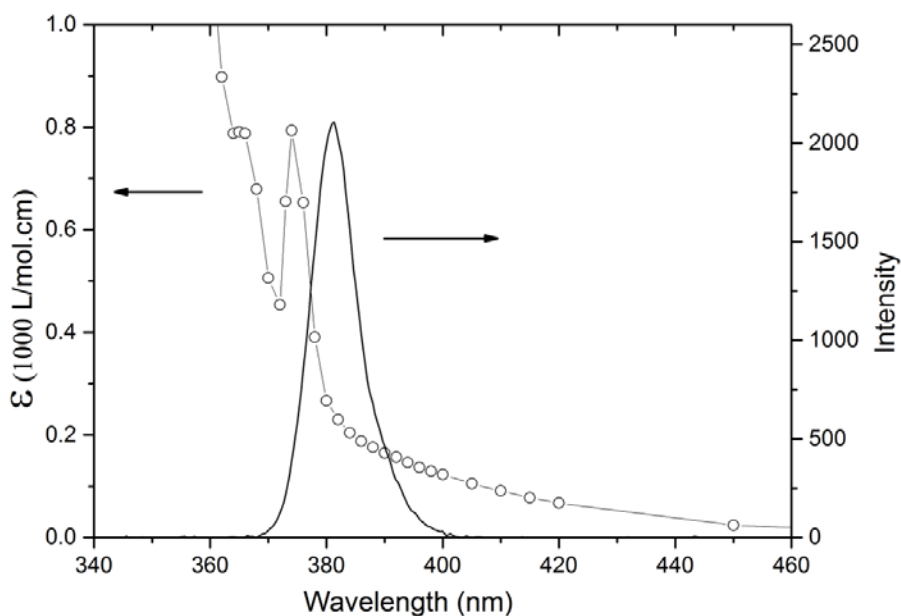


Figure 3.8. The UV emission spectrum of the LED lamps together with the extinction coefficient of MPy in the same wavelength region.

The CCD camera used was a Ricoh GX200. The focal length of the camera was fixed at 10 cm (the distance from the camera lens to the center of the RFG cell), as were the aperture at  $f/4.4$  and the ISO at 100. The shutter time,  $s$ , was changed manually up to a maximum of 4 seconds with several values taken for each sample. The images of the fluorescence of the RFG samples were stored on an SD disk as raw DNG and JPEG files.

The files were analysed using the open source software program ImageJ (US National Institutes of Health). The 8-bit JPEG files could be imported directly. The 16-bit DNG files were imported via the "DCraw" plug-in (<http://ij-plugins.sourceforge.net/plugins/dcraw/>). The images were color-separated into red, green and blue channels with separate pixel levels (gray scale values),  $P_R$ ,  $P_G$  and  $P_B$ . The blue component was used for analysis since this is closest to the peak

of the fluorescent emission of MPy. Pixel saturation in the blue channel, which might not be revealed in an average RGB analysis, is in this way avoided. After color separation a rectangular region of interest (ROI) in the blue channel image was selected and the average pixel level measured. The small background level in a non-irradiated area was subtracted from that in the irradiated sample.

A very dilute, homogeneous cyclohexane solution of the fluorescence standard 9, 10-diphenyl anthracene (DPA) was used to test the homogeneity of illumination of the sample volume and the dependence of the pixel level on the light intensity falling on the camera. A  $P_B$ (DNG) image of such a solution taken using the setup in figure 3.6 is shown in figure 3.9.

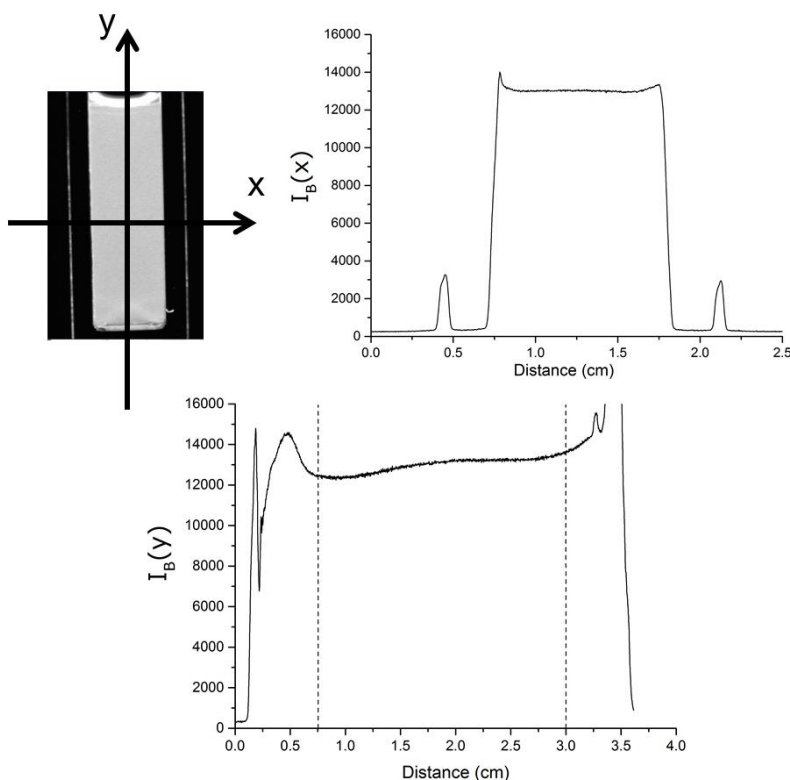


Figure 3.9. Top left: a  $P_B$ (DNG) image of a 3.5 cm long DPA solution in a 1 cm square cell used to test the uniformity of the LED UV light. Top right: A lateral, x-axis scan across the width of the cell. Bottom: A longitudinal, y-axis scan from the bottom of the cell to above the liquid meniscus.

In figures 3.10A&B are shown the dependences on the shutter time of the camera of the  $P_B$  levels derived from the DNG and JPEG files. The  $P_B$ (DNG) values are seen to be perfectly linear with shutter time, whereas the  $P_B$ (JPEG) values display a complex sigmoid dependence. The latter results from the compression algorithms applied by the camera software to produce images that, when reproduced, approach those of human color perception. For the present purpose however it is the raw, linear information that is relevant. The value of  $P_B$ (DNG)/s, in

blue pixel levels per second, is proportional to the intensity of the fluorescence of a sample and will be denoted  $I_B$  in subsequent sections.

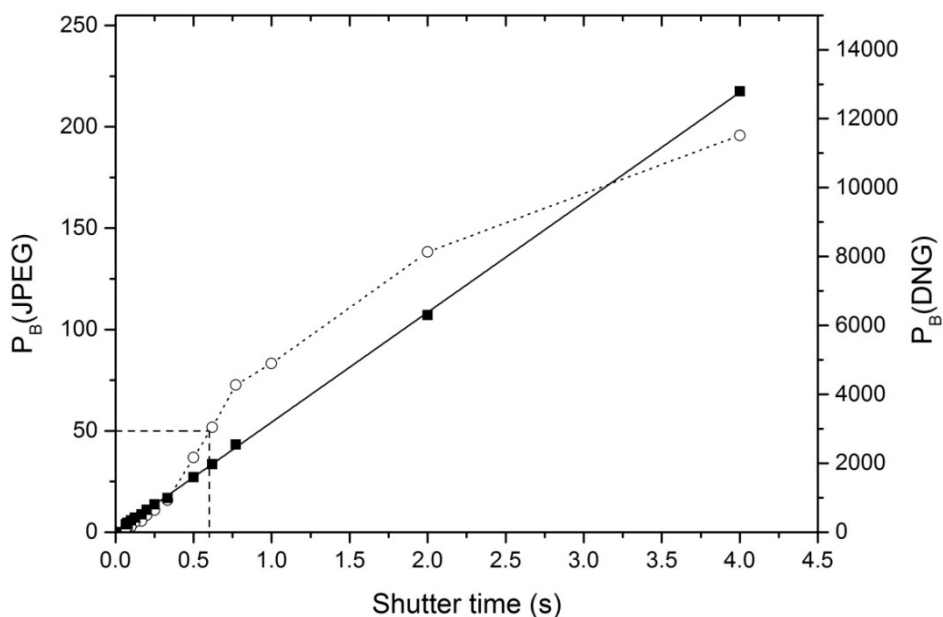


Figure 3.10A. The blue pixel levels,  $P_B$ , as a function of the camera shutter time,  $s$ , for a dilute solution of 9,10-diphenyl anthracene in cyclohexane. Open circles from JPEG files. Filled squares from DNG files. The full line is a linear best fit to the DNG data. The dotted lines simply join the points of the JPEG data.

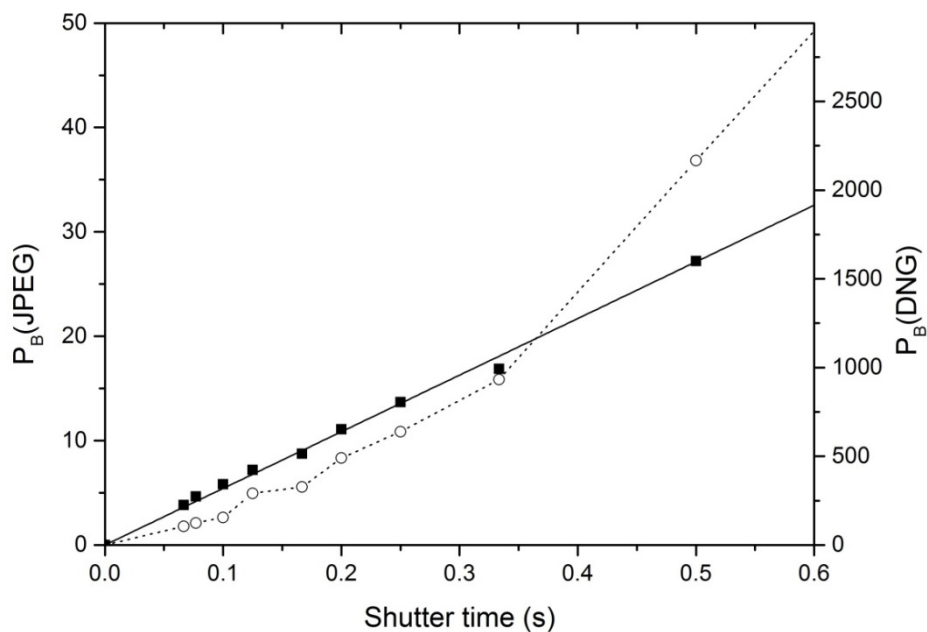


Figure 3.10B. An enlarged version of the data in the area defined by the dashed lines in figure 3.10A.

Initially, the effect on the fluorescence intensity of the DPA solution of blocking off one of the lamps was investigated. This resulted in a decrease in  $I_B$  at  $x = 0$  by a factor of 2.0 showing the incident intensity of the two lamps,  $I_0$ , to be equal.

The uniformity of UV excitation within the sample volume can be determined from scans such as those illustrated in figure 3.9. For scans made along the  $x$ -axis,  $I_B(x)$  should be proportional to the local intensity of the UV light penetrating the sample, i.e.  $I_B(x) = \Psi I_{ex}(x)$  with  $\Psi$  a constant dependent on the spectroscopic properties of the solution and the settings of the camera.

For two opposing UV sources each of initial intensity  $I_0$  at the surface of the medium,

$$I_{ex}(x) = I_0[10^{-\alpha x} + 10^{-\alpha(w-x)}] \quad (3.1)$$

In (3.1)  $\alpha \text{ cm}^{-1}$  is the decadic attenuation coefficient of the solution towards the incident UV light. Accordingly, the fluorescence should display a minimum in the center of the cell as given by equation (3.2) and shown in figure 3.11.

$$I_{ex}(x)/I_{ex}(0) = [10^{-\alpha x} + 10^{-\alpha(w-x)}]/[1 + 10^{-\alpha x}] \quad (3.2)$$

The ratio of the intensity in the center of the cell to that at the sides is given by,

$$I_{ex}(w/2)/I_{ex}(0) = 2 \times 10^{-\alpha w/2}/[1 + 10^{-\alpha x}] \quad (3.3)$$

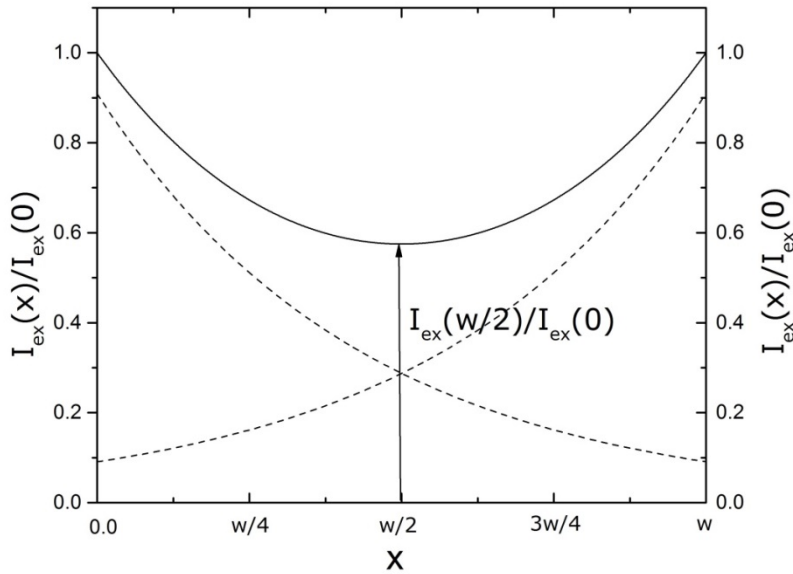


Figure 3.11. Attenuation of the UV excitation light in an absorbing medium. Exponential decay curves of the light from one direction (dashed lines) and the total intensity in the medium (full line).

For the DPA solution used in figure 3.9 the optical density at the wavelength maximum of the UV lamps was less than  $0.05 \text{ cm}^{-1}$ . Therefore, the maximum decrease in fluorescence intensity in the  $x$ -axis scan would be expected to be less than 1%, as is found. A more

pronounced example of this effect of UV attenuation is shown in the results section (figure 3.20) where higher optical densities of MPy solutions are used.

The longitudinal, y-axis scan displays artifacts at the dielectric interfaces in the region of the cell glass bottom and the liquid meniscus. The dashed vertical lines in figure 3.9 define a region between 0.5 cm above the bottom of the cell and 0.5 cm below the meniscus. Within this region the intensity varies smoothly by a few percent and reflects the y-axis variation in the intensity of the lamps. For measurements in which spatial resolution is of importance such variations will have to be taken into account possibly using a lookup table based on DPA solution data.

### 3.3. Results and Discussion

In the following sections the radio-fluorogenic (RFG) properties of a solution of maleimido-pyrene in tertiary-butyl acrylate are demonstrated and the effects of accumulated dose, dose rate and concentration of MPy on the intensity of the fluorescence are investigated.

#### 3.3.1. Spectrophotometer and spectrofluorimeter measurements

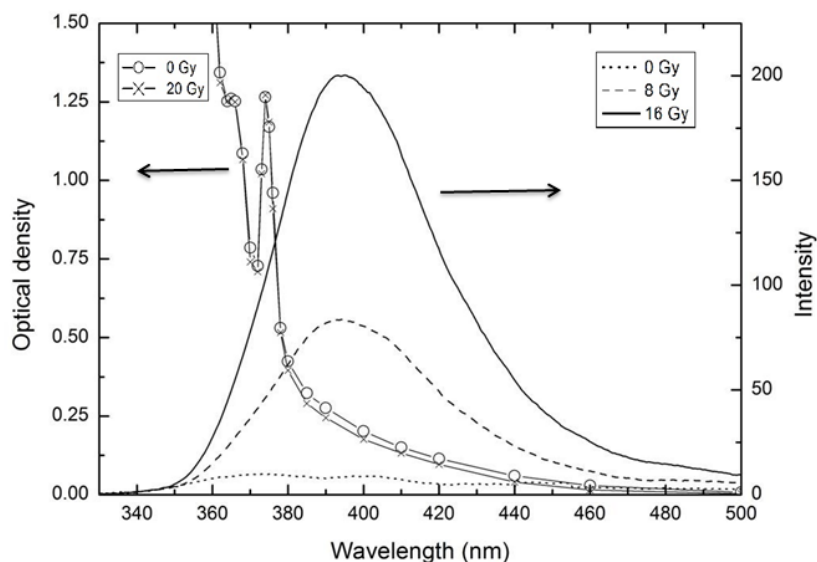


Figure 3.12. The fluorescent emission from a 0.6 mM solution of MPy in TBA on excitation at 365 nm before irradiation (dotted line) and after doses of 8 Gy (dashed line) and 16 Gy (full line). Also shown is the optical density of a 1.8 mM solution before (circles) and after (crosses) irradiation with a dose of 20 Gy.

The radio-fluorogenic (RFG) effect is illustrated by the spectrofluorimeter measurements shown in figure 3.12. Prior to  $\gamma$ -ray irradiation the MPy solution is non-fluorescent but becomes

increasingly fluorescent on irradiation with doses of 8 and 16 Gy. The RFG effect is caused by the change, from a maleimido moiety to a succinimido moiety on co-polymerization of MPy, i.e. conversion of the carbon-carbon double bond of MPy into a single bond, as illustrated in figure 3.1. In MPy the maleimido moiety quenches the fluorescence of  $S_1$  by providing a pathway to a non-emissive triplet state of lower energy. On saturation of the maleimido double bond a triplet pathway is no longer energetically favorable and the direct (partly emissive) transition from  $S_1$  to the ground state  $S_0$  becomes the favored pathway.

The dramatic increase in fluorescence contrasts with the lack of sensitivity to high-energy radiation of either the absorption spectrum or the clarity of the solution, which is also illustrated in figure 3.12. This constancy of optical density and clarity on irradiation is particularly important when considering the corrections for attenuation of the excitation light and self-absorption or scattering of the fluorescence that have to be made to emission intensities in bulk 3-dimensional systems.

The absorption remains unchanged because the near UV absorption spectrum of MPy is controlled mainly by the aromatic pyrene moiety, which remains unchanged on co-polymerization. The unchanged clarity of the irradiated solution can be explained by the physico-chemical similarity between the polymer formed, PTBA, and the bulk TBA solvent. A difference of refractive index due to a density change in the irradiated region does however occur and can actually be observed in RFG gels immediately after irradiation. In other polymer-gel dosimetry media the organic polymer is formed in a mainly aqueous medium which results in precipitation and turbidity (Baselga et al, 1989; Maryanski et al, 1994; Maryanski et al, 1996). The latter effect is difficult to quantify but has been proposed as a measure of the local dose deposition (Maryanski et al, 1996; Gore et al, 1996).

The fluorescence displays a maximum intensity,  $I_{FL}$ , at a wavelength,  $\lambda_{max}$ , of 395 nm. The dependence of  $I_{FL}$  on dose for different MPy concentrations is shown in figure 3.13. At all concentrations the dose dependence is seen to be superlinear, similar to that found for the monomer-to-polymer conversion,  $C_M$ , in pure TBA (Yao et al, 2014; figure 2.9 in chapter 2).

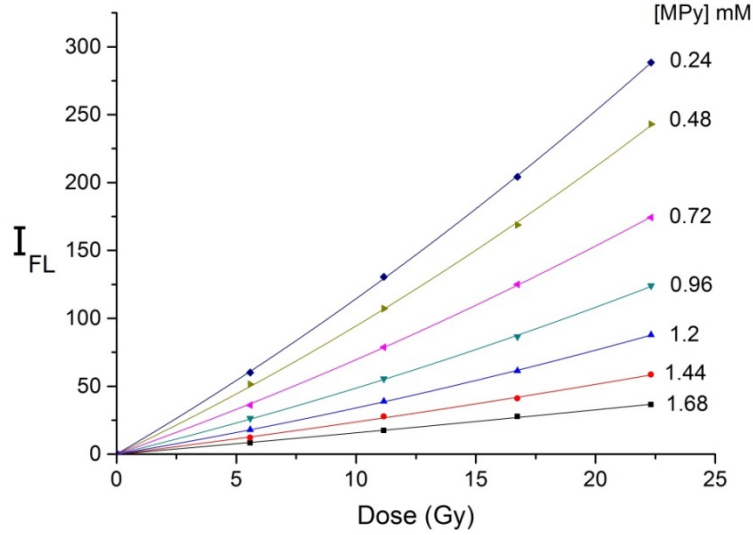


Figure 3.13. The dose dependence of the radiation-induced fluorescence intensity,  $I_{FL}$ , of MPy/TBA solutions of concentration shown on the right, as measured using the spectrofluorimeter set-up in figure 3.5. Dose rate 1.76 Gy/min.

The lines drawn in figure 3.13 are best fits to the data using the empirical expression 3.4 and the values of  $A_{FL}$  and  $K_{FL}$  are listed in table 3.2.

$$I_{FL} = (1 + A_{FL}D)K_{FL}D \quad (3.4)$$

Table 3.2 The best-fit parameters  $A_{FL}$  and  $K_{FL}$  in relationship 3.4 corresponding to the full lines drawn through the data points in figure 3.13. Dose rate 1.76 Gy/min.

[MPy] (mM)	$K_{FL}$ (Gy <sup>-1</sup> )	$A_{FL}$ (Gy <sup>-1</sup> )
0.24	10.25	0.0116
0.48	8.30	0.0138
0.72	6.25	0.0113
0.96	4.32	0.0126
1.20	2.98	0.0142
1.44	2.17	0.0092
1.68	1.51	0.0039

The low dose limiting value of  $dI_{FL}/dD$ ,  $K_{FL}$ , is plotted against MPy concentration in figure 3.14 for data obtained using the GC200 source ( $D' = 1.76$  Gy/min). An initially surprising aspect of the results was the large *decrease* in  $K_{FL}$ , by a factor of 6.9, over the 7-fold *increase* in MPy concentration. A large part of this decrease can be attributed to the measurement set-up used



(see figure 3.5). Thus the fluorescence is monitored at a depth  $d$  in the solution by a  $30\mu\text{m}$  optical fiber and at this depth the intensity of the 365 nm excitation light will have decreased by a factor  $10^{-\alpha d}$  with  $\alpha_{365} = 791 \times [\text{MPy}] \text{ cm}^{-1}$ . The output of the fluorimeter is therefore not a linear function of the fluorescent intensity of the solution if it were to be homogeneously illuminated, i.e.  $\alpha_{365} = 0$ . However, even making the maximum correction possible for attenuation of the excitation light, i.e. assuming  $d = 1 \text{ cm}$ , the fluorescence intensity normalized to the excitation intensity would increase by only a factor of 2.7 over the 7-fold increase in MPy concentration. This is still much lower than the linear dependence initially expected! This will be discussed further, together with the dose rate dependence and superlinear behaviour, after first presenting the results of the fluorescence imaging and monomer conversion measurements.

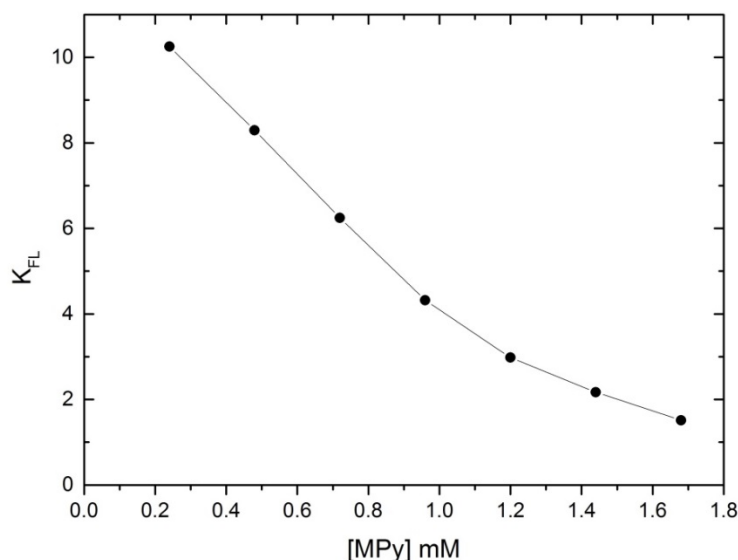


Figure 3.14. The MPy concentration dependence of  $K_{FL}$ ; the slope of the linear dose dependence of the fluorescence intensity at low conversions, as measured using the spectrofluorimeter for solutions irradiated with the GC200 source ( $D' = 1.76 \text{ Gy/min}$ ).

### 3.3.2. CCD camera fluorescence imaging

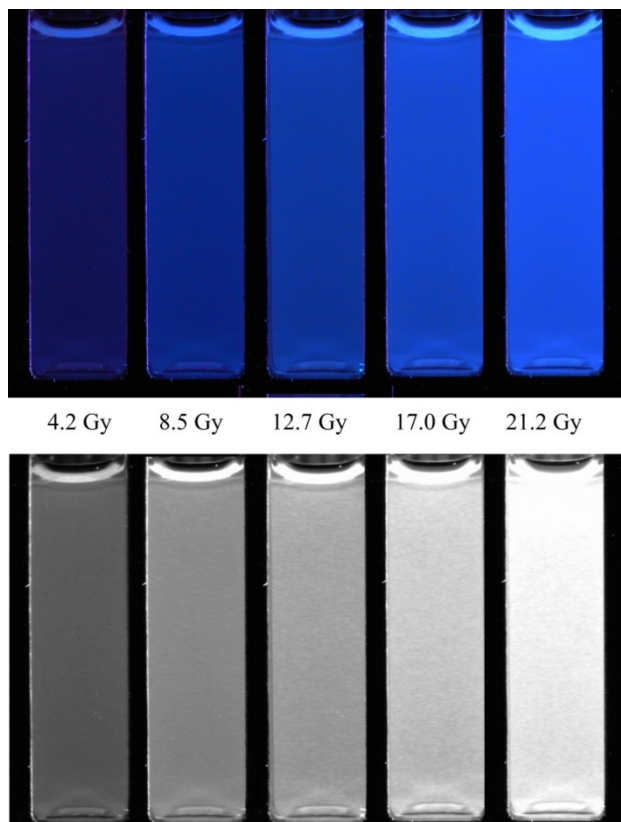


Figure 3.15. Above: full color JPEG images of a 0.53 mM MPy/TBA solution in a 1 cm cell irradiated with the doses shown. Below: the corresponding blue pixel gray-scale images.

The RFG effect is illustrated in figure 3.15 by the full-color JPEG images of a 1 cm square cell containing a 0.53 mM MPy solution in TBA subjected to accumulated doses from 4.2 to 21.2 Gy, and measured using the imaging set-up shown in figure 3.6. Also shown in figure 3.15 are the corresponding gray-scale, blue-pixel-level ( $P_B$ ) images that have been color-separated from the RGB data using ImageJ.

As was shown in section 3.2.5, the 16 bit, "raw" DNG files provide a linear measure of the radiant intensity of a medium. In figure 3.16 the linear dependence of  $P_B(\text{DNG})$  on shutter time for a 1.46 mM solution of MPy subjected to increasing radiation doses is shown. The "intensity" of an image,  $I_{IM}$ , is defined here as the slope of a DNG blue-pixel-level versus shutter-time plot, i.e.  $I_{IM} = P_B(\text{DNG})/s$ . The dependence of  $I_{IM}$  on dose, derived from the slopes of the plots in figure 3.16, is shown in figure 3.17. A superlinear dependence is found, similar to that for  $I_{FL}$  in the previous section and for monomer to polymer conversion,  $C_M$ , in pure TBA (Yao et al, 2014; figure 2.9 in chapter 2). The full line in the figure is a best fit based on an analogous relationship to 3.4, i.e.

$$I_{IM} = (1 + A_{IM}D)K_{IM}D \quad (3.5)$$

The dashed straight line in figure 3.17 is the low-dose limiting linear dependence of  $I_{IM}$  on dose with slope  $K_{IM}$ .

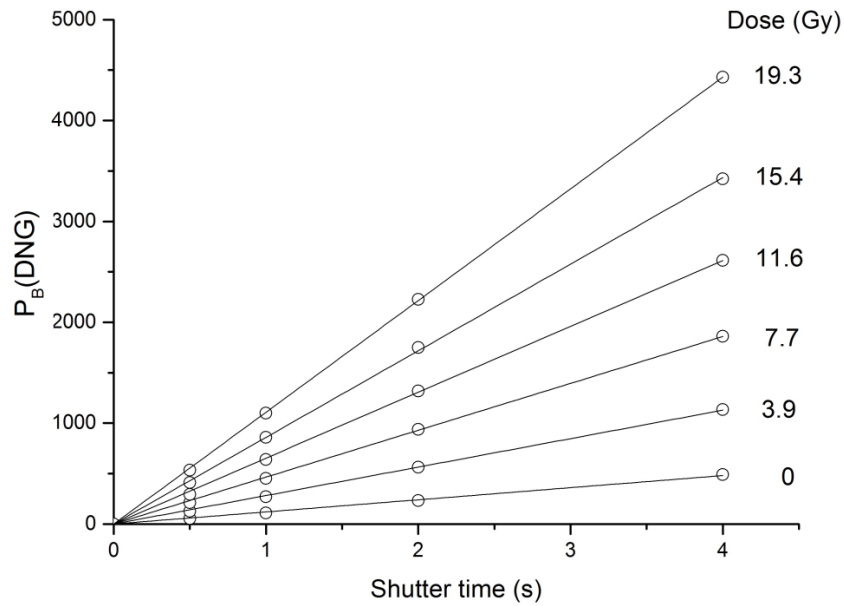


Figure 3.16. The DNG blue pixel level,  $P_B(DNG)$ , as a function of shutter time for a 1.46 mM solution of MPy irradiated in a 1 cm square cell for the doses shown on the right. The full lines are linear best fits to the data.

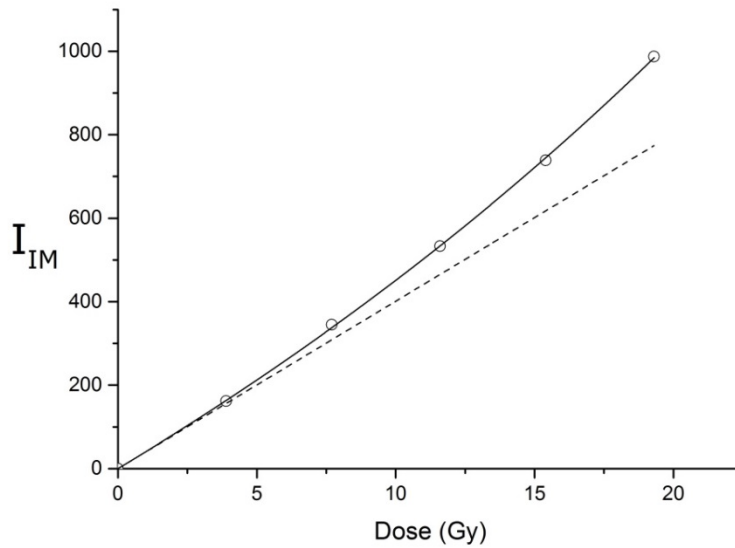


Figure 3.17. The slopes of the straight-line fits in figure 3.16 as a function of dose. The full line is a best fit based on relationship 3.5 and the dashed line corresponds to the low dose, limiting linear dependence of this relationship.

Measurements similar to the above have been made for a range of MPy concentrations and the results using the GC200 source are presented in figure 3.18. The full lines through the data are best fits using 3.5 and the corresponding  $K_{IM}$  and  $A_{IM}$  values are listed in table 3.3. In addition to the data for the GC200 source ( $D' = 1.76$  Gy/min) values of the fit parameters determined using the high dose rate GC220 source ( $D' = 23.7$  Gy/min) are listed.

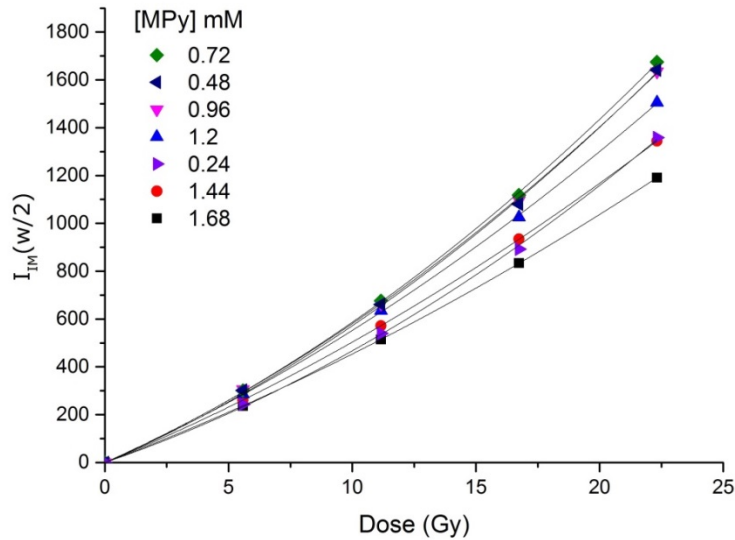


Figure 3.18. The image intensity at the center of a 1 cm cell,  $I_{IM}(w/2)$ , as a function of accumulated dose for MPy solutions of concentration given on the left, listed in order of the magnitude of the corresponding  $I_{IM}$  data points. The full lines are best-fits to the data points using relationship 3.5.

Table 3.3. The best-fit parameters  $K_{IM}$  and  $A_{IM}$  to the  $I_{IM}$  versus dose data in figure 3.18 including corrections for the attenuation of the UV excitation light,  $f_{ex}$  and self-absorption of the fluorescence,  $f_{sa}$ .

D'	[MPy]	$K_{IM}$	$A_{IM}$	$\alpha_{ex}$	$f_{ex}$	$f_{ex}K_{IM}$	$\alpha_{sa}$	$f_{sa}$	$f_{ex}f_{sa}K_{IM}$
(cGy/s)	(mM)	(Gy <sup>-1</sup> )	(Gy <sup>-1</sup> )	(cm <sup>-1</sup> )		(Gy <sup>-1</sup> )	(cm <sup>-1</sup> )		(Gy <sup>-1</sup> )
2.93	0.24	35.5	0.0316	0.071	1.085	38.5	0.043	1.051	40.5
	0.48	44.3	0.0291	0.142	1.177	52.1	0.087	1.104	57.5
	0.72	45.6	0.0287	0.212	1.277	58.2	0.130	1.158	67.4
	0.96	46.0	0.0262	0.283	1.386	63.8	0.174	1.214	77.4
	1.20	45.5	0.0215	0.354	1.503	68.3	0.217	1.271	86.9
	1.44	42.3	0.0190	0.425	1.631	69.0	0.261	1.330	91.8
	1.68	38.9	0.0167	0.496	1.769	68.8	0.304	1.391	95.7
39.5	0.219	13.5	0.0065	0.0646	1.077	14.6	0.040	1.047	15.2
	0.320	17.0	0.0082	0.0944	1.115	19.0	0.058	1.068	20.3
	0.555	24.6	0.0072	0.1637	1.207	29.7	0.100	1.120	33.4
	1.043	27.0	0.0091	0.3077	1.425	38.5	0.189	1.233	47.5
	1.807	26.9	0.0063	0.5331	1.847	49.8	0.327	1.424	70.9

Rather surprisingly, the fluorescence intensities for the GC200 source measurements were found to be only slightly dependent on MPy concentration with that for the highest concentration within 10% of that for the lowest concentration. This is shown by the plot of the  $K_{IM}$  values against [MPy] in figure. 3.19.

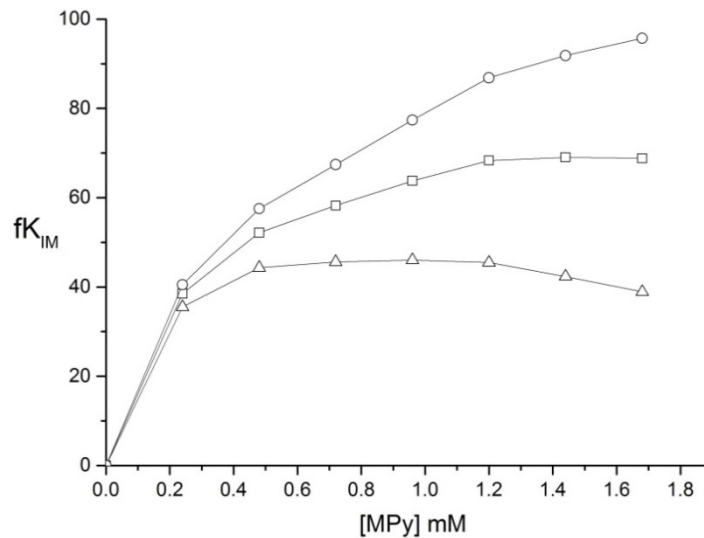


Figure 3.19. The linear dose dependence of the fluorescence at low conversions without corrections,  $f = 1$  (triangles), or with corrections for attenuation of the UV excitation light,  $f = f_{ex}$  (squares) and for self-absorption,  $f = f_{ex}f_{sa}$  (circles); see table 3.3.

As for the fluorimeter measurements in the previous section, consideration has to be given to the increasing attenuation of the excitation light with increasing optical density of the solutions. In the present imaging set-up the intensity of the UV excitation light,  $I_{\text{ex}}$ , varies along the x-axis according to equation 3.2. This dependence is illustrated in figure 3.11 for an optical density of 1.0. For the very dilute DPA solution ( $\text{OD} < 0.05$ ) used as a monitor in section 3.2.5, this results in less than a 1% change in  $I_{\text{ex}}$ , and hence in the fluorescence intensity, across the width of the cell. With the larger optical densities of the MPy solutions used however this effect becomes important and results in a variable fluorescence, even for media with a uniform distribution of fluorescent molecules.

This effect is illustrated in figure 3.20 by the image of an irradiated solution of MPy in a 2 cm square cell. The dip in the intensity of the fluorescence in the center of the cell is clearly visible in the blue pixel image and is quantified in the  $I_{\text{IM}}(x)$  scan in the lower part of the figure. A best fit to the variation of the intensity with depth using equation 3.3 is shown in figure 3.21, which is an expanded version of 3.20. From this fit the effective attenuation coefficient of the solution was found to be  $0.403 \text{ cm}^{-1}$ . This compares well with the value of  $0.4304 \text{ cm}^{-1}$  calculated using the average extinction coefficient of  $295 \text{ L/mol}\cdot\text{cm}$  for the UV excitation light and the MPy concentration of  $1.46 \text{ mM}$ .

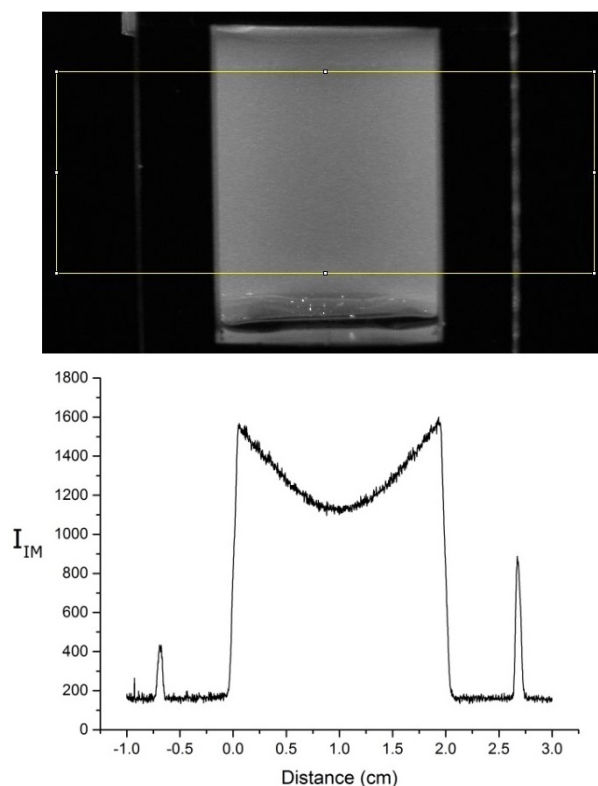


Figure 3.20. Upper: A fluorescent image of an irradiated (11.5 Gy), saturated MPy solution in a 2 cm square cell. The rectangular area shown was scanned to provide the  $I_{\text{IM}}(x)$  profile shown in the lower part of the figure. The sharp peaks are artifacts occurring at the outer, aluminum/air interfaces of the cell holder.

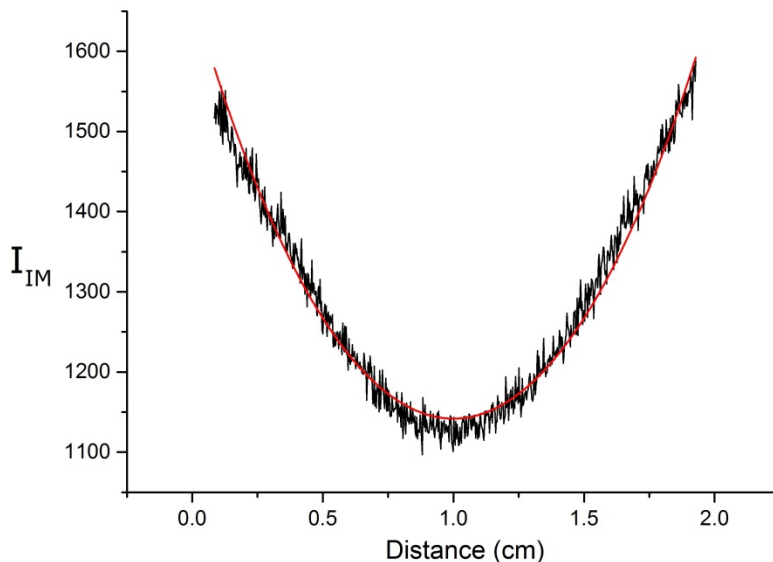


Figure 3.21. An expanded version of the  $I_{IM}(x)$  data in figure 3.20. The smooth full line in red is a best-fit to the data using equation 3.2 with  $\alpha = 0.403 \text{ cm}^{-1}$ .

The  $K_{IM}$  values in table 3.3 have been corrected for the attenuation of the UV excitation light by the factor  $f_{ex} = 10^{\alpha_{ex}w/2}$  with  $w/2 = 0.5 \text{ cm}$  and  $\alpha_{ex} = 295x[\text{MPy}] \text{ cm}^{-1}$ . This correction results in  $f_{ex}K_{IM}$  values, i.e. the low-dose limiting fluorescence intensities per unit dose normalized to the intensity of the UV excitation light. A further correction is necessary because of self-absorption of the fluorescence. For a homogeneously fluorescent solution self-absorption results in a loss of intensity in the  $z$  direction (see figure 3.7) by a factor  $[1 - 10^{-\alpha_{sa}d}]/\alpha_{sa}\ln 10$  hence the need for a correction factor  $f_{sa}$  which is the reciprocal of this. Here  $\alpha_{sa} = \langle \epsilon \rangle_{sa}[\text{MPy}]$  is the average attenuation coefficient of the fluorescence. The average extinction coefficient for self-absorption is given by  $\langle \epsilon \rangle_{sa} = \Sigma[I_{FL}(\lambda)\epsilon(\lambda)]/\Sigma I_{FL}(\lambda) = 181 \text{ L/mol/cm}$  from the spectra in figure 3.12. This correction has been applied to obtain the values of  $f_{ex}f_{sa}K_{IM}$  listed in the final column of table 3.3 and plotted against  $[\text{MPy}]$  in figure 3.19.

The fully corrected value of  $K_{IM}$ , denoted for simplicity  $fK_{IM}$ , is proportional to the yield per unit dose at low conversion of the copolymerized radiofluorogenic compound S (in the present case MPy).  $fK_{IM}$  is found to increase by a factor of only 2.3 while the MPy concentration increases by a factor of 7.0. The dependence of the incorporation of MPy on MPy concentration is apparently much less than linear; a conclusion also reached in the previous section. This will be discussed in more detail after first considering the effects of MPy on the basic polymerization process.

### 3.3.3. Monomer conversion and gel formation

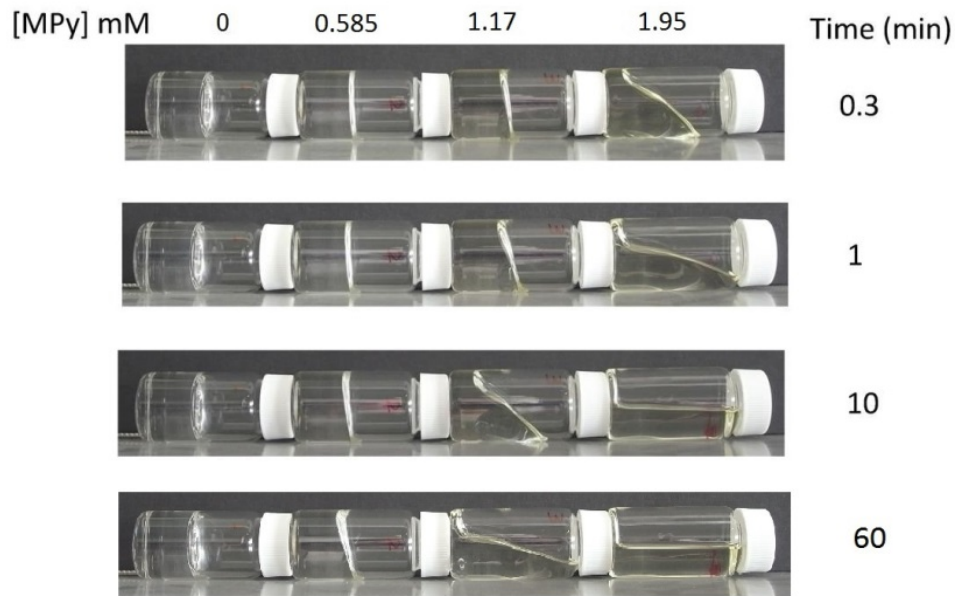


Figure 3.22. Four irradiated (17 Gy) liquid scintillation vials (LSVs) containing 10 mL of deaerated solutions of MPy in TBA with the concentrations shown above, laid on their sides after irradiation and photographed at the elapsed times shown on the right.

The first indication that the basic polymerization process in TBA was negatively influenced by the presence of MPy was the observation that for the same dose the viscosity of irradiated MPy solutions was lower than for pure TBA. This is illustrated in figure 3.22 where the meniscus creep of irradiated MPy solutions is compared with that for pure TBA. The effect is particularly apparent for the saturated, ~2mM MPy solution which displays considerable meniscus flow even within a minute of being laid on its side whereas pure TBA, for the same dose, shows little meniscus displacement even after an hour. Clearly the polymerization and cross-linking reactions responsible for gellation are hindered by the presence of MPy. This was confirmed by measurement of the monomer conversion in the solutions shown in figure 3.22. The decrease in  $C_M$  with increasing concentration of MPy is shown in figure 3.23.



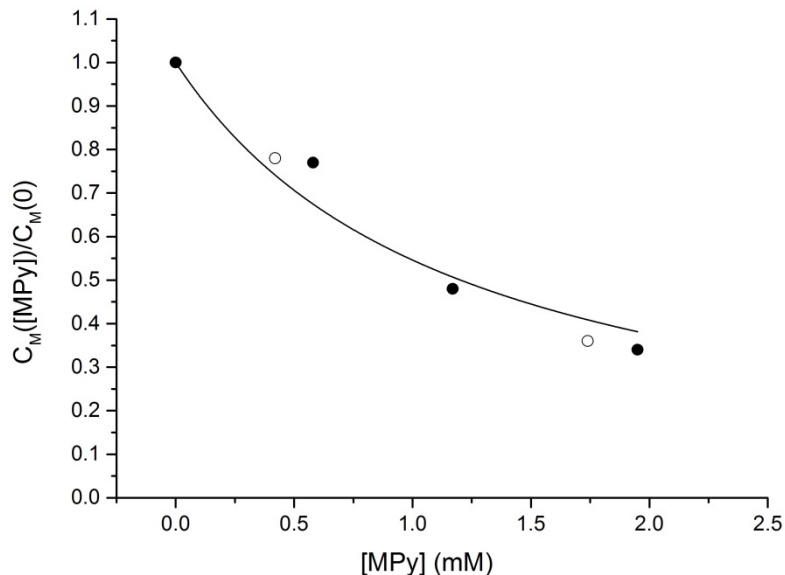
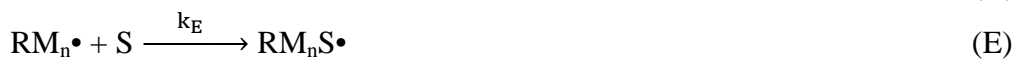


Figure 3.23. The normalized monomer conversion,  $C_M([MPy])/C_M(0)$ , after a dose of 17 Gy as a function of MPy concentration. The filled circles are the monomer conversion values determined for the LSV samples shown in figure 3.22.

An explanation of this negative effect of MPy requires consideration of the basic processes occurring during free-radical polymerization of the pure monomer M, reactions A to D, and the additional processes that occur in the presence of a low concentration of a co-polymerizable monomer S, reactions E to H.



In the absence of S, monomer-to-polymer conversion is determined by the rate of radical formation via A,  $F(R\bullet)$  mol.L<sup>-1</sup>s<sup>-1</sup>, and the rate coefficients in Lmol<sup>-1</sup>s<sup>-1</sup> of chain propagation,  $k_p$ , (reaction C) and radical-radical termination,  $k_t$ , (reaction D). For low conversions and constant rate coefficients the fractional monomer-to-polymer conversion,  $C_M$ , after a dose D Gy at a dose rate D' Gy/s is given by expression 3.6 (Yao et al, 2014, Luthjens et al, 2001).

$$C_M = k_p[F(R\bullet)/2k_t]^{1/2}D/D' \quad (3.6)$$

Substituting in 3.6 for  $F(R\bullet) = \Gamma D'$  with  $\Gamma$  the yield of free radicals in moles per liter per gray ( $\Gamma = \rho g(R\bullet)$  with  $\rho$  the density of the medium in kg/L and  $g(R\bullet)$  the radiolytic yield of free radicals in mol.joule<sup>-1</sup>).

$$C_M = k_p[\Gamma/2k_tD']^{1/2}D \quad (3.7)$$

$C_M$  should therefore increase linearly with dose at low conversions with a slope,  $K_{CM} = k_p[\Gamma/2k_tD']^{1/2}$ , that is inversely proportional to the square root of the dose rate.

The predicted linear dependence of  $C_M$  on dose at low conversions and the inverse square root dependence on dose rate was demonstrated for pure TBA in chapter 2, figure 2.9. At higher conversions a negative deviation of  $C_M$  from the low-dose linear dependence might be expected due to the decreasing concentration of monomer (Luthjens et al, 2001). However,  $C_M$  is in fact found to deviate from the low-dose linear behaviour in a *positive* sense. This superlinear behaviour is attributed to a gradual decrease in  $k_t$ , the diffusion controlled rate coefficient for radical-radical combination and disproportionation reactions, as the viscosity of the medium increases. This has been taken into account empirically by including an additional term, which tends to unity for low doses/monomer conversions.

$$C_M = (1 + A_{CM}D)K_{CM}D \quad (3.8)$$

Equation 3.8 provides good fits to the data for pure TBA from which values of  $K_{CM} = 1.43 \times 10^{-3}/\sqrt{D'} \text{ Gy}^{-1}$  and  $A_{CM} = 0.0010/\sqrt{D'} \text{ Gy}^{-1}$  for  $D'$  in Gy/s have been determined (Yao et al, 2014). This superlinear dependence on dose is also found for  $C_M$  in MPy/TBA solutions and for the fluorescence of such solutions, as pointed out in the previous sections.

Considering the influence of an additive S on the overall degree of polymerization and the incorporation of S via reactions E through H: the presence of very low, mM concentrations of S should have a negligible effect on the rate of formation of free-radicals via A or on the chain initiation process B. Also, the rate coefficient of reaction G between a terminal bulk-monomer radical and a monomer (TBA) molecule should be similar to that for the pure monomer, i.e.  $k_G \approx k_p$ . The rate coefficient for the diffusion controlled radical-radical termination reaction H would also be expected to be insensitive to the nature of the radicals involved, hence  $k_H \approx k_t$ . If the rate coefficient for reaction E is different to that for reaction C, i.e.  $k_E \neq k_p$ , this would affect the amount of S co-polymerised but would have little effect on the overall monomer conversion. If however the rate coefficient of the chain propagation step F,  $k_F$ , is lower than for C, i.e.  $k_F < k_p$ , chain growth will be retarded and  $C_M$  will decrease.

It has been found that the polymerization of maleimide derivatives is much slower than for acrylates (Haas 1973, Matsumoto et al 1990, Frahn et al 2001, Agarwal et al 2003) so that the condition  $k_F \ll k_p$  would be expected to apply in the present case for which S is maleimido-

pyrene. This results in reaction E becoming effectively a chain terminating reaction. Under these conditions the monomer conversion of TBA will decrease in the presence of MPy according to,

$$C_M([S]) = k_p(\Gamma/2k_tD')^{0.5}D/(1 + k_E[S]/(2k_t\Gamma D')^{0.5}) \quad (3.9)$$

or, expressed relative to the conversion in the absence of S,

$$C_M([S])/C_M(0) = 1/(1 + B[S]/\sqrt{D'}); \text{ with } B = k_E/(2k_t\Gamma)^{0.5} \quad (3.10)$$

The full line drawn in figure 3.23 for the MPy dependence of  $C_M([MPy])/C_M(0)$  is based on equation 3.10 with  $B/\sqrt{D'} = 0.83 \times 10^3$  L/mol.

### 3.3.4. The MPy concentration and dose rate dependence of the fluorescence

The fluorescence intensity in an RFG medium will be proportional to the concentration of fluorogenic solute molecules that have been incorporated into polymer chains, i.e.  $[M_nS]$ . For the conditions set out in the previous section this is, for low conversions,

$$[M_nS\bullet] = k_E[S](\Gamma/2k_tD')^{0.5}D/(1 + k_E[S]/(2k_t\Gamma D')^{0.5}) \quad (3.11)$$

The fluorescence intensity per unit dose, after correction for attenuation of the excitation light and self-absorption,  $fK_{IM}$ , is then proportional to  $d[M_nS\bullet]/dD$  with a proportionality factor C,

$$fK_{IM} = Ck_E[S](\Gamma/2k_tD')^{0.5}/(1 + k_E[S]/(2k_t\Gamma D')^{0.5}) \quad (3.12)$$

Comparison of 3.12 with 3.9 leads to the following relationship between the fluorescence and the monomer conversion, for measurements carried out at the same dose rate.

$$fK_{IM}/[S] = (Ck_E/k_p)C_M \quad (3.13)$$

According to 3.13  $fK_{IM}/[S]$  should be proportional to  $C_M$ . Both parameters are plotted as a function of MPy concentration in figure 3.24 and the agreement in the concentration dependences is considered good, particularly in view of the completely different parameters and their methods of measurement.

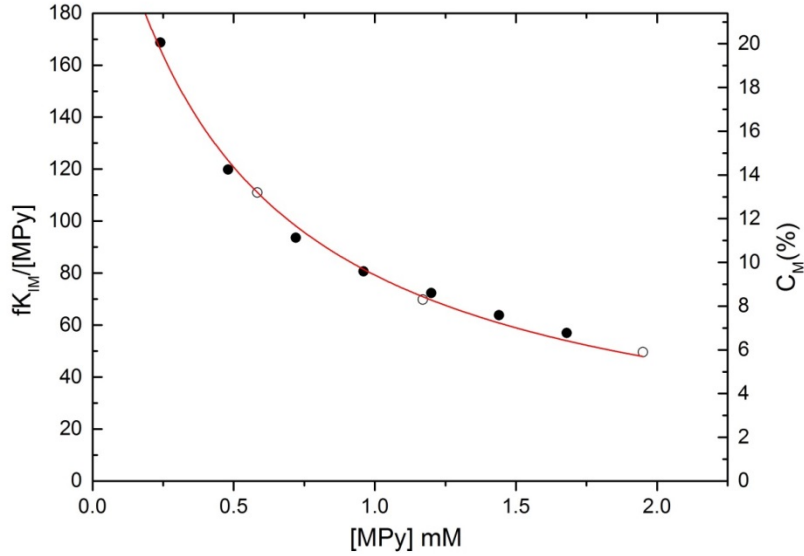


Figure 3.24. A comparison of the MPy concentration dependence of the monomer conversion,  $C_M$ , determined gravimetrically, with the parameter  $fK_{IM}/[MPy]$  derived from fluorescence imaging (see relationship 3.13). Dose rates 1.69 Gy/min and 1.76 Gy/min respectively.

Multiplying the nominator and denominator in equation 3.12 by  $(2k_t\Gamma D')^{1/2}/k_E[S]$  results in,

$$fK_{IM} = C\Gamma / (1 + (2k_t\Gamma D')^{0.5}/k_E[S]) \quad (3.14)$$

from which, on substituting  $E = k_E/(2k_t\Gamma)^{0.5}$ ,

$$fK_{IM} = C\Gamma / (1 + \sqrt{D'}/E[S]) \quad (3.15)$$

From 3.15 it is apparent that plots of  $1/fK_{IM}$  against  $\sqrt{D'}/[S]$ , for different dose rates and solute concentrations, should fall on a common straight line with intercept  $1/C\Gamma$  and slope  $1/CE$ . Such plots of the data in table 3.3 are shown in figure 3.25 for dose rates of 1.76 Gy/min and 23.7 Gy/min. From the straight line fit to the combined data the intercept gives  $C\Gamma = 111 \text{ pixel-level}\cdot\text{s}^{-1}\cdot\text{Gy}^{-1}$  and from the ratio of the intercept to slope  $E = 0.453 \text{ s}^{0.5}\cdot\text{mM}^{-1}\cdot\text{Gy}^{-0.5}$ .

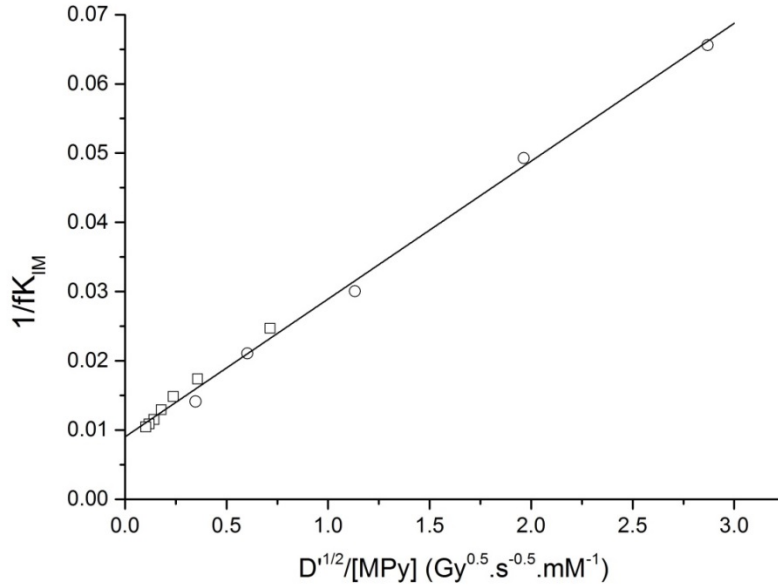


Figure 3.25. A plot of the reciprocal of the corrected fluorescence per unit dose  $fK_{IM}$  against the reciprocal of the MPy concentration divided by the square root of the dose rate for dose rates of 1.76 Gy/min (squares) and 23.7 Gy/min (circles); see equation 3.16.

### 3.3.5. An RFG solution as dosimeter

When used as a dosimeter the fluorescence of an RFG solution is measured after exposure for a time  $t$  to a radiation field of unknown dose rate  $D'$  Gy/s. The fluorescence is then compared with calibration measurements using a source or sources of known dose rate and a fixed imaging system, as in the previous section. From measurements made at different exposure times the low-conversion limiting, linear dependence of intensity on time,  $\Phi_{IM} = (dI_{IM}/dt)_{t \rightarrow 0}$ , can be determined from best fits based on a superlinear relationship analogous to 3.5, i.e.

$$I_{IM} = (1 + \Theta_{IM}t)\Phi_{IM}t \quad (3.16)$$

The absorption corrected value of  $\Phi_{IM}$ ,  $f\Phi_{IM} = fK_{IM}D'$ , is given by,

$$f\Phi_{IM} = C\Gamma D' / (1 + \sqrt{D'/E[S]}) \quad (3.17)$$

Equation 3.17 is a quadratic in  $\sqrt{D'}$  which has the general solution,

$$\sqrt{D'} = f\Phi_{IM} \{1 + (1 + 4C\Gamma E^2[S]^2/f\Phi_{IM})^{1/2}\} / 2E[S]C\Gamma \quad (3.18)$$

For low solute concentrations and high dose rates 3.18 tends to 3.19.

$$D' = (f\Phi_{IM}/C\Gamma E[S])^2 \quad (3.19)$$

For low dose rates and high solute concentrations 3.19 tends to,

$$D' = f\Phi_{IM}/C\Gamma \quad (3.20)$$

In the first limit the dose rate is proportional to the square of the fluorescence intensity and in the second limit to the first power.

In practical cases the dependence will lie between the two limits and be given by the more complex relationship 3.18. However, if the values of  $C\Gamma$  and  $E$  are known the dose rate can be calculated from the fluorescence intensity of a solution of concentration  $[S]$ . The values of  $C\Gamma$  and  $E$ , applicable for the fluorescence imaging set-up used, can be determined from a plot as shown in figure 3.25 by carrying out measurements at several solute concentrations using a source of known dose rate. It is worth noting that only a single known-dose-rate source is necessary for calibration of  $C\Gamma$  and  $E$ .

We have tested the applicability of 3.18 using the values of  $C\Gamma = 110.86$  and  $E = 0.453$  determined in the previous section from a plot of  $1/fK_{IM}$  against  $\sqrt{D'}/[MPy]$ . These parameters have been used to back calculate the dose rates of the two gamma ray sources from the measurements given in table 3.4. The agreement between the dose rates calculated and the actual (in this case known) dose rates is within 10% apart from for the highest MPy concentration at the highest dose rate. Clearly blind tests should be made in which sources are used with dose rates unknown to those making the dosimetry estimates.

Table 3.4. Dose rate back-calculation based on  $C\Gamma = 111$  and  $E = 0.453$  in equation 3.18.

Source/D' (Gy/s)	[MPy] (mM)	$fK_{IM}$	$f\Phi_{IM}$	$D'_{calc}$ (Gy/s)	$\Delta D'$ (%)
GC200 0.0293	0.24	40.5	1.187	0.0269	-8.4
	0.48	57.5	1.685	0.0267	-9.1
	0.72	67.4	1.975	0.0268	-8.7
	0.96	77.4	2.268	0.0285	-3.1
	1.20	86.9	2.546	0.0304	3.5
	1.44	91.8	2.690	0.0309	5.1
	1.68	95.7	2.804	0.0312	6.4
GC220 0.395	0.219	15.2	6.004	0.4007	1.5
	0.320	20.3	8.019	0.3793	-3.9
	0.555	33.4	13.193	0.4261	7.9
	1.043	47.5	18.763	0.3934	-0.4
	1.807	70.9	28.006	0.4619	17.0

### 3.4. Conclusions

Millimolar solutions of maleimido-pyrene (MPy) in tertiary-butyl acrylate (TBA) display a permanent blue fluorescence in UV light after exposure to ionizing radiation. For a given MPy concentration the intensity of the fluorescence, as measured by a fibre-optic spectrofluorimeter or a CCD camera, increases with radiation exposure with a dependence on dose that is superlinear and can be fit with the empirical relationship  $I = (1 + AD)KD$ . The range of dose over which the fluorescence can be readily measured is from a few gray to tens of gray. The intensity does not increase linearly with increasing concentration of MPy. This has two causes: one is the increase in optical density of the solution as the concentration of MPy increases which results in attenuation of the UV excitation light and self-absorption of the fluorescence; the second is caused by MPy acting as a chain terminator and reducing the overall polymer yield. The former effect can be corrected for since the absorption spectrum (extinction coefficient) of MPy has been accurately measured, as have the spectra of the UV excitation sources and the fluorescence. Importantly, the optical density and clarity of the solutions remain unchanged on irradiation so that preirradiation optical densities can be used for corrections.

The negative effect of MPy on the polymerization process is observed as a decrease in viscosity of irradiated solutions compared with pure TBA and a corresponding decrease in the monomer-to-polymer conversion. This effect is attributed to a much lower rate of chain propagation involving reaction between a maleimido radical chain-end and a TBA molecule than an acrylate radical chain-end and TBA. Steady-state solutions to a reaction scheme in which MPy acts as a chain terminator are found to be in good agreement with the dependences on solute concentration and dose rate found.

If used as a dosimetric medium the general relationship between the (unknown) dose rate,  $D'$ , and the low-polymer-conversion fluorescence intensity per unit time,  $\Theta$ , of an MPy/TBA solution is,

$$\sqrt{D'} = \Theta(1 + (1 + a^2/b\Theta)^{0.5})/2a \quad (3.21)$$

The parameters  $a$  and  $b$  can be determined from the optical properties of the solution and the fluorescence measured at different solute concentrations using a source of known dose rate and the same fluorescence measurement system. In the limit of low solute concentrations and high dose rates 3.21 tends to

$$\sqrt{D'} = \Theta/a \quad (3.22)$$

and for high concentrations and low dose rates,

$$D' = \Theta/4b \quad (3.23)$$

## References

Agarwal, P., Yu, Q., Harant, A., Berglund, K.A., 2003. Synthesis and characterization of polymaleimide. *Industrial & Engineering Chemistry Research* 42, 2881-2884.

Baselga, J., Llorente, M.A., Hernandez-Fuentes, I. and Pierola, I.F., 1989. Polyacrylamide gels. Process of network formation. *European polymer journal* 25, 477-480.

Du, H., Fuh, R. C.A., Li, J., Corkan, L.A., Lindsey, J.S., 1998. PhotochemCAD: A Computer-Aided Design and Research Tool in Photochemistry, *Photochemistry and Photobiology* 68(2), 141-142.

<http://ij-plugins.sourceforge.net/plugins/dcraw/>

Eaton, D.F. 1988. Reference materials for fluorescence measurement. *Pure and Applied Chemistry* 60 1107-1114.

Gore, J.C., Ranade, M., Maryanski, M.J. and Schulz, R.J., 1996. Radiation dose distributions in three dimensions from tomographic optical density scanning of polymer gels: I. Development of an optical scanner. *Physics in Medicine and Biology* 41, 2695-2704.

Haas, H., 1973. Maleimide polymers. II Radical polymerization kinetics. *Journal of Polymer Science* 11, 315-318.

Hamai, S., Hirayama, F., 1983. Actinometric determination of absolute fluorescence quantum yields. *Journal of Physical Chemistry* 87, 83-89.

Matsumoto, A., Kubota, T., Otsu, T., 1990. Radical polymerization of N-(alkyl-substituted phenyl)maleimides: Synthesis of thermally stable polymers soluble in non-polar solvents. *Macromolecules* 23, 4508-4513.

Maryanski, M.J., Schulz, R.J., Ibbott, G.S., Gatenby, J.C., Xie, J., Horton, D. and Gore, J.C., 1994. Magnetic resonance imaging of radiation dose distributions using a polymer-gel dosimeter. *Physics in Medicine and Biology* 39, 1437-1455.

Maryanski, M.J., Zastavker, Y.Z. and Gore, J.C., 1996. Radiation dose distributions in three dimensions from tomographic optical density scanning of polymer gels: II. Optical properties of the BANG polymer gel. *Physics in Medicine and Biology* 41, 2705-2717.

Tanaka, J., 1965. The electronic spectra of pyrene, chrysene, azulene, coronene and tetracene crystals. *Bulletin of the Chemical Society of Japan* 38(1), 86-102.



Warman, J.M., Luthjens, L.H., de Haas, M.P., 2009a. In-situ radiation dosimetry based on Radio-Fluorogenic Co-Polymerization. *Journal of Physics: Conference Series* 164, 012048 (1-5)

Warman, J.M., Luthjens, L.H., de Haas, M.P., 2009b. High-energy radiation monitoring based on radio-fluorogenic co-polymerization. I: Small volume in-situ probe. *Physics in Medicine and Biology* 54, 3185-3200.

Warman, J.M., de Haas, M.P., Luthjens, L.H., 2011a. High-energy radiation monitoring based on radio-fluorogenic co-polymerization II: fixed fluorescent images of collimated X-ray beams using an RFCP gel. *Physics in Medicine and Biology* 56, 1487-1508.

Warman, J.M., de Haas, M.P., Luthjens, L.H., Murrer, H.P., 2011b. A radio-fluorogenic organic gel for real-time, 3D radiation dosimetry. *Advanced Materials* 23, 4953-4955. <http://dx.doi.org/10.1002/adma.201102831>

Warman, J.M., de Haas, M.P., Luthjens, L.H., Hom, M.L., 2013a. High-energy radiation monitoring based on radio-fluorogenic co-polymerization III: fluorescent images of the cross-section and depth-dose profile of a 3 MV electron beam. *Radiation Physics and Chemistry* 84, 129-135. <http://dx.doi.org/10.1016/j.radphyschem.2012.06.031>

Warman, J.M., de Haas, M.P., Luthjens, L.H., Kavatsyuk, O., van Goethem, M-J., Kiewiet, H.H., Brandenburg, S., 2013b. Fixed fluorescent images of an 80 MeV proton pencil beam. *Radiation Physics and Chemistry* 85, 179-181.

Yao, T., Denkova, A.G., Warman, J.M., 2014. Polymer-gel formation and reformation on irradiation of tertiary-butyl acrylate. *Radiation Physics and Chemistry* 97, 147-152.

## **Chapter 4**

# **A comparative study of the fluorogenic compounds N-(1-pyrenyl)maleimide, "MPy", and N-(1-pyrenyl)acrylamide, "PyAM"**

### **4.1. Introduction**

N-(1-pyrenyl)maleimide or maleimido-pyrene, "MPy", has been used exclusively as the fluorogenic component in recent applications of radio-fluorogenic gels (Warman et al, 2011a,b; 2013a,b) because of its ready commercial availability. As shown in the previous chapter however MPy does have disadvantages due to the much slower propagation rate of a terminal maleimido radical compared with that of the TBA acrylate radical end group. This results in a decrease in the degree of polymerization of TBA for a given radiation dose in the presence of MPy, and hence to a decrease in the dose sensitivity of the fluorescence. It has been found that maleimide derivatives in general polymerize much slower than acrylates or acrylamides (Van Herk, 2000; Haas, 1973). We therefore thought it worthwhile to study the effect of replacing the maleimide group of MPy with an acrylamide group giving N-(1-pyrenyl)acrylamide, "PyAM". The

structures of MPy and PyAM are shown in figure 4.1. The hope was that the fluorogenic properties of MPy would be retained while the negative effect on chain polymerization would be absent, resulting in a higher fluorescence sensitivity of a PyAM-based RFG gel. To this end. PyAM was synthesised in the chemistry department of the university and subjected to a series of tests similar to those applied to MPy. The results of this comparative study of the radiation-chemical and optical properties of the two compounds are reported here.

## 4.2. Materials and methods

### 4.2.1. Materials

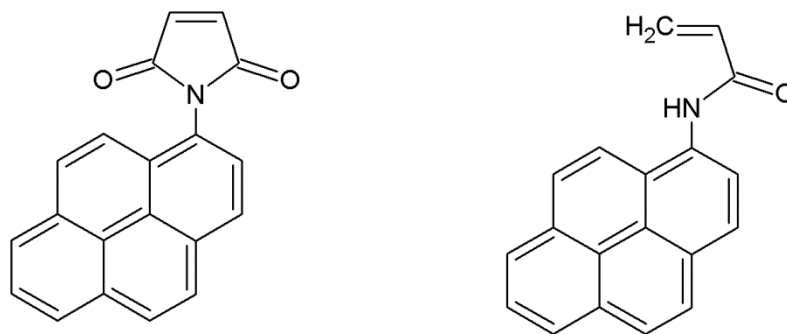


Figure 4.1. The molecular structures of N-(1-pyrenyl)maleimide, "MPy" (left) and N-(1-pyrenyl)acrylamide, "PyAM" (right).

The molecular structures of the two compounds are shown in figure 4.1. MPy is commercially available in gram quantities from Sigma-Aldrich as compound P7908 (price ~250 euro/g). It is a yellow solid of molecular weight 297 g/mol. It dissolves readily in dioxane, which was used as solvent for the accurate determination of the optical absorption extinction coefficient given in chapter 3, table 3.1. It dissolves only partially with mechanical shaking in TBA to yield a suspension that can be decanted to give a slightly yellow, saturated solution with an MPy concentration of ~2 millimolar (~2 mM).

No commercial source of PyAM could be found. Therefore it was synthesized by Dr Chandan Maity, postdoctoral scientist in the group of professor Rienk Eelkema in the Advanced Soft Matter Department of Chemical Engineering of the university as follows: N-(1-Pyrenyl)acrylamide (PyAm): Acryl chloride (0.09 mL, 1.1 mmol) was added slowly to a solution of 1-aminopyrene (0.22 g, 1.0 mmol) in CH<sub>2</sub>Cl<sub>2</sub> (10.0 mL) and Et<sub>3</sub>N (0.15 mL, 1.0 mmol). The reaction mixture was stirred at room temperature, whereupon a cloudy solution appeared as

triethylamine chloride precipitated from solution. After completion of the reaction, it was filtered through celite and concentrated under reduced pressure. The crude substance was purified by column chromatography (silica gel, CHCl<sub>3</sub>) to obtain the desired compound as pale white solid (0.17 g, 65 %). <sup>1</sup>H NMR (THF-d<sub>8</sub>, 400 MHz): δ = 9.55 (s, 1H, CONH), 8.66 (s, 1H, ArH), 8.16 (d, J = 9.2 Hz, 1H, ArH), 8.07 (t, J = 7.3 Hz, 3H, ArH), 8.03 (d, J = 9.3 Hz, 1H, ArH), 7.99 (t, J = 8.9 Hz, 1H, ArH), 7.95 (q, J = 7.6 Hz, 1H, ArH), 6.66 (t, J = 15.2 Hz, 1H, COCH=CH<sub>2</sub>), 6.51 (d, J = 6.8 Hz, 1H, CH=CHH), 5.77 (d, J = 9.9 Hz, 1H, CH=CHH). <sup>13</sup>C NMR (THF-d<sub>8</sub>, 100 MHz): δ = 133.3, 133.0, 132.9, 132.7, 132.2, 129.6, 128.3, 128.0, 127.3, 127.1, 127.0, 126.1, 126.0, 125.9, 125.6, 123.1, 122.2. The compound is an off-white powder with a molecular weight of 271 g/mol. It also dissolves readily in dioxane, which was used to measure the extinction coefficient. In an attempt to make a 1 mM solution in TBA a fine cloudy suspension was obtained even after vigorous shaking. Filtration of this turbulent suspension resulted in a clear saturated solution with a PyAM concentration of ~0.6 mM. The TBA purification and the glove-box deaeration procedures used were the same as in chapters 2 and 3.

#### 4.2.2. Optical equipment

For extinction coefficient measurements solutions with accurately known concentrations of MPy and PyAM in the good solvent paradiioxane were prepared. The spectra were measured over the range 300 to 500 nm using a Kontron Instruments Uvikon 940 spectrophotometer. Emission spectra of irradiated solutions were measured using an Ocean Optics fiber-optic spectrofluorimeter (model SD2000) with an LED excitation source with  $\lambda_{\text{max}}$  365 nm as shown in chapter 3, figure 3.5. Imaging of the fluorescence of irradiated solutions in 1 cm square cells was carried out using LED UV excitation ( $\lambda_{\text{max}}$  381 nm) and the digital camera set-up also shown in chapter 3, figure 3.6. Diagnostics of the images were made using ImageJ which is freely downloadable from the National Institutes of Health. (Rasband W.S., 2009)

#### 4.2.3. Irradiation equipment

Only the GC200 (Atomic Energy of Canada) cobalt-60,  $\gamma$ -ray source was used for the measurements in this chapter. The dose rate was  $\sim 2 \text{ Gy min}^{-1}$ , determined by Fricke dosimetry and calculated on the day of irradiation based on the 5.27 years half-life of the natural decay of cobalt-60.

## 4.3. Results and Discussion

### 4.3.1. Optical absorption spectra

The wavelength dependences of the extinction coefficients of MPy and PyAM over the range 300 to 500 nm are shown in figures 4.2 and 4.3 respectively. The values for PyAM are listed in table 4.1 and those for MPy are tabulated in chapter 3, table 3.1. The two spectra are seen to be very different: MPy has a highly structured spectrum with sharp vibrational bands and a prompt  $S_0 \rightarrow S_2$  cut-off at  $\sim 360$  nm; for PyAM the spectrum is unstructured and broad, extending to close to 400 nm. This large difference came initially as a surprise. However, on reviewing the literature it became apparent that substitution at the 1 position of pyrene may have a dramatic effect on the absorption spectrum. In the case of unsubstituted pyrene the  $S_0 \rightarrow S_1$  transition is symmetry forbidden, which also appears to be the case after substitution of the maleimido moiety. The extremely weak absorption attributable to this transition is shown much expanded in figure 4.2. On the other hand, substitution of the structurally quite similar (see figure 4.1) acrylamide moiety results in a strong perturbation of the basic pyrene spectrum; broadening the vibrational features and making  $S_0 \rightarrow S_1$  an allowed transition. This is probably caused by the lone pair on the nitrogen in PyAM, which introduces the possibility of charge-transfer excited states. A similar effect has been found on substitution of a simple amino group at the 1 position as shown in figure 4.4 (Soustek et al, 2008).

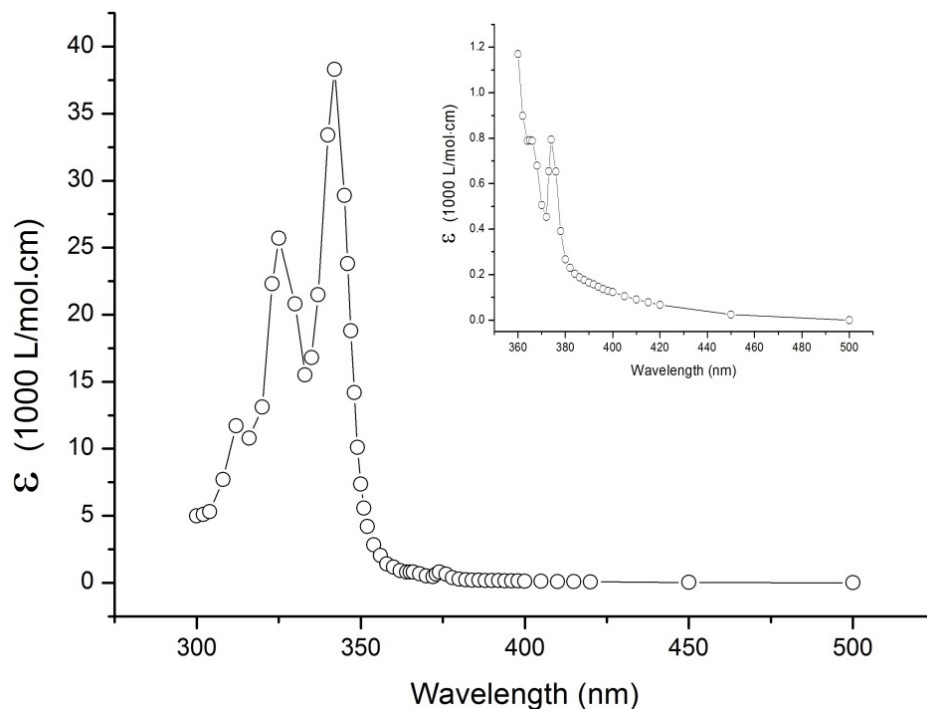


Figure 4.2. The wavelength dependence of the extinction coefficient of MPy. The very weak  $S_0 \rightarrow S_1$  absorption above 360 nm is expanded in the insert.

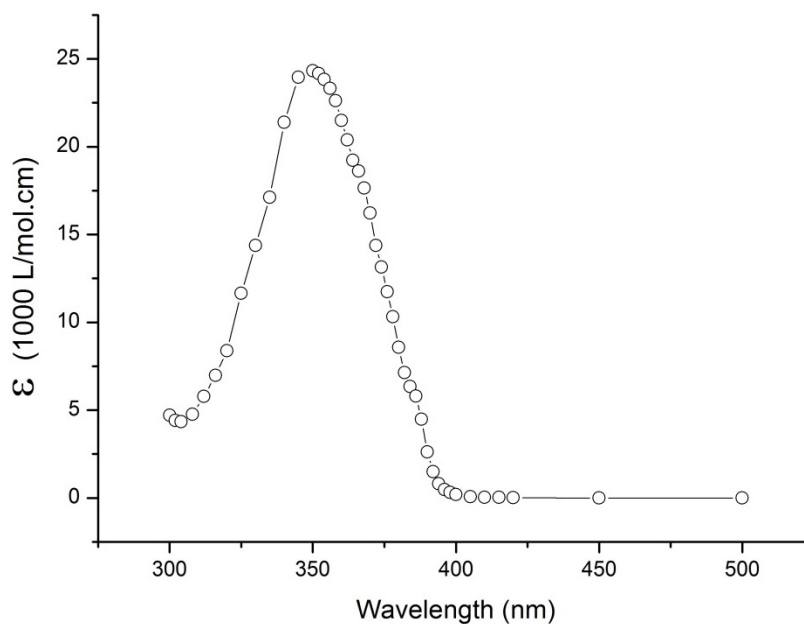


Figure 4.3. The wavelength dependence of the extinction coefficient of PyAM.

Table 4.1. Extinction coefficients of PyAM at selected wavelengths in the 300 - 500 spectral region.

Wavelength (nm)	$\epsilon \times 10^{-3}$ (L/mol.cm)	Wavelength (nm)	$\epsilon \times 10^{-3}$ (L/mol.cm)	Wavelength (nm)	$\epsilon \times 10^{-3}$ (L/mol.cm)
300	4.71	356	23.32	386	5.80
302	4.41	358	22.61	388	4.48
304	4.34	360	21.50	390	2.61
308	4.76	362	20.38	392	1.50
312	5.79	364	19.22	394	0.80
316	6.97	366	18.61	396	0.48
320	8.39	368	17.64	398	0.32
325	11.65	370	16.22	400	0.20
330	14.37	372	14.38	405	0.07
335	17.12	374	13.14	410	0.04
340	21.38	376	11.74	415	0.03
345	23.95	378	10.32	420	0.01
350	24.33	380	8.57	450	0.00
352	24.16	382	7.13	500	0
354	23.83	384	6.34		

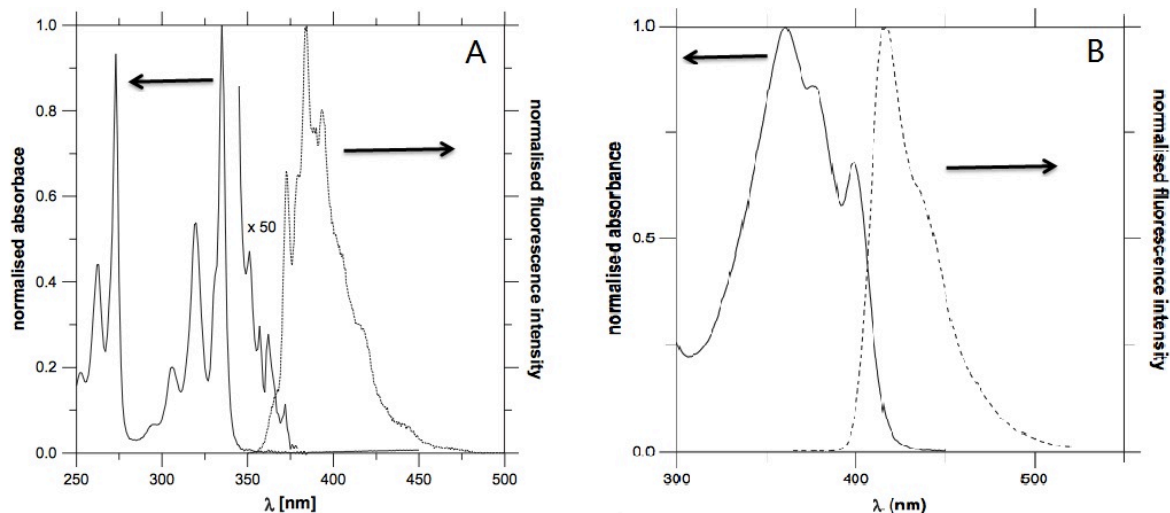


Figure 4.4. The absorption and emission spectra of pyrene (A) and 1-aminopyrene (B) from Soustek et al, 2008.

Of particular importance for the application of the two compounds is the large difference, by a factor of approximately 30, in the extinction coefficients in the 380 nm region, the region of the emission of the LED UV excitation sources used. This aspect will be discussed further after considering the fluorescence of the compounds.

#### 4.3.2. Optical emission spectra

Of essence for the function of a fluorogenic compound in a radio-fluorogenic medium, is that it is initially non-fluorescent or only very weakly fluorescent. Its intrinsic fluorescence is only released by a chemical modification that, in the present case, involves the conversion of an ethylnic double bond to a single bond. This can be brought about by reaction with thiols which has resulted in the widespread use of MPy in molecular biology for the fluorescent labeling of proteins (Bains et al, 2011). In the present application the double bond is converted to a single bond by incorporation of the molecule into a growing polymer chain as illustrated in figure 3.1 (chapter 3). The effect was shown for an irradiated solution of MPy in TBA in figure 3.12 (chapter 3). A similar increase in the fluorescence of a solution of PyAM in TBA is illustrated in figure 4.5. Both compounds display the requisite lack of fluorescence prior to irradiation indicating that the emissive  $S_1 \rightarrow S_0$  transition found for pyrene has been completely quenched. This is presumably due to the introduction into the manifold of states of a non-emissive charge-transfer or triplet state below  $S_1$ . The eventual radiation-induced fluorescence is broad and structureless for both compounds with emission maxima of 394 nm for MPy and 407 nm for PyAM.

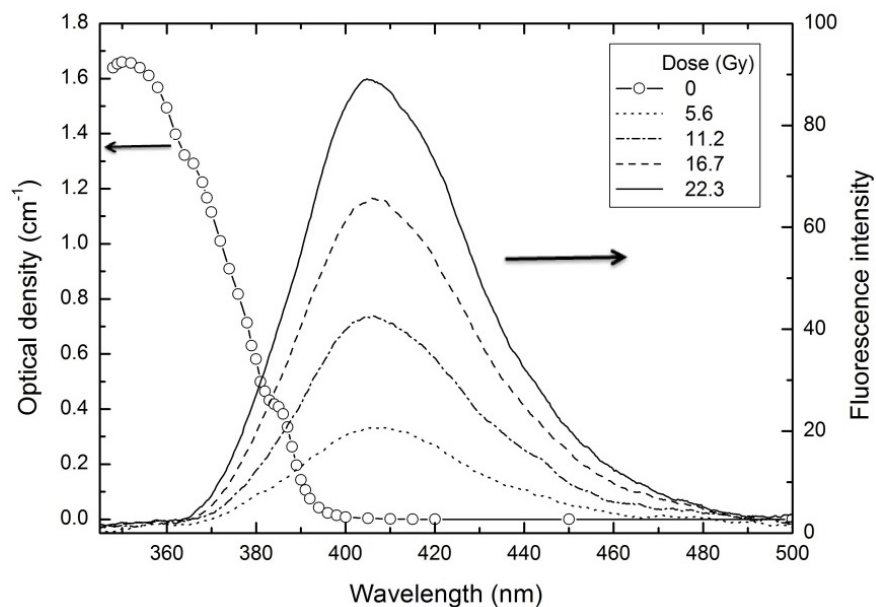


Figure 4.5. The increase in fluorescence on irradiation of a TBA solution of PyAM. The absorption spectrum above 340 nm is shown by the circles.

A quantitative comparison of the absolute fluorescence intensities using the Ocean Optics spectrofluorimeter was not possible because of the large optical densities of the compounds at the excitation wavelength of 365 nm and the fiber-optic method of probing the emissions as explained in section 3.3.1. of chapter 3. In figure 4.6 the intensity of the fluorescence is plotted as a function of the radiation dose with the values for the two compounds normalized at the highest dose. Both compounds are seen to display a superlinear increase with dose.

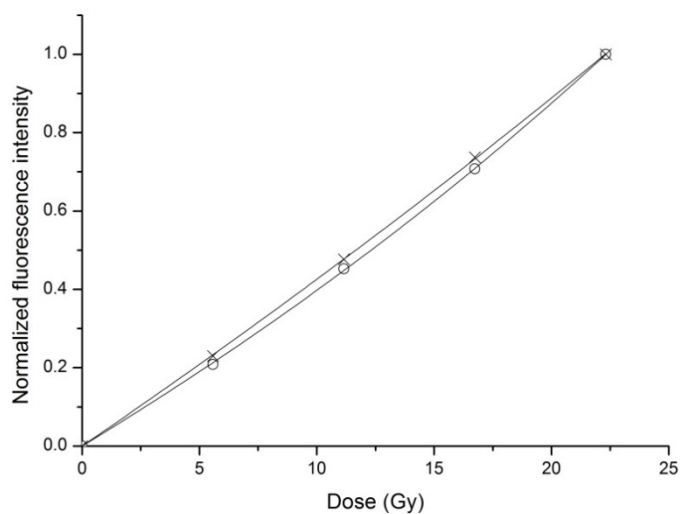


Figure 4.6. The fluorescence intensity at  $\lambda_{\max}$  as a function of the radiation dose for TBA solutions of MPy (open circles) and PyAM (crosses). The data have been normalized at a dose of 22 Gy.



### 4.3.3. Gel formation and monomer conversion

As pointed out in the introduction, the main reason for looking into other fluorogens was the finding that the currently used MPy decreased the degree of monomer conversion for a given dose compared with that for pure TBA. This is ascribed to a much slower rate of propagation associated with a maleimido radical chain end-group compared with an acrylate radical end-group. The effect was most clearly visible as the reduction in the viscosity of solutions irradiated to the same dose but with an increasing concentration of MPy as shown in figure 4.7. Since acrylamides tend to polymerize as rapidly as acrylates, it was thought that substitution of the maleimide group with an acrylamide group might result in at least a reduced negative effect of the fluorogen on the polymerization process and, as a result, an increased sensitivity of the corresponding RFG gel.

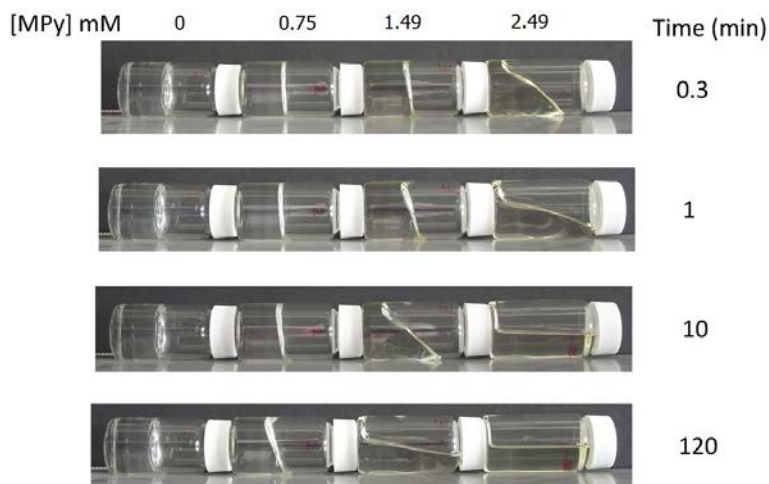


Figure 4.7. Four irradiated ( $\sim 17$  Gy) liquid scintillation vials (LSVs), containing 10 mL deaerated solutions of MPy in TBA of the concentrations shown, laid on their side for the elapsed times shown on the right.

Similar viscosity measurements are shown in figure 4.8 for PyAM/TBA solutions. Unfortunately a negative influence on the viscosity is also apparent indicating a retardation of polymerization also by PyAM. Comparing the results with those for MPy indicates that PyAM has, if anything, a greater negative effect (by approximately a factor of two) on the polymerization process.

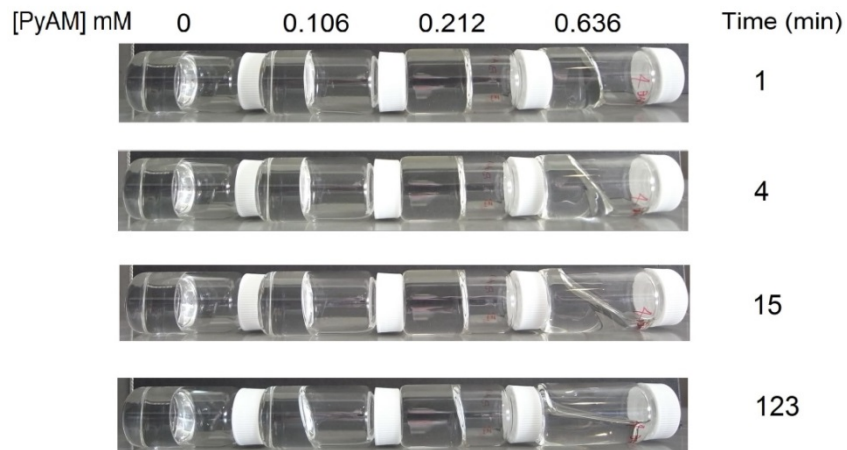


Figure 4.8. Four irradiated (~17 Gy) liquid scintillation vials (LSVs), containing 10 mL deaerated solutions of PyAM in TBA of the concentrations shown, laid on their side for the elapsed times shown on the right.

A more quantitative measure of the effect on the extent of polymerization has been obtained by monomer evacuation and gravimetric analysis of the solutions used for the viscous flow measurements. The monomer conversion,  $C_M$ , is plotted against solute concentration in figure 4.9. The decrease in  $C_M$  with increasing concentration is seen to be, if anything, greater for PyAM than for MPy. This supports the qualitative conclusion on the basis of the meniscus flow observations in figures 4.7 and 4.8.

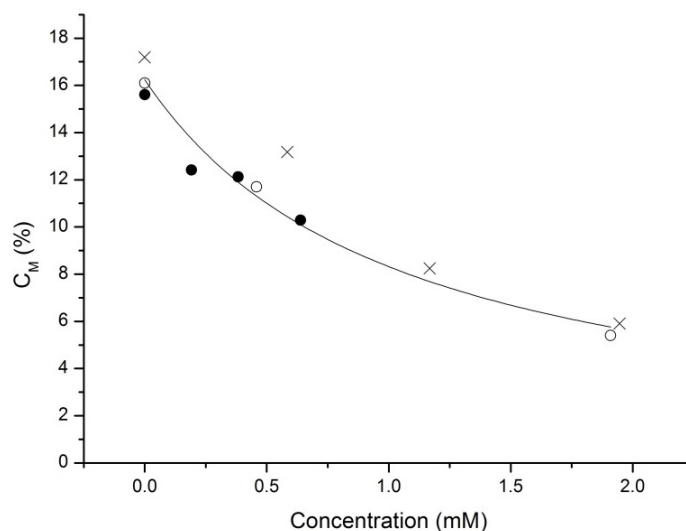


Figure 4.9. The monomer conversion,  $C_M$ , in the TBA solutions of MPy (crosses) and PyAM (closed circles) used in figures 4.7 and 4.8 respectively, as a function of the solute concentration. Also included are results for an earlier series of measurements using MPy (open circles).

#### 4.3.4. Fluorescence imaging

Deaerated solutions of MPy and PyAM in TBA, contained in 1 cm square cells, were irradiated in the GC200  $\gamma$ -ray source and fluorescence images were made using the set-up shown in figure 3.6 of chapter 3. Full-colour, JPEG images of the two cells are shown in figure 4.10, one containing a 0.304 mM solution of MPy in TBA and the other a 0.212 mM solution of PyAM. The camera exposure parameters and the irradiation dose of  $\sim 20$  Gy were the same.

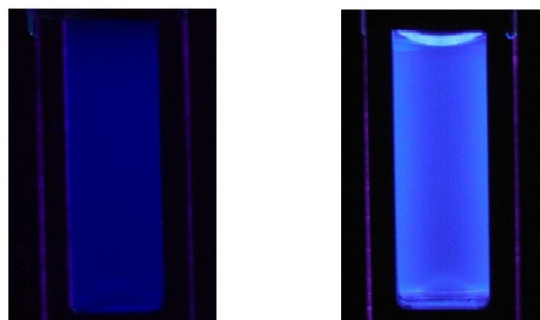


Figure 4.10. Full-colour JPEG images of the fluorescence from 1 cm square cells containing TBA solutions of 0.304 mM MPy (left) and 0.212 mM PyAM (right) both gamma-ray irradiated with a dose of  $\sim 20$  Gy.

It is qualitatively apparent in figure 4.10 that the intensity of the fluorescence of the PyAM solution is significantly higher than of the MPy solution. It is also apparent that the fluorescence of the MPy solution is quite uniform over the width of the cell whereas for the PyAM solution there is a clear "dip" in the intensity in the middle of the cell. This is shown more clearly in figure 4.11 by scans across the raw DNG images (blue pixels only) in figure 4.10.

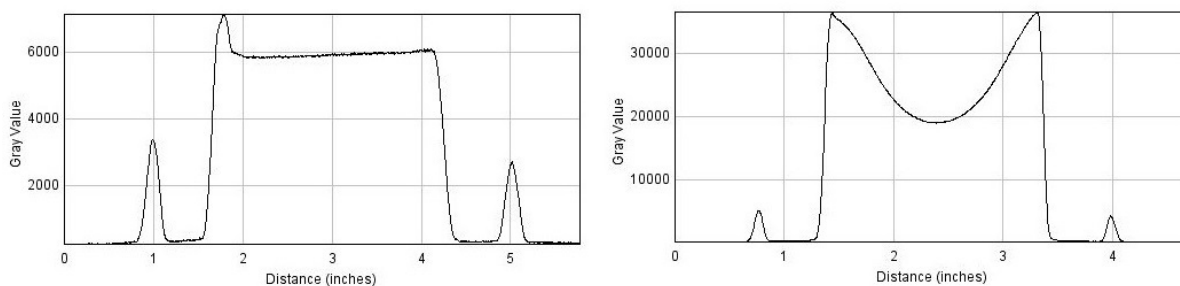


Figure 4.11. Scans across the images shown in figure 4.10, using ImageJ software, of the linear raw DNG blue pixel levels,  $P_B$ . The sharp blips are artifacts caused by scattered-light at the outer edges of the aluminum cell holder.

The large difference in the images, despite the similarity of the solute concentrations and the fixed excitation light intensity and camera settings, results mainly from the large difference in

the extinction coefficients of the two compounds at the excitation wavelength of  $381 \pm 5$  nm:  $\sim 250 \text{ M}^{-1}\text{cm}^{-1}$  for MPy and  $7900 \text{ M}^{-1}\text{cm}^{-1}$  for PyAM. For the concentrations used this corresponds to optical densities of  $0.08 \text{ cm}^{-1}$  and  $1.67 \text{ cm}^{-1}$  respectively. Due to the attenuation of the UV light in the cell by the fluorogen, the intensity of the fluorescence is expected to vary with depth,  $x$ , according to,

$$I(x)/I(0) = [10^{-\text{OD}x} + 10^{-\text{OD}(w-x)}]/[1 + 10^{-\text{OD}w}] \quad (4.1)$$

Figure 4.12 shows a best-fit to the intensity scan within the PyAM solution using equation 4.1 with an optical density of  $1.34 \text{ cm}^{-1}$ . This is close to the value of  $1.67$  based on the known concentration of the PyAM solution and its extinction coefficient at close to the wavelength maximum of the UV excitation light.

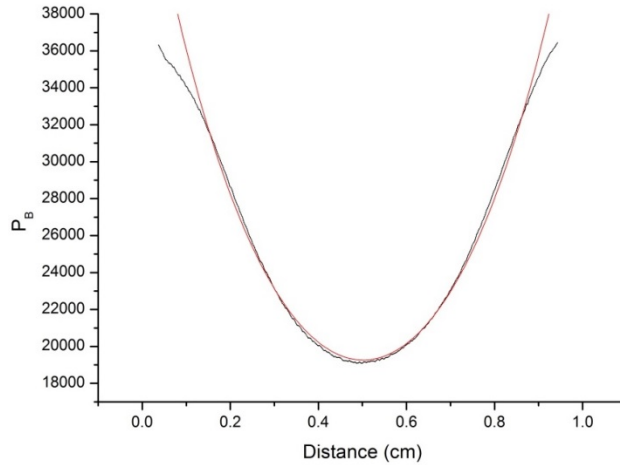


Figure 4.12. A fit (red curve) to the fluorescence dip found for the PyAM solution using equation 4.1 with an optical density of  $1.34 \text{ cm}^{-1}$ .

For comparison of the two solutions we can take the fluorescence intensity at the center of the cells which is related to the intensity expected in the absence of attenuation of the excitation light,  $I_0$ , by,

$$I(w/2)/I_0 = 10^{-\text{OD}w/2} \quad (4.2)$$

This indicates that the fluorescence is decreased by less than 10% due to the attenuation effect for the MPy solution compared with a decrease by a factor of 4.3 for the PyAM solution. The actual values of the intensities at the center of the cells are plotted against dose in figure 4.13. Even without taking into account the attenuation effect, the values for the PyAM solution are considerably higher than for the MPy solution; by a factor of 3.5. If the attenuation effect is taken into account this would indicate that the fluorescence intensity of the PyAM solution for the same dose is potentially an order of magnitude larger than for MPy. This could be due to a larger yield,

higher extinction coefficient or greater fluorescent quantum yield of the co-polymerised product from PyAM or a combination of all 3. A contributing factor could also be the longer wavelength of the fluorescence maximum of irradiated PyAM solutions, 407 versus 394 nm, due to the ~400 nm cut-off of the blue-pixel filter of the camera.

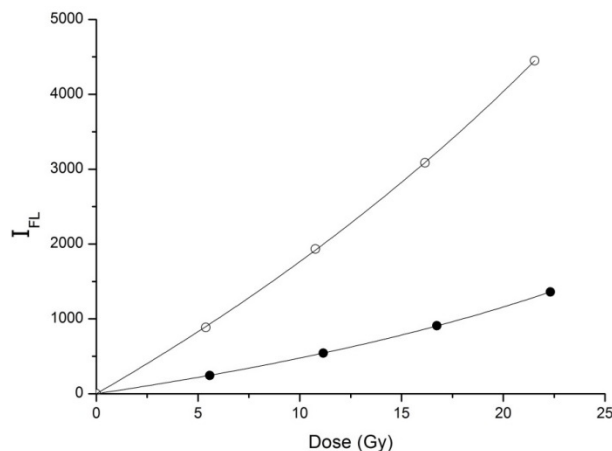


Figure 4.13. The fluorescence intensities at the middle of the cells as a function of irradiation dose for MPy (closed circles) and PyAM (open circles) solutions of concentration 0.304 mM and 0.212 mM respectively.

## 4.4. Conclusions

N-(1-pyrenyl)acrylamide, PyAM, is found to have the basic property required of a fluorogenic compound for application in the formation of radio-fluorogenic gels: it dissolves in a polymerizable monomer such as TBA to form a solution that is non-fluorescent but which becomes highly fluorescent when exposed to high-energy radiation. For the same dose the intensity of the fluorescence is in fact substantially higher than for an MPy solution of similar concentration, by a factor of 3 or more. PyAM has however certain disadvantages. Firstly, the negative effect on the degree of TBA polymerization found with MPy is if anything worse for PyAM. Also the solubility in TBA is much smaller: saturated concentration 0.6 mM as opposed to 1.7 mM for MPy. The main problem however is the much higher extinction coefficient of PyAM in the  $381 \pm 5$  nm wavelength region of the UV excitation light;  $7950 \text{ cm}^{-1}$  versus  $250 \text{ cm}^{-1}$ . This results in a strong attenuation of the excitation light even within a 1 cm wide cell for a solute concentration considerably less than 1 mM. This would make its application to 3D dosimetry, even in small sample volumes, very difficult to analyse. In addition, the ready commercial availability of MPy makes it suitable even for laboratories without associated synthetic possibilities.

The present results demonstrate one of the properties of MPy that make it appropriate as a fluorogenic probe; the forbidden nature of the first  $S_0$  to  $S_1$  absorption. This results effectively in

a large Stokes-shift between the first absorption band and the emission. Excitation of a fluorescent product can then be carried out with wavelengths within this Stokes-shift region with minimal attenuation by the non-polymerized form of the fluorogene. This property should be taken into account when deciding on other possible substitutes for MPy.

## References

Bains, G., Patel, A.B., Narayanaswami, V. 2011. Pyrene: A probe to study protein conformation and conformational changes. *Molecules* 16, 7909-7935.

Haas, H.C., 1973. Maleimide polymers. II Radical polymerisation kinetics. *Journal of Polymer Science* 11, 315-318.

Rasband, W.S., 2009. ImageJ US National Institutes of Health, MD, USA. <http://rsb.info.nih.gov/ij/>

Soustek, P., Michl, M., Almonasy, N., Machalicky, O., Dvorak, M., Lycka, A. 2008. The synthesis and fluorescence of N-substituted 1- and 2-aminopyrenes. *Dyes and Pigments* 78, 139-147.

Van Herk, A.M., 2000, Pulsed initiation polymerization as a means of obtaining propagation rate coefficients in free-radical polymerizations. II Review up to 2000. *Macromolecular Theory and Simulations* 9, 433-441.

Warman, J.M., de Haas, M.P., Luthjens, L.H., 2011a. High-energy radiation monitoring based on radio-fluorogenic co-polymerization II: fixed fluorescent images of collimated X-ray beams using an RFCP gel. *Physics in Medicine and Biology* 56, 1487-1508.

Warman, J.M., de Haas, M.P., Luthjens, L.H., Murrer, H.P., 2011b. A radio-fluorogenic organic gel for real-time, 3D radiation dosimetry. *Advanced Materials* 23, 4953-4955. <http://dx.doi.org/10.1002/adma.201102831>

Warman, J.M., de Haas, M.P., Luthjens, L.H., Hom, M.L., 2013a. High-energy radiation monitoring based on radio-fluorogenic co-polymerization III: fluorescent images of the cross-section and depth-dose profile of a 3 MV electron beam. *Radiation Physics and Chemistry* 84, 129-135. <http://dx.doi.org/10.1016/j.radphyschem.2012.06.031>

Warman, J.M., de Haas, M.P., Luthjens, L.H., Kavatsyuk, O., van Goethem, M-J., Kiewiet, H.H., Brandenburg, S., 2013b. Fixed fluorescent images of an 80 MeV proton pencil beam. *Radiation Physics and Chemistry* 85, 179-181. <http://dx.doi.org/10.1016/j.radphyschem.2012.11.011>



## **Chapter 5**

# **The preparation and properties of a reformed radio-fluorogenic (RFG) gel**

### **5.1. Introduction**

In chapter 3 the radio-fluorogenic effect was demonstrated for solutions of maleimido-pyrene (MPy) in tertiary-butyl acrylate (TBA) homogeneously irradiated with gamma-rays and the underlying reaction is illustrated in figure 3.1. In order to apply the effect to the study of complex radiation fields it is necessary to "fix" the fluorescent image in space. This requires that the medium is quasi-rigid, restricting the free diffusion of the radiolytic products responsible for the fluorescent effect. It was found by Warman et al. (2011a) that TBA itself forms a quasi-rigid gel after irradiation to a monomer conversion of approximately 15%. The gel displays no tendency to flow on a timescale of an hour or more, as shown in chapter 2 (figure 2.7) (Yao et al. 2014). Dilute solutions of MPy in TBA are also found to gel on irradiation and pre-irradiation of MPy



solutions might then be considered to be a solution to the problem. However, as shown in chapter 3 (figure 3.22), these gels are less rigid than for pure TBA due to a chain-limiting effect of the solute. Also a gel formed by homogeneous irradiation of an MPy/TBA solution is fluorescent over its whole volume. This can considerably reduce the dynamic range and spatial resolution of subsequent fluorescent images of complex radiation fields.

The problem can be solved by preparing reformed gels in which the polymer matrix is first formed by irradiation of pure TBA to a conversion of approximately 15%. The remaining TBA monomer is then evaporated off, replaced with a dilute solution of MPy in TBA and allowed to swell back to the original rigid gel, which now contains the fluorogenic compound. This swelling of poly(butyl acrylate) has been suggested as a method for the recovery of organic solvents (Kattan and Al-Kassiri, 2010). The procedure is illustrated in figure 5.1. The present chapter concerns the preparation of such reformed radio-fluorogenic gels, and their physical and optical properties.

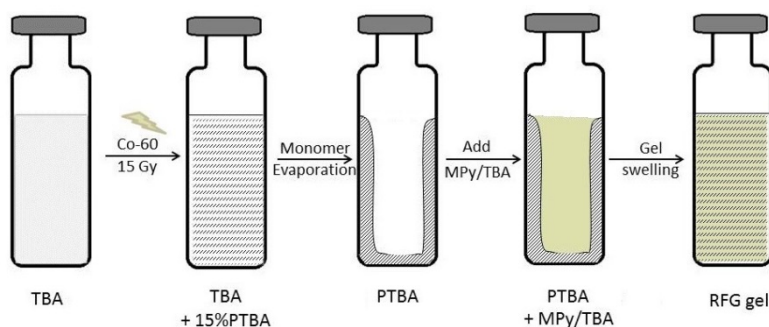


Figure 5.1. A pictorial representation of the processes involved in the preparation of a reformed radio-fluorogenic (RFG) gel from tertiary-butyl acrylate (TBA) and maleimido-pyrene (MPy).

## 5.2. Materials and Methods

### 5.2.1. Reformed radio-fluorogenic (RFG) gel preparation

The components of the gels used in the present chapter are the same as those in chapters 2 and 3: tertiary-butyl acrylate (TBA) from Sigma-Aldrich (#327182) and N-(1-pyrenyl)maleimide or maleimido-pyrene (MPy) also from Sigma-Aldrich (#P7908). The physical properties of the individual components have been given in the materials and methods sections of previous chapters. The reformation procedure begins with the pipetting (in a nitrogen-flushed glove box) of a volume,  $V_1$ , of pure de-aerated TBA into the cell (empty weight  $W_1$ ) to be used for imaging. The cell is capped, removed from the glove box and irradiated to a dose of approximately 15 Gy (close to 15% monomer conversion) in the GC200 gamma-ray source with a dose rate of approximately 2 Gy/min. The cell is then uncapped and placed in a vacuum oven at room

temperature for several days for removal of remaining monomer after which it is reweighed uncapped,  $W_2$ . The cell is then transferred to the glove box which also contains a de-aerated MPy/TBA solution of the approximate concentration required for the measurements. After a day standing in the glove box a volume  $V_2$  of the solution equal to that of the monomer evacuated off;  $V_2 = V_1 - (W_2 - W_1)/\rho_{TBA}$  with  $\rho_{TBA}$  the density of TBA,  $0.89 \text{ kg.L}^{-1}$ , was pipetted into the cell. It was then allowed to stand for a period of approximately two weeks to allow swelling of the polymer, PTBA, back to a rigid gel now containing MPy. A sample of the deaerated solution was also placed in a 1 cm square cell for measurement of the optical density at 365 nm and accurate calculation of the MPy concentration,  $[\text{MPy}]_{\text{soltn}} = \text{OD}_{365}/791 \text{ mol.L}^{-1}$ . The concentration of MPy in the reformed gel was then calculated from,  $[\text{MPy}]_{\text{gel}} = [\text{MPy}]_{\text{soltn}} V_2/[V_2 + (W_2 - W_1)/\rho_{PTBA}]$ , with  $\rho_{PTBA}$  the density of PTBA,  $1.09 \text{ kg.L}^{-1}$ .

As mentioned in the introduction, one of the major advantages of the reformed gel approach is the much higher rigidity of the gel for the same MPy concentration. This is illustrated in figure 5.2 by two gels both containing approximately 1 mM MPy; one prepared as described above and one formed by direct irradiation of the MPy solution with the same dose as that used for formation of the reformed gel. The reformed gel displays no tendency to flow even after an hour whereas the irradiated solution begins to flow even after a few minutes.

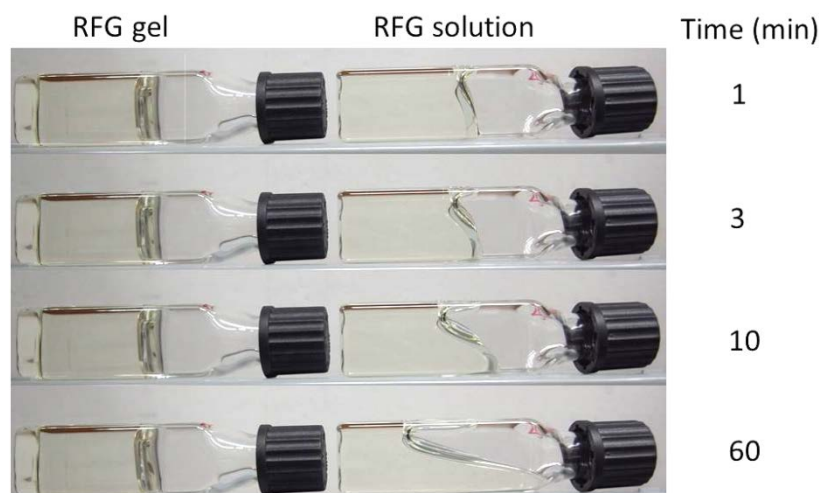


Figure 5.2. The meniscus creep of TBA gels containing  $\sim 1 \text{ mM}$  MPy after the times lying in a horizontal position given on the right. Left: A gel reformed by swelling polyTBA from 14 Gy-irradiated pure TBA with a  $\sim 1 \text{ mM}$  TBA solution of MPy. Right: A gel formed by irradiation of a  $\sim 1 \text{ mM}$  solution of MPy in TBA with a dose of 14 Gy.

A second advantage is the very low fluorescence of a reformed gel compared with that of an irradiated solution. This is illustrated in figure 5.3 by the fluorescent images of the  $\sim 1 \text{ mM}$  MPy gels shown in figure 5.2. It can further be seen in figure 5.3 that subsequent irradiation of the reformed gel with the same dose as used for the solution results in an increase in fluorescence that is even greater than that found for the direct irradiation of the solution.

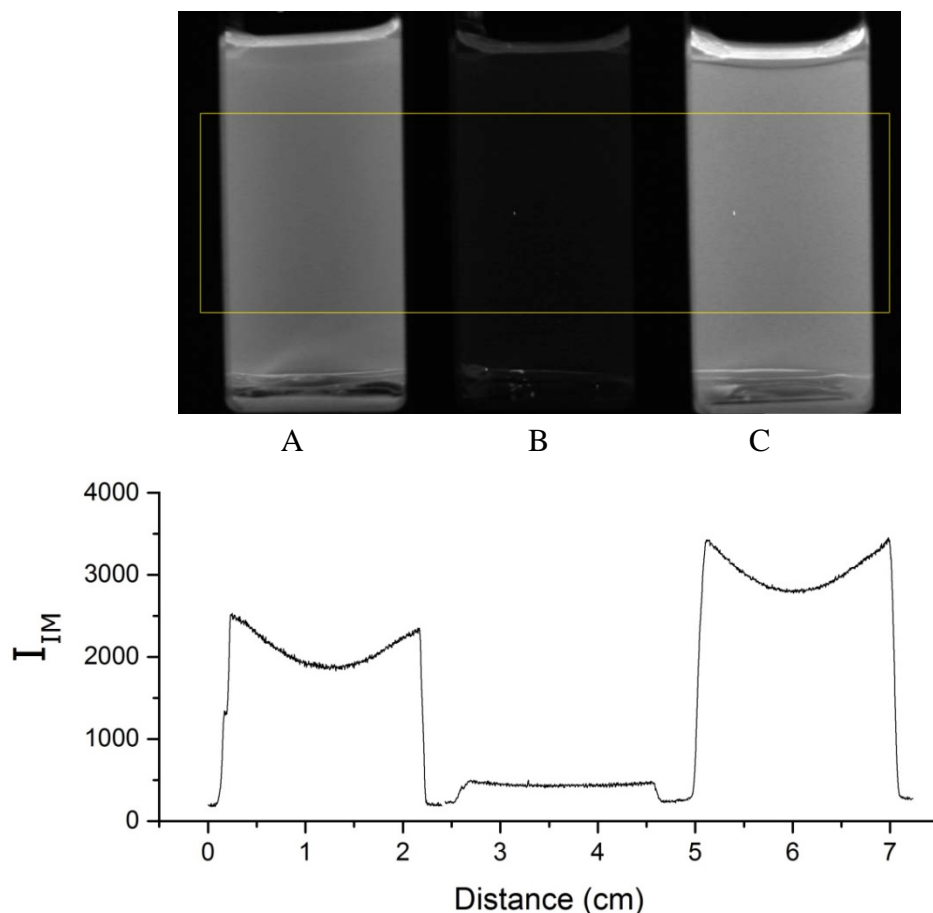


Figure 5.3. Upper figure: blue pixel JPEG images of the fluorescence of TBA gels. A: A gel formed by irradiation of a  $\sim 1$  mM solution of MPy in TBA with a dose of 14 Gy. B: A gel formed by swelling polyTBA from 14 Gy irradiated pure TBA with a  $\sim 1$  mM solution of MPy in TBA. C: The reformed gel after irradiation with a dose of 14 Gy. Lower figure: a scan across the gels of the DNG blue pixel level using ImageJ.

### 5.2.2. The radiation sources

The radiation sources used in the present chapter were the same gamma ray sources, GC200 and GC220, previously described in chapter 2. The dose rates were on the order of 2 and 30 Gy/minute respectively and the actual dose rate on the day of irradiation was calculated using the known decay half-life of cobalt-60 of 5.27 years. The dose rate could be varied using a cylindrical lead attenuator, height 135 mm, outer diameter 85 mm and wall thickness 18.5 mm, placed in the cavities of GC200 and GC220. The attenuation factor of the attenuator was determined to be 3.39 using MD-V3 radio-chromic film which is shown in chapter 6 to be dose rate independent. A small correction to the doses was applied to take into account the transit times of the gamma sources of 9.3 and 4.9 seconds respectively. These transit times were also determined using radio-chromic film (see chapter 6).

### 5.2.3. Fluorescence measurement

Measurements of the fluorescence were made using the same equipment as in chapter 3 with the Ocean Optics spectro-fluorimeter (figure 3.5) for spectral measurements and the CCD camera set-up (figure 3.6) for overall intensity measurements. The type of cells and cell holders used are illustrated in figure 3.7. The ultraviolet light sources were produced by 4PICO ([www.4PICO.NL](http://www.4PICO.NL)). They consisted of a 16.3 cm long, linear array of 22 light emitting diodes with a rectangular Fresnel lens for beam control. Two lenses were used: a 2" lens which produced a well-collimated, uniform beam approximately 20 mm wide, and a 3" lens that produced a divergent beam with a central intensity measured using a 9,10-diphenyl anthracene (DPA) solution in the cell holder position a factor of 3.27 lower than for the 2" lens. The lenses were covered with a 1 mm thick UG1 ("Woods glass" from Schott) filter to attenuate any visible wavelength components of the LED emission. The spectrum of the resulting beam,  $I(\lambda)_{EX}$ , had a maximum at 381 nm and an FWHM of ~10 nm. This is shown in figure 3.8 together with the absorption spectrum of MPy in the same wavelength region. The effective, mean value of the MPy extinction coefficient,  $\bar{\epsilon}_{EX}$ , for this excitation spectrum is  $\Sigma[I(\lambda)_{EX}\epsilon(\lambda)]/\Sigma I(\lambda)_{EX} = 294.8 \text{ L/mol.cm}$ .

The CCD camera used was a Ricoh GX200. The focal length of the camera was fixed at 10 cm (the distance from the camera lens to the center of the RFG cell). Over the period of the measurements the ISO was fixed at 100 and apertures of f/3.5 and f/4.4 were used. The pixel level measured using the latter aperture was a factor of 0.694 that for the former. The shutter time,  $s$ , was changed manually up to a maximum of 4 seconds with several values taken for each sample. The images of the fluorescence were stored on an SD disk as JPEG and raw DNG files. A very dilute, homogeneous cyclohexane solution of the fluorescence standard DPA was used to test the uniformity of illumination of the sample volume.

The files were analysed using the open source software program ImageJ (US National Institutes of Health). The 8-bit JPEG files could be imported directly. The 16-bit DNG files were imported via the "DCraw" plug-in (<http://ij-plugins.sourceforge.net/plugins/dcraw/>). The images were color-separated into red, green and blue channels with separate pixel levels (gray scale values),  $P_R$ ,  $P_G$  and  $P_B$ . The blue component of the DNG files,  $P_B$ , was used for analysis since the spectrum is closest to that of the fluorescent emission of MPy. The fluorescence intensity of the image,  $I_{IM}$ , was equated with the slope of  $P_B$  against the camera "shutter time",  $s$ . The small background level in a non-irradiated area was subtracted from that in the irradiated sample. Scans across samples, as shown in figure 5.3 (lower) could also be made.

$I_{IM}$  is proportional to the photon flux emitted by the sample,  $\Phi$ , with a proportionality factor which was denoted  $C$  in chapter 3, i.e.  $I_{IM} = C\Phi$ . The factors affecting the value of  $C$  are the sensitivity of detection, determined by the camera settings, and the intensity of the UV excitation light. In chapter 3 data were obtained using a 3" Fresnel lens and an f-number of 4.4 whereas in this chapter the 2" lens was used with an f-number of 3.5. These changes result in an overall increase in sensitivity for the data in this chapter by  $3.27/0.694$  or  $C_5/C_3 = 4.72$ .

### 5.3. Results and Discussion

As pointed out in the introduction, the reasons for using a reformed radio-fluorogenic gel rather than a gel formed directly by irradiation of an RFG solution with the same MPy concentration are twofold: the viscosity of the former is much greater than that of the latter and the background (zero dose) fluorescence of the former is much smaller. In the following sections we present results on the reproducibility of the reformed RFG gel preparation procedure, on the post-irradiation fluorescence stability and its dependence on dose, dose rate, and MPy concentration.

#### 5.3.1. Reproducibility of reformed RFG gels

We have tested the reproducibility of the method of preparing reformed RFG gels by making a batch of 9 samples in 1cm square cells. The optical densities of the 9 samples at 365 nm were measured and found to be  $0.364 \pm 0.010 \text{ cm}^{-1}$ , corresponding to a concentration of 0.460 mM MPy with a standard error of less than 3%. Four of the samples were irradiated in GC200 and five in GC220 and the results of the dependence of the fluorescence intensity,  $I_{IM}$ , on accumulated dose are shown in figure 5.4.

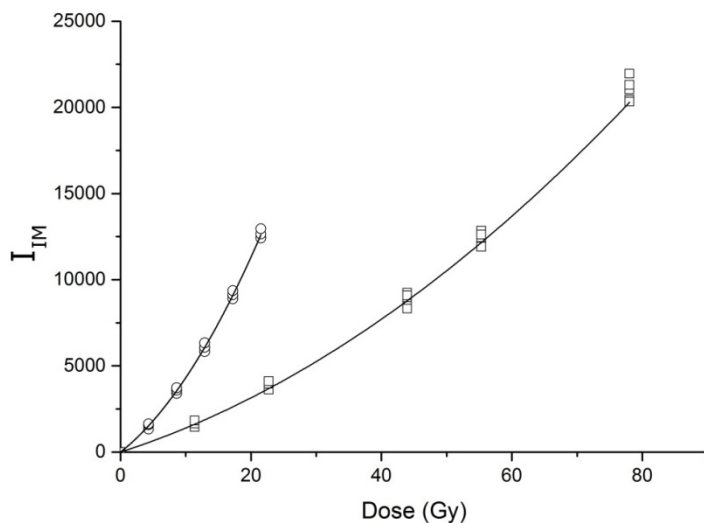


Figure 5.4. The dose dependence of the fluorescence intensity,  $I_{IM}$ , of several RFG gel samples (0.46 mM MPy) prepared in one batch and irradiated at dose rates of 1.43 Gy/min (circles, 4 samples) and 19.7 Gy/min (squares, 5 samples). The full lines are best-fits for all the samples at a given dose rate using equation 5.1.

As for MPy/TBA solutions, the dose dependence is found to be super-linear. The full lines drawn in the figure are best fits using the same relationship that was used to fit the solution data in chapter 3.

$$I_{IM} = (1 + A_{IM}D)K_{IM}D \quad (5.1)$$

The best fit values are  $A_{IM} = 0.0449$  and  $0.0154 \text{ Gy}^{-1}$ , and  $K_{IM} = 298$  and  $122 \text{ Gy}^{-1}$  for the low (1.43 Gy/min) and high (19.7 Gy/min) dose rate sources respectively.

The full data set is listed in table 5.1. Individual RMS deviations have been calculated for the 5 different doses studied for each dose rate. While the number of data points is small, the results do indicate a general trend of a larger uncertainty for the lowest dose decreasing towards an error level of 3% or less for the highest doses. This tendency is illustrated graphically in figure 5.5 by the scatter of the points in the (linear) plots of  $I_{IM}/D$  versus dose. A possible explanation is that small, irreproducible remnants of oxygen are present in some of the samples which can result in a delay in the onset of the polymerization process due to free-radical scavenging by  $O_2$ .

Table 5.1. The fluorescence intensities of 9 "identically prepared" reformed gel samples as a function of dose for irradiations in the GC200 (4 samples) and GC220 (5 samples) gamma ray sources. The percentile standard deviations for a given dose are given in the final column. The MPy concentration of the samples as measured by the  $OD_{365}$  was 0.46 mM with a standard deviation of 2.8%.

D'	D	$I_{IM}$					$\sigma$
(Gy/min)	(Gy)						(%)
1.43	4.30	1535	1331	1581	1639		7.6
	8.60	3582	3402	3594	3727		3.2
	12.9	6040	5824	6077	6328		2.9
	17.2	9065	8895	9128	9359		1.8
	21.5	12446	12417	12649	12958		1.7
19.7	11.4	1634	1452	1795	1644	1831	8.1
	22.7	3878	3631	4045	3958	4115	4.3
	44.0	8711	8321	8968	9242	9091	3.6
	55.3	12306	11920	12457	12850	12624	2.5
	78.0	20444	20334	21042	21952	21305	2.8

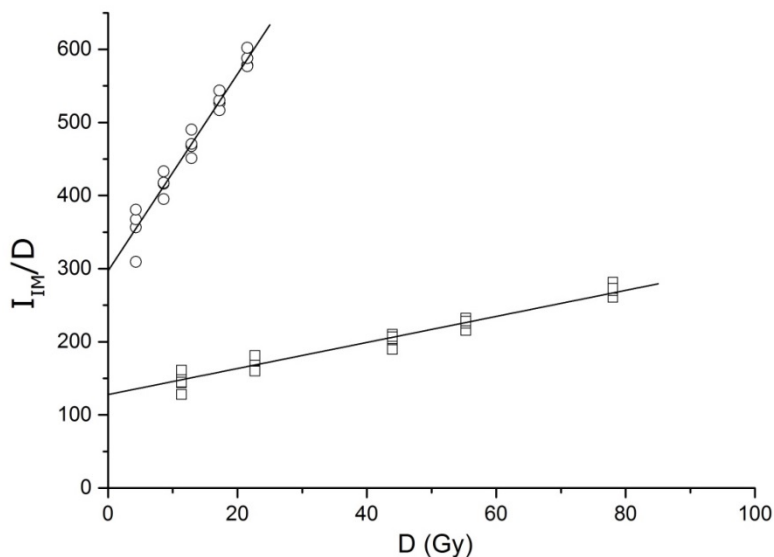


Figure 5.5. Plots of the data in table 5.1, for RFG gels with [MPy] = 0.46 mM, as the dose-normalized fluorescence against dose with linear best-fit straight lines as expected from equation 5.1 with intercept =  $K_{IM}$ , slope/intercept =  $A_{IM}$  for dose rates of 1.43 Gy/min (circles) and 19.76 Gy/min (squares). The values from the linear fits of parameter  $K_{IM}$  and  $A_{IM}$  are 297.0  $Gy^{-1}$  and 0.04532  $Gy^{-1}$ , 127.8  $Gy^{-1}$  and 0.01394  $Gy^{-1}$  for GC200 and GC220 respectively.

### 5.3.2. Post-irradiation effects

To study post-irradiation effects a ~1 mM MPy reformed gel sample was prepared in a 2 cm square cell and irradiated with a dose of 13.8 Gy in GC200. The fluorescence,  $I_{IM}$ , was then measured in the imaging set-up shown in figure 3.7. Measurements were made at increasing times after irradiation with the cell kept in the dark between measurements. The results, up to an elapsed time of approximately a week, are shown in figure 5.6. The fluorescence displays a post-irradiation growth by approximately 10% over a timescale of hours after which it remains constant within a few percent. Within the first hour after irradiation the fluorescence changes by less than 3%. A follow-up measurement after 1 month was found to be ~3% lower than the value found after 1 week.

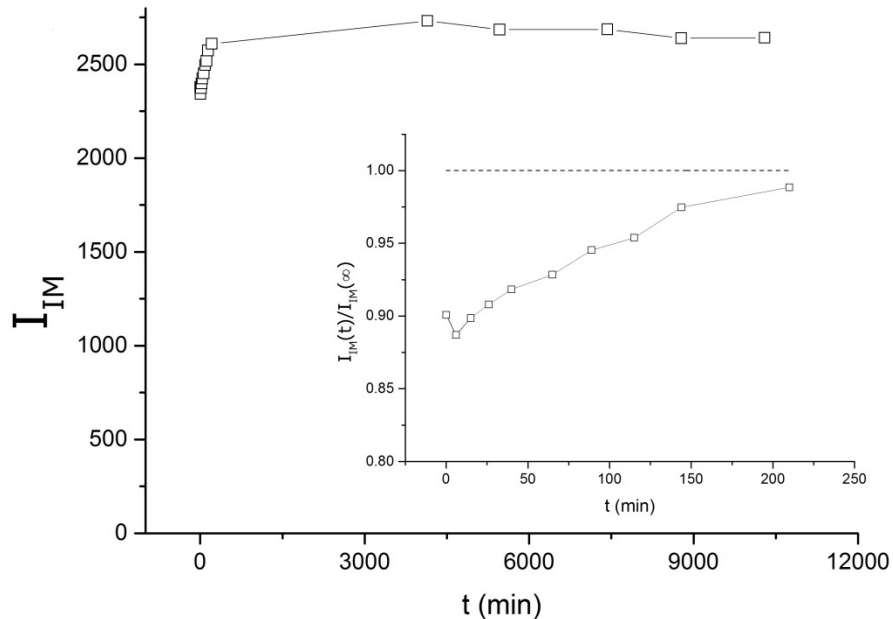


Figure 5.6. Main figure: The post-irradiation fluorescence of a reformed RFG gel kept in the dark for up to a week after irradiation. Inset: The increase in fluorescence over the first few hours after irradiation normalized by the long-time plateau value (dashed line).

The growth observed is probably due to free-radicals which remain after termination of the irradiation and undergo delayed polymerization with further MPy incorporation. It was found that continuous exposure of the irradiated sample to the UV excitation light resulted in a gradual increase of the fluorescence presumably due to the photolytic formation of free-radicals. It is important therefore to minimize UV exposure during measurements and exclude it between measurements by using a cell cover or a UV shutter system. The gels were insensitive to exposure to room (fluorescent tube) lighting but were never-the-less always stored at room temperature in the dark after a day of measurements.

### 5.3.3. The dose rate dependence

To investigate the effect of dose rate on the fluorescence intensity, a batch of four 1 cm square cells was prepared containing reformed gels with  $[MPy] = 0.57$  mM. The cells were irradiated in the gamma ray sources with and without the lead attenuator present. In this way the following dose rates were obtained: 0.54, 1.83, 7.4 and 25.3 Gy/min. The dependence of the fluorescence intensity on accumulated dose for these dose rates is shown in figure 5.7. The values of  $A_{IM}$  and  $K_{IM}$  determined from best fits according to (5.1) are listed in table 5.2. As can be seen, both parameters decrease with increasing dose rate. This will be further discussed after first considering the effects of MPy concentration.



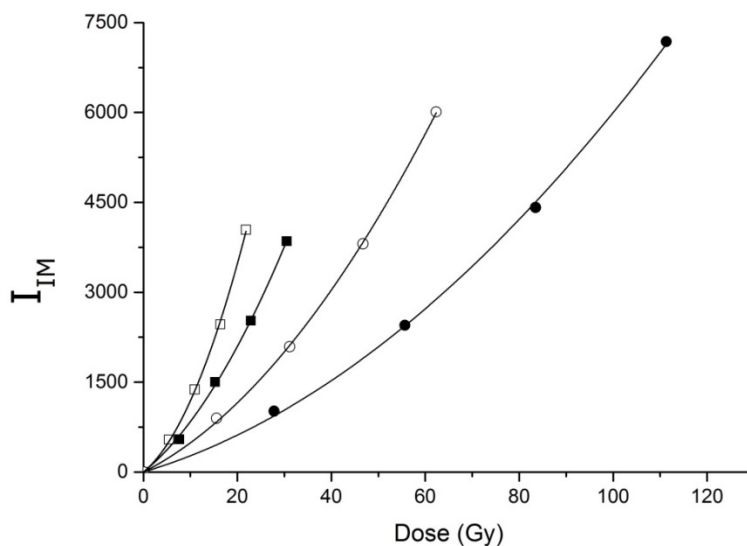


Figure 5.7. The gel fluorescence intensity,  $I_{IM}$ , plotted as a function of accumulated dose for the RFG gels ( $[MPy] = 0.57 \text{ mM}$ ) irradiated with dose rates of 0.54 (open squares), 1.83 (filled squares), 7.4 (open circles) and 25.3 (filled circles) Gy/min. The full lines are best fits to the data points according to relationship 5.1 with the corresponding values of  $A_{IM}$  and  $K_{IM}$  listed in table 5.2.

Table 5.2. The parameters  $K_{IM}$  and  $A_{IM}$  corresponding to the best-fits to the  $I_{IM}$  versus dose data in figure 5.6 for RFG gels with  $[MPy] = 0.57 \text{ mM}$ . The correction factor,  $f$ , for the combined attenuation of UV excitation light and self-absorption of the fluorescence was  $f = 1.36$ .

Dose rate (Gy/min)	$\sqrt{D'}/[MPy]$ ( $\text{Gy}^{0.5}/\text{s}^{0.5}\text{mM}$ )	$K_{IM}$ (1/Gy)	$A_{IM}$ (1/Gy)	$fK_{IM}$ (1/Gy)	$1/fK_{IM}$ (Gy)
0.54	0.167	302.4	0.0857	411.3	0.00243
1.83	0.308	300.5	0.0323	408.0	0.00245
7.42	0.620	187.3	0.0229	254.7	0.00393
25.3	1.145	110.9	0.0155	150.8	0.00663

#### 5.3.4. The MPy concentration dependence

Two sets of four RFG gels were prepared in 1 cm square cells with MPy concentrations between 0.3 and 2 mM. The concentrations were determined from optical density measurements of the gels at 365 nm. These gels were irradiated separately in GC200 and GC220 to increasing radiation doses and the increase in fluorescence intensity was measured. The values of  $I_{IM}(w/2)$ , the intensity at the middle of the gel (see figure 3.11, chapter 3), are plotted against dose in figure 5.8.

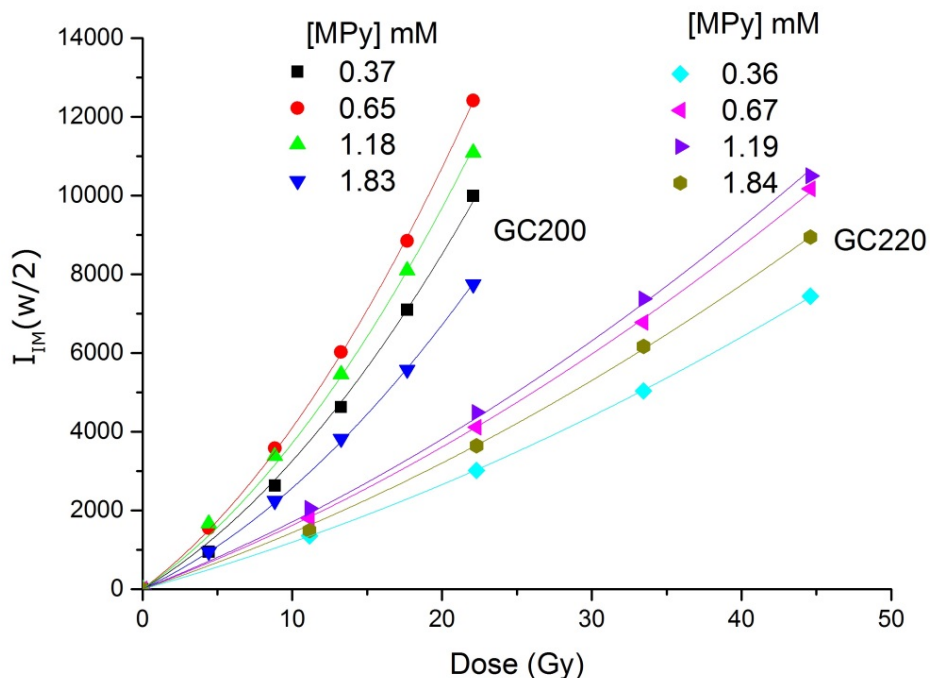


Figure 5.8. The gel fluorescence intensity,  $I_{IM}$ , plotted as a function of accumulated dose for the MPy concentrations given to the left of a given source. The full lines are best fits to the data points using equation 5.1.

The individual gel data sets in figure 5.8 have been fitted using equation 5.1 and the values of  $K_{IM}$  and  $A_{IM}$  are listed in table 5.3. The correction factors,  $f_{ex}$  and  $f_{sa}$ , for attenuation of the UV excitation light and fluorescence self-absorption are also given in the table. The ultimate corrected values  $fK_{IM}$  with  $f = f_{ex}f_{sa}$  are listed in the last column of the table. In figure 5.9 the initial and corrected values of  $K_{IM}$  are plotted against [MPy]. As for the solution data in chapter 3 (figure 3.19) the low dose intensity dependence does not display a monotonic increase with MPy concentration but rather tends to approach a saturation, plateau value even after correction. This is indicative of a negative effect of MPy on the (co)polymerization process at elevated concentrations that will be discussed in the next section.

Table 5.3. The parameters  $K_{IM}$  and  $A_{IM}$  corresponding to the best-fits to the  $I_{IM}$  versus dose data in figure 5.8. In column 5 and 6 are the correction factors,  $f_{ex}$  and  $f_{sa}$ , for the attenuation of the UV excitation light and self-absorption of the fluorescence respectively. In column 7 the correction factor  $f$  is the product of  $f_{ex}$  and  $f_{sa}$ .

D'	[MPy]	$K_{IM}$	$A_{IM}$	$f_{ex}$	$f_{sa}$	$f$	$fK_{IM}$
(Gy/min)	(mM)	(1/Gy)	(1/Gy)				(1/Gy)
1.40	0.37	187.3	0.0644	1.134	1.079	1.223	229.1
	0.65	294.1	0.0409	1.247	1.142	1.424	418.6
	1.18	300.1	0.0301	1.495	1.267	1.894	568.3
	1.83	188.9	0.0386	1.861	1.429	2.659	502.3
19.4	0.36	103.9	0.0136	1.131	1.077	1.218	126.5
	0.67	137.6	0.0146	1.254	1.145	1.436	197.6
	1.19	168.7	0.0089	1.496	1.268	1.896	319.9
	1.84	123.3	0.0142	1.867	1.432	2.673	329.7

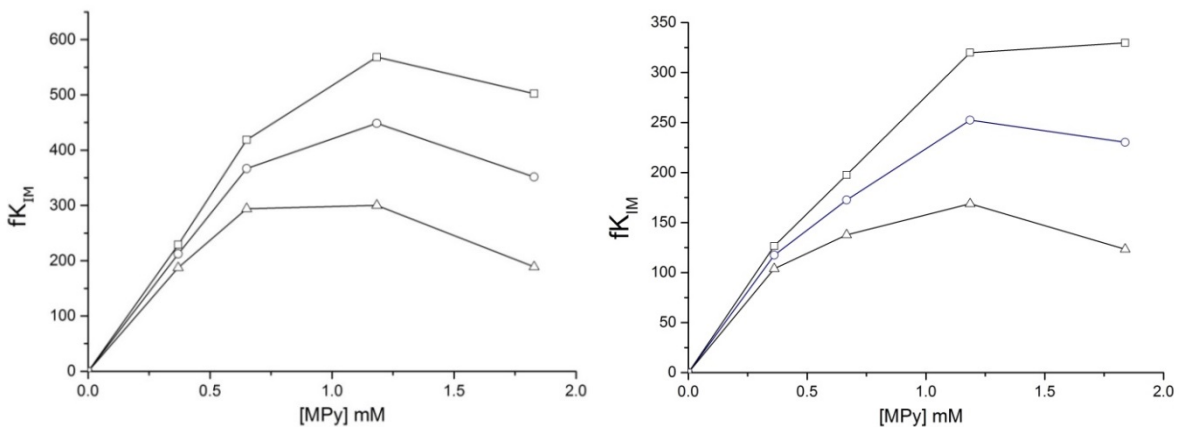
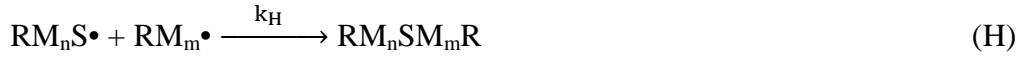
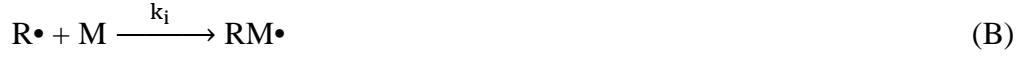


Figure 5.9. The linear dose dependence of the fluorescence at low conversions without corrections,  $f = 1$  (triangles), or with corrections for attenuation of the UV excitation light,  $f = f_{ex}$  (circles) and for self-absorption,  $f = f_{ex}f_{sa}$  (squares). Left: dose rate 1.40 Gy/min; right: dose rate 19.4 Gy/min.

### 5.3.5. Combined dose rate and MPy concentration dependences

In the following sections we consider the combined effects of dose rate and MPy concentration on the radiation-induced fluorescence of a reformed RFG gel. The gels consist of approximately 15% of a 3D matrix of PTBA, 85% monomer TBA (section 2.3.3), and approximately 0.01% MPy as the active fluorogenic component. As was shown in chapter 2, the further polymerization of monomer TBA within such a matrix appears to still occur "homogeneously" with, in the case of pure TBA, an inverse dependence on the square root of the dose rate. Homogeneous reaction

kinetics, as applied in the case of RFG solutions in chapter 3, may therefore also be assumed to apply in the present case of reformed RFG gels. The following reaction scheme is therefore taken to be also applicable.



#### 5.3.5.1. The low-conversion, linear dose dependence

The reaction scheme given above contains no secondary reactions that may result from radiation-induced products or physical changes of the medium. Kinetic solutions of A through H refer therefore to the limiting (low conversion), linear dose dependence given by the parameter  $fK_{IM}$ . Accordingly, as for the solutions in chapter 3, the fluorescence intensity will be proportional to the concentration of fluorogenic solute molecules that have been incorporated into polymer chains, i.e.  $[M_nS\bullet]$ . This is,

$$fK_{IM} = C[M_nS\bullet] = Ck_E[S](\Gamma/2k_tD')^{0.5}D/(1 + k_E[S]/(2k_t\Gamma D')^{0.5}) \quad (5.2)$$

In (5.2)  $\Gamma$  is the yield of free radicals in moles per liter per gray which is equal to  $\rho g(R\bullet)$  with  $\rho$  the density of the medium in kg/L and  $g(R\bullet)$  the radiolytic yield of free radicals in mol/joule.  $C$  is the "sensitivity" factor for fluorescence detection.

Substitution for  $E = k_E/(2k_t\Gamma)^{0.5}$  in (5.2) and rearrangement gives,

$$1/fK_{IM} = (1 + \sqrt{D'/E[S]})/C\Gamma \quad (5.3)$$

According to (5.3) it should be possible to unify all of the dose rate *and* concentration dependent data in a linear plot of  $1/fK_{IM}$  against the square root of the dose rate divided by the solute concentration  $[S]$ . Such a plot of the combined data from figures 5.4, 5.7 and 5.8 (tables 5.1, 5.2 and 5.3) is shown in figure 5.10. While there is considerable scatter, the data are quite well described by the straight line drawn in the figure.

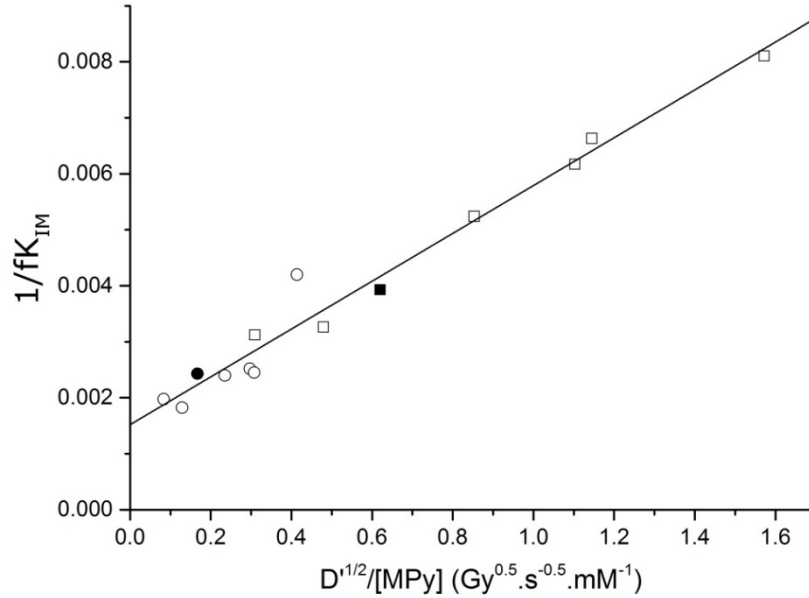


Figure 5.10. A plot of the reciprocal of  $fK_{IM}$  against  $\sqrt{D'}/[MPy]$ , from the data in figures 5.4, 5.6 and 5.7 (tables 5.1, 5.2 and 5.3), which according to equation (5.3) should be linear. The symbols refer to irradiations carried out using GC200 (circles) or GC220 (squares) without (open symbols) or with (filled symbols) the lead attenuator.

The best linear fit to the combined data gives  $C\Gamma = 606 \text{ pixel-level.s}^{-1}.\text{Gy}^{-1}$  and, from the intercept/slope  $E = 0.41 \text{ s}^{0.5}.\text{mM}^{-1}.\text{Gy}^{-0.5}$ . These values are to be compared with those of  $C\Gamma = 524 \text{ pixel-level.s}^{-1}.\text{Gy}^{-1}$  and  $E = 0.45 \text{ s}^{0.5}.\text{mM}^{-1}.\text{Gy}^{-0.5}$  determined for the RFG solution measurements in chapter 3 (see section 5.2.3. for differences in the sensitivity factor C). An increase by 16% in the free radical yield,  $\Gamma = \rho g(R\bullet)$  moles per liter per gray, in going from the solution to the gel is indicated. This can in part be attributed to the 6% higher density of the gel. The remaining 10% indicates a slightly higher free-radical formation rate in the reformed gel. The decrease by approximately 10% in the parameter  $E = k_E/(2k_t\Gamma)^{0.5}$ , can be ascribed mainly to the 16% increase in  $\Gamma$ .

### 5.3.5.2. The superlinear dependence on dose

The superlinear dependence of the fluorescence intensity of an RFG gel on dose is thought to be due to an increase in viscosity of the medium on polymer formation that results in a decrease in the diffusion-controlled radical recombination rate coefficient. The effect is expressed by the  $A_{IM}$  factor in equation 5.1. As can be seen from the data in tables 5.2 and 5.3 there is a general tendency for  $A_{IM}$  to decrease with increasing MPy concentration and with increasing dose rate. This tendency agrees with the explanation of the effect given above since for a given dose an increase in both  $[MPy]$  and  $D'$  results in a decrease in the degree of polymerization,  $C_M$ , which is given by,

$$C_M([S]) = k_p(\Gamma/2k_tD')^{0.5}D/(1 + k_E[S]/(2k_t\Gamma D')^{0.5}) \quad (5.4)$$

$A_{IM}$  might therefore be expected to obey the following relationship to a first approximation,

$$A_{IM} \propto k_p\Gamma/k_E[S](1 + \sqrt{D'/E[S]}) \quad (5.5)$$

which on rearrangement gives,

$$1/A_{IM}[S] \propto k_E(1 + \sqrt{D'/E[S]})/k_p\Gamma \quad (5.6)$$

Accordingly  $1/A_{IM}[\text{MPy}]$  is plotted against  $\sqrt{D'}/[\text{MPy}]$  in figure 5.11 and while the data are admittedly very scattered there does appear to be a correlation with an approximate linear dependence given by the straight line drawn.

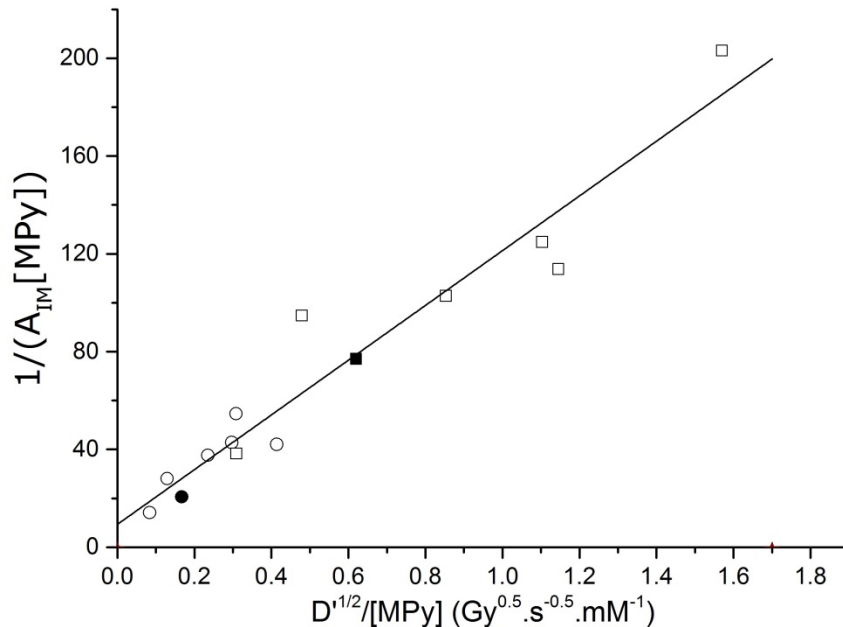


Figure 5.11. A plot of the reciprocal of the product  $A_{IM}[\text{MPy}]$  against  $\sqrt{D'}/[\text{MPy}]$ , from the data in figures 5.4, 5.6 and 5.7 (tables 5.1, 5.2 and 5.3), which according to equation (5.6) should be linear. The symbols refer to irradiations carried out using GC200 (circles) or GC220 (squares) without (open symbols) or with (filled symbols) the lead attenuator.

## 5.4. Conclusions

A rigid gel matrix consisting of 15% polymerized tertiary-butyl acrylate (TBA) containing millimolar concentrations of the fluorogenic compound maleimido-pyrene (MPy) can be

prepared by reformation (swelling) of a pre-prepared TBA polymer matrix using a dilute solution of MPy in TBA. The reproducibility of the MPy concentration, as measured by the optical density of a batch of 9 gels, is better than 3%. The gels are radio-fluorogenic with negligible fluorescence when freshly prepared but have a readily measureable fluorescence in UV light after exposure to high-energy radiation with doses of a few gray. A post irradiation growth of approximately 10% in the fluorescence intensity occurs over the first few hours after which it remains constant within 3% for up to at least 1 week.

The fluorescence intensity,  $I_{IM}$ , measured using raw DNG files from a digital CCD camera and analyzed using ImageJ, increases with radiation dose superlinearly and obeys the relationship

$$I_{IM} = (1 + A_{IM}D)K_{IM}D \quad (5.1)$$

The dependence of the  $A_{IM}$  and  $K_{IM}$  parameters on dose rate and MPy concentration have been measured and tabulated. The value of  $K_{IM}$  measured has to be corrected by a factor  $f$  for the attenuation of the UV excitation light in the gel and for the self-absorption of the fluorescence. The low conversion, limiting linear dose dependence represented by  $fK_{IM}$  is found to increase with MPy concentration but approaches a plateau at the highest concentrations. This behavior is attributed to the chain terminating effect of MPy, evidence for which was previously found in the solution measurements in chapter 3. Accordingly,  $fK_{IM}$  is found to obey relationship (5.3) which predicts a linear dependence of  $1/fK_{IM}$  on  $\sqrt{D'}/[MPy]$  as is found.

$$fK_{IM} = C\Gamma/(1 + \sqrt{D'}/E[MPy]) \quad (5.3)$$

In (5.3)  $C\Gamma$  is proportional to the yield of free radicals  $\Gamma$  in moles per litre and  $E$  is a constant reflecting the competition between chain termination by MPy and radical-radical recombination. Using (5.3) data with different dose rates and different MPy concentrations can therefore be unified.

It is suggested that the superlinearity in the monomer conversion and the intensity of the fluorescence is due to an increase in viscosity of the medium on polymerization resulting in a decrease in the rate of (diffusion-controlled) radical-radical recombination. Assuming as a first approximation  $A_{IM}$  to be proportional to the low conversion yield of polymer results in the relationship,

$$A_{IM} \propto k_p\Gamma/k_E[S](1 + \sqrt{D'}/E[MPy]) \quad (5.5)$$

An approximate linear relationship between  $1/A_{IM}[S]$  and  $\sqrt{D'}/[MPy]$  as expected on the basis of (5.5) is in fact found.

## References

Kattan, M., Al-Kassiri, H., 2010. Radiation-induced polymerization of butyl acrylate for recovery of organic solvents. *Journal of Applied Polymer Science* 115, 3623-3627.

Warman, J.M., de Haas, M.P., Luthjens, L.H., 2011a. High-energy radiation monitoring based on radio-fluorogenic co-polymerization II: fixed fluorescent images of collimated X-ray beams using an RFCP gel. *Physics in Medicine and Biology* 56, 1487-1508.

Yao, T., Denkova, A.G., Warman, J.M., 2014. Polymer-gel formation and reformation on irradiation of tertiary-butyl acrylate. *Radiation Physics and Chemistry* 97, 147-152.





## Chapter 6

# The dose and dose-rate dependences of four radiochromic films currently used for (2D) radiation dosimetry<sup>5</sup>

### 6.1. Introduction

Radiochromic (RC) films undergo a permanent change in color (absorption spectrum) on exposure to high-energy radiation. Most of the color change is immediate, with a slower, post-irradiation change that can continue for days (Klassen et al, 1997). A post-irradiation chemical development process, which is required for the silver-halide-based radiographic films used in early film-dosimetry measurements (Ehrlich, 1954; Dudley, 1956; Dutreix and Dutreix, 1969), is not necessary. This advantage, together with their near tissue equivalence and relative insensitivity to the nature of the high-energy radiation used, has resulted in radiochromic films becoming increasingly accepted within the clinical physics radiotherapy community, particularly in applications where high spatial dose resolution is required (Metcalf et al, 1993; McLaughlin

---

<sup>5</sup> This chapter has been accepted by Radiation Physics and Chemistry in 2016 for Publication.

et al, 1996; Valnitsky, 1997; Niroomand-Rad et al, 1998; Shiomi et al, 2000; Butson, M.J. et al, 2003; Zeidan et al, 2004; Cheung et al, 2006; Soares, 2006, 2007; Devic, 2011; Palmer et al, 2013). This acceptance is due largely to the introduction of the GafChromic solid-state-polymerization-based films in the late 1980's. These were initially adopted for industrial applications in equipment sterilization and food-irradiation dosimetry in the 100 Gy to several kGy region (Saylor et al, 1988; McLaughlin et al, 1988, 1991; Chu et al, 1990). Since then many improvements in film quality and sensitivity have been made and a choice of films covering the cGy to kGy range is now available (<http://www.gafchromic.com/gafchromic-film/radiotherapy-films/index.asp>). Extensive reviews of the subject with advisory protocols for applications have regularly appeared (Klassen et al, 1997; Niroomand-Rad et al, 1998; Butson, M.J. et al, 2003; Devic et al, 2005; Lynch et al, 2006; Soares, 2006, 2007; Matney et al, 2010; Borca et al, 2013; Papaconstadopoulos et al, 2014).

A development that has increased the general applicability of radiochromic films has been the advent of flat-bed scanners capable of producing highly-uniform, full-color, digital images of films with high spatial resolution. The use of such scanners however involves several potential sources of error, which have been the subject of much debate and recommendations (Devic et al, 2004, 2005; Lynch et al, 2006; Soares, 2007; Matney et al, 2010; Papaconstadopoulos et al, 2014; Lewis and Chan, 2015). The place of radiochromic film within the overall arsenal for dose monitoring of high-energy radiation is outlined in the extensive reviews by Low et al, 2011 and Hill et al, 2014.

The continuing development of revised film formulations and structures has led to a somewhat bewildering list of code names for films past and present covering dose ranges from cGy to kGy. We are particularly interested in the range of a few Gray to tens of Gray, since this is the range used for creating 3D dose images using our radio-fluorogenic (RFG) gel method (Warman et al, 2011a,b; 2013a, Yao et al, 2015). Our interest in radiochromic films arises from the suggested dose rate *independence* compared with the intrinsic dose rate *dependence* of an RFG gel, which was illustrated in the previous chapters. We envisage being able to derive quantitative 3D dose distributions of complex radiation fields by combining the two methods. To this end we have carried out a thorough study of the dose and dose rate dependences of GafChromic films with sensitivities in the 1 to 100 Gy range. These are at the time of writing EBT3, MD-V3, HD-V2 and HD-810. The last is still in use but is no longer supplied.

## 6.2. Materials and Methods

### 6.2.1. Radiochromic films

The four GafChromic films studied were obtained from Promis Electro-Optics B.V. (PEO): “EBT3” Lot Nr A04041202; “MD-V3” Lot Nr A03051201; “HD-810” Lot Nr R2507H810; “HD-V2” a single sample sheet of unknown Lot number. The type HD-810 is no longer in

production and has been replaced in the product range for high dose measurements by HD-V2. Apart from HD-810, which has initially a light-blue hue, the films were yellow, turning to green and eventually dark blue on exposure, as shown by the full-color images of MD-V3 film in figure 6.1.

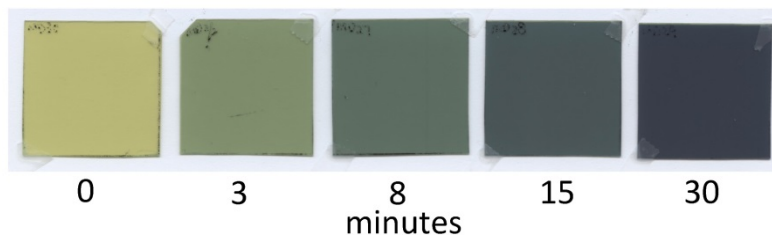


Figure 6.1. Full color images, in reflection on a white background using an EPSON V700 flatbed scanner, of 20x20 mm<sup>2</sup> MD-V3 film samples irradiated in a cobalt-60 gamma-ray source at *ca* 2 Gy/min for the exposure times shown.

The films were stored in the dark at 5 °C when not in use. The preparation and irradiation of film samples took place after equilibration at room temperature. Exhaustive technical, operational and performance information on the films is available on the website of the supplier: <http://www.gafchromic.com/gafchromic-film/radiotherapy-films/index.asp>.

## 6.2.2. Irradiation

### 6.2.2.1. 200 kVp X-rays

The X-ray source used was a Philips MCN 321 variable-energy X-ray tube with a 4 mm square, tilted tungsten target and a 4 mm thick beryllium exit window. No X-ray filter plate was inserted into the filter holder adjacent to the exit window. In the present experiments an accelerating voltage of 200 kV was used with a maximum e-beam current of 15 mA.

The dose rate,  $D'$  Gy/min, was measured routinely using a 35 cm<sup>3</sup>, atmospheric-air ionization chamber, IC, ("37D X-ray Exposure Meter" D.A. Pitman Instruments Ltd [now Vinten Instruments Ltd]) that was annually calibrated (Dutch Metrology Institute). The IC was mounted on an optical rail in line with the X-ray beam. An alignment laser (Laserglow Technologies, "Galileo PRO") was used to position the beam at the centre of the IC. The dose rates at source-to-surface distance (SSD) 50 and 100 cm were routinely measured and were close to 1.0 and 0.25 Gy/min respectively for the maximum, 15 mA, beam current. As shown in section 6.3.2.1, there was effectively a delay of 2.1 seconds in reaching the equilibrium dose rate based on the current and voltage settings. This delay was subtracted from the time set on the exposure auto-timer in order to determine the dose from the value of  $D'$ , the long-time equilibrium value measured using the IC.

The RC films were exposed with an interposed beam collimator. The collimator was a 120x120 mm square, 27 mm thick sandwich of Al(3 mm)/Pb(21 mm)/Al(3 mm) with a central 10.0 mm square aperture. This was mounted in a holder on the optical rail and the aperture was aligned with the centre of the X-ray beam using the alignment laser. Film samples (20x20 mm<sup>2</sup>) were taped across the aperture on the distal side of the collimator. During irradiation of the film the ionization chamber was raised above the collimator and was used simply to monitor the beam stability.

#### 6.2.2.2. <sup>60</sup>Co 1.17 and 1.33 MeV $\gamma$ -rays

Two <sup>60</sup>Co  $\gamma$ -ray sources were used: a GC200 (Atomic Energy of Canada) and a GC220 (Nordion) with dose rates, measured by Fricke dosimetry (Klassen et al, 1999, McEwen et al, 2014) of ~2 and ~30 Gy/min respectively during the period of the present measurements. The actual dose rate on a given date was adjusted for the natural 2,778 days exponential decay (5.27 year half-life) of <sup>60</sup>Co. The irradiation chambers were cylindrical with diameter/height dimensions in mm of 85/115 and 110/200 respectively. They are illustrated in figures 2.4 and 2.5 in chapter 2.

For irradiation, 20 mm square film samples were sandwiched between PMMA blocks at least 5 mm thick and placed centrally in the chamber of a gamma ray source. The exposure of the samples was determined by the time,  $t$ , set on the auto-timer of the source. The timer is triggered by a micro-switch that is tripped on complete insertion of the chamber. With such mechanically loaded sources there is invariably an effective “transit time”,  $\Delta t$ , during which the sample is exposed to radiation both prior to and subsequent to complete insertion. This transit time must be added to the set time to obtain the total dose absorbed. The method of linear back-extrapolation used to determine  $\Delta t$  is presented in section 6.3.2. The values determined for GC200 and GC220 were  $9.3 \pm 0.7$  s and  $4.9 \pm 0.4$  s respectively. These times correspond to additional doses of ~0.3 Gy and ~2 Gy respectively for each insertion and removal procedure in GC200 and GC220 respectively.

### 6.2.3. *Digitalization and quantification*

#### 6.2.3.1. Flatbed scanning

The reader is referred to the extensive literature on the preparation, procedures and potential sources of error associated with radiochromic film scanning and dosimetry (Devic et al 2004, 2005; Lynch et al, 2006; Soares, 2006, 2007; Matney et al, 2010; Borca et al, 2013; Papaconstadopoulos et al, 2014; Schoenfeld et al, 2014; Mathot et al, 2014; Huet et al, 2014; Dreindl et al, 2014; Lewis and Chan, 2015). Some discussion exists as to the best mode of monitoring changes in optical density of films using flatbed scanners: in transmission mode, as suggested by the film manufacturer and applied by many past and present users; or in reflection

mode which has received more attention recently (Butson E. et al, 2011; Kalef-Ezra et al, 2008; Mendez et al, 2014; Farah et al, 2014; Papaconstadopoulos et al, 2014).

We have used an Epson V700 flatbed scanner to provide digitalized, 48-bit RGB images of the films. The scanner could be used in either transmission or reflection mode. In the former the light transmitted by a film placed on the glass plate of the scanner is recorded. In the latter mode, which was used exclusively to obtain the data presented in this report, the film samples were mounted on an A4 sheet of matt, white paper and images were recorded in the "copy" mode. The reflectivity of the paper used was  $93.8 \pm 0.8\%$  over the full A4 width for both red and green pixels. The pixel noise bandwidth at 300 dpi was less than 0.02%. The use of the reflection mode with a white paper backing had the added advantages of well-defined positional mounting of the film samples and ease of archiving multiple-sample series. This method was actually suggested some time ago by Butson, E. et al, 2011 as a procedure free of the lateral distortions found using the transmission method (Lewis and Chan, 2015). We confirm their conclusion (see section 6.2.3.2).

In agreement with other studies (Klassen et al, 1997), an increase of a few percent in the optical density of the films was found to occur within a day or two of being irradiated. To allow for this, only data from scans taken at least 48 hours after irradiation are included in the present analysis. In applications where *spatially-resolved*, relative dose imaging takes priority over *quantitative dosimetry*, radiochromic film can be used as a fast-feedback (minutes), medium (Rink et al, 2005a,b). Real-time, *in-situ* monitoring using radiochromic film for complex radiation fields is however made difficult by the *ex-situ* optical scanning and data analysis procedures required.

#### 6.2.3.2. Image analysis using ImageJ

The full color, 48 bit TIFF output files from the scanner were imported into the, freely downloadable, National Institutes of Health software program ImageJ (<http://rsb.info.nih.gov/ij/download.html>). The RGB files were split into the separate 16-bit red, green and blue pixel images and the mean pixel level,  $P$ , within a defined area of the film (usually *ca*  $10 \times 10 \text{ mm}^2$ ) was then determined. In addition to the values for a given radiation dose,  $P(D)$ , a measurement was made of an unirradiated film sample,  $P(0)$ , cut from the same sheet.

To test the uniformity of the scanning procedure we have carried out the following measurements: ten  $20 \times 20 \text{ mm}^2$  samples of EBT3 were cut from a single sheet. Five were irradiated separately in exactly the same position within the cavity of the GC200 source with a dose of 1.84 Gy and five were left unirradiated. The five samples were taped in place across the width of an A4 sheet of white paper with the outermost films placed close to the edges, as shown in figure 6.2. A scan across the irradiated films at 300 dpi (118 pixels/cm) is also shown in the figure.

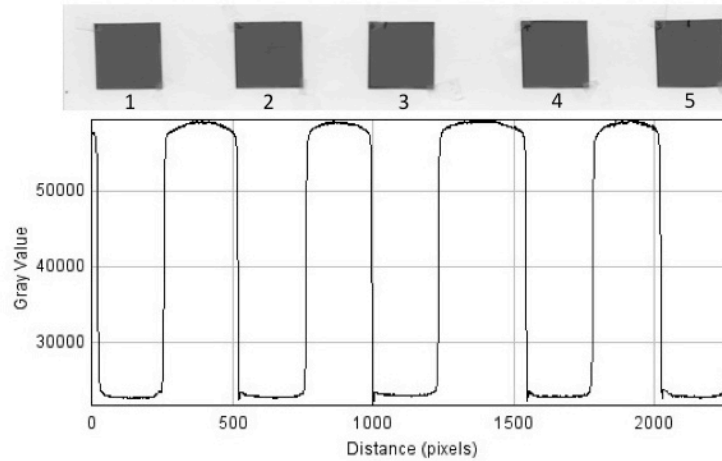


Figure 6.2. Upper: The positioning of the 5 identically irradiated, 20x20 mm<sup>2</sup> EBT3 films across the full 210 mm width of an A4 sheet of white paper. Lower: A scan at 300 dpi across the films of the 16-bit gray values of the red pixels. The gray value is equivalent to the "pixel level", P, which is used in the text to prevent confusion with gray, Gy, used as the unit of radiation dose.

The "red" pixel levels of the irradiated films, P(D), at the different positions numbered from left to right, are given in table 6.1. Also given are the values of P(0) determined for the unirradiated films and the corresponding values of P(D)/P(0). The absolute pixel values and the P(0)-normalized values are all within 1% of their average values. No evidence is found for film inhomogeneity or the lateral edge effects found using the transmission method (Lewis and Chan, 2015). A further test in which a single irradiated film (#3) was placed at the different lateral positions (data also given in table 6.1) showed deviations of P(D)/P(0) from the average to be within  $\pm 0.5\%$ .

Table 6.1. Red channel pixel levels for five unirradiated EBT3 films, P(0), and 5 irradiated films, P(D) with D = 1.84 Gy, placed across an A4 sheet of white paper as shown in figure 6.2.

<b>Position L&gt;R</b>	<b>1</b>	<b>2</b>	<b>3</b>	<b>4</b>	<b>5</b>	<b>average</b>
Film nr.	6	7	8	9	10	
P(0)	41092	41260	41256	41377	41459	41289
Film nr.	1	2	3	4	5	
P(D)	22763	22832	23057	22868	22913	22887
P(D)/P(0)	0.554	0.553	0.559	0.553	0.553	0.554
Film nr.	3	3	3	3	3	
P(D)	22955	23021	22980	22986	23022	22993
P(D)/P(0)	0.559	0.558	0.557	0.556	0.555	0.557

### 6.2.3.3. Parameterization of the P(D) data

The film supplier suggests in the "user guidelines" that the relationship,

$$P(D) = [a + bD]/[c + D] \quad (6.1)$$

provides a good fit to the dose dependence of the raw pixel data for GafChromic films. We have confirmed that (6.1) does indeed give a good description of the data for the four films studied in the present work. We have therefore adopted the same basic relationship but prefer the following form, in terms of the normalized variable P(D)/P(0) with P(0) the pixel level for the unirradiated film,

$$P(D)/P(0) = (1 + hD/m)/(1 + D/m) \quad (6.2)$$

This form has the advantage that **h** and **m** have meaningful significance: **h** (= **bc/a** in 6.1) is the plateau level, P( $\infty$ )/P(0), approached at "infinite" dose, and **m** (= **c** in 6.1) Gy is the "median dose", *i.e.* the dose for which P(D)/P(0) = (1 + **h**)/2, the half-value of the 1 to **h** dynamic range of P(D)/P(0). The use of **m** and **h** facilitates quantitative comparisons between different batches or types of film, and between different measurement techniques or dosimetry groups.

The fact that **h** values larger than zero are found, can be ascribed to the ultimate degree of polymerization of the diacetylene micro-crystals achieved by irradiation being less than 100% [Chance et al, 1979]. This can also be due, partly, to the presence of the radiation-insensitive, yellow "marker" dye in the more recent films. In this regard it is worth pointing out that for the (discontinued) HD-810 film, which contains no marker dye, **h** is found to be closer to zero.

Rearrangement of 6.2 yields the following relationship for determining the value of an unknown dose from a single normalized pixel value.

$$D_{\text{calc}} = m[1 - P(D)/P(0)]/[P(D)/P(0) - h] \quad (6.3)$$

When used as a 3D dosimetric medium for complex radiation fields, it is the *dose rate* at a particular point in space that is of interest. If **m** and **h** are dose rate independent, the (unknown) dose rate is obtained by simply dividing 6.3 by the time of exposure to the radiation, **t<sub>ir</sub>**.

$$D'_{\text{calc}} = m[1 - P(D)/P(0)]/[P(D)/P(0) - h]/t_{\text{ir}} \quad (6.4)$$

For practical applications, it is therefore important to know whether **m** and **h** are in fact independent of the *nature* and the *dose rate* of the high-energy radiation used. Determining this dependence, or lack of it, is a principal aim of the present study. A secondary problem, pertinent to highly sensitive dosimeters, is that of the value of **t<sub>ir</sub>**, which is not necessarily equal to the



exposure time set on the auto-timer of the source. This is dealt with for the present sources in section 6.3.2.

The results of radiochromic film measurements are often discussed in terms of the *netOD* rather than the primary  $P(D)/P(0)$  data. According to Beer's Law, the intensity of light,  $I$ , after passing through an absorbing medium of optical density,  $OD$ , is given by,

$$I/I_0 = 10^{-OD} \quad (6.5)$$

In (6.5)  $I_0$  is the incident light intensity. Accordingly the ratio of the intensity of light passing through an *irradiated* radiochromic film to that for the film prior to irradiation is,

$$I(D)/I(0) = P(D)/P(0) = 10^{-[OD(D) - OD(0)]} \quad (6.6)$$

Defining  $[OD(D) - OD(0)]$  as the *netOD* results in the following relationship,

$$\text{netOD} = \text{Log}_{10}[P(0)/P(D)] \quad (6.7)$$

The netOD is equal to the product of the concentration of the absorbing radiolytic product ( $c$  mol.L<sup>-1</sup>), its extinction coefficient ( $\epsilon$  L.mol<sup>-1</sup>.cm<sup>-1</sup>) and the path length ( $\lambda$  cm).

We see no particular advantage in using the netOD for dosimetry purposes over the primary, untransformed  $P(D)/P(0)$  data. The latter is used exclusively therefore in the following sections. Curve fitting using "Origin" software was used to derive best-fit **m** and **h** values using 6.2. The standard deviation,  $\sigma$ , of the median dose was also determined.

## 6.3. Results and Discussion

### 6.3.1. Color-separated pixel data

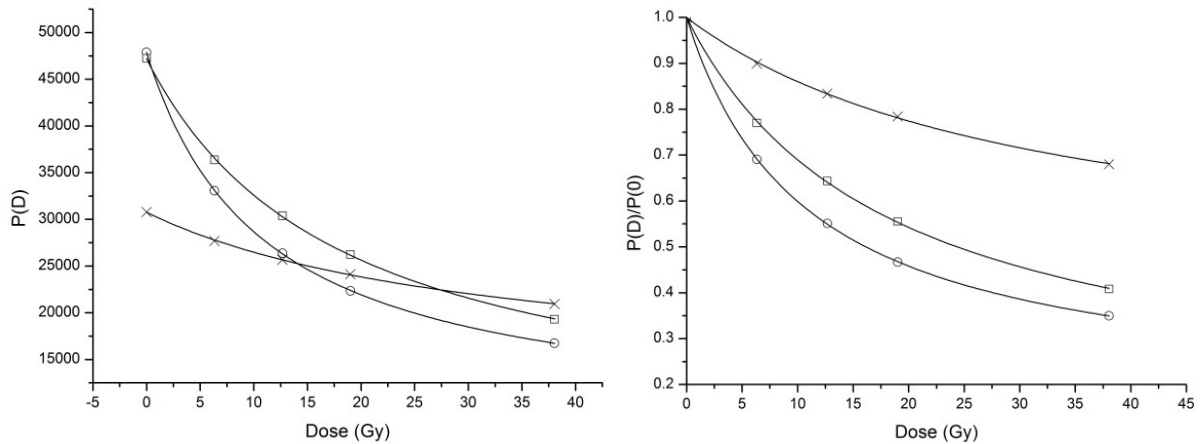


Figure 6.3. Left: the dose dependences of the red (circles), green (squares) and blue (crosses) pixel levels,  $P(D)$ , on irradiation of MD-V3 film with 200 kVp X-rays at *ca* 1 Gy/min. Right: the pixel levels normalized by the zero dose value. The full lines are best fits using equation 6.2.

As mentioned in section 6.2.3.2, the individual red, green and blue pixel levels can be separated using ImageJ. In figure 6.3 is shown the difference in dose dependence of the three color bands ( $P_R$ ,  $P_G$  and  $P_B$ ) and the normalized values,  $P(D)/P(0)$ , for an X-ray irradiated MD-V3 film. The plots are characteristic of all four films with the highest sensitivity for the red pixels, somewhat lower for the green, and even lower for the blue, as has generally been found. The values of  $\mathbf{m}$  ( $\mathbf{h}$ ) corresponding to the best-fit lines drawn in figure 6.3 for  $P_R$ ,  $P_G$  and  $P_B$  pixels respectively are 11.0 Gy (0.173), 18.6 Gy (0.130), and 31.8 Gy (0.414).

The large value of  $\mathbf{h}$  for the blue pixels ( $>0.4$ ) is characteristic of all film types tested and results in a relatively small dynamic range of  $P(D)/P(0)$  values. Therefore, only data using the red and green pixels are reported in subsequent sections.

### 6.3.2. Start-stop dose corrections

The dose delivered to a medium by a source of radiation is determined by the duration of the irradiation multiplied by the dose rate. Most often irradiations are carried out on timescales for which the dose rate can be taken to be constant and the value of  $D'$  is taken to be that reached long after any initial relaxation processes have taken place. When dealing with high-sensitivity, cumulative dosimeters however, the time between initiating the irradiation procedure and achieving the steady state condition can be of the same order as the "exposure time",  $\mathbf{t}$ , set on the source timer. This can result in the dose delivered being different to that given by  $\mathbf{t}D'$ . This error can be expressed in terms of an effective delay time  $\Delta\mathbf{t}$ , which can be positive or negative depending on the start-stop method of controlling the radiation source. The dose delivered for a set exposure time  $\mathbf{t}$  is then given by  $[\mathbf{t} + \Delta\mathbf{t}]D'$ .

The value of  $\Delta\mathbf{t}$  can be determined by considering a rearranged version of (6.4) with  $[\mathbf{t} + \Delta\mathbf{t}]$  substituted for  $\mathbf{t}_{ir}$ , and  $P_0$  the level for the unirradiated film,

$$[1 - P(t)/P_0]/[P(t)/P_0 - h] = F(t) = D'[t + \Delta t]/m \quad (6.8)$$

A plot of the function  $F(t)$  against the set exposure time,  $t$ , should therefore be linear with an intercept on the  $t$  axis of  $-\Delta t$  at  $F(t) = 0$ . Results of such plots made on timescales of seconds, as expected for the delay times involved, are shown below for the X-ray and  $\gamma$ -ray sources. The values of  $h$  used were those determined from data extending to much longer timescales which are presented in section 6.3.3.

The value of  $\Delta t$  corresponds to an additional dose of  $\Delta t D'$  Gy and any error in the determination of  $\Delta t$  will result in a systematic offset error in dose and hence in the value of  $m$  determined. This plays a particularly important role for the GC220 measurements for which an error of just 0.2 seconds in  $\Delta t$  corresponds to an error in dose, and hence  $m$ , of approximately 0.1 Gy. This is discussed further below.

#### 6.3.2.1. The X-ray source on-off delay time

In the case of the X-ray source, pressing the "start" button initiates the increase of the electron beam current and beam voltage to their equilibrium, set values. After the set exposure time  $t$  the current and voltage are turned off and decrease back to zero. This rise and fall can result in an effective delay time,  $\Delta t$ , in the development of the steady state dose rate and hence in a dose different to  $tD'$  with  $D'$  the equilibrium value determined using the ionization chamber. This is particularly important for short exposures with highly sensitive cumulative dosimeters such as EBT3 film.

The values of  $P(t)/P_0$  for EBT3 film irradiated with 200 kVp X-rays for time settings of 5 to 25 seconds are listed in table 6.2 together with the corresponding values of  $F(t)$  using  $h = 0.190$  and  $0.098$  for red and green pixels respectively as determined from longer exposure measurements (see figure 6.6).  $F(t)$  is plotted against  $t$  in figure 6.4. A straight line fit to the data gives, from the intercept at  $F(t) = 0$ ,  $\Delta t = -2.09 \pm 0.34$  s and  $-2.22 \pm 0.41$  s for the red and green pixel data respectively. A deduction in the set exposure time of 2.1 seconds has therefore been applied for each separate start-stop exposure. For an equilibrium dose rate of 1 Gy/min (15 mA at SSD 50 cm) this corresponds to the subtraction of 0.035 Gy with a systematic offset error in  $m$  of  $\pm 0.007$  Gy.

Table 6.2. The dependence of the normalized pixel level,  $P(t)/P_0$ , on the set exposure time,  $t$ , for EBT3 film ( $h = 0.190$  red,  $0.098$  green) in the 200 kVp, 15 mA X-ray beam (SSD = 50 cm) and the GC200  $\gamma$ -ray source, and for MD-V3 film ( $h = 0.182$  red,  $0.136$  green) in the GC220  $\gamma$ -ray source.

film/source	$t$ (s)	$P(t)/P_0$		$F(t)$	
		red	green	red	green
EBT3/200kV <sub>p</sub> X-ray	5	0.973	0.981	0.034	0.022
	10	0.933	0.954	0.089	0.054
	15	0.901	0.929	0.137	0.086
	20	0.862	0.898	0.202	0.127
	25	0.834	0.874	0.254	0.162
EBT3/GC200 $\gamma$ -ray	1	0.861	0.895	0.205	0.134
	3	0.835	0.875	0.252	0.161
	5	0.814	0.858	0.293	0.186
	7	0.803	0.849	0.317	0.201
	9	0.778	0.826	0.371	0.238
	11	0.757	0.808	0.421	0.270
	13	0.746	0.801	0.448	0.283
MD-V3/GC220 $\gamma$ -ray	2	0.836	0.890	0.247	0.146
	4	0.802	0.864	0.314	0.185
	6	0.767	0.837	0.392	0.230
	8	0.735	0.811	0.471	0.278
	10	0.715	0.794	0.526	0.310

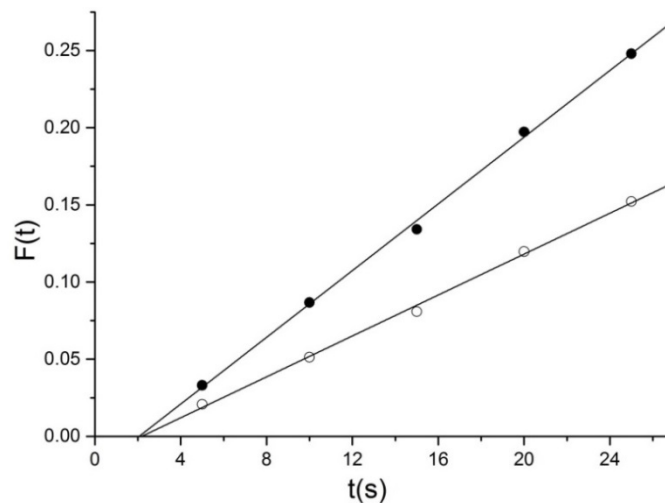
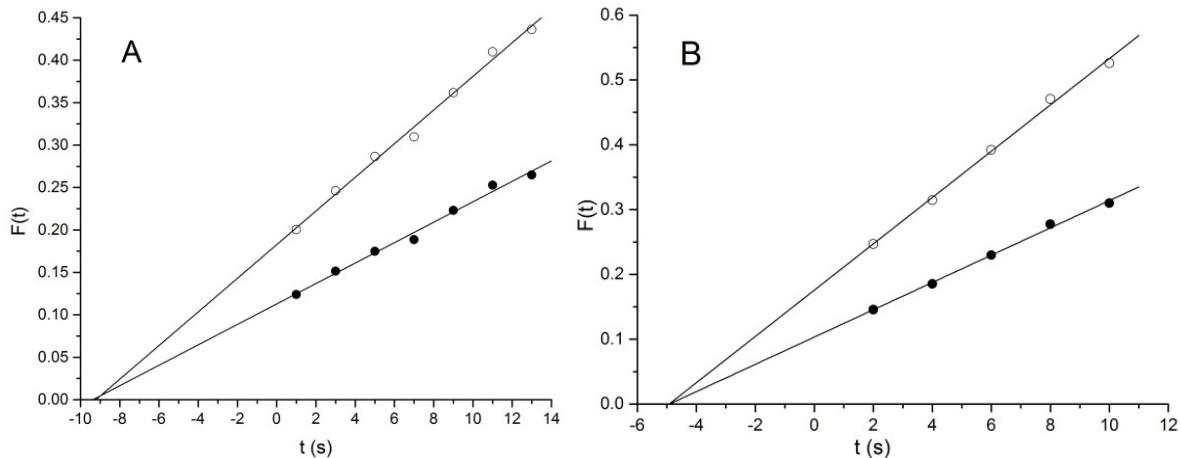


Figure 6.4. Plots of the function  $F(t)$ , defined in (6.8) and listed in table 6.2, for the EBT3 film in the X-ray beam against the set exposure time for red pixels (filled circles) and green pixels (open circles). The lines are linear best fits to the data points as expected according to (6.8) with intercepts corresponding to  $\Delta t = -2.09$  s and  $-2.22$  s respectively.

### 6.3.2.2. The $^{60}\text{Co}$ $\gamma$ -ray sources transit times

In the case of the cobalt sources, pressing the start button initiates mechanical transport of the sample to the "hot" region of the source. On complete insertion a micro-switch is tripped starting the timer. This mechanical loading results in a "transit time",  $\Delta t$ , during which the sample is exposed to radiation prior and subsequent to full insertion for the set-time  $t$ . We have determined the value of  $\Delta t$  for the two cobalt sources by measuring the change in absorption of film samples that display a measurable change for times of a few seconds, *i.e.* of the order expected for  $\Delta t$ . For this reason we have chosen EBT3 film for the GC200 source and MD-V3 film for the GC220 source. The results are given in table 6.2 and are plotted in figures 6.5A and 6.5B. The  $h$  values used to determine  $F(t)$  for the red and green pixels were 0.190 and 0.098 for EBT3, and 0.182 and 0.136 for MD-V3.



Figures 6.5A&B. Plots of the function  $F(t)$ , defined in (6.8) and listed in table 6.2, against the set time for red pixels (open symbols) and green pixels (filled symbols). Left: EBT3 film in GC200. Right: MD-V3 film in GC220. The lines are linear best fits to the data points as expected according to (6.8) with intercepts in A and B corresponding to  $\Delta t = 9.3 \pm 0.7$  s and  $4.9 \pm 0.4$  s respectively.

The values of  $\Delta t$  obtained from linear best-fits to the  $F(t)$  data are  $9.3 \pm 0.7$  s and  $4.9 \pm 0.4$  s for GC200 and GC220 respectively. These values have accordingly been added to the set times for each exposure to calculate the total dose for each sample irradiated. The  $\Delta t$  values correspond to additional doses of 0.31 Gy and 2.45 Gy per insertion for the GC200 and GC220 dose rates of 2 Gy/min and 30 Gy/min respectively. This correction is particularly important for measurements where several film samples were irradiated together and removed separately after a different number of exposures. The standard deviations of  $\Delta t$  correspond to systematic offset errors in  $m$  of  $\pm 0.02$  and  $\pm 0.20$  Gy for measurements using GC200 and GC220 respectively.

### 6.3.3. Dose and dose rate dependences

In this section we present data obtained for a given film type using the different radiation sources with more than an order of magnitude variation in dose rate.

#### 6.3.3.1. EBT3

EBT3 is at present the most favored radiochromic film for radiotherapy applications mainly because its range encompasses that of the doses of a few gray frequently used in fractionated-dose IMRT protocols. The potential role in the quality assurance (QA) of actual treatment protocols has resulted in EBT3 and its forerunner EBTs being the subject of many studies (Butson, M.J. et al, 2006, 2009, 2010; Cheung et al, 2006; Lynch et al, 2006; Su et al, 2007; Fuss et al, 2007; Arjomandy et al, 2010; Matney et al, 2010; Sorriaux et al, 2012; Massillon-JL et al, 2012; Borca et al, 2013; Papaconstadopoulos et al, 2014).

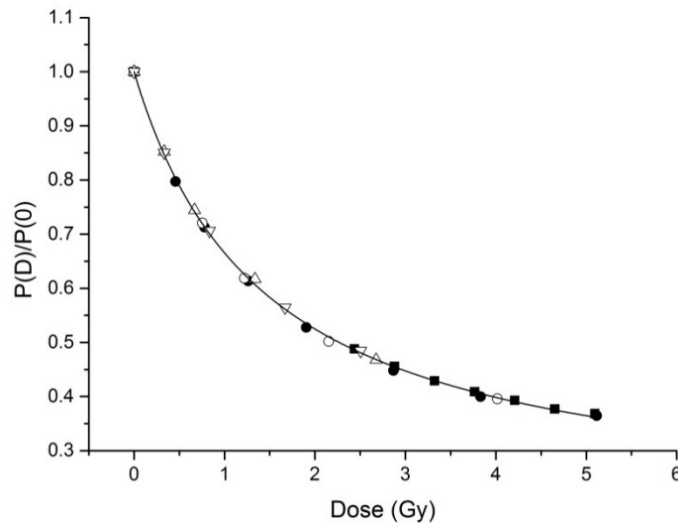


Figure 6.6. Normalized red pixel levels as a function of dose for irradiation of EBT3 film with 200 kVp X-rays at 0.166 Gy/min (down triangles) and 0.661 Gy/min (up triangles), and  $^{60}\text{Co}$   $\gamma$ -rays at 1.86 Gy/min (circles), 1.96 Gy/min (filled circles) and 26.4 Gy/min (filled squares). The open and filled symbols correspond to irradiations made on two separate dates. The full line is a best fit to the combined data based on equation (6.2) with  $\mathbf{m} = 1.42$  and  $\mathbf{h} = 0.190$ .

The dose dependence of the normalized red pixel level for EBT3 film for all X-ray and  $\gamma$ -ray data sets are plotted in figure 6.6. The open and filled symbols in the figure are for measurements carried out on two different dates. As can be seen, the combined data, which cover a 160-fold range of dose rate, are well described by the full line drawn through the points. This line is based on a best overall fit using equation (6.2) with  $\mathbf{m} = 1.424$  Gy ( $\sigma = 0.027$  Gy) and  $\mathbf{h} = 0.190$ . A similar plot for the green pixel data gives best-fit values of  $\mathbf{m} = 2.398$  Gy ( $\sigma = 0.073$  Gy) and  $\mathbf{h} = 0.098$ .

Table 6.3. The median dose  $\mathbf{m}$  Gy with standard deviation  $\sigma$  from best fits to individual red pixel data sets for EBT3 film using equation (6.2) and a common value of  $\mathbf{h} = 0.190$ .

Source	Dose rate (Gy/min)	$\mathbf{m}$ (Gy)	$\sigma$ (Gy)
200 kVp X-ray	0.166	1.44	0.009
	0.661	1.44	0.020
$^{60}\text{Co}$ $\gamma$ -ray	1.86	1.40	0.021
	1.96	1.38	0.011
	26.4	1.48	0.009
combined fit		1.42	0.027

Best fits have also been made to the individual data sets using a common value of  $\mathbf{h} = 0.190$  and the values of  $\mathbf{m}$  are listed in table 6.3. The median dose values found are all within  $\pm 4\%$  ( $2\sigma$ ) of the value of  $\mathbf{m} = 1.42$  Gy found from the best fit to the combined data sets shown by the full line drawn in figure 6.6. Clear-cut conclusions about specific effects of the nature or dose rate of the radiation on the sensitivity of the film cannot therefore be made.

The indication of a slightly lower sensitivity of EBT3 towards 200 kVp X-rays (95 keV equivalent) than  $^{60}\text{Co}$   $\gamma$ -rays (1.25 MeV average) would be in agreement with the results of previous studies. In a (single dose) study of early EBT film using X-rays from 50 to 18000 kVp [Butson, M.J. et al, 2006], the sensitivity was found to be lower by a few percent for energies below 250 kVp. A later study of EBT2 film however showed a less pronounced decrease in sensitivity (Butson, M.J. et al, 2010). A lower sensitivity might also be expected based on the energy attenuation coefficients of GafChromic film found for photon energies of 50, 100, 150, 200, and 1250 keV of 2.905, 2.368, 2.674, 2.894 and 2.906 respectively (Hubbel and Seltzer, 1996).

The increase in  $\mathbf{m}$  (decrease in sensitivity) from 1.39 Gy to 1.48 Gy found in going from the low to the high  $\gamma$ -ray dose rate is within the systematic offset error of  $\pm 0.16$  Gy incurred when using the GC220 source (see section 6.3.2.2). We conclude therefore that over the 14-fold increase in  $\gamma$ -ray dose rate the sensitivity of EBT3 film may decrease but by less than 20%.

### 6.3.3.2. MD-V3

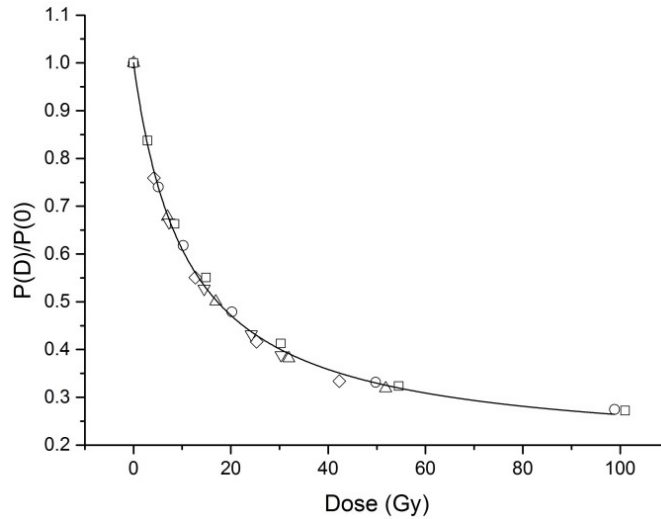


Figure 6.7. The red pixel level for MD-V3 film as a function of dose for X-ray irradiation at 0.242 Gy/min (up triangle), 0.422 Gy/min (diamond) and 0.996 Gy/min (down triangle), or  $\gamma$ -ray irradiation at 1.79 Gy/min (circles) and 24.7 Gy/min (squares). The full line drawn through the points is a best-fit using  $\mathbf{m} = 11.1$  Gy and  $\mathbf{h} = 0.182$  in equation (6.2).

The results of X-ray and  $\gamma$ -ray measurements are plotted together in figure 6.7. As for EBT3 the combined data are seen to be described quite well by the full line which was calculated using equation (6.2) with  $\mathbf{m} = 11.1$  Gy ( $\sigma = 0.37$  Gy) and  $\mathbf{h} = 0.182$ . A similar plot for the green pixels gave  $\mathbf{m} = 19.2$  Gy ( $\sigma = 0.61$  Gy) and  $\mathbf{h} = 0.136$ .

Table 6.4. The median dose  $\mathbf{m}$  Gy for MD-V3 film from best fits to individual red pixel data sets using equation (6.2) with a common value of  $\mathbf{h} = 0.182$ .

Source	Dose rate (Gy/min)	$\mathbf{m}$ (Gy)	$\sigma$ (Gy)
200 kV <sub>p</sub> X-ray	0.242	10.6	0.07
	0.422	10.2	0.13
	0.996	10.7	0.11
<sup>60</sup> Co $\gamma$ -ray	1.79	11.6	0.17
	24.7	12.4	0.14
combined fit		11.1	0.37

Best fits to the individual X-ray and  $\gamma$ -ray data sets have been made using equation (6.2) with a common value of  $\mathbf{h} = 0.182$  and the resulting median dose values are listed in table 6.4. In the case of MD-V3 the sensitivity towards low energy X-rays appears to somewhat higher than



for cobalt-60  $\gamma$ -rays of similar dose rate. The values are however within  $\pm 6\%$  of the average of  $\mathbf{m} = 10.9$  Gy. The decrease by approximately 7% in sensitivity of the film in going from a  $\gamma$ -ray dose rate of 1.79 Gy/min to 24.7 Gy/min is close to the combined  $2\sigma$  error limits and can therefore only be taken as an indication that there may be an actual decrease in sensitivity by a few percent at a dose rate close to 30 Gy/min.

### 6.3.3.3. HD-V2 and HD-810

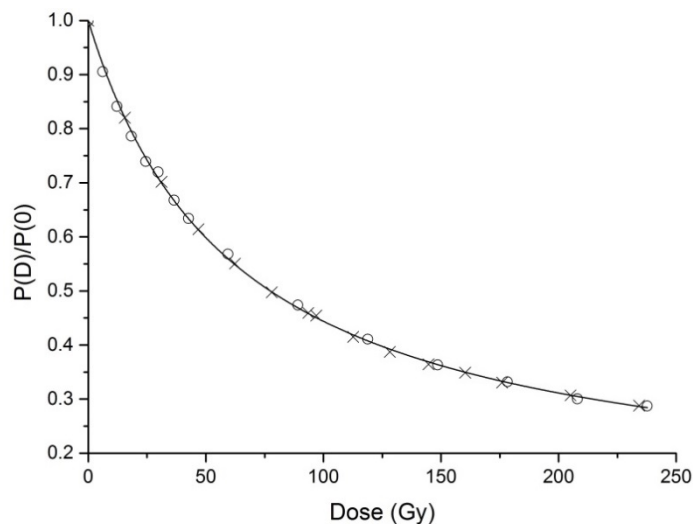


Figure 6.8. The red pixel dose dependence of  $P(D)/P(0)$  for HD-V2 film  $^{60}\text{Co}$   $\gamma$ -ray irradiated with dose rates of 1.97 and 27.1 Gy/min. The full line is a best fit to the combined data sets using equation (6.2) with  $\mathbf{m} = 63.6$  Gy and  $\mathbf{h} = 0.093$ .

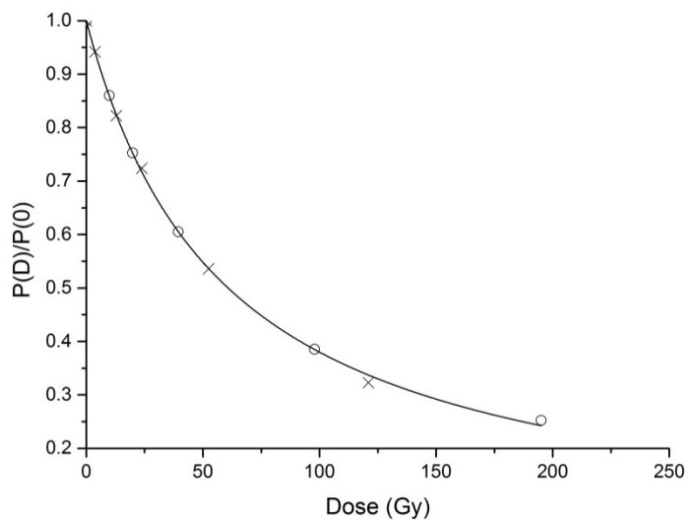


Figure 6.9. The red pixel dose dependence of  $P(D)/P(0)$  for HD-810 film  $^{60}\text{Co}$   $\gamma$ -ray irradiated with dose rates of 1.94 and 26.6 Gy/min. The full line is a best fit to the combined data sets using equation (6.2) with  $\mathbf{m} = 60.6$  Gy and  $\mathbf{h} = 0.007$ .

The median dose of approximately 60 Gy found for the films HD-V2 and HD-810 made measurements using the X-ray source, with a maximum dose rate at 50 cm of approximately 1 Gy/min, impractically long. Only  $\gamma$ -ray measurements have therefore been carried out with these films and the results are shown in figures 6.8 and 6.9. For both films the combined data are well described by (6.2). The full lines drawn in figures 6.8 and 6.9 correspond to red pixel values of  $\mathbf{m} = 63.6$  Gy ( $\sigma = 0.90$  Gy) and  $60.6$  Gy ( $\sigma = 1.61$  Gy) and  $\mathbf{h} = 0.093$  and  $0.007$  respectively. The values for the green pixels were  $\mathbf{m} = 117.7$  Gy and  $142.3$  Gy, and  $\mathbf{h} = 0.20$  and  $0.10$ .

Fits to the separate dose rate data sets for HD-V2 gave  $\mathbf{m} = 63.7$  Gy ( $\sigma = 0.62$  Gy) and  $63.5$  Gy ( $\sigma = 0.24$  Gy) for  $1.97$  and  $27.1$  Gy/min respectively. For HD-810 film the analogous values were  $60.9$  Gy ( $\sigma = 0.64$  Gy) and  $60.2$  Gy ( $\sigma = 1.03$  Gy) for dose rates of  $1.94$  Gy/min and  $26.6$  Gy/min. We conclude that there is no dependence on dose rate for the HD films over the range studied within an uncertainty of  $\pm 3\%$ . This is in agreement with an earlier study of a film similar to HD-810 by Saylor et al, 1988, who found no measureable dose rate dependence over the range from  $0.02$  to  $200$  Gy/min.

## 6.4. Conclusions

The combination of an EPSON V700 flatbed scanner in reflection mode and the NIH freeware program ImageJ provides a convenient, inexpensive, and reproducible method of relative dosimetry using radiochromic films. For ease of positioning and archiving the films can be mounted on a good quality white paper background, as suggested by Butson et al, 2011.

The red, green and blue pixel levels ( $P_R$ ,  $P_G$  and  $P_B$ ) for the four GafChromic films investigated, EBT3, MD-V3, HD-V2 and HD-810, all display a dependence on dose,  $D$ , that can be well-described by the function  $P(D)/P(0) = (1 + \mathbf{h}D/\mathbf{m})/(1 + D/\mathbf{m})$  with  $P(0)$  the level for the unirradiated film. This is mathematically the same relationship as that suggested in the manual supplied by the manufacturer, i.e.  $P(D) = [\mathbf{a} + \mathbf{b}D]/[\mathbf{c} + D]$ . In our revised form the fit parameters have physical significance:  $\mathbf{h}$  is the saturation level,  $P(\infty)/P(0)$ , approached at high doses, and  $\mathbf{m}$  is the 'median dose' for which  $P(D)/P(0) = (1+\mathbf{h})/2$  which is the half-point of the dynamic range of the film between  $P(D)/P(0) = 1$  and  $\mathbf{h}$ .

For all films  $\mathbf{h}$  was found to be larger than  $0.4$  for the blue pixels. This results in a dynamic range that is too small for accurate dose measurements. Therefore, only values of  $\mathbf{m}$  and  $\mathbf{h}$  are given in table 6.5 for red and green pixels. The values listed are those derived from best fits to combined X-ray and  $\gamma$ -ray measurements for a particular film.

Table 6.5. The median dose  $\mathbf{m}$  Gy, saturation level  $\mathbf{h} = P(\infty)/P(0)$ , and 80/20 dose range (see text) for the films investigated.

Film	red pixels			green pixels		
	$\mathbf{m}$ (Gy)	$\mathbf{h}$	range (Gy)	$\mathbf{m}$ (Gy)	$\mathbf{h}$	range (Gy)
EBT3	1.42	0.190	0.4 - 5.7	2.4	0.098	0.6 - 9.6
MD-V3	11.1	0.182	2.8 - 44	19.2	0.136	4.8 - 77
HD-810	60.6	0.007	15 - 242	142.3	0.099	36 - 569
HD-V2	63.6	0.093	16 - 254	117.7	0.201	29 - 471

Deciding on the "applicable dose range" (ADR) of a particular film is somewhat arbitrary and depends to a certain extent on the method of measurement of the radio-chromatic change. We have chosen for the lower and upper dose range values those for which  $P(D)/P(0)$  corresponds to 80% and 20% of the dynamic range from 1 to  $\mathbf{h}$ . The corresponding lower and upper dose values,  $\mathbf{m}/4$  and  $4\mathbf{m}$ , are listed in table 6.5. As can be seen there is considerable overlap between the films, with ranges extending from a low of 0.4 Gy for EBT3 to a high of a few hundred Gy for the HD films. The values lie within the ADRs given for the individual films by the supplier (<http://www.gafchromic.com/gafchromic-film/radiotherapy-films/index.asp>). Defining the useable range as 90% to 10% of the dynamic range of  $P(D)/P(0)$  would extend the ADR of a given film from  $\mathbf{m}/9$  to  $9\mathbf{m}$  with however an increase in the error at the low and high dose extremes .

A primary aim of the work in the present chapter was to find the film that is best suited to cover the dose range from a few gray to a few tens of gray used in our radio-fluorogenic gel studies presented in previous chapters. The MD-V3 80/20 range of 2.8 to 44 Gy best fulfills this requirement. It is important for the complementary application of radiochromic film that the sensitivity of the film is (close to) dose rate independent in order to provide spatial calibration of RFG gel measurements which are dose-rate-dependent. MD-V3 film also satisfies this requirement.

## References

Arjomandy, B., Taylor, F., Anand, A., Sahoo, N., Gillin, M., Prado, K., Vicic, M., 2010. Energy dependence and dose response of Gafchromic EBT2 film over a wide range of photon, electron, and proton beam energies. *Medical Physics* 37, 1942-1947.

Borca, C.B., Pasquino, M., Russo, G., Grosso, P., Cante, D., Sciacero, P., Girelli, G., La Porta, M.R., Tofani, S., 2013. Dosimetric characterization and use of GAFCHROMIC EBT3 film for IMRT dose verification. *Journal of Applied Clinical Medical Physics* 14, 158-171.

Butson, E., Alnawaf, H., Yu, P.K.N., 2011. Scanner uniformity improvements for radiochromic film analysis with matt reflectance backing. *Australasian Physical & Engineering Sciences in Medicine* 34, 401-407.

Butson, M.J., Yu, P.K.N., Cheung T., Metcalfe, P., 2003. Radiochromic film for medical dosimetry. *Materials Science and Engineering R41*, 61-120.

Butson, M. J., Cheung, T., Yu, P. K. N., 2006. Weak energy dependence of EBT gafchromic film dose response in the 50 kVp-10 MVp X-ray range. *Applied Radiation and Isotopes* 64, 60-62.

Butson, M. J., Cheung, T., Yu, P. K. N., Alnawaf, H., 2009. Dose and absorption spectra response of EBT2 Gafchromic film to high energy x-rays. *Australasian Physical & Engineering Sciences in Medicine* 32, 196-202.

Butson, M. J., Yu, P. K. N., Cheung, T., Alnawaf, H., 2010. Energy response of the new EBT2 radiochromic film to x-ray radiation, *Radiation Measurements* 45, 836-839.

Chance, R.R., Patel, G.N., Witt, J.D., 1979. Thermal effects on the optical properties of single crystals and solution-cast films of urethane substituted polydiacetylenes. *Journal of Chemical Physics* 71, 206-211

Cheung, T., Butson, M.J., Yu, P.K., 2006. Measurement of high energy x-ray beam penumbra with Gafchromic<sup>TM</sup> EBT radiochromic film. *Medical Physics* 33, 2912-2914.

Chu, R. D. H., VanDyke, G., Lewis, D. F., O'Hara, K. P. J., Buckland, B. R., Dinelle, F., 1990. GafChromic dosimetry media: a new high dose rate thin film routine dosimeter and dose mapping tool. *Radiation Physics and Chemistry* 35, 767-773.

Devic, S., Seuntjens, J., Hegyi, G., Podgorsak, E. B., Soares, C. G., Kirov, A. S., Ali, I., Williamson, J. F., Elizondo, A., 2004. Dosimetric properties of improved GafChromic films for seven different digitizers. *Medical Physics* 31, 2392-2401.

Devic, S., Seuntjens, J., Sham, E., Podgorsak, E. B., Schmidlein, C. R., Kirov, A. S., Soares, C. G., 2005. Precise radiochromic film dosimetry using a flat-bed document scanner. *Medical Physics* 32, 2245-2253.

Devic, S., 2011. Radiochromic film dosimetry: Past, present and future. *Physica Medica* 27, 122-134.

Dreindl, R., Georg, D., Stock,., 2014. Radiochromic film dosimetry: Considerations on precision and accuracy for EBT2 and EBT3 type films. *Zeitschrift für Medizinische Physik* 24, 153-163.

Dudley, R.A., 1956. Photographic film dosimetry. In "Radiation Dosimetry" (Academic Press, Inc. New York, NY.) G.J. Hine & G.L. Brownell, Eds

Dutreix, J., Dutreix, A., 1969. Film dosimetry of high-energy electrons, *Annals of the New York Academy of Sciences* 161, 33-43.

Ehrlich J.L., 1954. Photographic dosimetry of X and Gamma rays. National Bureau of Standards, handbook nr. 57.

Farah, N., Francis, Z., Abboud, M., 2014. Analysis of the EBT3 Gafchromic film irradiated with 6 MV photons and 6 MeV electrons using reflective mode scanners. *Physica Medica*, 708-712.

Fuss, M., Sturtewagen, E., De Wagter, C., Georg, D., 2007. Dosimetric characterization of GafChromic EBT film and its implication on film dosimetry quality assurance. *Physics in Medicine and Biology* 52, 4211-4225.

Hill, R., Healy, B., Hollaway, L., Kuncic, Z., Thwaites, D., Baldock, C., 2014. Advances in kilovoltage x-ray beam dosimetry. *Physics in Medicine and Biology* 59, R183-R231.

Hubbell, J.H., Seltzer, S.M., 1996. Tables of X-ray mass attenuation coefficients and mass energy-absorption coefficients from 1 keV to 20 MeV for elements  $Z = 1$  to 92 and 48 additional substances of dosimetric interest. NISTIR 5632 (<http://www.nist.gov/pml/data/xraycoef/index.cfm>)

Huet, C., Moignier, C., Fontaine, J., Clairand, I., 2014. Characterization of the gafchromic EBT3 films for dose distribution measurements in stereotactic radiotherapy. *Radiation Measurements* 71, 364-368.

Kalef-Ezra, J., Karava, K., 2008. Radiochromic film dosimetry: reflection vs transmission scanning. *Medical Physics* 35, 2308-2311.

Klassen, N.V., van der Zwan, L., Cygler, J., 1997. GafChromic MD-55: Investigated as a precision dosimeter. *Medical Physics* 24, 1924-1935.

Klassen, N.V., Shortt, K.R., Seuntens, J., Ross, C.K., 1999. Fricke dosimetry: the difference between  $G(\text{Fe}^{3+})$  for  $^{60}\text{Co}$   $\gamma$ -rays and high-energy x-rays. *Physics in Medicine and Biology* 44, 1609-1624.

Lewis, D., Chan, M.F., 2015. Correcting lateral response artifacts from flatbed scanners for radiochromic film dosimetry. *Medical Physics* 42, 416-429.

Low, D.A., Moran, J.M., Dempsey, J.F., Dong, L., Oldham, M., 2011. Dosimetry tools and techniques for IMRT. *Medical Physics* 38, 1313-1338.

Lynch, B.D., Kozelka, J., Ranada, M.K., Li, J.G., Simon, W.E., Dempsey, J.F., 2006. Important considerations for radiochromic film dosimetry with flatbed CCD scanners and EBT GAFCHROMIC<sup>®</sup> film. *Medical Physics* 33, 4551-4556.

Massillon-JL, G., Chin-Tsao, S-T., Domingo-Munoz, I., Chan, M. F., 2012. Energy dependence of the new GafChromic EBT3 film: dose response curves for 50 kV, 6 and 15 MV X-ray beams. *International Journal of Medical Physics, Clinical Engineering and Radiation Oncology* 1, 60-65.

Matney, J.E., Parker, B.C., Neck, D.W., Henkelmann, G., Rosen, I.I., 2010. Evaluation of a commercial flatbed document scanner and radiographic film scanner for radiochromic EBT film dosimetry. *Journal of Applied Clinical Medical Physics* 11, 198-208.

Mathot, M., Sobczak, S., Hoornaert, M-T., 2014. Gafchromic film dosimetry: Four years experience using FilmQA Pro software and Epson flatbed scanners. *Physica Medica* 30, 871-877.

McEwen, M., El Gamal, I., Mainegra-Hing, E., Cojocar, C., 2014. Determination of the radiation chemical yield (G) for the Fricke chemical dosimetry system in photon and electron beams. Report NRC-PIRS-1980 (National Research Council of Canada, Ottawa)

McLaughlin, W. L., Humphreys, J. C., Hocken, D., Chappas, W. J., 1988. Radiochromic dosimetry for validation and commissioning of industrial radiation processes. *Radiation Physics and Chemistry* 31, 505-514.

McLaughlin, W.L., Yun-Dong, C., Soares, C.G., Miller, A., van Dyk, G., Lewis, D.F., 1991. Sensitometry of the response of a new radiochromic film dosimeter to gamma radiation and electron beams. *Nuclear Instruments and Methods in Physics Research*, A302, 165-176.

McLaughlin, W.L., Puh, J.M., Al-Sheikhly, M., Christou, C.A., Miller, A., Kovacs, A., Wojnarovits, L., Lewis, D.F., 1996. Novel radiochromic films for clinical dosimetry. *Radiation Protection Dosimetry* 66, 263-268.

Mendez, I., Hartman, V., Hudej, R., Strojnik, A. Casar, B., 2014. Gafchromic EBT2 film dosimetry in reflection mode with a novel plan-based calibration method. *Medical Physics* 40, 011720.

Metcalfe, P., Kron, T., Elliott, A., Wong, T., 1993. Dosimetry of 6-MV x-ray beam penumbra. *Medical Physics* 20, 1439-1446.

Niroomand-Rad, A., Blackwell, C.R., Coursey, B.M., Gall, K.P., Galvin, J.M., McLaughlin, W.L., Meigooni, A.S., Nath, R., Rodgers, J.E., Soares, C.G., 1998. Radiochromic film dosimetry: Recommendation of AAPM radiation therapy task group 55. *Medical Physics* 25, 2093-2115.

Palmer, A.L., Lee, C., Ratcliffe, A.J. Bradley, D., Nisbet, A., 2013. Design and implementation of a film dosimetry audit tool for comparison of planned and delivered dose distributions in high dose rate (HDR) brachytherapy. *Physics in Medicine and Biology* 58, 6623-6640.

Papaconstadopoulos, P., Hegyi, G., Seuntjens, J., Slobodan, D., 2014. A protocol for EBT3 radiochromic film dosimetry using reflection scanning. *Medical Physics* 41, 122101.

Rink, A., Vitkin, I.A., Jaffray, D. A. 2005a. Suitability of radiochromic medium for real-time optical measurements of ionizing radiation dose. *Medical Physics* 32, 1140-1155.

Rink, A., Vitkin, I.A., Jaffray, D.A. 2005b. Characterization and real-time optical measurements of ionizing radiation dose response for a new radiochromic medium. *Medical Physics* 32, 2510-2516.

Saylor M.C., Tamargo, T.T., McLaughlin, W.L., Khan, H.M., Lewis, D.F., Schenfele, R.D., 1988. A thin film recording medium for use in food irradiation. *Radiation Physics and Chemistry* 31, 529-536.

Schoenfeld, A.A., Poppinga, D., Harder, D., Doerner, K-J., Poppe, B., 2014. The artifacts of radiochromic film dosimetry with flatbed scanners and their causation by light scattering from radiation-induced polymers. *Physics in Medicine and Biology* 59. 3575-3597.

Shiomi, H., Takehiro, I., Satoaki, N., Toshihiko, I., 2000. Quality assurance for an image-guided frameless radiosurgery system using radiochromic film. *Radiation Medicine* 18, 107-113.

Soares, C.G., 2006. New developments in radiochromic film dosimetry. *Radiation Protection Dosimetry* 120, 100-106.

Soares, C. G., 2007. Radiochromic film dosimetry, *Radiation Measurements* 41, S100-S116.

Sorriaux, J., Kacperek, A., Rossomme, S. Lee, J. A., Bertrand, D., Vynckier, S., Sterpin, E., 2012. Evaluation of Gafchromic EBT3 films characteristics in therapy photon, electron and proton beams. *Physica Medica: European Journal of Medical Physics* 29, 599-606.

Su, F-C., Liu, Y., Stathakis, S., Shi, C., Esquivel, C., Papanikolaou, N., 2007. Dosimetry characteristics of GafChromic EBT film responding to therapeutic electron beams. *Applied Radiation and Isotopes* 65, 1187-1192.

Valnitsky, S.M., 1997. Radiochromic film dosimetry for clinical proton beams. *Applied Radiation and Isotopes* 48, 643-651.

Warman, J.M., de Haas, M.P., Luthjens, L.H., 2011a. High-energy radiation monitoring based on radio-fluorogenic co-polymerization II: fixed fluorescent images of collimated X-ray beams using an RFCP gel. *Physics in Medicine and Biology* 56, 1487-1508.

Warman, J.M., de Haas, M.P., Luthjens, L.H., Murrer H.P., 2011b. A radio-fluorogenic organic gel for real-time, 3D radiation dosimetry. *Advanced Materials* 23, 4953-4955. <http://dx.doi.org/10.1002/adma.201102831>

Warman, J.M., de Haas, M.P., Luthjens, L.H., Hom M.L., 2013a. High-energy radiation monitoring based on radio-fluorogenic co-polymerization III: fluorescent images of the cross-section and depth-dose profile of a 3 MV electron beam. *Radiation Physics and Chemistry* 84, 129-135. <http://dx.doi.org/10.1016/j.radphyschem.2012.06.031>

Warman, J.M., de Haas, M.P., Luthjens, L.H., Kavatsyuk O., van Goethem M-J., Kiewiet H.H., Brandenburg S., 2013b. Fixed fluorescent images of an 80 MeV proton pencil beam. *Radiation Physics and Chemistry* 85, 179-181. <http://dx.doi.org/10.1016/j.radphyschem.2012.11.011>

Yao, T, Gasparini, Denkova A.G., Warman, J.M., 2015. Radiation-chemical and optical properties of a radio-fluorogenic gel. *Journal of Physics: Conference Series* 573, 012036/1-4.





## Chapter 7

# Bulk and tomographic fluorescent imaging of X-ray beams<sup>6</sup>

### 7.1. Introduction

In previous chapters we have been concerned with the radiation-induced fluorescence from radio-fluorogenic solutions and gels that were homogeneously irradiated with gamma rays. The interest centered on the determination of the dependence of the fluorescence intensity on absorbed dose and dose rate. This was considered necessary in order to provide a basis for the quantitative application of RFG gels to studies of complex radiation fields. In this chapter we have used our in-house X-ray source to provide collimated beams of 200 kVp X-rays that produce fluorescent

---

<sup>6</sup> This chapter is based on the paper "Light slit scanning prototype for 3D imaging of RFG gel" submitted, authors A. Gasparini, T. Yao, L. H. Luthjens, J. M. Warman, S. Stallinga, M. P. de Haas, A. G. Denkova.

tracks in RFG gels. These allow measurements of the spatial resolution of the technique and of the complexities resulting from the use of crossed beams of different geometry. Ultimately we demonstrate how a relatively simple slit-scanning method can be used to provide tomographic fluorescent images. These images can be combined to give full, three-dimensional representations of the radiation absorbed that can be spatially manipulated and arbitrarily dissected.

## 7.2. Materials and methods

### 7.2.1. Materials

The components of the gels used in the present chapter are the same as those in chapters 3 and 5: tertiary-butyl acrylate (TBA) from Sigma-Aldrich (#327182) and N-(1-pyrenyl)maleimide or maleimido-pyrene (MPy) also from Sigma-Aldrich (#P7908). The physical properties of the individual components have been given in the materials and methods sections of chapters 2 and 3. All gels used were prepared by the reformation procedure outlined in chapter 5. Briefly, a given volume of pure, deaerated TBA is pipetted into the cell to be used in a nitrogen-flushed glove box. The cell is capped, removed from the glove box and irradiated to a dose of approximately 15 Gy (close to 15% monomer conversion) in the GC200 gamma-ray source. The cell is then uncapped and placed in a vacuum oven at room temperature for several days for removal of remaining monomer. The cell is then transferred to the glove box and a de-aerated MPy/TBA solution of the same volume as the monomer removed by evacuation is added. The cell is allowed to stand for a period of approximately two weeks to allow swelling of the polymer, PTBA, back to a rigid gel which now contains MPy. A sample of the deaerated MPy/TBA solution was also placed in a 1 cm square cell for measurement of the optical density at 365 nm which allowed accurate calculation of the MPy concentration in the gel.

The cells used in the present chapter were 40 mm square and contained a gel volume of approximately 70 cm<sup>3</sup>. An illustration of the optical clarity of the gel in such a cell is shown in figure 7.1. The gel shown had been subjected to irradiation with X-ray beams with a total dose of 40 Gy and its fluorescent image in UV light is shown in the Results and Discussion section (figure 7.8). As can be seen in figure 7.1, in normal room lighting the gel shows no indication of turbidity or color change in the irradiated regions.



Figure 7.1. A photograph in daylight of a 40x40 mm<sup>2</sup> square cell containing an RFG gel which had been irradiated with two, 10 mm diameter crossed X-ray beams each with an average dose of ~20 Gy. For a fluorescent image of the same gel see figure 7.8.

MD-V3 radiochromic film (Promis Electro-Optics B.V. Lot Nr A03051201) is used in this chapter to monitor the incident and exit cross-sections and doses delivered to the RFG gels by the X-ray beams. Details of the film measurement procedure and its response to high-energy photon irradiation are given in chapter 6. In that chapter we show that relationship 7.1 (6.2) gives a good description of the dose dependence of the color change on irradiation.

$$P(D)/P(0) = (1 + \mathbf{h}D/\mathbf{m})/(1 + D/\mathbf{m}) \quad (7.1)$$

In 7.1  $P(D)$  and  $P(0)$  are the pixel levels for the irradiated and unirradiated film respectively. The parameters  $\mathbf{h}$  and  $\mathbf{m}$  have the significance of being the plateau level,  $P(\infty)/P(0)$ , approached at “infinite” dose, and the “median dose”, *i.e.* the dose for which  $P(D)/P(0) = (1 + \mathbf{h})/2$  respectively. Using the most sensitive, red pixels the values of  $\mathbf{h}$  and  $\mathbf{m}$  for MD-V3 film exposed to 200 kVp X-rays were determined to be 0.182 and 10.5 Gy respectively. No dose rate dependence was found over the range from 0.25 to 1 Gy/min for the X-rays.

### 7.2.2. Irradiation facilities

The gamma ray source GC200 with a dose rate of approximately 2 Gy/min was used in the present chapter only for the initial, ~15% polymerization of pure TBA in the preparation procedure of the reformed gels. For beam studies an X-ray source was used.

The X-ray source was a Philips MCN 321 variable-energy X-ray tube with a 4 mm square,

tilted tungsten target and a 4 mm thick beryllium exit window. No X-ray filter plate was inserted into the filter holder adjacent to the exit window. In the present measurements an accelerating voltage of 200 kV was used with a maximum e-beam current of 15 mA. The dose rate,  $D'$  Gy/min, could be measured using a 35 cm<sup>3</sup>, atmospheric-air ionization chamber, IC, ("37D X-ray Exposure Meter" D.A. Pitman Instruments Ltd [now Vinten Instruments Ltd]) that was annually calibrated by the Dutch Metrology Institute. The dose rates at distances of 50 and 100 cm were routinely measured and were close to 1.0 and 0.25 Gy/min respectively for a 15 mA beam current. An alignment laser (Laserglow Technologies, "Galileo PRO") was used to position the beam with respect to beam collimators and the RFG cell which were mounted on an optical rail as shown in figure 7.2.

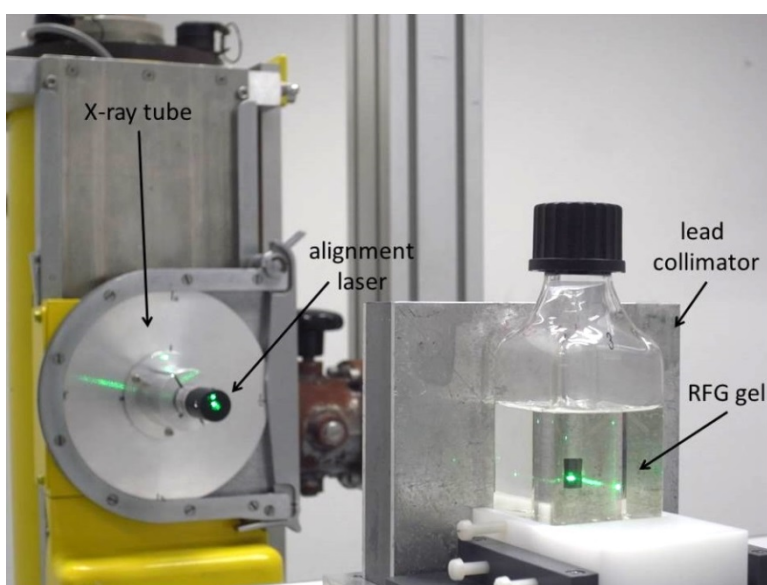


Figure 7.2. The X-ray apparatus with a 10 mm square lead collimator in front of a 40 mm square gel-containing cell on an optical rail with a laser beam for alignment.

The two collimators used were 120x120 mm square, 27 mm thick sandwiches of Al(3 mm)/Pb(21 mm)/Al(3 mm) with central apertures 10x10 mm square or 10 mm diameter round. The collimators were mounted in a holder on the optical rail and the X-ray beam was aligned with the centre of the aperture using the alignment laser as shown in figure 7.2. MD-V3 radiochromic film samples (30x30 mm<sup>2</sup>) were mounted on the front and back of the cell as illustrated in figure 7.3 to provide additional in situ, incident and exit dose information.

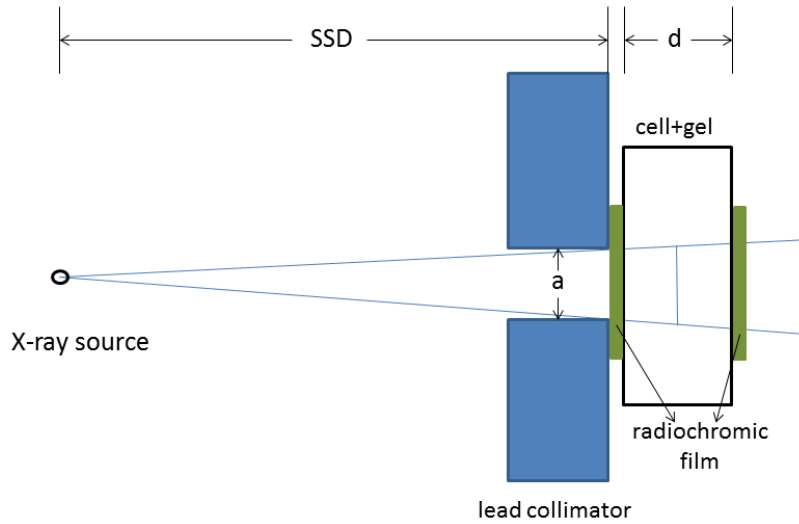


Figure 7.3. A schematic of the X-ray source, beam collimator and cell containing the RFG gel and including radiochromic film dosimeters.

### 7.2.3. Fluorescence imaging

#### 7.2.3.1. Bulk imaging

The set-up used for bulk imaging of irradiated RFG gels is illustrated in figure 7.4. It consists of two LED UV lamps (4PICO) in opposition at a distance of 30 cm and a CCD camera (Ricoh GX200) placed orthogonally in front of the RFG cell. In order to illuminate uniformly the 4 cm square samples a 3" Fresnel lens was used which produced a divergent UV excitation beam. More details of the UV lamps and camera settings are given in chapter 3 Materials and methods section. Images were stored as JPEG and DNG raw files. In the case of the 40 mm square cells the bottom was optically flat and photos could be taken with the cell on its side with the bottom facing the camera as is shown in figure 7.8 in section 7.3.2.

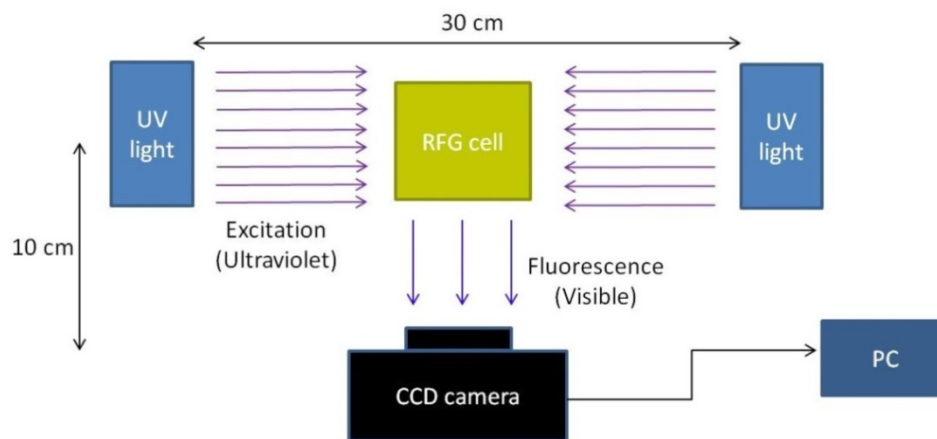


Figure 7.4. A schematic of the setup used for bulk imaging of irradiated RFG gels.

### 7.2.3.2. Tomographic imaging

In order to construct full 3D views of the deposition of dose in a complex radiation field, we have used a set-up that is basically the same as that used for bulk images but to which two components have been added. Firstly, the UV excitation light within the gel is restricted to a vertical sheet by interposition of panels with 2 mm slits for transmission of the UV beams. Secondly, the cell containing the gel is placed on a translation stage that allows it to be transported past the slits. Images are then taken as a function of the slit position with respect to the front face of the RFG gel, the parameter "z" shown in the schematic figure 7.5. Photographs of the actual set-up are shown in figure 7.6. The cell was advanced usually in 1 mm steps over the 40 mm depth of the RFG gel. In the system used in the present work advancement was carried out manually using a micrometer drive. A fully automated, computer controlled system is under construction.

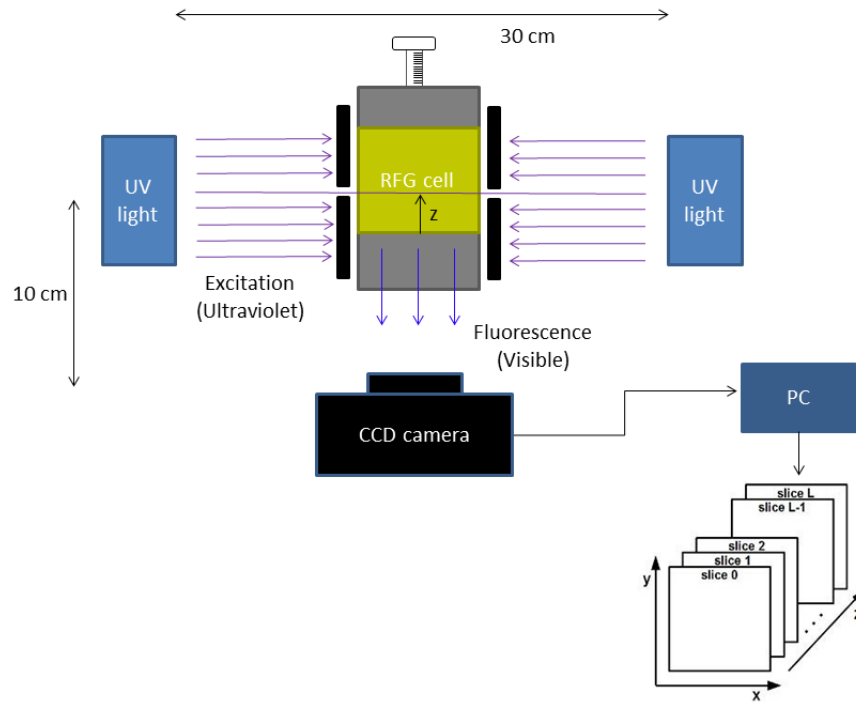


Figure 7.5. A schematic of the slit-scanning set up used for making stacks of tomographic fluorescent images. An animated video illustrating the operation of the apparatus can be viewed [here](#)<sup>7</sup>.

<sup>7</sup> All animations associated with figures are to be found at the link: <https://surfdrive.surf.nl/files/index.php/s/q62QaUDIAhtkhJP>

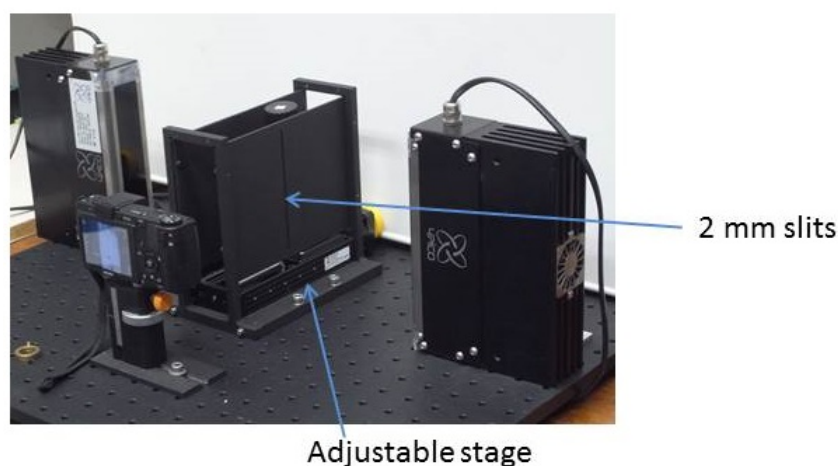
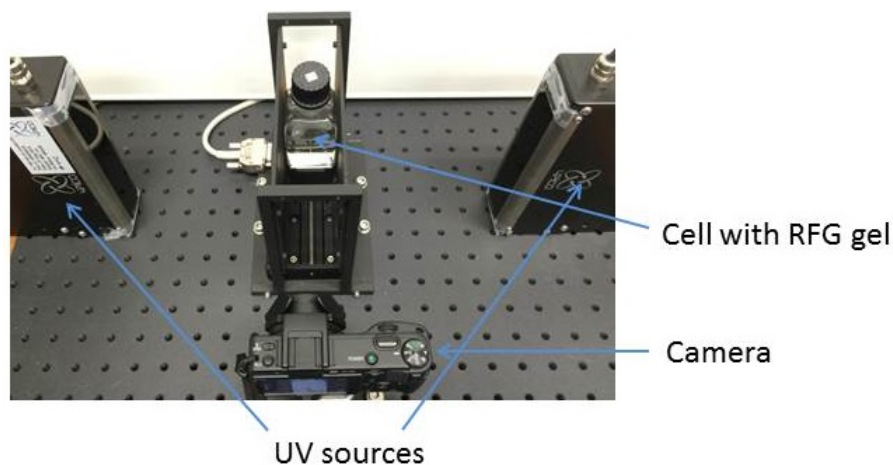


Figure 7.6. Photographs of the actual slit-scanning fluorescence tomography set-up shown schematically in figure 7.5.

#### 7.2.4. Image analysis using ImageJ

The 8-bit JPEG and 16-bit DNG raw files were imported into ImageJ (Rasband 1997) either directly or using the "DCraw" plug-in (<http://ij-plugins.sourceforge.net/plugins/dcraw/>) respectively. The DNG files provide images that are linearly dependent on the emission intensity of the sample (see figure 3.10 in chapter 3). The much smaller, but non-linear, JPEG files are used to provide visual representations of the fluorescence. The images were color-separated into red, green and blue channels with separate pixel levels (gray scale values),  $P_R$ ,  $P_G$  and  $P_B$ . Since the sensitivity of the blue pixel filter coincided best with the wavelength dependence of the fluorescence, the DNG  $P_B$  values per second camera "shutter" time have been used as a measure of the fluorescence intensity,  $I_{IM}$ .

Two-dimensional scans of the fluorescence intensity across the irradiated areas of individual images were made using the "plot profile" analysis function of ImageJ. This could be



used to determine parameters such as the width, maximum intensity and 20 to 80% "penumbra" (spatial dispersion) of beams images.

### *7.2.5. Construction of 3D representations from tomographic images*

3D representations can be constructed from the collection of 2D tomographic images taken at different slit positions as illustrated in figure 7.5. The JPEG files are used to produce three-dimensional visual images that can be rotated and viewed from different angles. The DNG (raw) files are used to produce quantitative dissections of a 3D image.

After importing a collection of slit-scanned images into ImageJ they are split into the separate red, green and blue pixel versions using "Image/Color/Split Channels". Only the blue component is used for image visualization and quantification. Bright and dark outliers are removed using the function "Process/Noise/Remove Outliers". The images are then stacked in the z direction using the "Image/Stacks/Images to Stack" function, and the stack, with file name, is saved. The "depth-cue parameters" (spatial dimensions) width, height and voxel depth required to produce the perspective of the projection are set under "Image/Properties". For example, for a scan with a distance between slices of 1 mm the dimensions in pixels would be 1, 1 and 56 based on a measured spatial resolution of 560 pixels/cm at the position of the slits for the camera settings used. The pixel levels between slices are taken to be equal to the average value of the two adjacent slices. 3D volume or ortho-slice (cross-section) views can be reconstructed from a given stack using the 3D Viewer plug-in (<https://imagej.nih.gov/ij/plugins/3d-viewer/>) under "Plugins/3D/3D Viewer".

The volume rendering using the procedure in ImageJ outlined above only shows the surface of the volume. Intensity variations within the volume cannot be seen. To produce 3D volume renderings that do display the internal intensity variations we have imported the stacked JPEG images saved in ImageJ into the image-processing platform BioImageXD (Kankaanpää et al., 2012) (<http://www.bioimagexd.net/>). This volume rendering uses pixel transparency to create semi-translucent structures in which a parameter  $\alpha$  is applied to represent the opacity of the pixels (Rueden and Eliceiri, 2007). The pixel transparency reveals the structures beneath the outer surface of the volume. The 3D image can be manually rotated or automatically rotated at a given animation speed to produce a movie version.

As mentioned above, the 16 bit DNG files were used to produce quantitative dissections of a 3D image and were initially corrected for spatial resolution, UV absorption, and self-absorption in ImageJ. Afterwards, the DNG files were stacked together and saved as TIFF images. The TIFF images were then uploaded in Matlab and linear interpolation is made in between two slice images for making a 3D fluorescence intensity distribution. Tomographic views can be made and analyzed from different orthogonal planes. The quantitative 3D dose distribution can be obtained by converting the fluorescence intensity to absorbed dose using equation 3.18 (5.3).

## 7.3. Results and discussion

### 7.3.1. Radiochromic film measurements

Two 30x30 mm<sup>2</sup> MD-V3 films were attached to the front and back (X-ray entrance and exit sides) of a 40x40 mm<sup>2</sup> (id) cell that was situated behind the 10 mm square collimator at an SSD of 50 cm, as shown in figure 7.3. The films were irradiated with 200 kVp X-rays at an IC measured dose rate of 0.942 Gy/min for 20 minutes. Full colour images of the irradiated areas in the MD-V3 films are shown in figure 7.7 together with a scan in ImageJ of the red pixel level across the films. The half-widths of the images are 10.04 mm (front) and 10.90 mm (back) indicating expansion of the beam by 8.6% over the SSD change from 50 cm to 54.4 cm. This is in agreement with the increase by 8.8% expected on the basis of a conical beam.

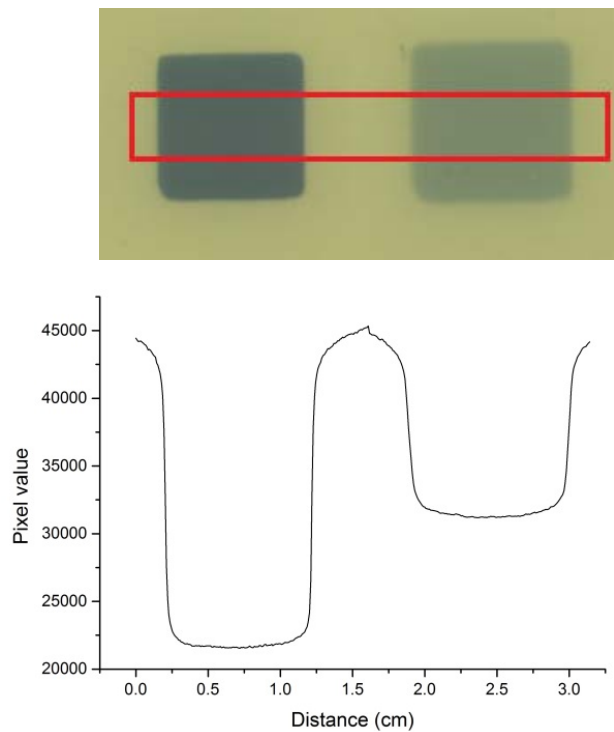


Figure 7.7. Upper: The coloration of MD-V3 films attached to the front (left) and back (right) of a 40 mm square (id) cell containing an RFG gel, on irradiation with a 10 mm collimated X-ray beam; dose ~20 Gy. Lower: A scan of the red pixel level across the upper images.

Measurements of the front and back optical absorptions have been made for an empty cell and one containing an RFG gel. The dose rates have been calculated using equation 7.2 (6.4 in chapter 6) with  $\mathbf{m} = 10.5$  Gy and  $\mathbf{h} = 0.182$  for 200 kVp X-rays from table 6.4 in chapter 6.

$$D'_{\text{calc}} = \mathbf{m}[1 - P(D)/P(0)]/[P(D)/P(0) - \mathbf{h}]/\mathbf{t}_{\text{ir}} \quad (7.2)$$

In 7.2,  $P(D)$  and  $P(0)$  are the pixel levels in the irradiated and unirradiated parts of the film,  $m$  and  $h$  are the median dose in Gy and the saturation level of  $P(D)/P(0)$  approached at high doses, and  $t_{ir}$  is the duration of the irradiation.

The dose rate decreases on penetrating the cell due to the conical nature of the beam and attenuation by the intervening media, i.e.

$$D'_b/D'_f = (SSD_f/SSD_b)^2 \exp[-(\mu\rho d)_w + (\mu\rho d)_c] \quad (7.3)$$

In 7.3 the subscripts b and f denote values at the back and front of the cell respectively,  $\mu$   $\text{cm}^2/\text{g}$  is the mass attenuation coefficient,  $\rho$   $\text{g}/\text{cm}^3$  the density and  $d$  cm the pathlength through the cell wall (subscript w) or cell contents (subscript c). The parameter  $(SSD_f/SSD_b)^2$  determined from the 8.6% increase in the width of the beam is 0.85. For the empty cell the attenuation due to the air in the cell ( $\mu \approx 0.15$   $\text{cm}^2/\text{g}$ ,  $\rho = 0.0012$   $\text{g}/\text{cm}^3$  and  $d = 4$  cm) is negligible. The attenuation due to the walls of the cell can therefore be determined from the empty cell values of 1.001 for  $D'_f$  and 0.666 for  $D'_b$  to be  $(\mu\rho d)_w = 0.244$ . Taking  $\rho \approx 2.3$   $\text{g}/\text{cm}^3$  for borosilicate glass and a wall thickness of 1.9 mm gives a value for the mass attenuation coefficient of 0.28  $\text{cm}^2/\text{g}$ . This is within the range for borosilicate glass of 0.30 to 0.12 for 50 to 200 keV photons (Hubbel and Seltzer, 1996). For the gel filled cell the values of  $D'_f$  and  $D'_b$  were 0.991 and 0.377 which gives a total attenuation parameter  $[(\mu\rho d)_w + (\mu\rho d)_c] = 0.804$ . Subtracting the value of  $(\mu\rho d)_w = 0.244$  determined above leaves  $(\mu\rho d)_c = 0.560$  for the attenuation due to the gel. With a gel density of 0.91  $\text{g}/\text{cm}^3$  and a pathlength of 40 mm this results in a gel mass attenuation coefficient for 200 kVp X-rays of 0.154  $\text{cm}^2/\text{g}$ . This value lies within the limits of 0.21 to 0.13 found for 50 to 200 keV photons in PMMA, a compound of very similar chemical composition (Hubbel and Seltzer, 1996).

In addition to the half-widths given above the 20 to 80% rise and fall of the absorption images (the "penumbra") have been measured and are 0.43 mm and 0.96 mm for the front and rear films. The ultimate spatial resolution of the film will be determined by the pixel resolution of the recording CCD device and the length of the polymer chains produced. The former corresponds to a distance of approximately 0.02 mm in the set-up used. Taking the degree of polymerization in the film to be similar to the value on the order of  $10^5$  monomer units per polymer chain gives a length scale also close to 0.02 mm. Therefore, the larger penumbra values determined can be mainly attributed to the edge dispersion of the collimated beam resulting in part from the 4 mm size of the tungsten target.

### 7.3.2. Bulk RFG gel measurements

The apparatus used for photographically recording fluorescent images from the bulk of an irradiated gel is shown in figure 7.4. Its use to make images of gels irradiated with single X-ray beams has been reported previously (Warman 2009). Here we show results obtained with a more complex radiation field of orthogonally-crossed round and square beams. The ultimate aim was

to produce three-dimensional images of this complex radiation field and this is dealt with in subsequent sections. In this section we present single images of the fluorescence from the bulk of an RFG gel and show that even these can contain information on the 3D shape of fluorescent objects.

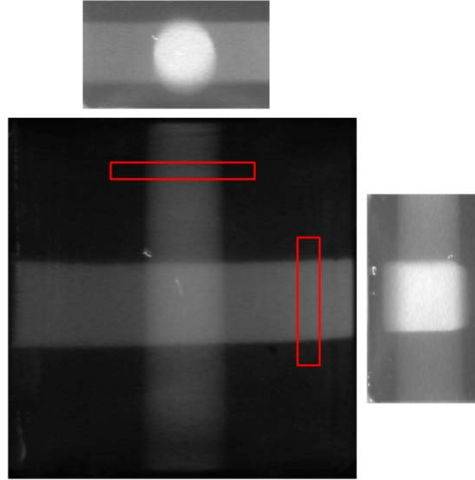


Figure 7.8. Main image: The JPEG blue pixel level of the fluorescence from an RFG gel contained in a 40x40 mm<sup>2</sup> cell irradiated with a 10 mm square beam (from right to left) and a 10 mm diameter round beam (from top to bottom) taken through the optically-flat bottom of the (lying) cell. Also images (top and right-side) taken through the sides of the (standing) cell in the direction of the beams. The red rectangles are the regions of the plot profile scans across the beams shown in figure 7.9.

Fluorescent images from a gel exposed to a 10 mm diameter round, collimated X-ray beam and a 10 mm square beam orthogonal to it are shown in figure 7.8. The upper and right-side images were taken with the cell standing and the camera looking along the axis of either the round or square beam respectively. The main image was taken through the (optically flat) bottom of the 40x40 mm<sup>2</sup> cell. This shows the increase in fluorescence intensity (radiation dose) at the crossing point of the beams. Even without the in-beam images it is possible to determine that one beam is square and the other round from the cross-section scans across the beams shown in red in figure 7.8. These scans are reproduced in figure 7.9 and clearly show the differences in shape. This is due to the fact that the fluorescence measured is the integral of that produced in the direction of observation.

For a round beam of radius  $r$  and uniform dose rate within the beam, the fluorescence is therefore proportional to the chord of the circular cross section, which gives for the change of the fluorescence intensity across the width of the beam,

$$I(w)/I_{\max} = [1 - ((w - w_{\max})/r)^2]^{0.5} \quad (7.4)$$

In 7.4,  $I_{\max}$  is the maximum central value with the dark background subtracted. The scan across the round beam in figure 7.9 left is seen to be fitted well with this relationship.

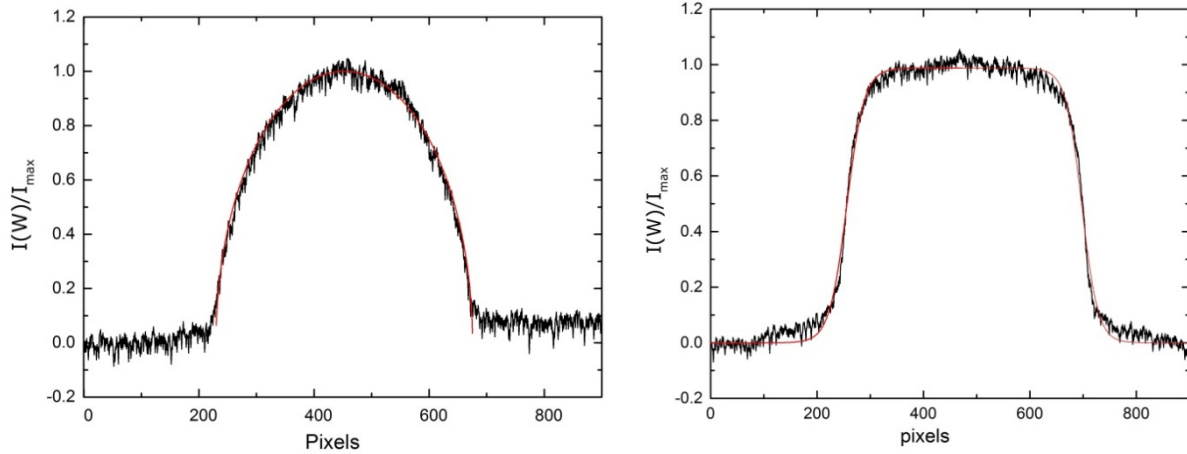


Figure 7.9. ImageJ scans of the pixel levels across the round (left) and square (right) beams as indicated by the red rectangles in figure 7.8. The red lines are fits to the data based on equations 7.4 and 7.5 for a round and a square beam respectively.

For a square beam with a nominal uniform dose distribution across the beam the fluorescence increases and decreases at both the edges of the beam. The change is sigmoidal and can be fitted with the Boltzmann sigmoid functions 7.5A and 7.5B for the increasing and decreasing edge respectively,

$$I(w)_I/I_{\max} = 1/(1 + \exp[-(w - W_I)/\delta W]) \quad (7.5A)$$

$$I(w)_D/I_{\max} = 1/(1 + \exp[(w - W_D)/\delta W]) \quad (7.5B)$$

The parameter  $W_I$  and  $W_D$  are the half points of the rise and fall sigmoids. Hence the difference  $(W_D - W_I)$  is the full width at half maximum FWHM,  $W$ , of the beam. The scan across the square beam shown in figure 7.9 can be fitted well with equations 7.5A&B using  $W = 444$  pixels and  $\delta W = 13$  pixels. The 20-80 percent penumbra of the beam is equal to  $2\ln 4\delta W = 36$  pixels or  $\sim 0.8$  mm.

### 7.3.3. Tomographic RFG gel measurements

The apparatus that enables a series of images of the fluorescence from thin (2 mm) slices of an irradiated RFG gel to be made was described in section 7.2.3.2 (figures 7.5 and 7.6). In this section we present results using this apparatus for a gel contained in a  $40 \times 40 \text{ mm}^2$  square cell of glass wall thickness  $\sim 2$  mm. The gel consisted of  $\sim 70$  mL of 20% pre-polymerized tertiary-butyl acrylate containing 0.30 mM ( $\sim 50$  ppm) maleimido-pyrene. The gel was perfectly clear and free of coloration in the visible ( $>400$  nm) even after irradiation, as shown in figure 7.1. By rotating the cell through 90 degrees on the translation stage slices of the irradiated gel could be made at position  $z$  parallel or perpendicular to the beam penetration direction  $d$ , as illustrated for a single beam in figure 7.10.

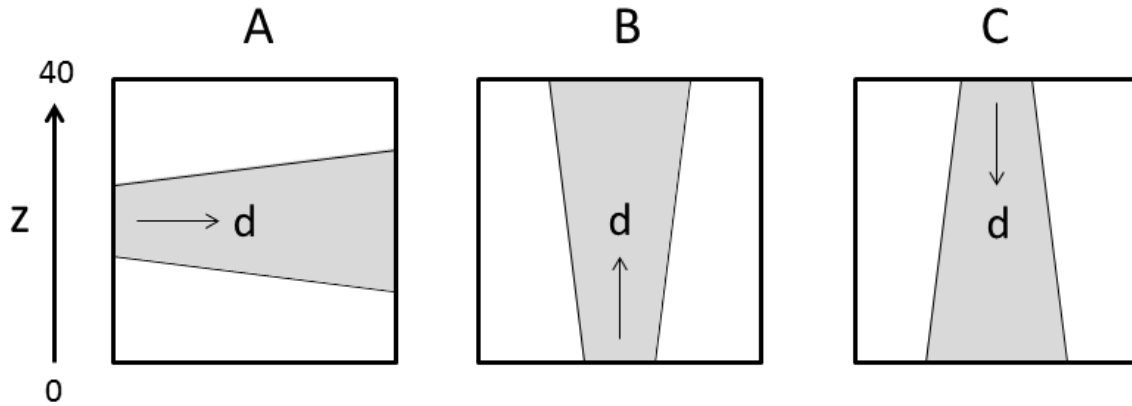


Figure 7.10. Views from above of the possible orientations for making slit scans of an irradiated 40 mm square gel by rotating the cell through 90 degrees.  $z$  is the distance from the slits to the side of the cell facing the camera (see figure 7.5).  $d$  is the penetration depth of the X-rays in the gel. The conical expansion of the beam is exaggerated in the figure.

#### 7.3.3.1. Single, square X-ray beam, lateral view

The gel was initially irradiated centrally from one side with a 10 mm square, collimated 200 kVp X-ray beam for 20 minutes at an incident dose rate of  $\sim 1.0$  Gy/min. A tomographic slice of the fluorescence taken at close to the central axis of the beam,  $z \approx 20$  mm in figure 7.10 configuration A, is shown in figure 7.11A. This illustrates qualitatively the gradual decrease in fluorescence intensity (dose rate) with penetration depth,  $d$ , in the gel due to attenuation of the X-rays. In addition the slight (ca 6%) conical beam expansion within the gel, as found with the radiochromic films in section 7.3.1, can be seen. The decrease in intensity is quantified in the scan of the DNG blue pixel level along the axis of the beam, shown in the lower part of figure 7.11A.

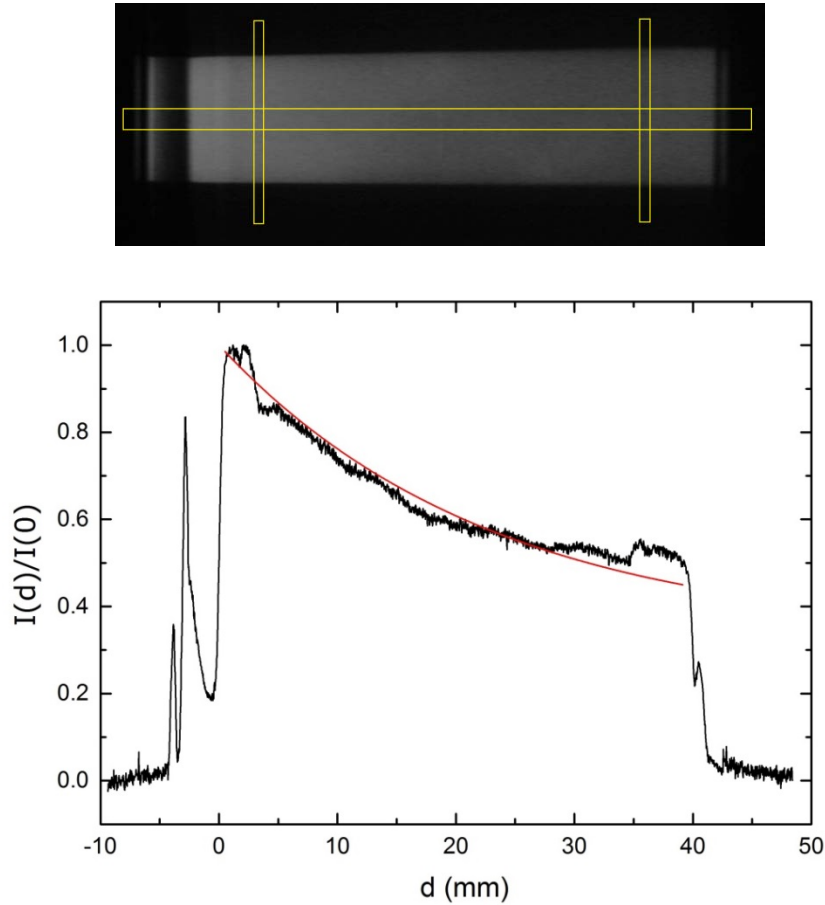


Figure 7.11A. Upper: The JPEG image of a 2 mm tomographic slice taken at the center ( $z = 20$  mm) of a 10 mm square X-ray beam incident on an RFG gel from the left; configuration A in figure 7.10. Lower: A rectangular scan of the blue pixel level of the DNG file along the axis of the beam. The sharp peak at -2 mm is due to fluorescent light scattering at the glass/air interface.

The decrease in fluorescence with X-ray penetration depth in the gel that can be seen in figure 7.11A lower reflects the gradual change in dose rate,  $D'(d)$ . This decreases due to conical beam expansion by a factor  $\Phi_{\text{con}} = [50.2/(50.2 + d)]^2$  and by X-ray attenuation with mass attenuation coefficient  $\mu$   $\text{cm}^2/\text{g}$ .

$$D'(d) = D'(0)\Phi_{\text{con}}\exp(-\mu\rho d) \quad (7.6)$$

$D'(d)$  can be calculated from the radio-chromic film data in section 7.3.1. using the mass attenuation coefficient values of  $0.28 \text{ cm}^2/\text{g}$  for the 0.19 cm thick glass wall of the cell ( $\rho = 2.3 \text{ g/cm}^3$ ) and  $0.154 \text{ cm}^2/\text{g}$  for the gel ( $\rho = 0.91 \text{ g/cm}^3$ ) together with the initial dose rate of 1.00 Gy/min as measured by the front RC film. Selected values of  $D'(d)$  are listed in table 7.1.

Table 7.1. A selection of calculated values of I(d)/I(0) based on equation 7.10 with dose rates determined from the RC film measurements. The correction factors for beam attenuation,  $\exp(-\mu\rho d)$ , conical beam expansion,  $\Phi_{\text{corr}}$ , and UV attenuation,  $UV_{\text{corr}}$ , are also given together with measured values of I(d)/I(0).

d (cm)	$\exp(-\mu\rho d)$	$\Phi_{\text{con}}$	D'(d) (Gy/min)	D'(d)/ D'(0)	$UV_{\text{corr}}$	I(d)/I(0)	
						calc	meas
0	1	1	0.885	1	1	1	1
1	0.869	0.961	0.739	0.835	0.943	0.76	0.76
2	0.756	0.925	0.618	0.698	0.925	0.61	0.60
3	0.657	0.890	0.517	0.584	0.943	0.51	0.55
4	0.571	0.858	0.434	0.490	1	0.45	0.49

The relationship between the fluorescence intensity and the dose rate is given by equation 5.1 in chapter 5 that, on substitution of  $D't_{\text{ir}}$  for  $D$ , becomes,

$$I(d) = [1 + AD'(d)t_{\text{ir}}]KD'(d)t_{\text{ir}} \quad (7.7)$$

with  $t_{\text{ir}}$  the X-ray exposure time. The parameter  $A$ , which defines the super-linearity on dose found, is  $0.045 \text{ Gy}^{-1}$  (section 5.3.1). The parameter  $K$ , which defines the limiting linear dependence on dose is dependent on dose rate and MPy concentration  $[S]$  according to equation 7.8 (equation 5.3 in chapter 5).

$$K = C\Gamma/(1 + \sqrt{D'(d)/E[S]}) \quad (7.8)$$

In 7.8  $C$  is the fluorescence sensitivity factor,  $\Gamma$  is the yield of free radicals in moles per liter per gray and  $E = k_E/(2k_t\Gamma)^{0.5}$  with  $k_E$  and  $k_t$  the rate coefficients of free radical reaction with MPy and radical-radical combination. The value of  $E$  has been determined to be  $0.41 \text{ s}^{0.5} \text{ mM}^{-1} \text{ Gy}^{-0.5}$  for the gel (section 5.3.5.1.). Finally the dip by 7.5% in the UV intensity,  $I_{\text{UV}}(d)/I_{\text{UV}}(0) = UV_{\text{corr}}$ , given by 7.9 (equation 3.2 in chapter 3) with  $OD = 0.087 \text{ cm}^{-1}$  must be taken into account.

$$UV_{\text{corr}} = \frac{\exp[-2.30dOD_{\text{UV}}] + \exp[-2.30(4 - d)OD_{\text{UV}}]}{1 + \exp[-2.30 \times 4 \times OD_{\text{UV}}]} \quad (7.9)$$

Combining all of the above results in the following expression for the expected dependence of the fluorescence on penetration distance for a 20 minute irradiation with  $D'$  in Gy/min.

$$\frac{I(d)}{I(0)} = \frac{[1 + 0.9D'(d)] [1 + 1.05\sqrt{D'(0)}] D'(d)}{[1 + 0.9D'(0)] [1 + 1.05\sqrt{D'(d)}] D'(0)} UV_{\text{corr}}(d) \quad (7.10)$$

In 7.6 and 7.9 distances are in cm and  $D'$  is in Gy/min. The red line drawn in figure 7.11A was calculated using 7.10 and the above parameters. Sample values are given in table 7.1. The agreement with the measured dependence of the fluorescence on depth is seen to be good.



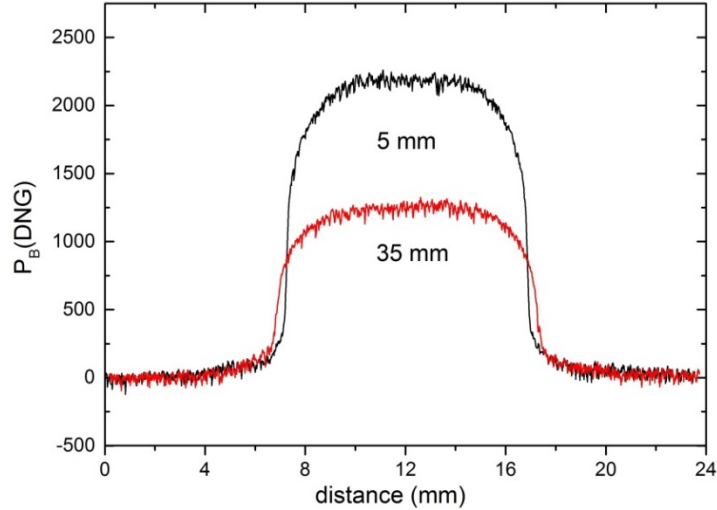


Figure 7.11B. Lateral scans of the fluorescence at approximately 5 mm and 35 mm into the beam as given in the figure. Illustrated by the vertical rectangles on the left and right in figure 7.11A upper.

In figure 7.11B are shown the lateral beam scans made at 5 mm and 35 mm penetration into the gel. The half widths of the beam determined at these positions are 579 and 621 pixels. This corresponds to an expansion of the beam by a factor of 1.058 over the 30 mm distance difference, which is in agreement with the factor of  $53.7/50.7 = 1.059$  expected for a conical beam. The 20 to 80 percent rise and fall distances ("penumbra") of the beam intensity are 40 and 56 pixels at 5 mm and 35 mm depth respectively. This corresponds to 0.67 and 0.94 mm using a pixel resolution of 59.4 pixels/mm. These agree with the penumbra values of RC films measured at the front and back sides of the glass cell, i.e. 0.43 mm and 0.96 mm. Over the 30 mm penetration distance the fluorescence intensity decreases from 2140 to 1210 blue-pixel-levels/second or 0.57%. This is in agreement with expectations based on equation 7.10.

#### 7.3.3.2. Single, square X-ray beam, longitudinal views

Slit scans were also made in the configurations B and C in figure 7.10. Forty slices, 1 mm apart were imaged. Sample slices at depths  $z$  of 5, 15, 25 and 35 mm are shown in figure 7.12. For both beam orientations the images show the expected decrease in fluorescence intensity with  $d$ , the penetration depth of the X-rays. What can also be seen is an increase in the size of the beam cross-section with increasing  $z$  in both cases. From the RC film and lateral scan measurements in previous sections, a ~6% increase in beam diameter due to the conical nature of the beam would have been expected with increasing  $d$  over 30 mm. However, the increase is considerably larger than 6% and, in the case of orientation C, it is even in the wrong direction. This can be explained if the spatial sensitivity of the images, in pixels per mm, is not constant but increases with  $z$ , i.e. with the length of gel between the slits and the camera.

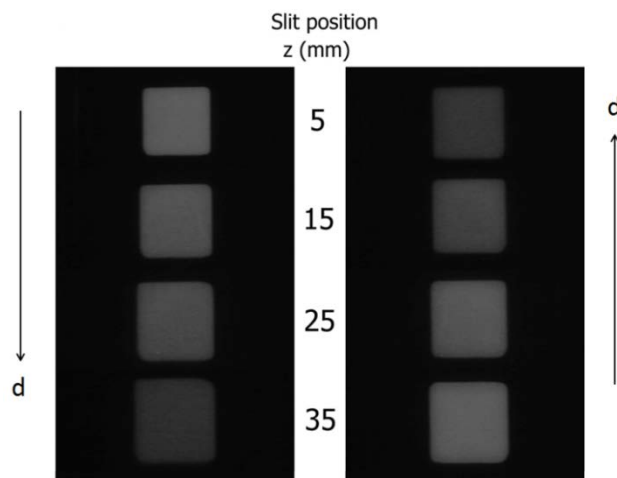


Figure 7.12. Samples of tomographic images of the fluorescence of 2 mm slices of the irradiated gel at different slit positions,  $z$ , with the penetration depth of the X-rays  $d = z$  mm (left) and  $d = (40 - z)$  mm (right) corresponding to configurations B and C in figure 7.10. A time-lapse movie of the full 40 slice scan can be viewed [here](#).

ImageJ scans of the DNG images of all 40 slices have been made and the selected values of the intensity of the beam,  $I_M$  (blue pixel level), and the measured half-width,  $W_m$ , in pixels are listed in table 7.2. Also listed are the actual beam widths in mm calculated on the basis of the conical expansion,  $W_c$ , as verified by the film measurements. The ratio  $W_m/W_c$  shown in the table gives then the  $z$  dependence of the spatial sensitivity,  $\Pi(z)$  in pixels per mm. This is seen to vary from 53.4 pixels per mm for  $z = 0$  to 66.6 pixels per mm for  $z = 40$ . The values obey quite well the linear dependence  $\Pi(z) = A + Bz$  with  $A = 53.7$  and  $B = 0.286$  derived from the best linear fit shown in figure 7.13.

Table 7.2. Selected measurements, from tomographic slices in scans 1 and 2, (B and C in figure 7.10), of the beam intensity,  $I$  (blue pixel level, shutter time 8 s), the beam half-width,  $W_m$ , in pixels (px), and the 20% to 80% "penumbra" values  $\delta W$ . Also listed is the beam width based on a conical divergence,  $W_c$  mm.

$z$ (mm)	Scan 1					Scan 2				
	$I_1$	$W_m$ (px)	$W_c$ (mm)	$W_m/W_c$ (px/mm)	$\delta W$ (px)	$I_2$	$W_m$ (px)	$W_c$ (mm)	$W_m/W_c$ (px/mm)	$\delta W$ (px)
0	2299	538	10.00	53.8	26	1228	571	10.80	52.9	45
5	2106	560	10.10	55.4	23	1165	594	10.70	55.5	43
10	1915	579	10.20	56.8	23	1289	602	10.60	56.8	37
15	1732	603	10.30	58.6	25	1405	605	10.50	57.6	43
20	1710	620	10.40	59.6	36	1586	614	10.40	59.0	35
25	1395	636	10.50	60.6	32	1659	626	10.30	60.8	30
30	1254	652	10.60	61.5	62	1801	637	10.20	62.5	30
35	1112	673	10.70	62.9	72	1899	647	10.10	64.1	24
40	1223	706	10.80	65.4	80	1970	677	10.00	67.7	45

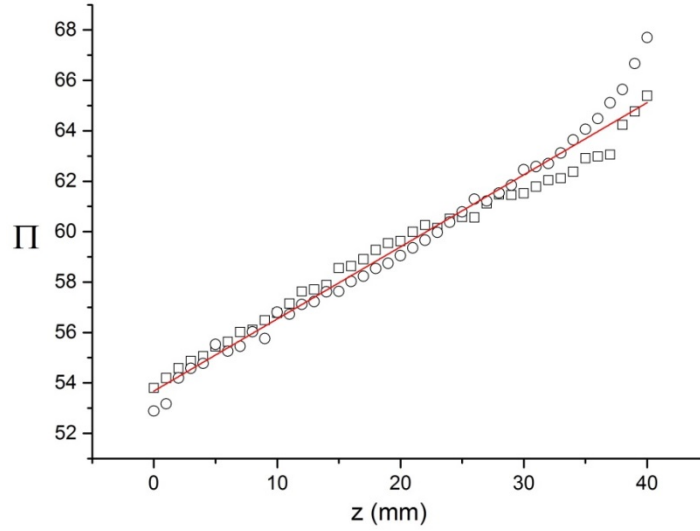


Figure 7.13. A plot of the pixel resolution,  $\Pi = W_m/W_c$  pixels per mm, as a function of the slit position  $z$  for scans made in the configurations B (squares) and C (circles) in figure 7.10. The red line is a linear fit to both data sets.

The intensity of the fluorescence in scans B and C,  $I_1(z)$  and  $I_2(z)$ , should be given by the following expressions with  $z$  in cm:

$$I_1(z) = I_1(0)\exp(-\beta z - 2.30OD_{sa}z)[W_{1c}(0)/W_{1c}(z)]^2/[\Pi(z)/\Pi(0)]^2 \quad (7.11)$$

$$I_2(z) = I_2(0)\exp(\beta z - 2.30OD_{sa}z)[W_{2c}(0)/W_{2c}(z)]^2/[\Pi(z)/\Pi(0)]^2 \quad (7.12)$$

In the above,  $\beta$  is the attenuation coefficient of the fluorescence due to X-ray attenuation in the medium,  $OD_{sa} \text{ cm}^{-1}$  is the optical density of the gel towards self-absorption of the fluorescence, and  $\Pi(z)$  is the number of pixels per cm. Note, no correction is considered necessary for the UV variation across the beam since this is less than 1% over the ~10 mm width and the same for all  $z$  values.

Dividing 7.11 by 7.12 results in the relationship 7.13. This operation removes dependences on the variable pixel spatial sensitivity and the self-absorption of the fluorescence.

$$\frac{I_1(z)W_{1c}(z)^2}{I_2(z)W_{2c}(z)^2} = \frac{I_1(0)W_{1c}(0)^2}{I_2(0)W_{2c}(0)^2} \exp(-2\beta z) \quad (7.13)$$

A plot of the logarithm of the left hand side of 7.13 against  $z$  should be a straight line of slope  $-2\beta$  which is shown to be the case in figure 7.14. From the linear fit to the data shown  $\beta = 0.151 \text{ cm}^{-1}$  which is close to the value of  $0.140 \text{ cm}^{-1}$  determined for X-ray attenuation in the gel from the RC film measurements in section 7.3.1.

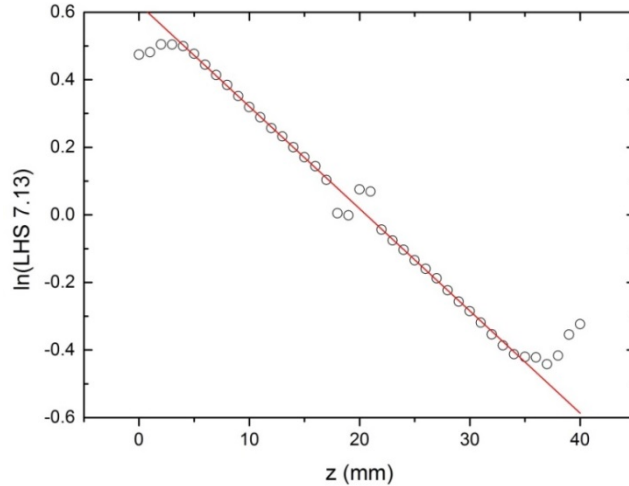


Figure 7.14. A plot of the natural logarithm of the left hand side of equation 7.13 (LHS 7.13) against slit position  $z$ . The red line is a best straight line fit. Deviations at the outer limits are due to optical anomalies close to the gel/glass interfaces.

### 7.3.3.3. Crossed square and round beams

To create a somewhat more complex radiation field we have carried out measurements on a  $40 \times 40 \times 40 \text{ mm}^3$  RFG gel which was irradiated with a 10 mm square X-ray beam followed by orthogonal irradiation with a 10 mm diameter round X-ray beam with incident doses of  $\sim 20 \text{ Gy}$  at  $\sim 1 \text{ Gy/min}$  for both beams. A photograph of the gel in room lighting (figure 7.1) shows that it remains clear and colorless after irradiation. A bulk image of the fluorescence of the gel taken through the bottom of the cell was shown and discussed in section 7.3.2.2 (figure 7.8). Here we present results of tomographic scans of the gel with 2 mm slices taken every mm along the beam axis of either the round beam (scan 1) or the square beam (scan 2). The conditions of the scans are illustrated in figure 7.15.

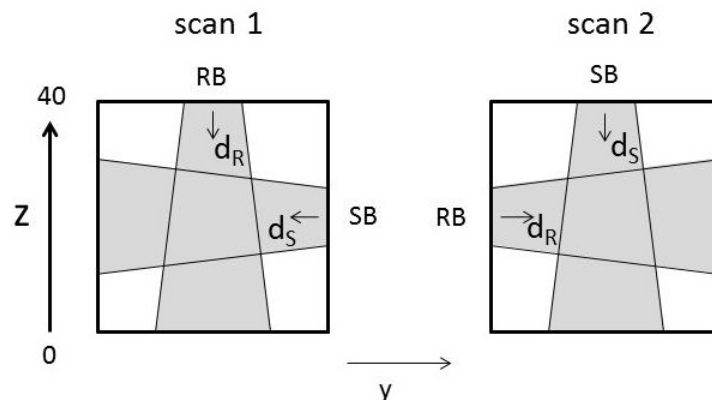


Figure 7.15. The conditions under which the double-beam irradiated RFG gel was scanned in the  $z$  direction: RB and SB indicate the incidence of the round and square X-ray beams with  $d_R$  and  $d_S$  the relative penetration depths. The view is from above the translation stage and the cell was simply turned through 90 degrees to obtain the separate scans.

Time-lapse movies made from all 40 slices of scans 1 and 2 in figure 7.15 can be viewed [here](#) under "Crossed beams slices scan along round beam" and "Crossed beams slices scan along square beam". Some individual slice images are shown in figure 7.16 at z values of 5, 15, 20, 25 and 35 mm. The increase in fluorescence intensity at the crossing point of the beams can be seen. The complexity is apparent from the difference between the view of the square, y-axis beam crossing the round, z-axis beam (scan 1) and the round, y-axis beam crossing the square, z-axis beam (scan 2) particularly at the edges of the crossing point at z = 15 and 25.

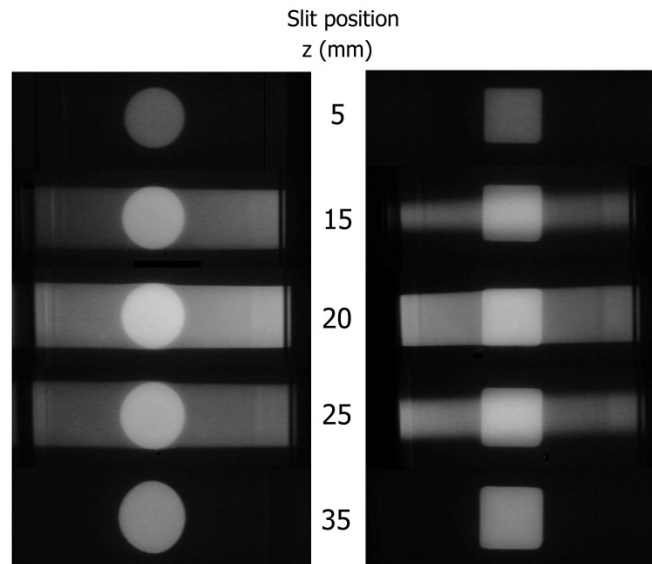


Figure 7.16. JPEG blue pixel level images of the fluorescence from slices of an RFG gel irradiated with crossed round and square 10 mm beams taken at the slit positions (z values) shown. For the gel and beam orientations see figure 7.15, scan 1 (left), scan 2 (right). Time-lapse movies of the full 40 slice scans in the direction of the round and square beams can be viewed [here](#).

Profiles of the fluorescence intensity from left to right along the y-axis of the images shown in figure 7.16 were derived from the raw DNG files and are shown in figure 7.17. The maximum intensity found, as expected, at the crossing point of the two beam axes,  $z = y = \sim 20$  mm is in both cases more than double the value for an individual beam from interpolation of the y dependence of the background single beam dependence at  $y = 20$  mm ( $\sim 1500$  pixels in figure 7.17). That the factor is greater than 2 for two beams with the same central dose rate is in agreement with the superlinear dependence of  $I_{IM}$  on dose found in previous chapters.

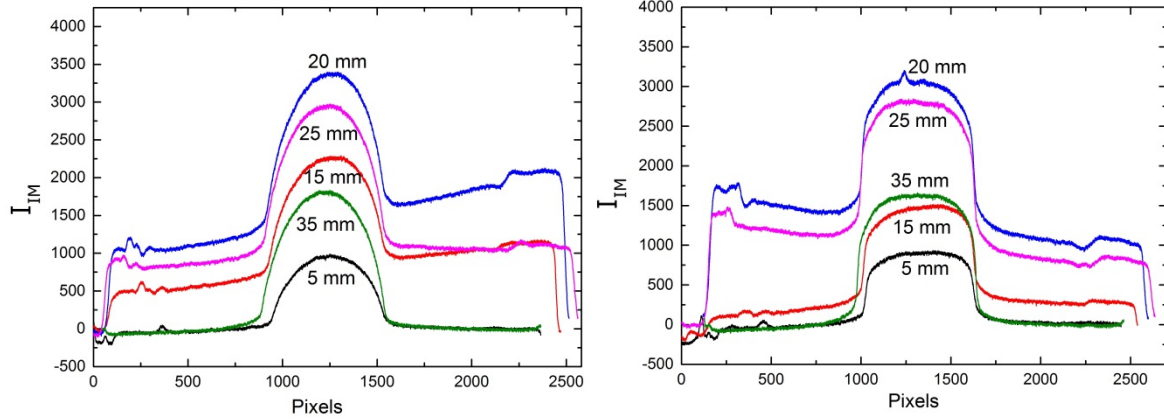


Figure 7.17. Profiles along the y-axis of the fluorescence intensity,  $I_{IM}$ , from the DNG files of the images in figure 7.16 at the slit positions given beside the scans.

### 7.3.4. 3D image reconstructions

In section 7.3.3 results were presented of tomographic fluorescence images of a radio-fluorogenic gel irradiated with collimated X-ray beams using the slit-scanning apparatus shown in figure 7.5. In section 7.2.5 it was explained how a series of such two-dimensional images could be processed to provide three-dimensional images of the fluorescence (chemical change) resulting from the passage of such beams through the gel medium. In this section we provide examples of such 3D reconstructions with 3D animation movies provided [here](#).

#### 7.3.4.1. Pictorial representations

For pictorial representations the JPEG files of the tomographic slices were used. Firstly because they have been pre-adjusted to provide visually relevant images when displayed, but mainly because they have been compressed to relatively small 8-bit records which are much easier to handle in video representations when dealing with a large number of files. In figure 7.18 are shown projections from two different angles of the 3D reconstruction of the track of the single square beam using the "3D Viewer" plug-in in ImageJ with the stack of 40 JPEG slices taken 1 mm apart in scan B figure 7.10.

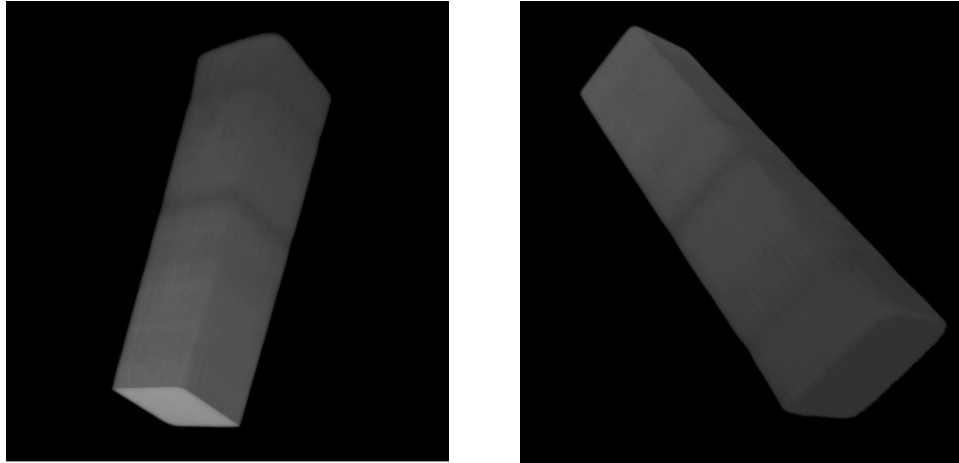


Figure 7.18. Projections of the 3-dimensional reconstruction of the square beam produced by "3D Viewer" in ImageJ from the 40 slices taken in scan B, figure 7.10. A pseudo-3D animation of the beam envelope is to be found [here](#).

As mentioned in section 7.2.5 the 3D Viewer reconstruction produces an envelope of the beam with no visual information as to the "structure" within. This lack of internal visual information is clearly apparent in the reconstruction in figure 7.19 of the crossed, round and square beams derived from scan 1 in figure 7.15. Here the more than a factor of 2 increase in intensity that can be seen in the individual slices (see figures 7.16 and 7.17) is hidden from view by the outer surface envelope of the beams.

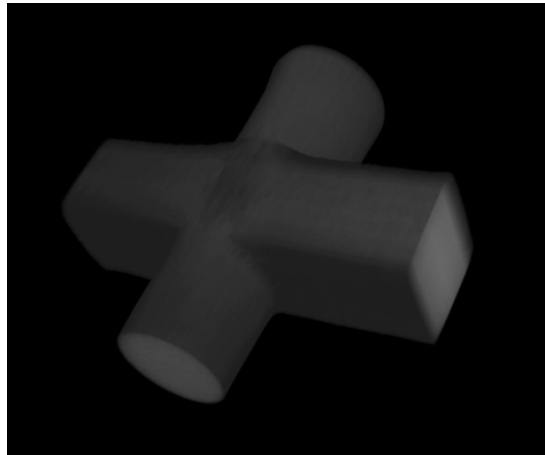


Figure 7.19. Projections of the 3-dimensional reconstruction of crossed beams using "3D Viewer" in ImageJ with a stack of 40 slices taken in scan 1, figure 7.15 along the axis of the round beam. A pseudo-3D animation is to be found [here](#).

To resolve the outer envelope problem we have used the software of BioImageXD that allows the pixels to be transparent. In this way a translucent 3D image is obtained, as shown in figure 7.20. In this, one can now clearly see the increased intensity in the overlap region of the beams.

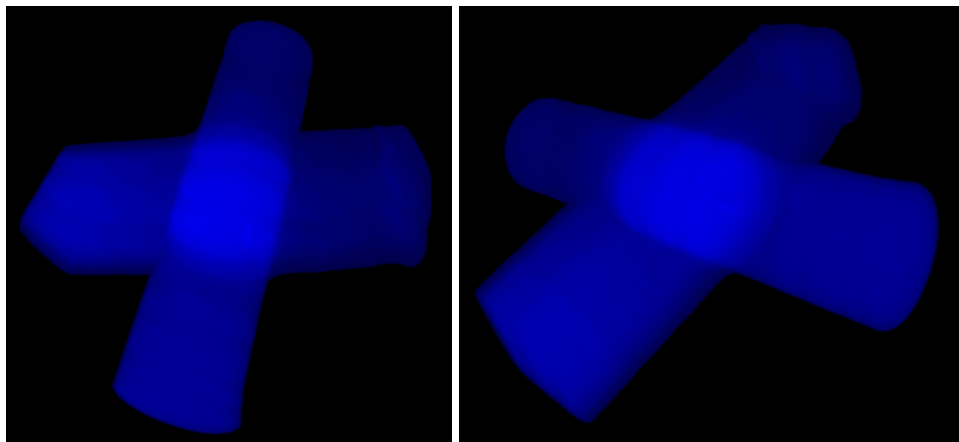


Figure 7.20. Projections of the 3-dimensional reconstruction of crossed beams using "BioImageXD" with a stack of 40 slices taken in scan 1, figure 7.15 along the axis of the round beam. A pseudo-3D animation is to be found [here](#).

#### 7.3.4.2. Quantitative dissections

The raw DNG files of the tomographic slices were used to provide quantitative measurements of the fluorescence intensity in the form of planar dissections of a 3D reconstruction. The individual files were first corrected in ImageJ for UV excitation light absorption in the x-y plane and self-absorption in the z direction due to passage of the fluorescence through the gel over a distance z mm. The blue channels of the stacked images were saved as TIFF files and further processed in Matlab using in-house software to perform linear interpolation between slices, and to take into account the variation in the pixel spatial response,  $\Pi(z)$  pixels per mm, in the voxel dimensions. Figure 7.21 is a 3D representation based on the DNG files with orthogonal dissection planes shown.



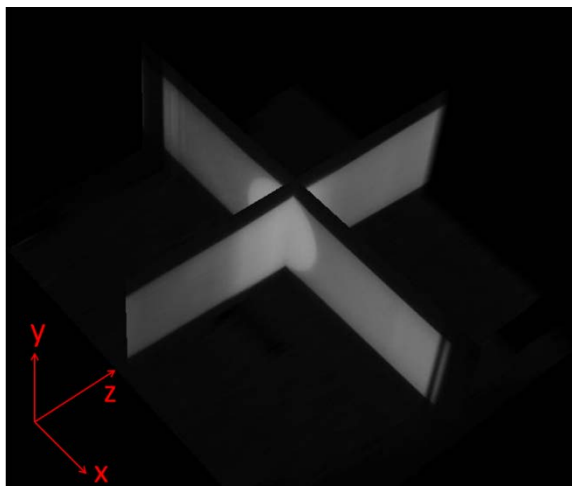


Figure 7.21. Orthoslices along the axes of crossed round and square X-ray beams from a 3D reconstruction using a 40-slice stack of corrected, raw DNG files from the single z-axis scan #1 in figure 7.15. A video of a scan of the x-z plane along the y-axis is presented [here](#).

In figure 7.22 is shown the intensity dependence in the x-z plane close to the crossing point of the beams. This view could only be obtained in the bulk image measurements (see figure 7.8) by making an image through the bottom of the cell. A movie of the image of the x-z plane moving along the y axis is shown on the website as "3D crossed-beams x-z plane scan along y".

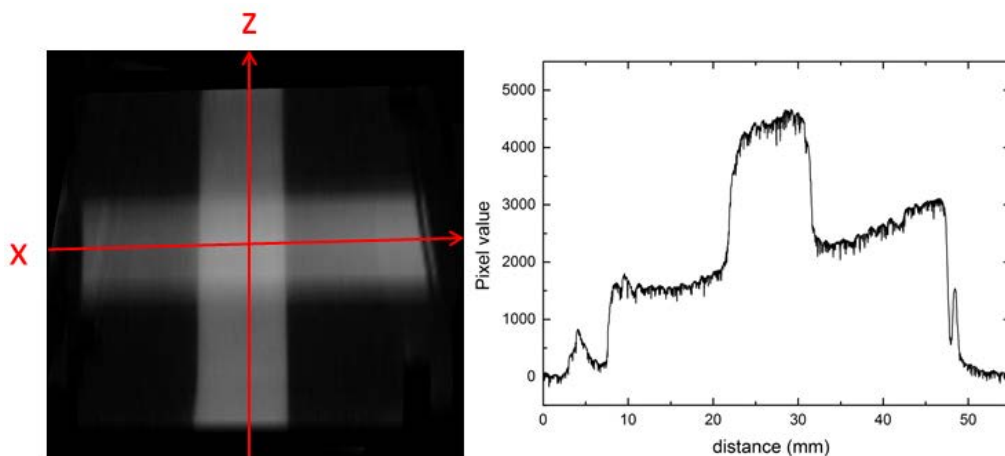


Figure 7.22. Left: The fluorescence intensity in the x-z plane close to the crossing point of the beams driven from a 3D reconstruction using the 40 tomographic slices from scan 1 in figure 7.15. Right: Scan of the fluorescence intensity along the x-axis.

The step of converting the intensity data to absolute 3D dose and dose rate information has not as yet been carried out and is ongoing together with the development of a fully automatic tomographic slit-scanning apparatus.

## 7.4. Conclusions

In this chapter we demonstrate the application of a radio-fluorogenic (RFG) gel to the monitoring of the energy deposition (chemical change) resulting from the passage of collimated X-ray beams. After irradiation, the gel remains clear and colorless in normal room lighting but in near-UV light (~380 nm) the tracks of the beams fluoresce with intensity proportional to the local dose. Digital photographic images of the fluorescence have been made either of a bulk 40x40x40 mm<sup>3</sup> gel volume or a series of 2 mm thick tomographic slices using a novel slit-scanning technique, described in section 7.2.3.2. Measurements have been carried out using a single, 10 mm square beam and a square beam orthogonally crossed by a 10 mm diameter round beam. Even in bulk images, round and square beams can be differentiated by the shape of lateral fluorescence scans across the beams that are dome-shaped and rectangle-shaped respectively.

Full 3D images can be constructed from a series of tomographic slices and viewed in pseudo-3D animation videos as shown [here](#). The reconstructions can be viewed as beam envelopes with no information as to the internal beam structure or as translucent images with pixel transparency to reveal internal variations of fluorescence intensity. For the 3D animations the JPEG files of the slices are used. For quantitative representations of the fluorescence intensity the raw DNG files are used to provide dissection planes through the 3D reconstruction. A number of processing procedures are required prior to reconstruction these are; correction for the self-absorption of the fluorescence in the z direction, for the UV light variation in the x-y plane, and for the change in pixel spatial sensitivity with z, plus a linear interpolation of the pixel level between slices. Conversion of the fluorescence intensity values into a local dose rate using relationships similar to those developed for homogeneous irradiation of solution and gel samples has not yet been implemented. More research into the dose and dose rate dependence of beam results is required for this.

In the work reported here the slit-scanning apparatus was operated manually. On the basis of the present results, a fully automated, computer controlled system is in development. By integrating this with image processing software, we hope ultimately to provide a user-friendly method of 3D imaging and dosimetry of complex radiation fields that is acceptable to the clinical radiotherapy community.

## References

Kankaanpää, P., Paavolainen, L., Tiitta, S., Karjalainen, M., Päivärinne, J., Nieminen, J., Marjomäki, V., Heino, J., White, D.J., 2012. BioImageXD: an open, general-purpose and high-throughput image-processing platform. *Nature methods* 9, 683-689.

Rasband, W.S., 1997. ImageJ. US National Institutes of Health, Bethesda, MD.

Rueden, C.T., Eliceiri, K.W., 2007. Visualization approaches for multidimensional biological image data. *Biotechniques* 43, 33-36.

Hubbell, J.H., Seltzer, S.M., 1996. Tables of X-ray mass attenuation coefficients and mass energy-absorption coefficients from 1 keV to 20 MeV for elements  $Z = 1$  to 92 and 48 additional substances of dosimetric interest. NISTIR 5632 (<http://www.nist.gov/pml/data/xraycoef/index.cfm> )

Warman, J.M., Luthjens, L.H., de Haas, M.P., 2009b. In-situ radiation dosimetry based on Radio-Fluorogenic Co-Polymerization, *Journal of Physics: Conference Series* 164, 012048.

# Summary

Polymer gels that change their chemical and/or physical properties upon exposure to ionizing radiation can in principle be applied as 3D radiation dosimeters as long as this change can be read out. To be qualified as a 3D radiation dosimeter in the clinic, a gel dosimeter should ideally meet the following requirements: 1) be readily available or easily and reproducibly prepared; 2) be stable and homogenous in time and space; 3) be (near-) tissue equivalent with a volume comparable to that applied in the clinic; 4) guarantee the quality assurance (QA) requirements of (sub)millimeter isotropic spatial resolution with an accuracy of 3% ( $3\sigma$ ) and a precision of 1% ( $3\sigma$ ); 5) be dose rate and energy independent and free from effects of temperature and pressure; 6) give an immediate (measurable) response. Different read-out techniques such as magnetic resonance imaging (MRI) and optical computed tomography (OCT) can be applied so that 3D information on the absorbed dose in the gel can be reconstructed. Many types of gel dosimeters have been investigated but gel dosimetry is still considered to be in the research phase and the introduction to routine clinical use is proceeding slowly. The radio-fluorogenic (RFG) gel studied in this thesis has several advantages over other polymer gels: it has only two components, i.e. the monomer tertiary-butyl acrylate (TBA) and the fluorogenic compound maleimido-pyrene (MPy), and is therefore more easily reproduced; it is optically clear after irradiation and the radiation-induced fluorescence is easily measured. In order to evaluate the potential of this gel in the clinic we have performed detailed research on the properties and behaviour of the RFG gel as dosimeter in this thesis.

In chapter 1, background information and literature relevant to this thesis are given including diagnostic methods, radiation therapy treatment procedures, and presently used or proposed dosimetry techniques. A brief history of previous work done on RFG gels before this thesis is also given in addition to an overview of the contents of the thesis..

In chapter 2, the aim of investigating radiation-induced polymerization using gels prepared by TBA alone is to provide a radiation-chemical basis of the gel for radio-fluorogenic dose-imaging applications. The dose and dose rate dependences are studied since these influence both the passive gel formation procedure and the active dosimetric co-polymerization process in a radio-fluorogenic solution or gel. The fractional monomer-to-polymer conversion,  $C_M$ , determined gravimetrically, increases super-linearly with dose,  $D$  Gy. Up to  $C_M \approx 40\%$ , and over the dose rate range  $D' = 3.5$  to  $49$  cGy.s<sup>-1</sup>, the dose dependence is given by  $C_M = [1 + AC_M]KD/\sqrt{D'}$  with  $K = 1.43 \times 10^{-3}$  Gy<sup>-0.5</sup>.s<sup>-0.5</sup> and  $A = 0.70$ . For  $C_M \geq 15\%$  the gel is quasi-rigid, displaying little tendency to flow on a timescale of an hour or more. TBA has two functions in the gel: first it forms a quasi-rigid, transparent 3D gel. This process is controllable and

reproducible. Second, TBA undergoes radiation-induced co-polymerization with a fluorogenic compound present within the gel network which will be further investigated in chapter 3.

In chapter 3, the radiation-induced changes in the physical and chemical properties of a radio-fluorogenic solution of MPy in TBA are presented. The solution remains optically clear and displays a permanent fluorescence in UV light after exposure to high-energy ionizing radiation. RFG solutions with different MPy concentrations were investigated and  $C_M$  was found to display a superlinear dependence on dose, as for TBA alone. However, the presence of MPy had a negative effect on the absolute value of  $C_M$  for the same radiation conditions. This reduction in overall polymer yield by MPy is attributed to a much slower propagation rate for maleimido radical chain ends than for the acrylate radicals of TBA. The blue pixel level,  $P_B$ , of raw DNG images of the fluorescence was found to be linear with camera shutter time and the intensity,  $I_{IM}$ , is defined as  $P_B/s$ .  $I_{IM}$  was found to have a superlinear dependence on dose and can be fitted using the relationship  $I_{IM} = (1 + A_{IM}D)K_{IM}D$ , where  $K_{IM}$  is the slope of the low-dose limiting linear dependence of  $I_{IM}$  on dose, and  $A_{IM}D$  is the superlinear increase of  $I_{IM}$  with dose. After correction for attenuation of the UV excitation light and self-absorption  $K_{IM}$  obeys the relationship  $K_{IM} = C\Gamma/(1 + \sqrt{D}/E[S])$  with  $E = 0.453 \text{ s}^{0.5} \cdot \text{mM}^{-1} \cdot \text{Gy}^{-0.5}$  and  $C\Gamma = 111 \text{ pixel-level} \cdot \text{s}^{-1} \cdot \text{Gy}^{-1}$  for the detection conditions used. This enables the determination of an unknown dose rate when the RFG solution is used as a dosimetric medium.

In chapter 4, the compound N-(1-pyrenyl)acrylamide (PyAM) is investigated with the hope of eliminating the negative effect that MPy has on monomer conversion and therefore on the fluorescence yield. In TUD-synthesized PyAM the maleimide group of MPy is replaced by an acrylamide group. The reasoning was based on the expectation that the acrylamide group in PyAM would polymerize faster than the maleimide group in MPy and close to the acrylate group of TBA. PyAM was in fact found to be fluorogenic with a similar emission spectrum when copolymerized to that for MPy. The fluorescence intensity was also superlinear with dose and a factor of 3 or more higher than for MPy under similar conditions of concentration and dose. Unfortunately the extinction coefficient of PyAM in the near UV (the excitation region) was found to be an order of magnitude larger than that of MPy. This results in a strong attenuation of the excitation light even within a 1 cm wide cell even for a solute concentration of  $\sim 1 \text{ mM}$ . This makes its application in 3D dosimetry, even in small sample volumes, less practical due to the large spatially dependent corrections for UV attenuation. Furthermore, PyAM shows an even greater negative effect on the degree of monomer conversion than MPy. Therefore it was decided to stay with commercially available MPy in the rest of this thesis.

In chapter 5, reformed RFG gels were investigated and compared with RFG solutions. The reformed gels were prepared by first irradiating the monomer TBA, which becomes quasi-rigid for  $\sim 15\%$  monomer-to-polymer conversion ( $C_M$ ). After removal of remaining monomer by evacuation, the gel is reformed by adding a volume of an MPy in TBA solution to the remaining polymer equal to the monomer removed and allowing this to swell for several days. The gel is radio-fluorogenic with no fluorescent background and has a measurable fluorescence signal in

UV light with a few Gy of high-energy ionizing radiation. The gel has good reproducibility and the same superlinear dose relationship as in the RFG solutions. The optically corrected fluorescence intensity in an RFG gel was found to obey the same relationship as in an RFG solution with similar values of the parameters  $CT$  and  $E$ . A post irradiation growth in fluorescence intensity is found to be approximately 10% over a few hours after which it remains constant within 3% for up to 1 week. A gel with MPy concentration of 0.3 mM in a 40 mm square cell is considered to be a good candidate for a dosimeter in complex radiation fields.

In chapter 6, the aim was to find a dose-rate independent radiochromic (RC) film that could provide complementary 2D dose information within the dose range used in RFG gel dosimetry, i.e. 2 to 40 Gy. Four radiochromic films (EBT3, MD-V3, HD-V2 and HD810) having different sensitivities to radiation were investigated. All four have high spatial resolution and good reproducibility. The change in absorption (pixel level  $P$ ) for all four films displays a dependence on dose given by  $P(D)/P(0) = (1 + hD/m)/(1 + D/m)$ , where  $h$  is the saturation level,  $P(\infty)/P(0)$ , approached at high doses, and  $m$  is the 'median dose' for which  $P(D)/P(0) = (1+h)/2$ , which is the half-point of the dynamic range of the film between  $P(D)/P(0) = 1$  and  $h$ . The four films were found to be dose rate independent and suitable for different dose ranges. MD-V3 film has a similar dose range, i.e. from a few Gy to tens of Gy, as that used in RFG gel dosimetry and is therefore considered to be the best reference 2D dosimeter in combination with an RFG gel for studying complex radiation fields.

In chapter 7, the aim is to demonstrate the application of a radio-fluorogenic (RFG) gel to the monitoring of non-homogeneous energy deposition (chemical change) in a bulk medium. For this purpose RFG gels of dimensions  $40 \times 40 \times 40 \text{ mm}^3$  were irradiated with an in-house X-ray source which provided collimated beams of 200 kVp X-rays, producing fluorescent tracks in the gels. Single beams and orthogonally-crossed square and round beams were studied. Initially fluorescent images were taken of the bulk gel medium. Finally a slit-scanning method was developed to generate tomographic fluorescent slices of an irradiated gel. Each fluorescent image was recorded by illuminating a thin (2 mm) layer of the gel with UV light and a stack of 40 images was produced by moving the gel on a stage past the slits 1 mm at a time. The JPEG images were used for "3D" views and animations while the raw DNG files provide quantitative cross-sections of the fluorescence intensity after 3D reconstruction, where the optical corrections were applied. The prototype of this slit-scanning device can produce 3D images of fluorescent samples with a resolution of  $\sim 1 \text{ mm}$  in the  $z$  (scanning) direction and much higher (inter-pixel distance) resolution in the  $x$ - $y$  plane.

In conclusion, the underlying radiation chemistry of a deaerated, radio-fluorogenic gel has been studied by measuring the effects of dose, dose rate and concentration of added fluorogenic compound on monomer to polymer conversion and viscosity. In the absence of additive the degree of polymerization increases superlinearly with accumulated dose and inversely with the square root of the dose rate for a given dose, in agreement with a free-radical induced chain reaction with radical-radical termination reactions. With added fluorogene the monomer

conversion and viscosity are decreased indicating a delaying of the chain polymerization process. This results in a dose rate dependence between the square root found for the pure monomer and none, which can be derived by solution of the kinetic equations in the mechanism proposed. The intensity of the fluorescence of an RFG gel, as measured by raw, digital CCD images, is directly proportional to the monomer conversion and also displays a superlinear dependence on dose. Three-dimensional reconstructions of the fluorescence in a gel subjected to irradiation with crossed X-ray beams is made possible by a simple slit-scanning technique that produces a stack of individual fluorescent slices. Applying the JPEG images 3D animations of the fluorescence of the irradiated volume can be made. Using the raw, DNG images quantitative representations of cross-sections through the image can be made. Conversion of the fluorescence intensity to a 3D dose distribution using the relationships and kinetic parameters developed for homogeneous irradiation of solution and gel samples remains to be implemented. A fully automated, user friendly version of the slit-scanning equipment, which is under construction, should make the method more appropriate for use in the clinic to validate computer-generated treatment plans in radiotherapy.

# Samenvatting

Polymere gels waarvan de chemische en/of fysische eigenschappen veranderen bij blootstelling aan ioniserende straling kunnen in beginsel worden gebruikt als 3D stralingsdosimeters, als de verandering kan worden uitgelezen. Om geschikt te zijn als 3D stralingsdosimeter in de medische kliniek moet een gel dosimeter in het ideale geval aan de volgende voorwaarden voldoen: 1) gemakkelijk beschikbaar zijn en reproduceerbaar te vervaardigen; 2) stabiel en homogeen zijn in de tijd over het hele volume; 3) (ongeveer) weefsel equivalent zijn voor straling over een volume zoals dat in de kliniek wordt gebruikt; 4) voldoen aan de voorwaarden voor kwaliteitsgarantie (QA = quality assurance) met een sub-millimeter isotrope ruimtelijke resolutie en een absolute dosisnauwkeurigheid van 3% ( $3\sigma$ ) en een reproduceerbaarheid van 1% ( $3\sigma$ ); 5) onafhankelijk zijn van dosistempo en kwantumenergie van de straling, en zonder effecten van temperatuur en druk; 6) een onmiddellijke (meetbare) respons opleveren. Verschillende uitleestechnieken als magnetische resonantie (MRI) en optische computer tomografie (OCT) kunnen worden toegepast om de 3D verdeling van de geabsorbeerde dosis in de gel te reconstrueren. Veel soorten gel dosimeters zijn onderzocht, maar gel dosimetrie bevindt zich nog steeds in de onderzoeksfase en de introductie in routinematig klinisch gebruik gaat langzaam. De radiofluorogene (RFG) gel bestudeerd in dit proefschrift heeft verschillende voordelen boven andere polymere gels: Hij bestaat slechts uit twee componenten, het monomeer tertiair-butyl acrylaat (TBA) en de fluorogene stof maleimido-pyreen (MPy), en is daarom gemakkelijker te reproduceren, optisch helder voor en na bestraling, en de stralingsgeïnduceerde fluorescentie kan gemakkelijk worden gemeten. Om de mogelijkheden van deze gel in de kliniek te evalueren is in dit proefschrift een gedetailleerd onderzoek gedaan naar de eigenschappen en het gedrag van de RFG gel als dosimeter.

In hoofdstuk 1 wordt achtergrond informatie en literatuur relevant voor dit proefschrift gegeven inclusief diagnostische methodes, behandelprocedures in de stralingstherapie, en tegenwoordig gebruikte of voorgestelde technieken. Een korte geschiedenis van eerder werk gedaan aan RFG gels vóór dit proefschrift wordt ook gegeven, samen met een overzicht van de inhoud van het proefschrift.

In hoofdstuk 2 is het doel de stralingsgeïnduceerde polymerisatie te onderzoeken van gels gemaakt met alleen TBA om een stralingschemische basis te verschaffen van de gel voor radiofluorogene dosisafbeelding toepassingen. De dosis- en dosissnelheid-afhankelijkheid worden bestudeerd omdat deze zowel de gelvorming procedure als het dosimetriscie copolymerisatieproces in een radiofluorogene oplossing of gel beïnvloeden. De gravimetrisch bepaalde fractie monomeer-polymeer conversie,  $C_M$ , neemt superlineair toe met de dosis  $D$ [Gy].



Tot  $C_M \approx 40\%$  en over het dosistempo gebied  $D' = 3,5$  tot  $49 \text{ cGy}\cdot\text{s}^{-1}$  wordt de dosisaafhankelijkheid gegeven door  $C_M = [1 + AC_M]KD/\sqrt{D'}$  met  $K = 1,43 \times 10^{-3} \text{ Gy}^{-0,5}\cdot\text{s}^{-0,5}$  en  $A = 0,70$ . Voor  $C_M \geq 15\%$  is de gel quasi vast en vertoont een geringe neiging om uit te vloeien op een tijdschaal van een uur of meer. TBA heeft twee functies in de gel: eerst vormt het een quasi vaste transparante 3D gel. Dit proces is beheersbaar en reproduceerbaar. In tweede instantie ondergaat TBA een stralings-geïnduceerde co-polymerisatie met een fluorogene stof, indien aanwezig in het gel netwerk, wat verder onderzocht zal worden in hoofdstuk 3.

In hoofdstuk 3 worden de stralings-geïnduceerde veranderingen in de fysische en chemische eigenschappen van een radiofluorogene oplossing van MPy in TBA gepresenteerd. De oplossing blijft optisch helder en vertoont een permanente fluorescentie in UV licht na bestraling met hoogenergetische ioniserende straling. RFG oplossingen met verschillende MPy concentraties werden onderzocht en er werd ontdekt dat  $C_M$  een superlineaire afhankelijkheid van de dosis had, net als TBA alleen. Echter de aanwezigheid van MPy had een negatief effect op de absolute waarde van  $C_M$  onder dezelfde bestralingscondities. Deze reductie van de totale polymeer opbrengst door MPy wordt toegeschreven aan een veel lagere propagatiesnelheid voor maleimido-radicaal keten einden dan voor de acrylaat radicalen van TBA. Het blauwe pixel niveau,  $P_B$ , van ruwe DNG afbeeldingen van de fluorescentie was lineair afhankelijk van de camera sluitertijd,  $s$ . De intensiteit,  $I_M$ , wordt gedefinieerd als  $P_B/s$ .  $I_M$  bleek superlineair af te hangen van de dosis en kan worden weergegeven met de vergelijking  $I_M = (1 + A_{IM} D)K_{IM} D$ , waarin de parameter  $K_{IM}$  de helling is van de lineaire afhankelijkheid van  $I_M$  voor de lage dosis limiet en  $A_{IM}D$  de superlineaire toename van  $I_M$  met de dosis. Na correctie voor verzwakking van het UV excitatie licht en zelfabsorptie voldoet  $K_{IM}$  aan de relatie  $K_{IM} = C\Gamma/(1 + \sqrt{D'/E[S]})$  met  $E = 0,453 \text{ s}^{0,5}\cdot\text{mM}^{-1}\cdot\text{Gy}^{-0,5}$  en  $C\Gamma = 111 \text{ pixel-niveau}\cdot\text{s}^{-1}\cdot\text{Gy}^{-1}$  voor de gebruikte detectie condities. Dit maakt bepaling van een onbekend dosistempo mogelijk als de RFG oplossing wordt gebruikt als dosimetrische substantie.

In hoofdstuk 4 wordt de stof N-(1-pyrenyl)acrylamide (PyAM) onderzocht in de hoop daarmee het negatieve effect van MPy op de monomeer conversie en daardoor op de fluorescentie opbrengst te elimineren. In het op de TUD gesynthetiseerde PyAM is de maleimide groep van MPy vervangen door een acrylamide groep. De redenering was gebaseerd op de verwachting dat de acrylamide groep in PyAM sneller zou polymeriseren dan de maleimide groep in MPy en dicht bij de acrylaat groep van TBA. PyAM bleek inderdaad fluorogeen met een emissiespectrum na copolymerisatie gelijk aan dat van MPy. De fluorescentie intensiteit was ook superlineair met de dosis en een factor 3 of meer hoger dan voor MPy bij dezelfde waarde van concentratie en dosis. Ongelukkigigerwijs bleek de extinctiecoëfficiënt van PyAM in het nabije UV (het excitatie gebied) een orde van grootte hoger dan die van MPy. Dat resulteert in een sterke verzwakking van het excitatie licht zelfs in een 1 cm cel bij een opgeloste concentratie van  $\sim 1 \text{ mM}$ . Dit maakt toepassing voor 3D dosimetrie, zelfs in kleine volumina, minder praktisch ten gevolge van de plaatsafhankelijke correcties voor UV verzwakking. Verder vertoont PyAM zelfs een groter negatief effect op de graad van monomeer conversie dan MPy. Daarom is besloten om het commercieel beschikbare MPy te blijven gebruiken in het vervolg van dit proefschrift.

In hoofdstuk 5 worden gereconstrueerde RFG gels onderzocht en vergeleken met RFG oplossingen. De gereconstrueerde gels werden gemaakt door eerst het monomeer TBA te bestralen dat quasi-vast wordt bij ~15% monomeer-naar-polymeer conversie ( $C_M$ ). Na verwijdering van resterend monomeer door evacuatie wordt de gel gereconstrueerd door toevoeging van een volume MPy opgelost in TBA, gelijk aan het volume verwijderd monomeer, aan het overgebleven polymeer en dit te laten zwellen gedurende enkele dagen. De gel is radiofluorogeen zonder fluorescerende achtergrond en geeft een meetbaar fluorescentie signaal in UV licht na een paar Gy aan hoogenergetische ioniserende straling. De gel heeft een goede reproduceerbaarheid en dezelfde superlineaire relatie als in de RFG oplossingen. De optisch gecorrigeerde fluorescentie intensiteit in een RFG gel voldoet aan dezelfde relatie als in een RFG oplossing met gelijke waarden voor de parameters  $CF$  en  $E$ . Een toename in fluorescentie intensiteit na bestraling van ongeveer 10% over een paar uur werd gevonden en deze blijft constant binnen 3% gedurende 1 week. Een gel met MPy concentratie van 0,3 mM in een  $40 \times 40 \times 70$  mm<sup>3</sup> cel wordt beschouwd als een goede kandidaat voor 3D dosimetrie in complexe stralingsvelden.

In hoofdstuk 6 was de doelstelling om een dosistempo onafhankelijke radiochrome (RC) film te vinden die complementaire 2D dosis informatie kon verschaffen over het dosisgebied gebruikt in RFG gel dosimetrie, van 2 tot 40 Gy. Vier radiochrome films (EBT3, MD-V3, HD-V2 en HD810) met verschillende gevoeligheid voor straling werden onderzocht. Alle vier hebben een hoge ruimtelijke resolutie. De verandering in absorptie (pixel niveau  $P$ ) voor alle vier de films vertoont een afhankelijkheid van de dosis gegeven door  $P(D)/P(0) = (1 + hD/m)/(1 + D/m)$  waar  $h$  het verzadigingsniveau bereikt bij hoge doses is en  $m$  de “mediane dosis” waarvoor  $P(D)/P(0) = 1$ , wat de halfwaarde is van de dynamische range van de film tussen  $P(D)/P(0) = 1$  en  $h$ . De films bleken dosissnelheid onafhankelijk en geschikt voor verschillende dosisgebieden. MD-V3 film heeft eenzelfde dosisgebied, van een paar Gy tot tientallen Gy, als gebruikt wordt in gel dosimetrie en wordt daarom beschouwd als de beste referentie 2D dosimeter in combinatie met een RFG gel voor het bestuderen van complexe stralingsvelden.

In hoofdstuk 7 is de doelstelling om de toepassing van een radiofluorogene (RFG) gel voor het monitoren van niet-homogene energiedepositie (chemische verandering) in een uitgebreid medium te demonstreren. Voor dit doel werden RFG gels met afmetingen van  $40 \times 40 \times 40$  cm<sup>3</sup> bestraald met een op het RID aanwezige Röntgen machine. Deze geeft gecollimeerde bundels van 200 kVp Röntgenstralen die fluorescerende sporen maken in de gels. Enkelvoudige bundels en orthogonaal kruisende vierkante en ronde bundels werden bestudeerd. Aanvankelijk werden afbeeldingen gemaakt van de fluorescentie van het hele gel medium. Later werd een lichtvlak scan methode ontwikkeld om fluorescerende tomografische plakken van een bestraalde gel te genereren. Elke fluorescentie afbeelding werd vastgelegd door een dunne (2 mm) laag van de gel met UV licht aan te stralen en een stapeling van 40 afbeeldingen werd gemaakt door de gel op een plateau in stappen van 1 mm langs de verlichtingsspleten te verplaatsen. De JPEG afbeeldingen werden gebruikt voor “3D” plaatjes en animaties, terwijl de ruwe DNG files kwantitatieve doorsneden van de fluorescentie intensiteit verschaffen na 3D reconstructie en

toepassing van de optische correcties. Het prototype van dit lichtvlak scan apparaat kan 3D afbeeldingen van fluorescerende monsters produceren met een resolutie van ~1 mm in de z (scan) richting en een veel hogere (inter- pixel afstand) resolutie in het xy vlak.

Concluderend is de fundamentele stralingschemie van een zuurstofvrije radiofluorogene gel bestudeerd door het meten van de effecten van dosis, dosistempo en concentratie van toegevoegde fluorogene stof op de monomeer naar polymeer conversie en viscositeit. Zonder de toegevoegde stof neemt de polymerisatiegraad superlineair toe met de opgebouwde dosis en omgekeerd met de wortel uit de dosissnelheid voor een gegeven dosis, in overeenstemming met een door vrije radicalen geïnduceerde ketenreactie met radicaal-radicaal terminatie. Met toegevoegde fluorogene stof namen de monomeer conversie en viscositeit af wat duidt op vertraging van het keten polymerisatie proces. Dit resulteert in een dosistempo afhankelijkheid tussen de wortelafhankelijkheid voor het pure monomeer en onafhankelijkheid, wat afgeleid kan worden door oplossing van de kinetiek vergelijkingen in het voorgestelde mechanisme. De intensiteit van de fluorescentie van een RFG gel, zoals gemeten uit ruwe digitale CCD afbeeldingen, is lineair evenredig met de monomeer conversie en vertoont een superlineaire afhankelijkheid van de dosis. Driedimensionale reconstructie van de fluorescentie in een gel blootgesteld aan bestraling met gekruiste Röntgen bundels wordt mogelijk gemaakt door een eenvoudige lichtvlak scan techniek die een stapeling van individuele fluorescerende plakken produceert. Met de JPEG afbeeldingen kunnen 3D animaties van de fluorescentie in het bestraalde volume gemaakt worden. Met de ruwe DNG afbeeldingen kunnen kwantitatieve weergaven van doorsneden van de afbeelding worden gemaakt. Omzetting van de fluorescentie intensiteit naar een 3D dosisverdeling door middel van de relaties en kinetische parameters ontwikkeld voor homogene bestraling van oplossingen en gel monsters moet nog worden geïmplementeerd. Een volledig geautomatiseerde, gebruikersvriendelijke versie van de lichtvlak scan apparatuur, die onder constructie is, moet de methode meer geschikt maken voor gebruik in de kliniek om computer gegenereerde behandelplannen in de radiotherapie te evalueren.

# Acknowledgements

I am very grateful that many people helped me tremendously in finishing my thesis and shared the most enjoyable time in the past four years. Words never sufficiently express my gratitude but I would like to express it to them.

I would like to thank my promotor Prof. Dr. Bert Wolterbeek. Thank you for giving me the opportunity to start my PhD research. I enjoyed the regular meetings discussing the project and the casual conversations that made me feel relaxed at RIH. I appreciate your kindness, visionary guidance and valuable advices during my PhD study.

I would like to thank my supervisor Dr. Antonia Denkova. Thank you for your continuous support and motivating me to become an independent researcher, to collaborate with group members and other research institutes. Thank you for reviewing my papers and draft thesis with valuable and inspirational advice. You have kindly created a free and open research environment at RIH that made me and other group members feel like a big family. I was always impressed by your enthusiasm and positive attitude towards work and family. You are a good model to me!

My special thanks to my advisor Dr. John Warman, who is the "father" of this research topic and is not paid by the university but comes twice a week for our meetings (and the beer). Thank you for your tremendous effort and helping me with patience in the research project. That is where I not only gained most of the knowledge but also useful tips for doing research. I value your critical mind that you could always point out my mistakes. You showed me that a PhD procedure is to produce a scientist capable of independent thought and novel research, including literature search of peer reviewed work. I have to decide that what I want to be and where I want to go with my life. Thanks to Lee and Thijs for reviewing my papers, translating the summary and giving useful advice for the thesis. Lee, I'm glad that you are always willing to share your knowledge of stones with me. And Thijs, thank you for the technical assistance with the experiments.

Alessia, you showed me a different way of being! I'm lucky to have you as my officemate and for working together with you for three years. Thank you for all the help you gave me in the experiments and the contribution to the new experimental setup. Thank you for the useful suggestions you gave for my papers and thesis. I learned from you how to cheer up about everything and share interesting things in life. Thank you for bringing in the coffee machine. We really enjoyed the quality coffee after daily lunch break. It was my unforgettable experience attending conferences and travel together with you in Sweden and Japan! Wish you all the best with your family members and a good life in Belgium!

Thanks to my office mates, Guzman, Ilza, Kaustab. You made the room warm and cozy. And of course during the enjoyable moment of the daily coffee break in our office together with Giacomo, Valerio, Francesco, Patricia, Pablo, Robin, Jasper, Vallin, Stephan, Eelco, Mohita and others. Thanks to all the members in the RIH group, Adrie, Astrid, Baukje, Dosti, Elisabeth, Folkert, Henk, Jose, Josette, Koos, Marcel, Marlies, Mehmet, Rupali, Tayser, Yvonne, Zheng, ... all together a comfortable atmosphere! I enjoyed the cookies Wednesday, High-Tea, and the wonderful beer time in 't Koepeltje! Boxue, thanks for the interesting chats! Ganglin, wish you a good time with your family and working in China. My thanks to the Chinese group in the RID, Bei, Beien, Bo, Bowei, Chuang, Fengjiao, Haixing, Hongde, Jiawei, Kun, Wenqin, Xiaoyu, Xinmin, Xuefei, Yaolin, Yibole, Zhaolong, Zhouzhou. Thank you for organizing the nice parties and your excellent Chinese cooking.

I would also like to thank my friends in Delft, van Dijk and Yong, for the Dutch lessons and sharing the fantastic time together. Boris, Gabi, Elwin, Heni, thank you for your kind invitation for parties and the cycling in the Netherlands. It was also a great time when we travelled together. Jianbin, Wenhao, Linfeng, Siqi, I wish you good work and a bright future in China with your PhD's degree of TU Delft.

Finally, I would like to express my appreciation to my parents for their constant love and support, and to my brother who has always been supportive to me and gave me encouragement. Lars, thank you for your company, sharing happiness and overcoming difficulties.

# Curriculum Vitae

Tiantian Yao was born on September 18<sup>th</sup> 1988 in Anhui Province, China. She obtained her Bachelor's degree in Applied Physics in 2012 at the University of Science and Technology of China. During her bachelor study she participated in the research project of particle simulation of Laser-Plasma-Interaction using LPIC++. From September 2012 to January 2017 she was a PhD candidate in the section Radiation and Isotopes for Health (RIH) of the department of Radiation Science and Technology at Delft University of Technology. Her PhD study was focused on 3D radiation dosimetry using a radio-fluorogenic gel under the supervision of Dr. ir. A.G. Denkova and Dr. J.M. Warman, which eventually led to this thesis. She is currently working in section RIH as a postdoctoral researcher on the project simulation of neutron activation for production of Ho-166 microspheres.

# List of Publications

1. **Yao, T.**, Denkova, A.G., Warman, J.M., 2014. Polymer-gel formation and reformation on irradiation of tertiary-butyl acrylate. *Radiation Physics and Chemistry* 97, 147-152.
2. **Yao, T.**, Gasparini, A., Denkova, A.G., Warman, J.M., 2015. Radiation-chemical and optical properties of a radio-fluorogenic gel. *Journal of Physics: Conference Series*. IOP Publishing, p. 012036.
3. **Yao, T.**, Luthjens, L.H., Gasparini, A., Warman, J.M., 2016. A study of four radiochromic films currently used for (2D) radiation dosimetry. *Radiation Physics and Chemistry*. *accepted for publication*.
4. **Yao, T.**, Gasparini, A., de Haas, M.P., Luthjens, L.H., Denkova, A.G., Warman, J.M.. The 3D reconstruction of ionizing-radiation beams using a radio-fluorogenic gel with tomographic fluorescent imaging. *Physics in Medicine and Biology*. *submitted*.
5. **Yao, T.**, Gasparini, A., Luthjens, L.H., Warman, J.M.. Radiation-chemical and optical properties of radio-fluorogenic solutions and gels. *in preparation*.
6. Gasparini, A., **Yao, T.**, Luthjens, L.H., Warman, J.M., de Haas, M.P., Denkova, A.G.. Light slit scanning prototype for 3D imaging of radio-fluorogenic gel dosimeters. *EPJ Techniques and Instrumentation*. *submitted*.
7. Gasparini, A., Gougy, L., **Yao, T.**, de Haas, M.P., Luthjens, L.H., Warman, J.M., Denkova, A.G.. Inter- and intra-batch dose accuracy in radio-fluorogenic gels for 3D dosimetry. *in preparation*.